The Thesis Committee for Brittney Maryah Pollard
Certifies that this is the approved version of the following thesis:

Reactivation of fractures as discrete shear zones from fluid enhanced reaction softening, Harquahala metamorphic core complex, west-central Arizona

APPROVED BY
SUPERVISING COMMITTEE:

Supervisor:

Sharon Mosher

John Singleton

Daniel Stockli

Whitney Behr

Reactivation of fractures as discrete shear zones from fluid enhanced reaction softening, Harquahala metamorphic core complex, west-central Arizona

by

Brittney Maryah Pollard, B.S.

Thesis

Presented to the Faculty of the Graduate School of

The University of Texas at Austin

in Partial Fulfillment

of the Requirements

for the Degree of

Master of Science in Geological Sciences

The University of Texas at Austin

May, 2014

Dedicated to my mother,

Constance Jo Wyzard

Acknowledgements

I have many people to thank for helping me over the course of this thesis research. First and foremost, I would like to thank my advisor, Sharon Mosher. Sharon managed to always be available to help me look at thin sections, answer questions, examine data, and provide advice, no matter how busy she was with her duties as Dean. I appreciate her ability to challenge me, her use of the Socratic method, and her impressive knowledge base. Most of all, however, I would like to thank Sharon for her constant support, for not pushing me too hard when I was struggling, and for never giving up on me. Her patience and understanding were crucial for my success in the program, and I am truly grateful!

Secondly, I would like to thank my committee member and mentor, John Singleton. John provided help and advice through every aspect of this research. He helped to train me in the field, assisted in much of my field work, showed me how to use Adobe Illustrator to make maps, and helped me with structural analysis. He also helped train me to do Electron Backscatter Diffraction (EBSD) analysis and to interpret the results. He taught me much of what I know about microstructures, helped me with thin section interpretations, exchanged countless long emails with me, served as a springboard for my ideas, and always answered my numerous questions in great detail.

I'm very thankful to my other two committee members, Danny Stockli and Whitney Behr. Danny taught me a lot about the origin and interpretation of microstructures, allowed me to use the Laser Ablation Inductively Coupled Plasma Mass Spectrometer (LA-ICP-MS) for U-Pb analysis, and helped greatly with data reduction and interpretation. I also would like to thank his wife, Lisa Stockli, for training me on the LA-ICP-MS and for teaching me how to reduce my data.

Whitney Behr was essential in helping me to identify holes in my interpretations overall. She challenged my interpretations and required me to defend my ideas; my final research conclusions are much better for it. I would like to thank her for looking at thin sections with me, exchanging long emails with me, discussing my data, helping me with my EBSD interpretations, and answering many questions.

I am thankful to Jim Gardner for allowing me to use the Fourier Transform Infrared (FTIR) Spectroscopy lab and for looking at a couple of thin sections with me. I am incredibly grateful for all the help, training, and advice I received from Kenny Befus on the FTIR spectroscopy portion of my study. Kenny trained me on sample prep and on how to use the spectrometer, but most importantly, he helped me to work through many of the kinks I encountered from conducting analyses on fine grained mylonites, which is no small challenge. I would also like to thank Gayle Gleason and Andy Kronenberg for answering my FTIR spectroscopy questions via email.

I'm thankful to Jaime Barnes for allowing me to use the stable isotope lab and for answering questions on sample prep, and to Toti Larson for analyzing my stable isotope samples, Liz Cassel for introducing me to stable isotope work, and Afu Lin for letting me borrow his tools and a microscope for sample prep. I am grateful to Mike Prior for prepping my zircon sample for U-Pb analysis, and to Mike Prior, Spencer Seaman, and Liz Cassel for help on running the LA-ICP-MS. I am also indebted to Donggao Zhou for training on electron microbeam techniques and for help on the ESEM, to Paul Betka whose talents in ESEM troubleshooting saved more than one of my sessions from failure, to Lauren Jacob who assisted with carbon coating, and to Greg Thompson for thin section construction. I would like to especially thank Tim Shin who acted as my representative in Texas when I was working in Idaho, fulfilling a million tiny favors for me that added

up to a lot. I am also extremely grateful to Sharon Mosher and the Jackson School of Geosciences for providing funding.

Lastly, I would like to thank my family and friends, particularly my brother, Ben, and boyfriend, Andrew, for all their support. I am most indebted to my mother, Connie, who passed away during the course of this thesis. My mother provided me with endless encouragement, support, and love during this program. Her role in my success in this program and elsewhere in my life cannot be overstated.

Abstract

Reactivation of fractures as discrete shear zones from fluid enhanced reaction softening, Harquahala metamorphic core complex, west-central Arizona

Brittney Maryah Pollard, M.S. Geo. Sci.

The University of Texas at Austin, 2014

Supervisor: Sharon Mosher

Discrete (mm- to m-scale) mylonitic shear zones in the northeastern Harquahala metamorphic core complex, Arizona, show evidence of fluid-mineral interactions catalyzing deformation and metamorphism. Many contain a deformed central epidote vein with adjacent bleached haloes and flanking paired shear zones that indicate significant fluid-rock interaction during deformation. An integration of structural and geochemical methods was employed to understand timing, metamorphic conditions, and physiochemical processes responsible for producing the discrete shear zones. Field and microstructural evidence suggest the zones initiated on antecedent fractures. Electron backscatter diffraction (EBSD) analyses show a significant coaxial contribution to the shear, and quartz deformation predominately by prism <a> slip, along with some rhomb <a> slip, suggesting amphibolite-facies conditions during shearing. Fourier Transform Infrared spectroscopy analyses of quartz reveal higher water contents within shear zones

than within country rocks, indicating fluid infiltration synchronous with shearing. Stable isotope analyses of quartz and feldspar from mylonites are consistent with an igneous or metamorphic fluid origin.

Microstructural observations suggest that the zone morphology with epidote veins, bleached haloes, and flanking discrete paired shear zones was developed predominantly from reaction softening mechanisms. The increase in deformation from bleached rock to flanking shear zones is marked by progressive modal increases in biotite and myrmekite, and modal decreases in K-feldspar, and locally epidote and titanite. Myrmekitic textures recrystallized readily and resulted in progressively greater grain size reduction of feldspar, which aided in the progressive alignment and linkage of the biotite grains, which together concentrated the deformation in bands. Volume reduction resulting from some of the metamorphic reactions may have led to a positive feedback cycle among fluid infiltration, metamorphism and deformation. U-Pb isotope analyses of syn-metamorphic titanite yield an age of ~70 Ma, suggesting the shear zones formed during cooling of the Late Cretaceous (75.5±1.3 Ma) Brown's Canyon pluton, consistent with their top-to-the-southwest sense of shear, rather than during top-to-the-northeast directed Miocene metamorphic core complex exhumation.

Petrography, EBSD analyses, and U-Pb dating of titanite from other (non-discrete) mylonites in the area imply most formed synchronously with the discrete shear zone mylonites. Only rare, scattered mylonites show features consistent with metamorphic core complex exhumation.

Table of Contents

List of Tables

List of Figures

Chapter 1: Introduction and Background

1.1 INTRODUCTION

The Harquahala Mountains exemplify a unique structural setting in which two very different tectonic domains spatially overlap (e.g., Richard, 1988; Spencer and Reynolds, 1990). The Harquahala Mountains form the easternmost range of the Late Cretaceous east-trending Maria Fold and Thrust Belt (MFTB), and form the southernmost metamorphic core complex (MCC) of the mid-Tertiary southeast-trending lower Colorado River extensional corridor, a region where large-magnitude extension was accommodated by the transport of middle crustal rocks to shallower levels along large low-angle normal faults (i.e., detachment faults; Figures 1.1, 1.2). The MCC footwall in the northeastern part of the Harquahala Mountains exposes the structurally deepest rocks of the range and is host to numerous sets of mylonitic shear zones that are anomalous in appearance, distribution, and kinematic history to both MFTB-style and MCC-style shear zones in the region. These shear zones overprint a penetratively deformed gneissic fabric that is similar to that exposed in many other MCC footwalls in Arizona and California (Richard, 1988). The shear zones are particularly well developed in the Stone Corral area of the Harquahala MCC (Figures 1.3-1.5).

The mylonitic fabrics in this area dip moderately to steeply south, have well-developed southwest-trending stretching lineations, display predominantly top-to-the-southwest senses of shear, and are composed of porphyroclasts in fine grained matrixes. Many mylonites are localized in discrete mm- to cm-scale zones (Figures 1.4, 1.5). These characteristics differ from the shear zones associated with the MFTB, which are spatially related to thrust faults, have a marked schistosity, weak lineation, top-to-the-south sense of shear, and a pronounced granoblastic texture (Richard et al., 1990). They

also differ from the shear zones associated with the Miocene MCCs, which are gently dipping, display a top-to-the-northeast sense of shear, and cover large kilometer-scale expanses of rock. In contrast to the Harquahala shear zones, discrete mm- to cm-scale shear zones in other MCCs tend to be isolated in areas near the detachment faults, having formed during the late, cooler periods of detachment faulting.

Despite these differences, the shear zones in the Harquahala MCC have been interpreted to have formed during Miocene MCC deformation, beginning with mylonitization in the few hundred meter thick Stone Corral ridge shear zone, and continuing with progressively more localized deformation into the very discrete (mm- to cm-scale) shear zones as the footwall was exhumed to shallower crustal levels (Richard et al., 1990). The uniqueness of the Harquahala shear zones relative to the shear zones of other MCCs has been attributed to the location of the Harquahala Mountains as the southernmost MCC in the Colorado River extensional corridor. At this border position, the Harquahala Mountains could have served as a transfer zone, in which extension was transferred from the middle crustal detachment fault system associated with the MCCs to a more distributed upper crustal system defined by multiple small and widespread normal faults in the hanging wall mountain ranges to the south and southeast (Richard et al., 1990). The anomalous shear zones, therefore, may be transitional between the broad, gently dipping, brittle-ductile style of mid-crustal MCC footwall deformation and the more distributed, steeply dipping, brittle style of upper crustal deformation characteristic of the bordering hanging wall mountain ranges.

However, seismic imaging of western Arizona has revealed that the MCC footwall deformation fabrics that are exposed in the northeastern Harquahala MCC continue into the subsurface beneath the mountains to the south, and then resurface again in the White Tank metamorphic core complex, which is outside the limits of the Colorado

River extensional corridor (Reynolds et al., 1994). Subsurface MCC-type fabrics seem to be regionally extensive as the mylonitic MCC fabrics exposed in the Buckskin-Rawhide, Harcuvar, and White Tank core complexes also continue into the subsurface. In some areas, the subsurface fabrics form elongate domes that may represent incipient MCC-type structures (Kruger et al., 2006). These data suggest that the Harquahala MCC does not mark the termination of the mid-crustal MCC-type extensional system but instead is simply the last exposure of the system in the Colorado River extensional corridor. In light of this seismic data, the transfer zone hypothesis and the origin of the anomalous shear zones need to be reevaluated.

In addition to the uncertain tectonic origin of the anomalous shear zones in the Harquahala Mountains, the physical and chemical processes that resulted in the localization of shear in discrete zones within relatively homogeneous granite are also unknown. Several different strain softening processes may be active during the formation of shear zones in general, including changes in deformation mechanisms, geometric softening (i.e., grain rotation and lattice reorientation for easy slip), continuous recrystallization, reaction softening, chemical softening, pore fluid effects, and shear heating (White et al., 1980). Many of these processes potentially may have interacted to form the shear zones in the Harquahala MCC.

Additionally, the presence of antecedent fractures may also have been an important control on shear zone development. Fractures may serve as weak planes that may be reactivated to accommodate further deformation. Mancktelow and Pennacchioni (2005) described discrete shear zones in the Tauern window of the eastern Alps that formed through the reactivation of older fractures. Many of these Alpine shear zones contain deformed central epidote veins surrounded by bleached haloes and flanking paired shear zones, which are very similar in appearance to some of the discrete shear

zones in the Harquahala MCC (Figure 1.5). The physical and chemical processes that resulted in the formation of the Harquahala shear zones into discrete zones, including the possible significance of antecedent fractures, are addressed in this thesis.

1.2 GEOLOGIC SETTING

The rocks of the Harquahala Mountains record an extremely long and complicated geologic history, with multiple stages of deformation and metamorphism spanning from the Precambrian through the Tertiary (Richard, 1988). Most of the earlier events have not been thoroughly studied in this particular range, and the details are in many cases poorly understood. The events active during the Cretaceous and Tertiary, however, have received much attention in recent decades (e.g., Hardy, 1984; Richard, 1988; Reynolds et al., 1988; Richard et al., 1990; Liviccari and Geissman, 2001). The three major deformation events that occurred during this time and the metamorphism associated with each of them are described below.

1.2.1 Late Jurassic-Cretaceous MFTB Deformation

The Maria Fold and Thrust Belt is composed of a band of mountain ranges trending approximately east-west across southeastern California and western Arizona (Figure 1.1). The mountain ranges are generally characterized by thick skinned deformation with thrust faults emplacing Precambrian rocks on Paleozoic and Mesozoic sections (see Spencer and Reynolds, 1990 for a review). The belt is also characterized by extensive folding, and the majority of the deformation tends to be south-vergent.

In the Harquahala Mountains, the Harquahala thrust system records a minimum of 16 kilometers of south-vergent slip (Richard, 1988). The timing of the deformation is poorly constrained between 160 to 69 Ma. The rocks in the range experienced gradually greater burial depths beneath the thrust from the southwest to the northeast, which

resulted in higher metamorphic temperatures and pressures in the northeastern part of the range. Peak metamorphism was static, occurring after movement on the thrust system ended. The metamorphic mineral assemblage of garnet, staurolite, and kyanite in the structurally deepest rocks in the range specify metamorphic temperatures of >500°C and pressures of ≥ 4.5 kbar (Richard, 1988).

1.2.2 Late Cretaceous Gneissic Deformation

A poorly understood stage of deformation that occurred post-MFTB-style contraction but pre-Miocene MCC-style extension is visible in the denuded interiors of several of the MCCs in Arizona, including the Buckskin-Rawhide, Harcuvar, White Tank, Santa Catalina-Rincon, and possibly the Coyote Mountains MCCs (Richard, personal comm., 2010). A similar type of deformation is present in the Whipple Mountains MCC of southeastern California (Richard, 1988). The deformation is typically characterized by widespread gneissic and/or migmatitic fabrics that were developed synchronously with the intrusion of Late Cretaceous plutons. Upper crustal structures that would balance this middle crustal deformation in magnitude have not been identified in any area; therefore, the event may have only affected mid-crustal rocks and died out at shallower crustal levels (Richard, 1988). Whether the deformation was the result of a late stage of contraction or an early stage of extension is unknown. However, because the deformation commenced relatively soon after thrust faulting ceased, and because the timing of the deformation is roughly coincident to the timing of the onset of flat slab subduction of the underlying Farallon Plate, the deformation may very well be the expression of late orogenic processes, such as synconvergent extension, that operated in the MFTB and other mountain ranges in southern Arizona (Bykerk-Kauffman, 1990; Richard, 1988).

Abundant evidence for synconvergent extension has been recognized throughout the MFTB and the Cordillera of the western U.S., and is commonly attributed to gravitational collapse processes (Hodges and Walker, 1992, and references therein; Boettcher and Mosher, 1998; Wells and Hoisch, 2008). The evidence for extension is found in the regional prevalence of normal-sense shear zones in the upper and middle crust that are of Late Cretaceous age. The gneissic and migmatitic deformation exposed in the MCC footwalls may be a more distributed style of this extension at deeper levels in the crust.

In the Harquahala Mountains, the deformation that resulted in the gneissic fabric was initiated soon after static amphibolite facies peak metamorphism occurred in the northeastern part of the range (Richard, 1988). The Brown's Canyon and Stone Corral granite plutons, interpreted to have originated from crustal melting of rocks at greater depth during post-thrust peak metamorphism, were emplaced during this time and then partially deformed on their margins. The rocks of the northeastern Harquahala Mountains were reworked into a pervasive gneissic fabric during the deformation event, whereas the shallower rocks of the north-central Harquahala Mountains adopted a west- to southwest-dipping schistose fabric cut by several folded and boudinaged pegmatites associated with the Brown's Canyon granite pluton (Richard, 1988). Importantly, mylonitic shear zones related to the Late Cretaceous deformation event have not been identified in the north-central or northeastern parts of the range.

Related deformation may have also been very mildly expressed in the Paleozoic metasedimentary rocks of the much shallower southwestern and south-central Harquahala Mountains (Richard, 1988). These rocks contain a minor post-thrusting, south- to southwest-dipping cleavage with stretching lineations trending 030°, northeast-vergent folds, and minor top-to-the-north ductile shear zones (Richard, 1988). This deformation,

where visible, is faint in the southwest and becomes more pronounced to the northeast, but cannot be absolutely correlated with the schistose and gneissic deformation in the north-central and northeastern part of the range. The deformation in the southwest and south-central section of the range is different in nature than the deformation in the north-central and northeastern section of the range, making the relationship between them unclear. The two sections may possibly represent the responses of shallower crust and deeper crust, respectively, to the same deformation event (Richard, 1988).

In the northeastern Harquahala Mountains, amphibolite-facies conditions persisted during this deformation event, but temperature and pressure were slightly lower than during static peak metamorphism (Richard, 1988). Two-feldspar geothermometry and phengite geobarometry performed on metamorphosed Harquahala granite and Brown's Canyon granite yielded temperatures and pressures between 470-570 °C and 3-4 kbar, respectively (Richard, 1988). The association of the growth of actinolitic hornblende across some of the fabric is also consistent with amphibolite-facies conditions (Richard, 1988). The age of post-thrust deformation and amphibolite facies metamorphism is estimated at ~69-72 Ma by $^{40}Ar/^{39}Ar$ age dating of hornblende in Brown's Canyon granite in the northeastern part of the range and of Proterozoic amphibolite in the central part of the range (Richard, 1988).

1.2.3 Miocene MCC Deformation

The MCCs of the lower Colorado River extensional corridor include the Whipple Mountains of southeastern California and the Buckskin-Rawhide, Harcuvar, and Harquahala Mountains of west-central Arizona (Figure 1.1). These MCCs are considered to be associated with one master detachment fault system, and therefore share a broadly similar kinematic history (Spencer and Reynolds, 1990). In the Harquahala Mountains,

detachment fault mylonitization initiated before the emplacement of Miocene dikes as some of these dikes crosscut mylonitized rocks below the Eagle Eye detachment fault. Mylonitization must have continued after dike emplacement because some of the mafic dikes are deformed by mylonitic shear zones (Richard et al., 1990). One of the mafic dikes outside of the study area yielded a total gas $^{40}Ar/^{39}Ar$ hornblende age of ~22 Ma (but did not yield a plateau age; Richard et al., 1990). Prior and Stockli (2013) have proposed a younger age of ~17-18 Ma for the initiation of detachment faulting on the basis of zircon (U-Th)/He ages.

The temperature of mylonitization in the Harquahala MCC is estimated to have been between ~300-400 °C on the basis of $^{40}Ar/^{39}Ar$ dating of biotite (with a closure temperature of ~300-350 °C, dependent on cooling rates; McDougall and Harrison, 1999) in rocks from the northeastern Harquahala MCC that yielded ages ranging from ~13-20 Ma, and $^{40}Ar/^{39}Ar$ dating of muscovite (with a closure temperature of ~350-400 °C; McDougall and Harrison, 1999; Harrison et al., 2009) that yielded an age of ~30 Ma (Richard et al., 1990). The detachment fault was likely still active around ~16 Ma because movement on the Bullard section of the detachment system in the adjacent Harcuvar Mountains postdates K-metasomatism and mineralization dated at ~16 and ~17 Ma. After detachment faulting ended, extension continued and was accommodated by younger high angle normal faults that crosscut the detachment fault. Extension may have continued through ~12-13 Ma on the basis of biotite and potassium feldspar $^{40}Ar/^{39}Ar$ analyses (Richard et al., 1990) and apatite (U-Th)/He analyses which yielded this age (Prior and Stockli, 2013).

The Eagle Eye detachment fault is a gently dipping normal fault with an estimated initial dip of ~30°-40° based on $^{40}Ar/^{39}Ar$ cooling ages obtained along the projected length of the detachment fault (Richard, 1988; Richard et al., 1990). This dip is also

supported by the restoration of tilted dikes to their originally vertical, pre-detachment fault orientation (Richard et al., 1990), although paleomagnetic data suggests the original dip may have been as shallow as ~15° (Livaccari and Geissman, 2001). Detachment faulting in the Harquahala Mountains resulted in displacement of the hanging wall to the northeast by a minimum of 18-25 km relative to the footwall on the basis of correlation of separated rock units (Richard, 1988). This displacement is much less than that estimated for the other ranges in the Whipple detachment system, which accommodated as much as 50-75 km of top-to-the-northeast movement (Reynolds and Spencer, 1985; Spencer and Reynolds, 1991).

1.3 Project Purpose and Methods

This study has been designed to integrate structural and geochemical techniques to understand the timing, metamorphic conditions, and physiochemical processes responsible for producing the discrete shear zones of the Stone Corral area in the Harquahala MCC (Figures 1.3-1.5). Additionally, the relationship, if any, between the discrete shear zones and the adjacent Stone Corral ridge shear zone was also investigated. A variety of methods were employed in this study to pursue these goals. Field work was conducted to map the spatial distribution of the shear zones in the Stone Corral area and to document their features. Detailed petrographic observations were attained to examine the conditions of deformation and metamorphism of the country rock and shear zones, to determine if the shear zones represented one or several episodes of deformation, and to identify the strain softening processes responsible for localizing deformation in the discrete shear zones and for producing the morphology of zones with central epidote veins, bleached haloes, and flanking paired shear zones (Figure 1.5).

A number of different analytical methods were employed as well, including electron backscatter diffraction analysis of quartz to determine the type of shear (coaxial vs. non-coaxial), the sense of shear, and the slip systems active during deformation. Fourier Transform Infrared spectroscopy of intragranular quartz was performed to examine if water was present during deformation. Stable isotope analysis of quartz, feldspar, and epidote was utilized to determine the sources of fluids that may have been present during deformation. U-Pb isotope analysis of zircon was undertaken to determine the age of the Brown's Canyon pluton, which hosts many of the shear zones, and U-Pb isotope analysis of syn-metamorphic (syn-mylonitic) titanite was undertaken to determine an age for the deformation of some of the shear zones.

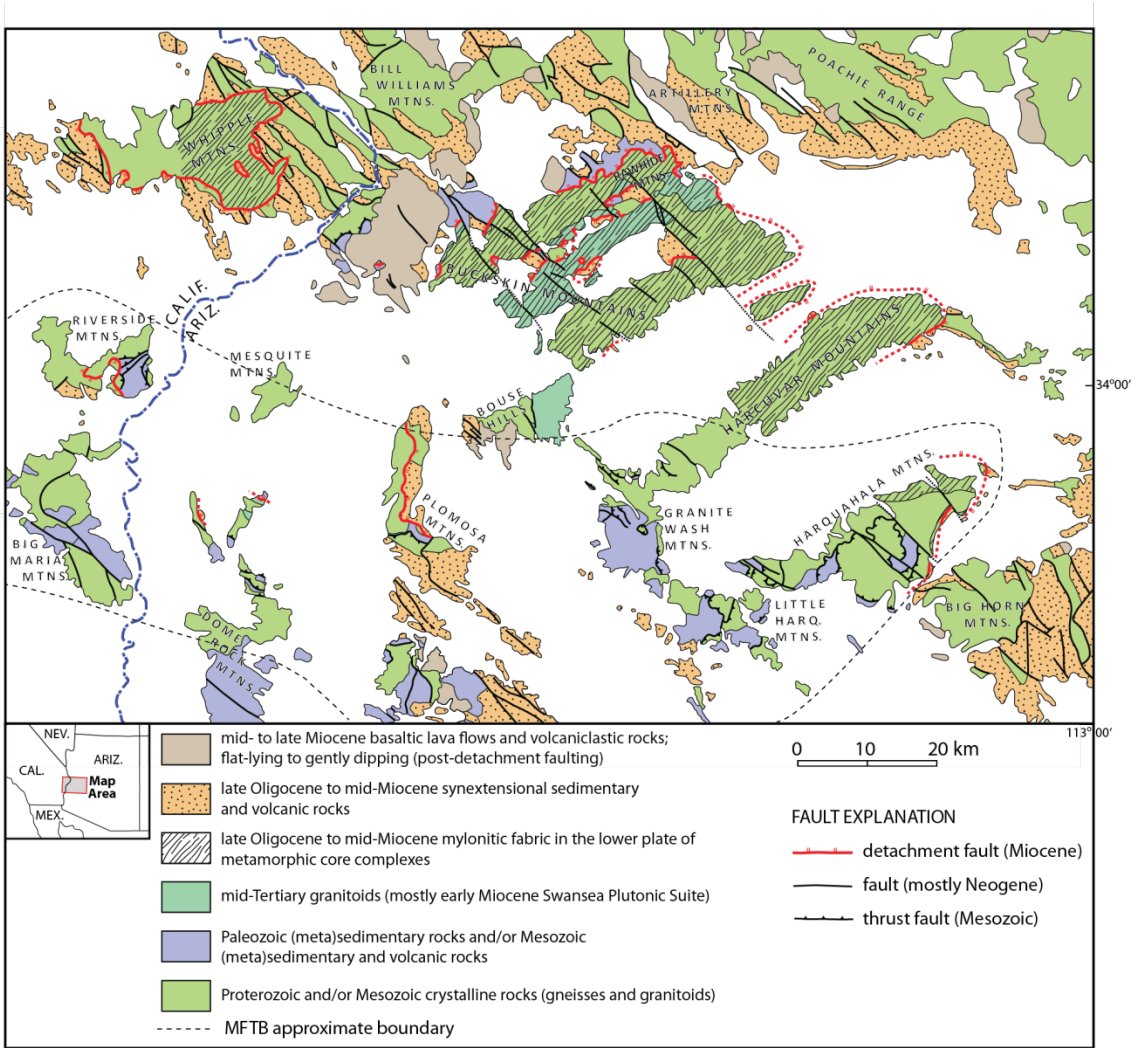

Figure 1.1: Geologic map of the lower Colorado River extensional corridor, southeastern California and west-central Arizona (from Singleton and Mosher, 2012; modified from Spencer and Reynolds, 1989). The black dotted line delineating the eastern portion of the MFTB is modified from Spencer and Reynolds (1990).

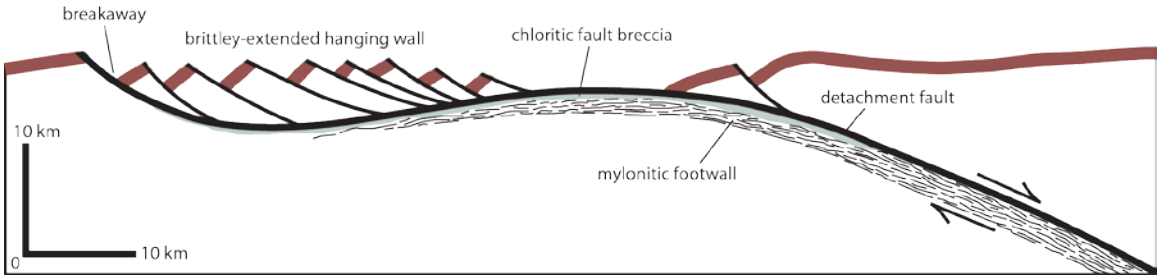

Figure 1.2: Simplified anatomy of a metamorphic core complex in cross-sectional view (from Singleton, 2011).

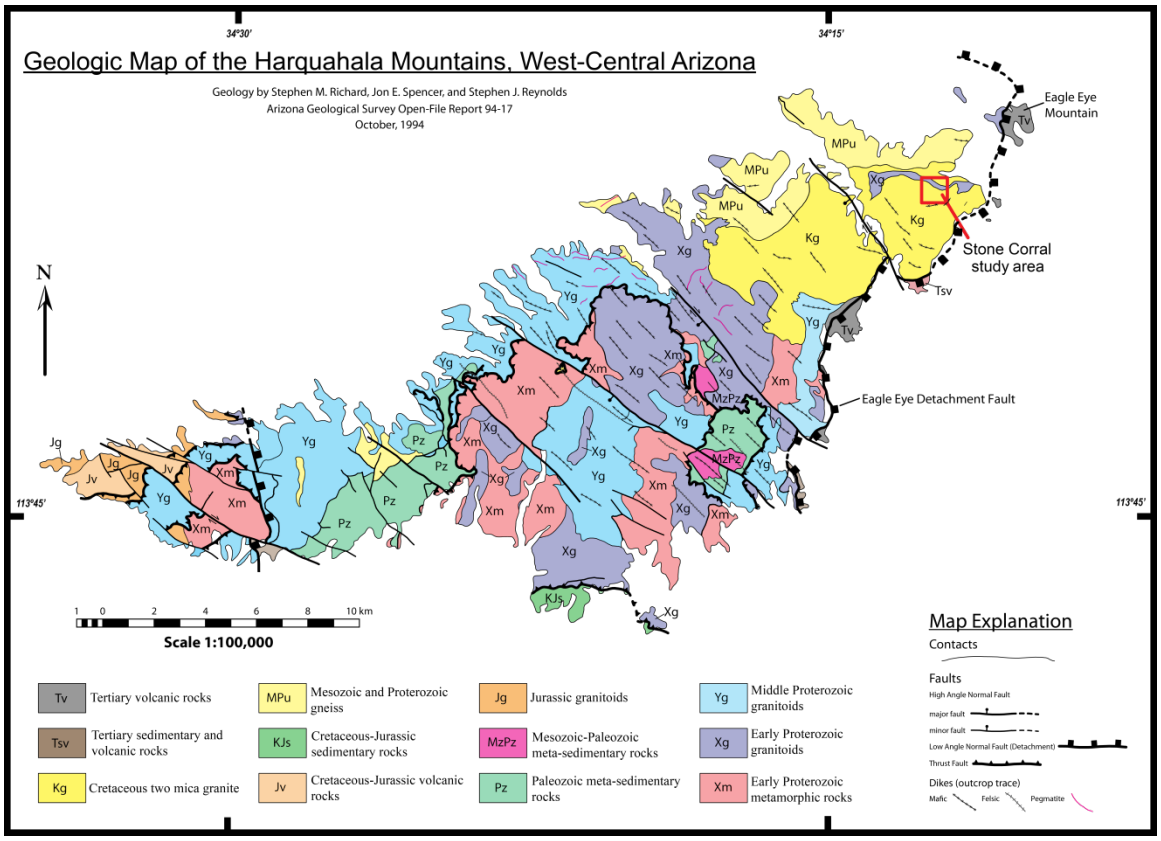

Figure 1.3: Geologic map of the Harquahala Mountains (from Prior and Stockli, 2013). The red box marks the location of the Stone Corral study area. The detachment fault that exhumed the Harquahala Mountains is best exposed on Eagle Eye Mountain.

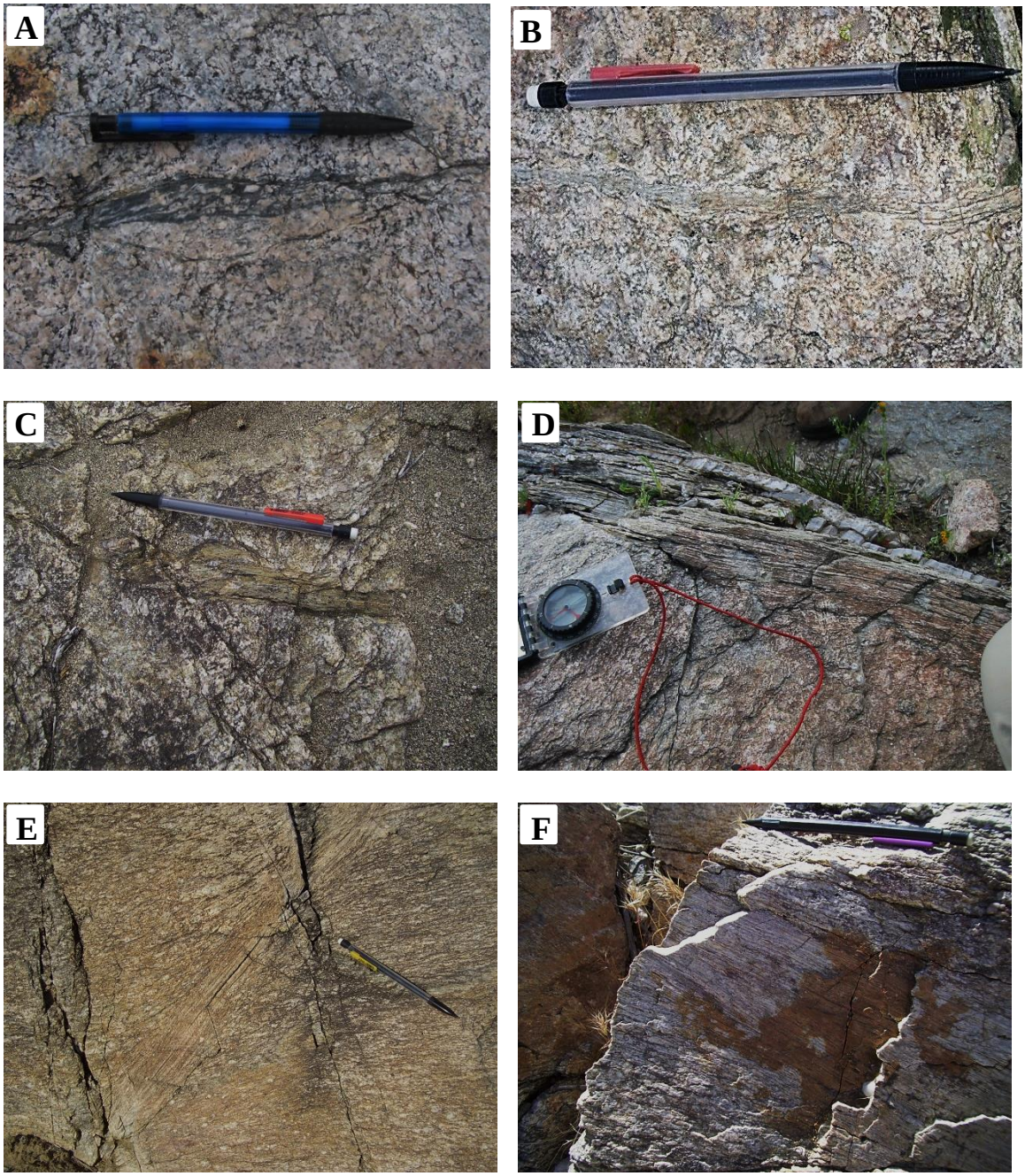

Figure 1.4: Photographs of discrete, narrow shear zones in the Stone Corral study area. Note the sharp boundaries between shear zones and country rocks. A-D) View looking down, south at top; E) Cross-sectional view facing west; F) Cross-sectional view facing east. Samples collected from locations: B) Sample 17; (D) Samples H1 (from shear zone) and H2 (from country rock).

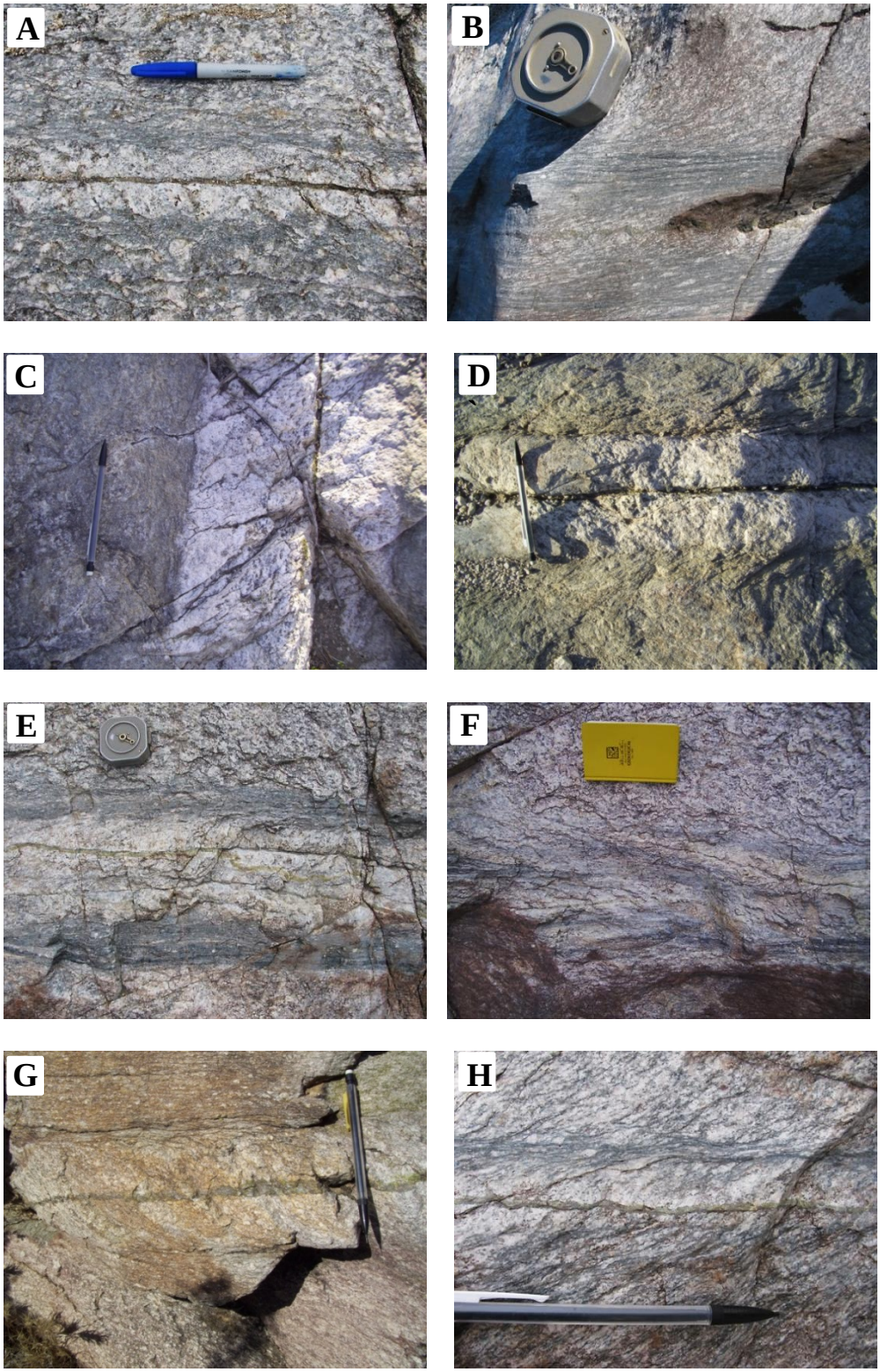

Figure 1.5: (caption continued on next page).

Figure 1.5: (continued from previous page). Photographs of discrete shear zones with a central epidote vein, bleached halo, and flanking paired shear zones morphology. A-D) Bleached haloes and flanking paired shear zones are symmetric around the central vein; B, E) Central epidote veins are folded; F) Discrete shear zone bifurcates to the left into multiple shear zones, similar in appearance to a fracture splay. This shear zone does not maintain thickness along strike; G) Central epidote vein crosscuts the foliation in the bleached halo; H) Bleached halo and flanking shear zone are only well developed above the vein; the vein crosscuts the country rock foliation below. Samples collected from locations: A) HQ-C; D) HAR-56; E-F) SCM-51; compare to hand sample in Figure 2.13B; G) HAR-16; compare to hand sample in Figure 2.13C.

Chapter 2: Field Work and Basic Structural Analysis

The ~1 km^2 Stone Corral study area, located in the northeastern end of the Harquahala Mountains, exposes numerous shear zones previously interpreted to have developed during Miocene metamorphic core complex exhumation (Richard et al., 1990). The most pronounced structural feature in the study area is the Stone Corral ridge shear zone, which is several hundred meters wide and is exposed along the northern face of Stone Corral ridge (Figures 2.1, 2.2), a large hill in the southern part of the area that is adjacent to Stone Corral mountain, a larger hill to the west that was informally named by Richard (1988). The discrete (mm- to m-scale) shear zones that are the primary focus of this study are exposed in a long narrow wash that trends eastward in the northern part of the study area and north-northeastward in the western part of the study area (Figure 2.1). Additionally, isolated ~0.5-1 m thick shear zones are located south of the Stone Corral ridge shear zone near the crest of Stone Corral ridge (Figures 2.1, 2.2). All the shear zones in the study area cut the S-type Late Cretaceous Brown's Canyon granite and Stone Corral granite, which intruded Proterozoic granite (Figure 1.3). Some of the Proterozoic granite may be interleaved with the Stone Corral granite within the study area (Richard, 1988; Richard et al., 1990), but the units are not decipherable in the field.

This chapter presents the results of the field portion of the study, including description of the country rocks and the different shear zones in the study area. In this thesis, the term "country rock" refers to the commonly foliated Late Cretaceous Brown's Canyon granite and Stone Corral granite that host the numerous shear zones in the study area. The discrete shear zones exposed in the wash in the northern part of the study area were studied in more detail. To test the hypothesis that the discrete shear zones initiated on antecedent fractures, detailed measurements were made on the thicknesses of the

discrete shear zones and the spacing between the shear zones so that fracture spacing analyses could be performed.

2.1 METHODS

Basic geological mapping in the Stone Corral area of the Harquahala Mountains was conducted at three different sites in the study area (Figure 2.1). One site was mapped at a 1:2,000 scale over an area of ~385 m x 470 m that encompasses a portion of the major (few hundred meters thick) Stone Corral ridge shear zone (Figure 2.2). The other two sites were mapped at a 1:200 scale in two small areas of the wash at the base of Stone Corral ridge (Figures 2.3, 2.4). One of these areas is located within the 1:2,000 map area, and the other is located farther to the east (Figure 2.1). These two areas provide the best exposure of the discrete shear zones, which are not well exposed outside of the wash. Cross-sections were constructed from the map data to document the spatial arrangements and geometry of the discrete shear zones in these two areas (Figure 2.5). Orientation, length, and thickness measurements were also collected from all the shear zones exposed in the wash between the two mapped areas, but because of the extreme length to width ratio of the wash, the maps were not extended to include the data. A total of thirty-nine samples of mylonite and country rock were collected from across the study area (Tables 2.1, 2.2); nearly all of the samples were oriented. Three additional mylonite samples were collected from the Eagle Eye detachment fault at Eagle Eye Mountain for comparison (Figure 1.3, Table 2.2).

To accurately determine the spacing between the discrete shear zones, measurements were collected across two transects perpendicular to the average strikes of the shear zones in the 1:200 scale mapped areas (Figures 2.3, 2.4). For each transect, a measuring tape was laid out across the study areas at a bearing of ~175° and the strike,

dip, and thickness of each shear zone were measured where the shear zones intersected the measuring tape (Figure 2.6). The spacing between the shear zones was also measured along the two transects. Detailed descriptions of each shear zone and the exposed lengths of the shear zones were also documented.

2.2 FIELD WORK RESULTS

2.2.1 Country Rock

The foliation in the country rock north of (and structurally below) the Stone Corral ridge shear zone differs in orientation from the country rock south of (and structurally above) the shear zone (Figure 2.7A). The country rock north of the shear zone has undergone more intense deformation, characterized by a moderate gneissic texture, which is locally protomylonitic, with feldspar porphyroclast-rich layers alternating with thin biotite-rich bands. In most areas this foliation is subhorizontal, but very subtle broad, undulating folds are present locally. A lineation is present on many outcrops but is typically subtle. In some places the lineation seems to be a mineral lineation, defined by slightly aligned mafic minerals, but at other places it seems to be a faint quartz stretching lineation. Both types of lineations generally trend to the northeast or southwest and are gently plunging. Some lineations, however, trend to the northwest and a single lineation trends to the southeast (Figure 2.7A).

The country rock south of the Stone Corral ridge shear zone lacks the subhorizontal gneissic texture of the country rock to the north. Aligned biotite in the rock defines a weak to moderate foliation in some outcrops, the intensity of which varies from outcrop to outcrop. The foliated rock generally grades into rock that appears to be undeformed farther to the south. The foliation in the rocks dips moderately southwest (Figure 2.7A).

2.2.2 Mylonitic Shear Zones

Several different types of mylonitic shear zones are present in the field area (Figures 1.4, 1.5, 2.8-2.10). In the northern part of the study area (north of the Stone Corral ridge shear zone), a few distinct types of shear zones are present. The discrete (mm- to m-scale) shear zones that are the main focus of this study are variably affected by bleaching and veining (Figures 1.4, 1.5, 2.9, 2.10). One atypical shear zone, located in the western 1:200 map area, is similar to many of the other discrete shear zones in style but has a very different orientation (Figure 2.3, from which sample SCM-4 was collected). Another type of shear zone present in the northern part of the study area forms thin (~1 mm) mylonitic veneers on fractured surfaces (Figure 2.8A-C). In the Stone Corral ridge shear zone, the mylonitization is continuous across the entire zone but varies in intensity (Figure 2.8D-E). In the southern part of the study area (south of the Stone Corral ridge shear zone), isolated ~0.5-1 meter-thick shear zones are present along the crest of Stone Corral ridge (Figures 2.1, 2.2, 2.8F). The field characteristics of these different sets of mylonites are discussed in detail, beginning with the mylonites in the northern part of the study area and continuing southward.

2.2.2.1 Discrete mylonitic shear zones

The discrete millimeter- to centimeter-scale (and more rarely, meter-scale) shear zones in the northern part of the study area comprise numerous subparallel sets that are exposed in the wash at the base of Stone Corral ridge. The shear zones dip moderately to steeply south-southeast (Figure 2.11A). The mylonites contain well-defined stretching lineations that plunge moderately southwest. Some display feldspar σ-type porphyroclasts that indicate a top-to-the-southwest sense of shear (Figure 2.12). The boundary between the individual shear zones and the country rock generally appears sharp, and in many areas, the country rock foliation is visibly reoriented into parallelism

with the shear zone boundary over a distance of only millimeters or a few centimeters (Figures 1.5B, 2.9A-C, 2.12B). The reorientation of the foliation into the shear zones along with the obliquity between the shear zone foliation and the shear zone boundary are the most widespread and reliable shear sense indicators at the outcrop scale, and indicate a top-to-the-southwest sense of shear (Figure 2.12B).

The shear zones range in thickness from a few millimeters to over a meter (Figure 2.13). The lengths of most of the shear zones cannot be traced to their terminations because of lack of exposure. A few of the smaller shear zones become non-mylonitized fractures along strike (Figure 2.4). Some of the shear zones can be followed along strike for tens of meters across several outcrops before losing exposure.

Many of the discrete zones in the area have been affected by bleaching and appear starkly white against the country rock (Figures 1.5, 2.10). In a small number of these zones, the bleached rock appears to be sheared and has no visible association with veins or central fractures. However, the bleached rock more commonly occurs as a less deformed halo around an epidote or quartz-epidote vein. Many of the epidote veins are also deformed, appearing broken, boudinaged, or folded (Figures 1.5B, E, 2.9D-F).

Discrete zones with the bleached halo morphology typically also display flanking paired mylonitic or ultramylonitic shear zones (Figure 1.5). In the small, poorly developed discrete zones in the area, the flanking zones are not penetratively mylonitized, but are characterized by biotite-lined shear bands crosscutting an older foliation. The closely spaced biotite bands parallel the bleached halo and vein (Figure 1.5A, H), and many of these small-scale zones may even lack a central vein (Figure 2.10A).

In some of the shear zones, the bleached haloes are symmetric about the central veins, whereas in others, the haloes exhibit a highly asymmetric pattern (Figure 1.5). Whereas shearing is generally most intense outside the border of the bleached halo

(typically in the form of flanking paired shear zones), in some cases, shear is most intense in rock that is wedged in the central fractured area (Figure 2.10B-C). In rare cases, no clear single boundary separates the bleached rock from the sheared rock as the bleaching and shearing overlap irregularly (Figure 2.10D). In some places, the fine-grained ultramylonitic flanking shear zones appear to be partially bleached as well (Fig. 2.14A). When rock samples of the shear zones are cut perpendicular to foliation and sub-parallel to lineation, the boundary between the bleached zones and the flanking paired shear zones looks much less sharp than in the field, with the bleached rock becoming progressively more intermixed with biotite-rich layers from the vein outward (Fig. 2.14B-C).

2.2.2.2 Atypical discrete mylonitic shear zone

A sole discrete mylonitic shear zone is present in the northern part of the study area that is oriented 128°, 60° southwest (Figures 2.3, 2.11A). The mylonite contains a stretching lineation that trends 253° and plunges 60°. The shear zone is 4 cm at its thickest section and includes a 1 cm thick quartz vein at one margin. The vein loses exposure as it is covered by alluvium in both directions along strike. The relationship of this shear zone to the other shear zones in the area is not clear. This shear zone is similar in style to the other discrete shear zones but cuts through the country rock at a very different orientation.

2.2.2.3 Mylonitized veneers on fractured surfaces

In several outcrops throughout the wash at the base of Stone Corral ridge, but particularly in the northeastern part of the study area, fractured surfaces contain an extremely thin (~1 mm) veneer of mylonite upon them (Figure 2.8A-C). These surfaces dip ~35° E-NE (Figure 2.11B). The thin mylonitized veneers do not continue into

neighboring outcrops and do not seem to represent through-going shear zones. These shear zones are, therefore, very different in both style and orientation than the other more common discrete shear zones in the area, but share a similar strike to the sole atypical shear zone described in the previous section.

2.2.2.4 The Stone Corral ridge shear zone

The Stone Corral ridge shear zone varies in apparent thickness along strike from ~125 meters in the eastern part of the study area to ~400 meters in the western part of the study area (Figures 2.1, 2.2). Rock exposure is not continuous in the shear zone as many portions of the shear zone are covered in rubble and colluvium. Overall, mylonitic foliation in the shear zone dips S to SW, and mylonitic lineations plunge variably from 5°-33° S-SW (Figure 2.11C). Rocks within the shear zone vary from protomylonites to ultramylonites (Figure 2.8D-E). The southern and northern boundaries of the shear zone are diffuse, grading into protomylonite and then to foliated country rock. The sense of shear in most of the outcrops is ambiguous, but some of the outcrops at the base of the shear zone (i.e., the northern boundary) contain very clear top-to-the-southwest σ-type feldspar porphyroclasts.

2.2.2.5 Isolated mylonitic shear zones

A few outcrops of non-deformed or slightly foliated granite in the southern part of the study area contain discrete mylonitic shear zones ~0.5-1 meter thick (Figures 2.1, 2.2, 2.8F). The shear zones have shallow to moderate SW to NW dips (Figure 2.11D). The zones contain very well developed stretching lineations with shallow to moderate SW plunges. The relationship of these shear zones to the Stone Corral ridge shear zone is not clear in the field.

2.2.3 Brittle Structures

Extension fractures and veins are widespread throughout the study area. A small number of these features were measured in the two mapped areas in the northern part of the study area where the discrete shear zones are located (Figures 2.3, 2.4). Several different sets of fractures and veins were present in a number of different orientations (Figure 2.7B), likely representing multiple episodes of brittle deformation. Some of the epidote veins are clearly pre- or syn-kinematic with the discrete shear zones as they are present within the zones and then deformed by them (Figures 1.5B, E, 2.9D-F). Other epidote veins, however, crosscut the shear zones and therefore must be younger. Shear fracture surfaces that display generally north-trending, gently plunging slickenlines are also present in the northwestern part of the study area (Figure 2.7C). Some of these striated surfaces are coated by epidote. Much more orientation data would need to be collected to discern amongst the differing sets of fractures and their relationships to each other.

2.3 Fracture Spacing Analysis

In the field, the discrete shear zones are very narrowly defined and locally represent thin layers of mylonite on extension fracture surfaces. These observations suggest that the zones may form a similar pattern as fractures. For this reason, a fracture spacing analysis was conducted.

2.3.1 Methods

Basic fracture spacing analysis was performed on the data collected from the transect lines in the two areas mapped at a 1:200 scale (Figures 2.3, 2.4). Two simple methodologies were used to determine if the spacing between the shear zones and the thicknesses of the shear zones could be related to patterns expected for fracture sets.

First, the coefficient of variation of fracture spacing (standard deviation divided by the mean of fracture spacing measurements) was determined for both study areas (after Gillespie et al., 1999). This calculation was performed to determine if the spacing between the shear zones is random (C_v ~1), clustered (C_v > 1), or evenly spaced (C_v ~0), and more importantly, to see if the results were consistent between the two mapped areas as would be expected if the shear zones formed during the same fracturing event and by the same mechanisms.

The second way of examining the significance of the spacing between the shear zones was to quantify how homogeneously or heterogeneously strain is accommodated in the fracture (i.e., shear zone) sets (Kuiper, 1960; Hooker et al., 2011). To determine this for the shear zones along the two transects, the cumulative thickness (a running sum of the thicknesses of the shear zones from the beginning to the end of the transect line) was plotted against shear zone position on the transect line (Figure 2.15). Homogeneous strain is represented by a line from the origin of the plot (at the position of the first fracture on the transect line) to the cumulative aperture value (at the position of the last fracture on the transect line). The more the cumulative thickness data vary from the line, the more heterogeneous is the strain. If the shear zones were evenly sized and spaced, they would plot on the line, whereas if the shear zones are clustered or have large variations in thicknesses, the data will vary from the line. To quantify the discrepancy between the data and the line, V' (variation) is used. V' is the sum of the absolute values of the maximum and minimum thickness discrepancy values from the homogeneous strain line divided by the cumulative thickness of the shear zones. A V' value of 0 would indicate absolute strain homogeneity whereas a V' value of 1 would indicate that all the strain was accommodated by one fracture (Hooker et al., 2011).

2.3.2 Results

The orientations of the shear zones, the spacing between the shear zones, and the thicknesses of the shear zones along the transect lines in the eastern and western mapped areas are presented in Tables 2.3 and 2.4. The locations of the transect lines and cross-sections constructed from data along the transect lines are presented in Figures 2.3-2.5. The coefficient of variation (C_v) for the spacing data from the two mapped areas differed greatly at 0.74 in the eastern mapped area (suggesting a random spacing if the shear zones initiated as fractures) and 2.29 in the western mapped area (suggesting a clustered spacing if the shear zones initiated as fractures; Table 2.5). The V' values for the two areas were more similar, with a value of 0.57 for the eastern mapped area and a value of 0.45 for the western mapped area, suggesting that strain accommodation was not homogeneous. However, the plots of the data look quite different with most of the points from the eastern transect line plotting above the line of homogeneous strain and most of the points from the western transect line plotting below the line of homogeneous strain (Figure 2.15).

2.3.3 Significance and Problems

The lack of consistency between the results of the fracture spacing analyses in the two mapped areas may result from a number of sampling problems within this study or from issues with processes involved in shear zone evolution. The sample size was extremely small in both mapped areas (both in the number of transect lines measured and in the number of shear zones per transect line). If exposure in the field was better, so that more shear zones were measurable, the results may be different. In the eastern area, a couple of fractures along the transect line were included that appeared to have a very slight amount of shear on them, but it was difficult to be sure. Including them may have affected the results. Also a few of the shear zones were not exposed sufficiently for the

dip to be determined, so the average dip of the two nearest shear zones was used as an estimate and the “true” thickness was calculated using that estimated dip and the width of the zone on the exposed surface. Thus the true thickness may have been incorrect and affected the analysis. Additionally, the fracture spacing analysis techniques were developed for opening mode fractures and not for shear zones. A major assumption in using fracture analysis on shear zones that may have initiated on fractures is that the thicknesses of the shear zones are the same as the thicknesses of the original fracture apertures, which is likely not a reasonable assumption.

2.3.4 Shear Zone Thickness Observations and Implications for Shear Zone Growth

Two outcrops in the study area provide compelling evidence that the discrete shear zones have not maintained their original thicknesses. In one outcrop, a well-developed shear zone appears to have bifurcated into smaller shear zones along its strike (Figure 1.5F). The major shear zone has the morphology defined by central epidote veins, a bleached halo, and flanking paired ultramylonitic shear zones. The smaller zones also have this morphology, but the relationship between the haloes and the ultramylonitic zones is less clear and more transitional. The thicknesses of the haloes and ultramylonitic zones vary along the lengths of the smaller zones. The bifurcation may represent a fracture splay that underwent subsequent bleaching and shearing. The resemblance of the bifurcated shear zone to a fracture splay supports the hypothesis that the discrete shear zones initiated on antecedent fractures.

In the other outcrop, two clearly distinctive 3 cm thick shear zones (without veins or bleaching) coalesce along their strikes into one shear zone (17 cm thick). One of the small shear zones strikes 085° and dips 38° S, whereas the other strikes 100° and dips 59° S. Where they converge, the second shear zone takes on the orientation of the first zone.

Interestingly, the resultant shear zone is thicker (17 cm) than the sum of the two smaller zones. This relationship suggests that the coalescence of smaller shear zones into larger zones may be an important mechanism for shear zone growth. One way this could occur is if the rock between the smaller shear zones experienced more fluid-rock interaction where these shear zones were closer together than farther apart, because this rock may have been infiltrated by fluids from both shear zones, resulting in a greater degree of reaction softening and subsequent shearing (see Chapter 9 for further discussion on reaction softening). Alternatively (or additionally), fracturing and shearing may be cyclical or coeval processes, in which the rock between the shear zones undergoes progressively more fracturing and subsequent shearing as bulk strain increases until the rock is pervasively sheared and a larger shear zone has formed (Mancktelow, 2009).

The thicknesses of 88 discrete shear zones were measured in the field and are presented in Figure 2.13. The most common shear zone thicknesses are ≤5 centimeters, and the majority of the shear zones are ≤40 centimeters thick. Only two shear zones with thicknesses between 40 and 100 centimeters were found. Four shear zones are 100 centimeters thick, and three shear zones are >100 centimeters thick. The gap in thicknesses between ~40-100 centimeters may be due to the coalescence of smaller shear zones into larger shear zones, skipping intermediate sizes. Small zones may converge to form larger zones that may then converge to form considerably larger zones. As larger and larger zones converge, certain intermediate thicknesses may not be attained. Of course, much better exposure would be needed and much more detailed data would have to be obtained to test this hypothesis.

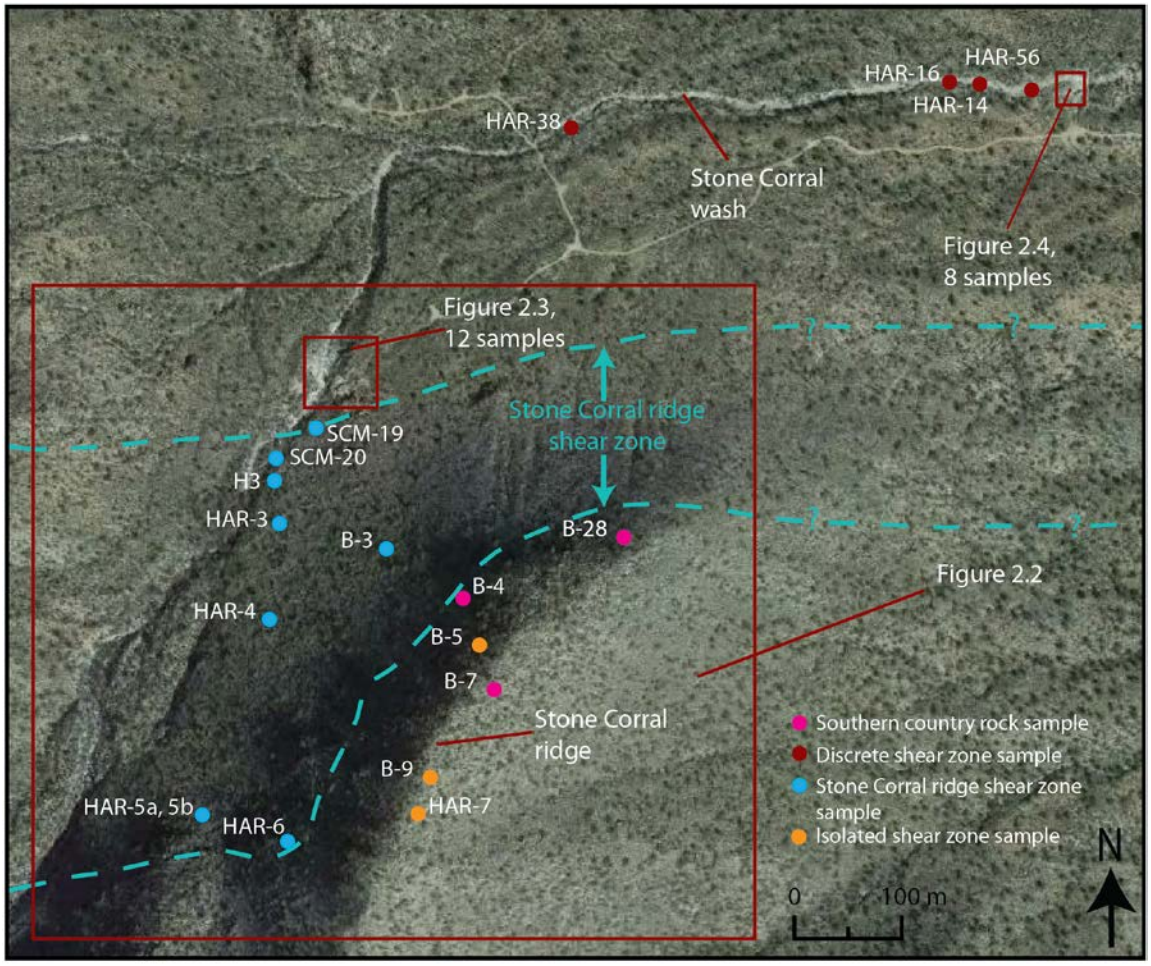

Figure 2.1: Areal photograph of the Stone Corral study area. Locations of mapped areas are documented. The boundaries of the Stone Corral ridge shear zone are outlined in blue. These boundaries were not mapped in detail outside of the area in Figure 2.2, but do extend across the entire study area. Note the locations of Stone Corral ridge and the Stone Corral wash (photograph from Google Earth).

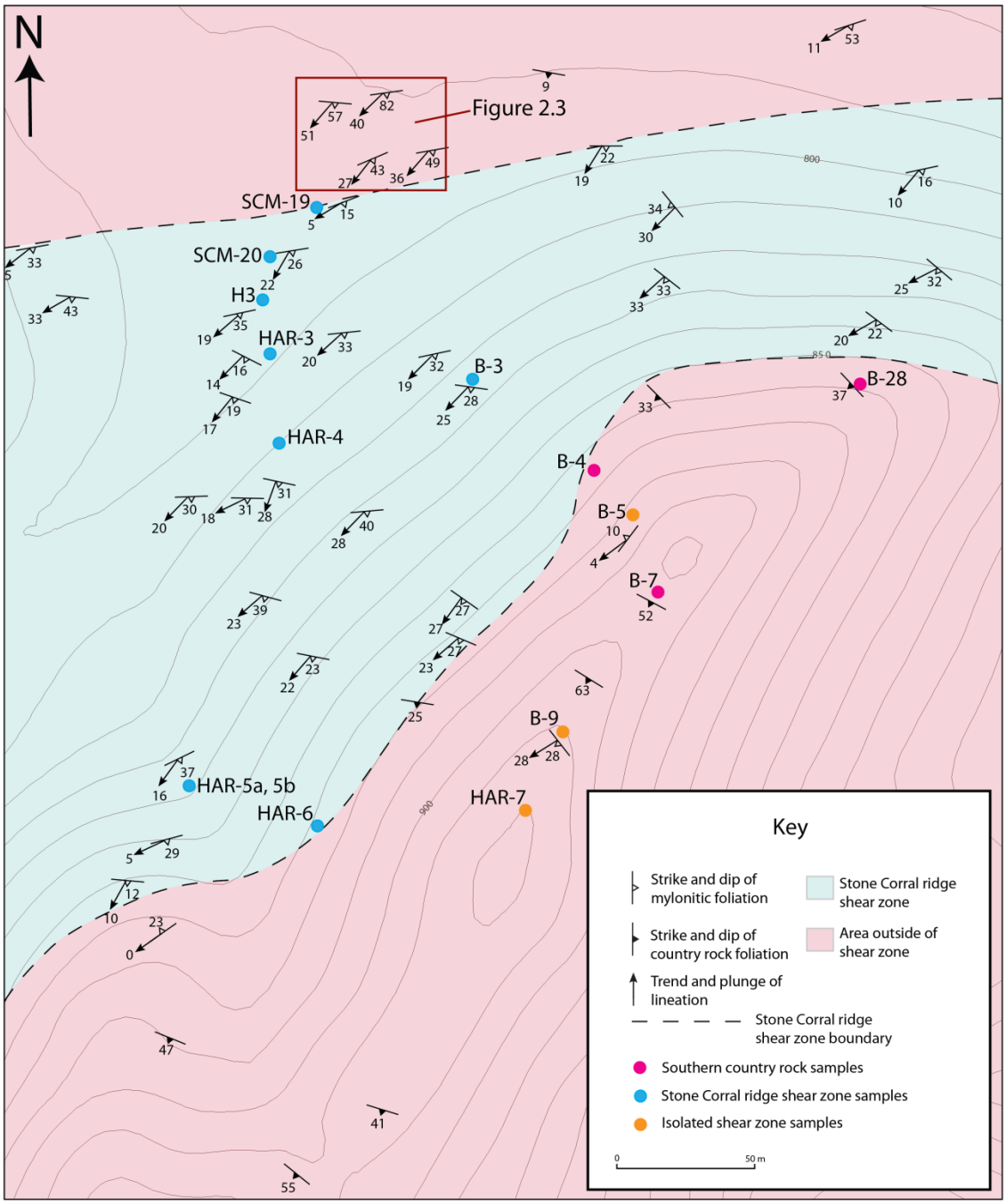

Figure 2.2: Geologic map at 1:2000 scale showing a portion of the Stone Corral ridge shear zone.

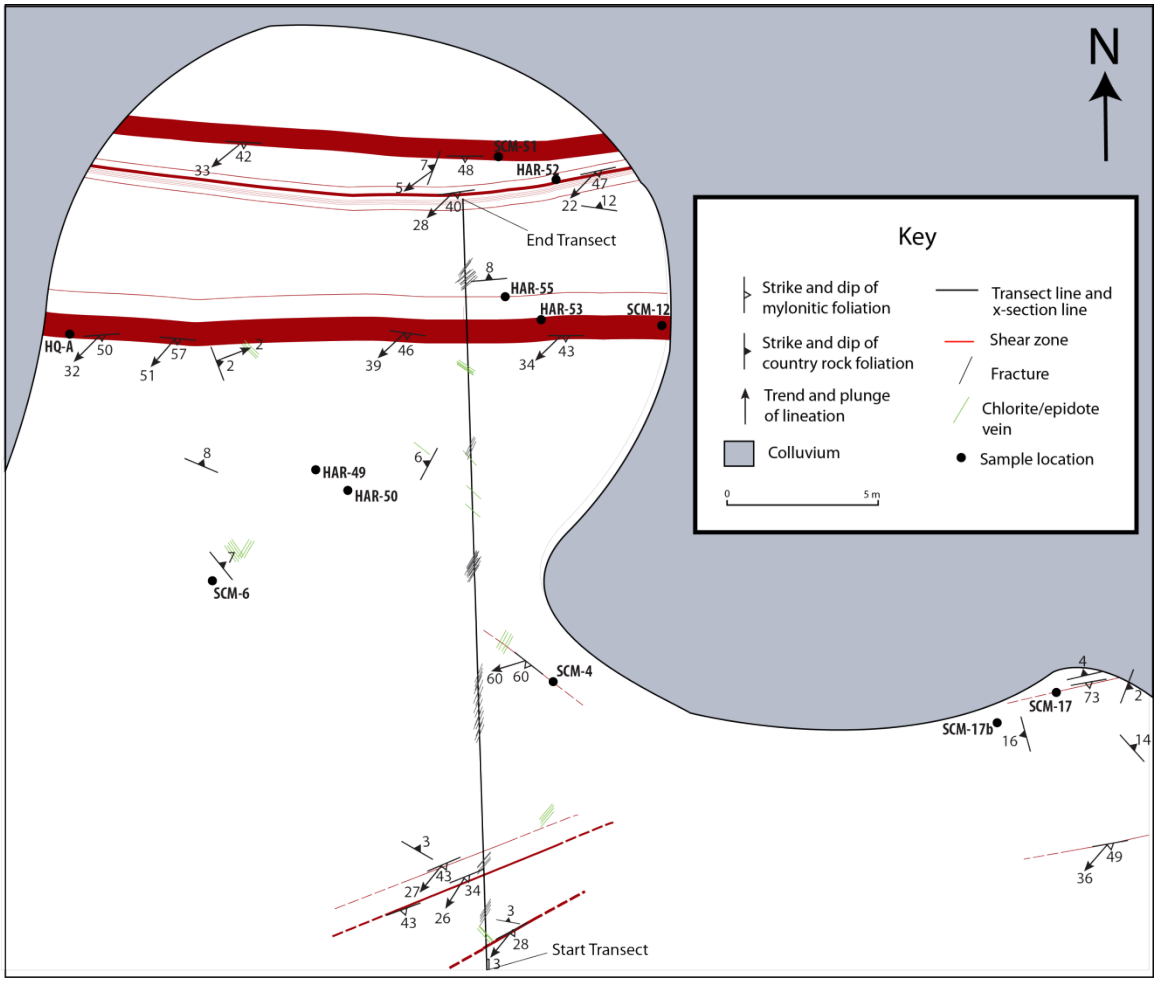

Figure 2.3: Geologic map at 1:200 scale showing the locations of discrete shear zones and the western transect line along which data was collected for fracture spacing analysis. A cross-section along this line is shown in Figure 2.5.

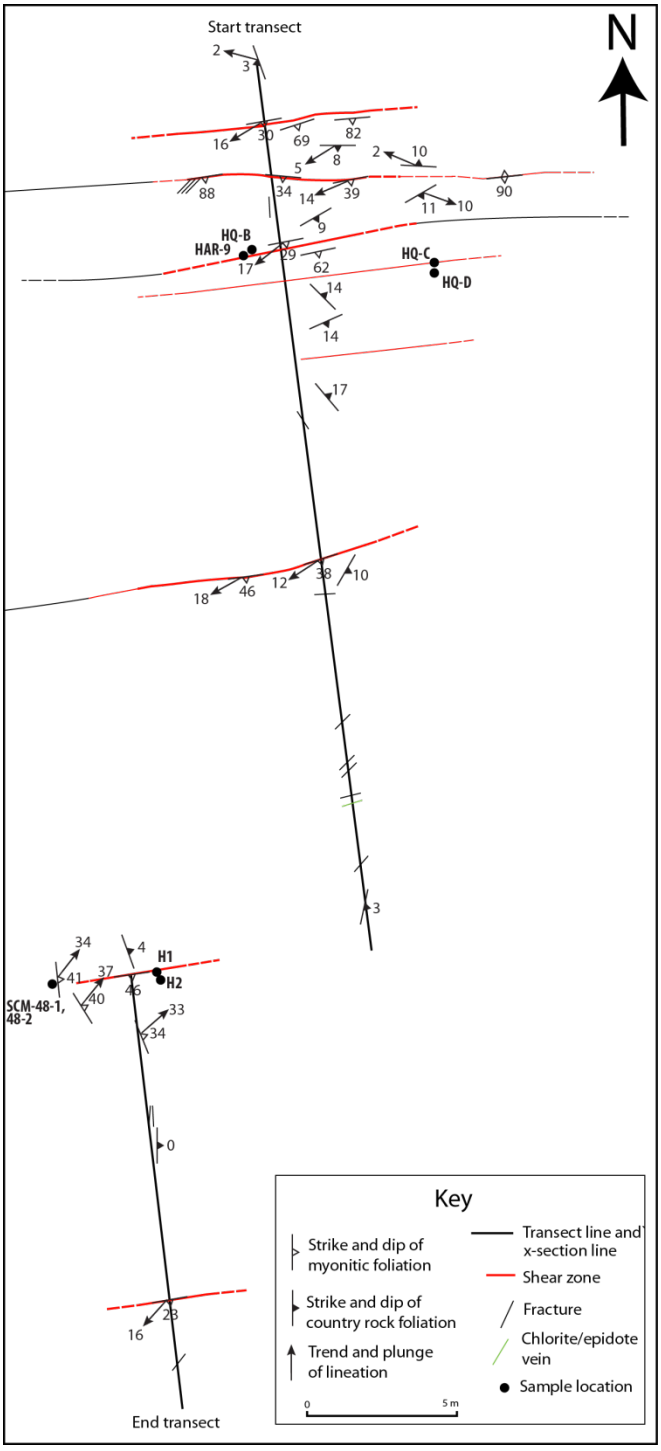

Figure 2.4: Geologic map at 1:200 scale showing the locations of discrete shear zones and the eastern transect line along which data was collected for fracture spacing analysis. A cross-section along this line is shown in Figure 2.5.

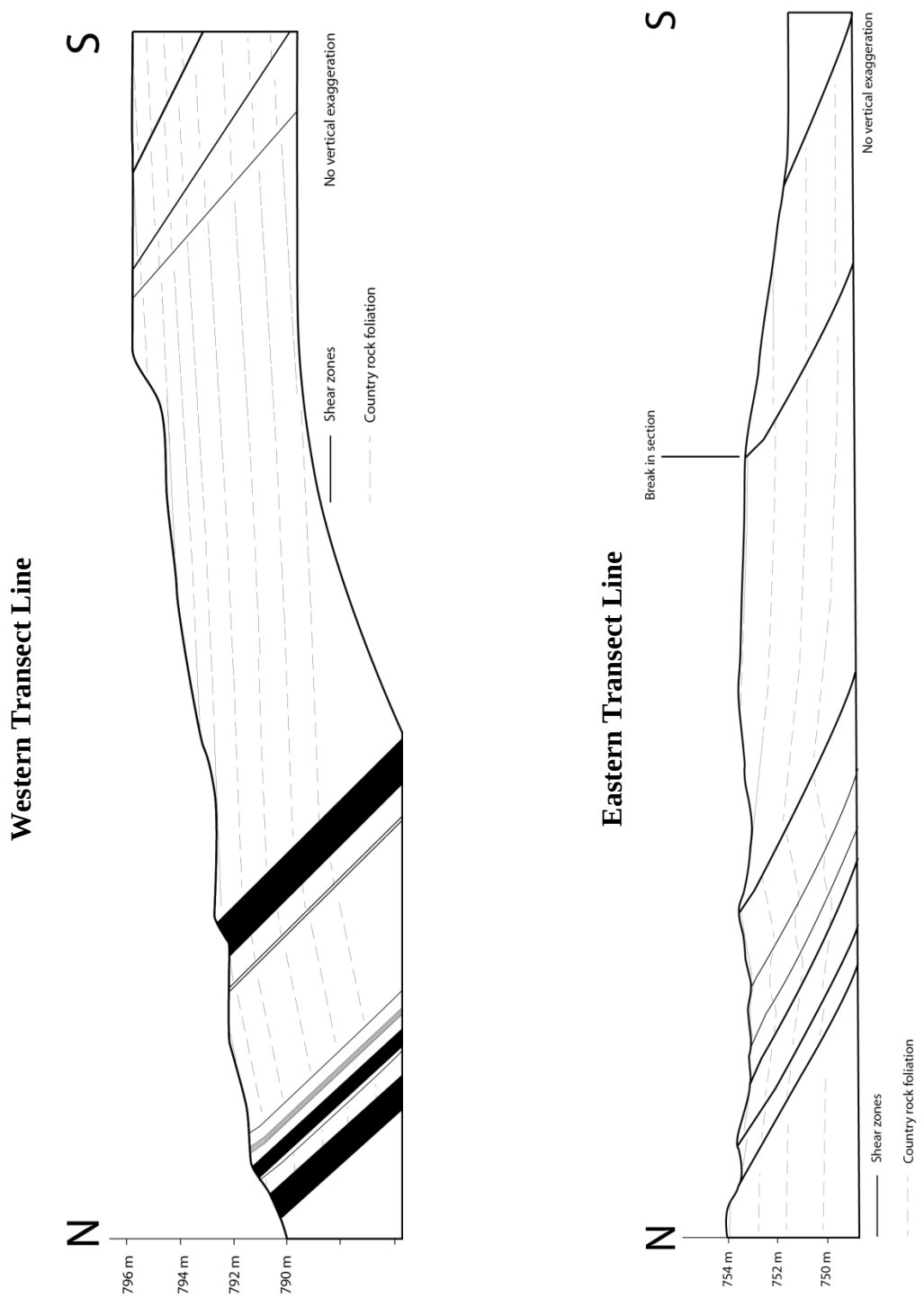

Figure 2.5: Cross-sections showing orientations and relative thicknesses of discrete shear zones along the western and eastern transects, respectively. The location of the western transect is shown in Figure 2.3 and the location of the eastern transect is shown in Figure 2.4.

Figure 2.6: Photograph of the eastern transect line looking south. Measurements of shear zone thickness, shear zone orientations, and the spacing between shear zones were made for each shear zone intersecting the measuring tape.

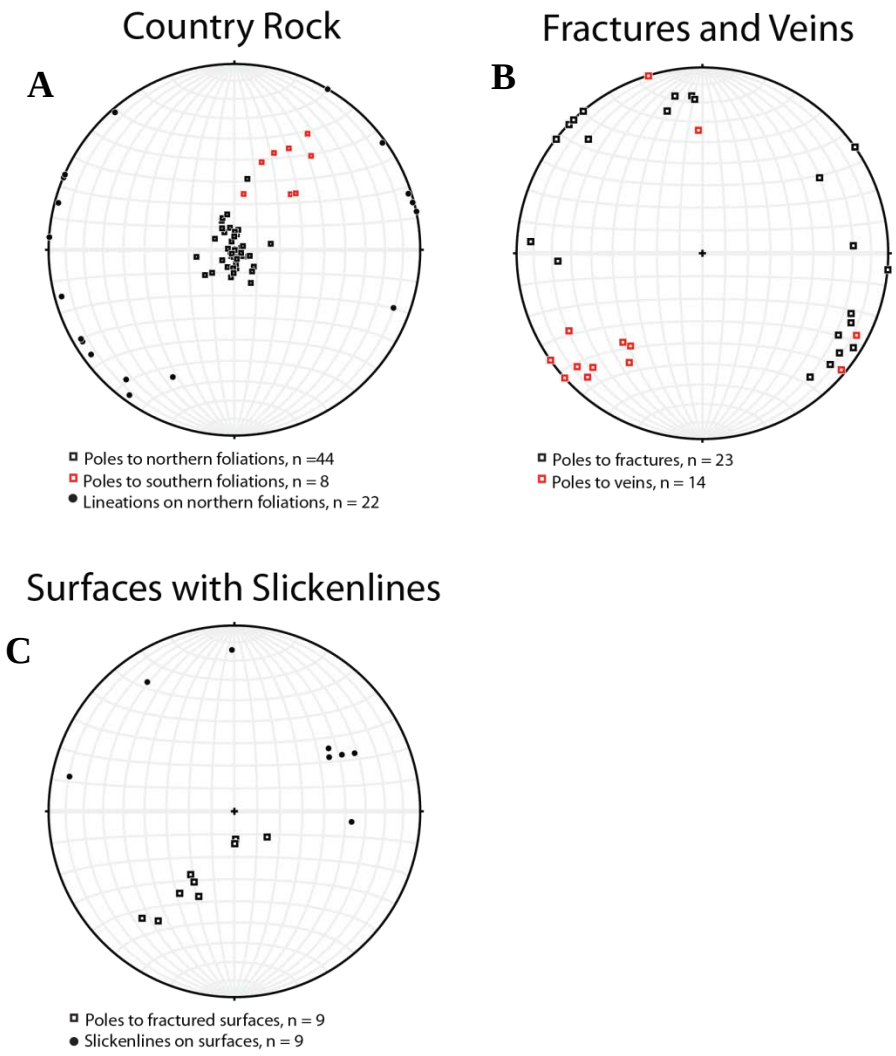

Figure 2.7: Stereograms of structural features in non-mylonitized rocks in the study area. B and C show orientations for extension fractures and shear fractures, respectively. Equal area, lower hemisphere projections.

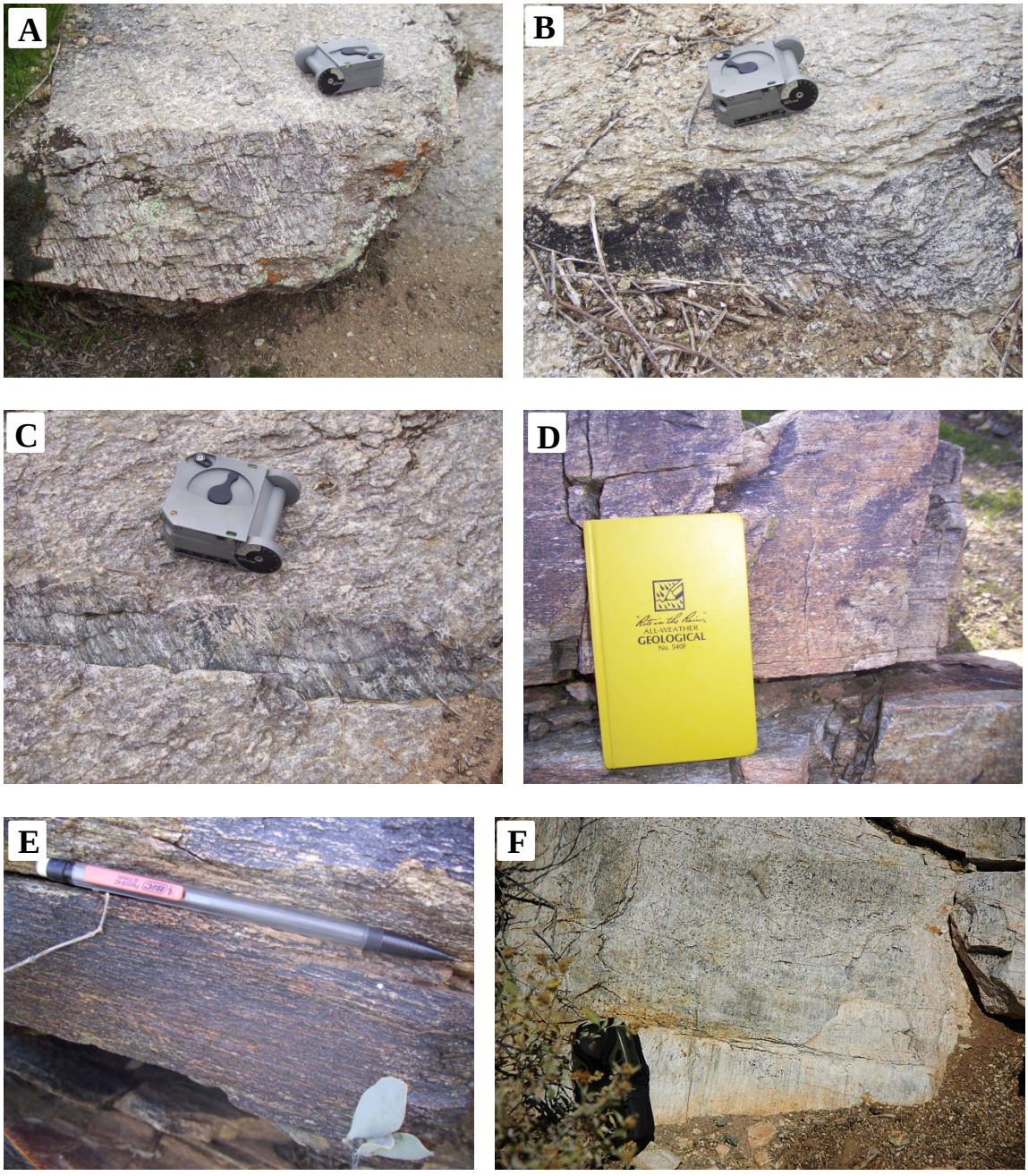

Figure 2.8: Photographs of mylonites in the field area. A-C) Thin mylonitic veneers on fractured surfaces; D-E) Mylonites in the Stone Corral ridge shear zone displaying different intensities of deformation; F) A strongly lineated surface of an isolated shear zone in the southern part of the study area.

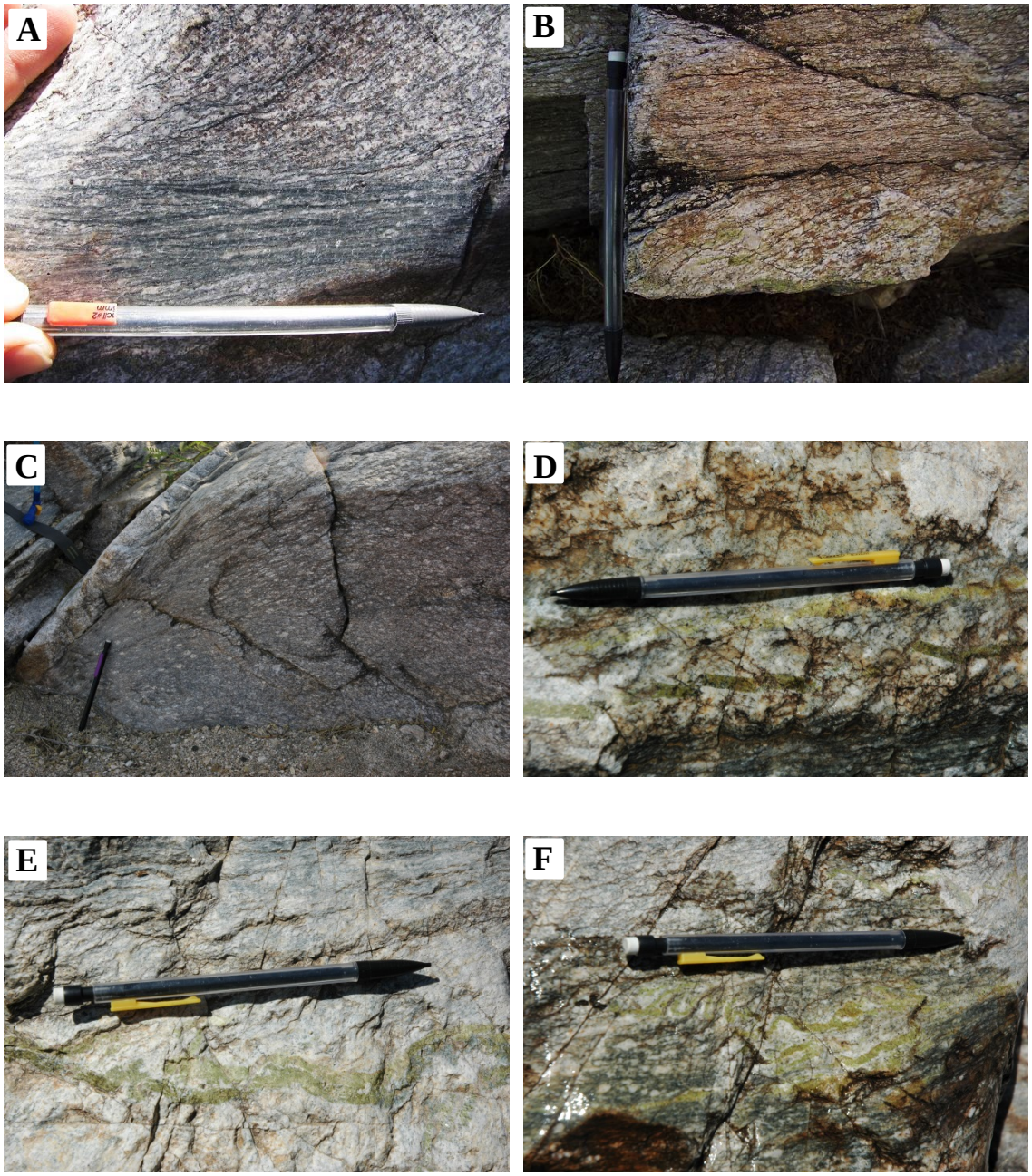

Figure 2.9: Features of discrete shear zones. A-C) Foliation reoriented into parallelism with shear zone boundary; D-F) Deformed central epidote vein in discrete zone. Sample SCM-51 was collected from the shear zone in D-F.

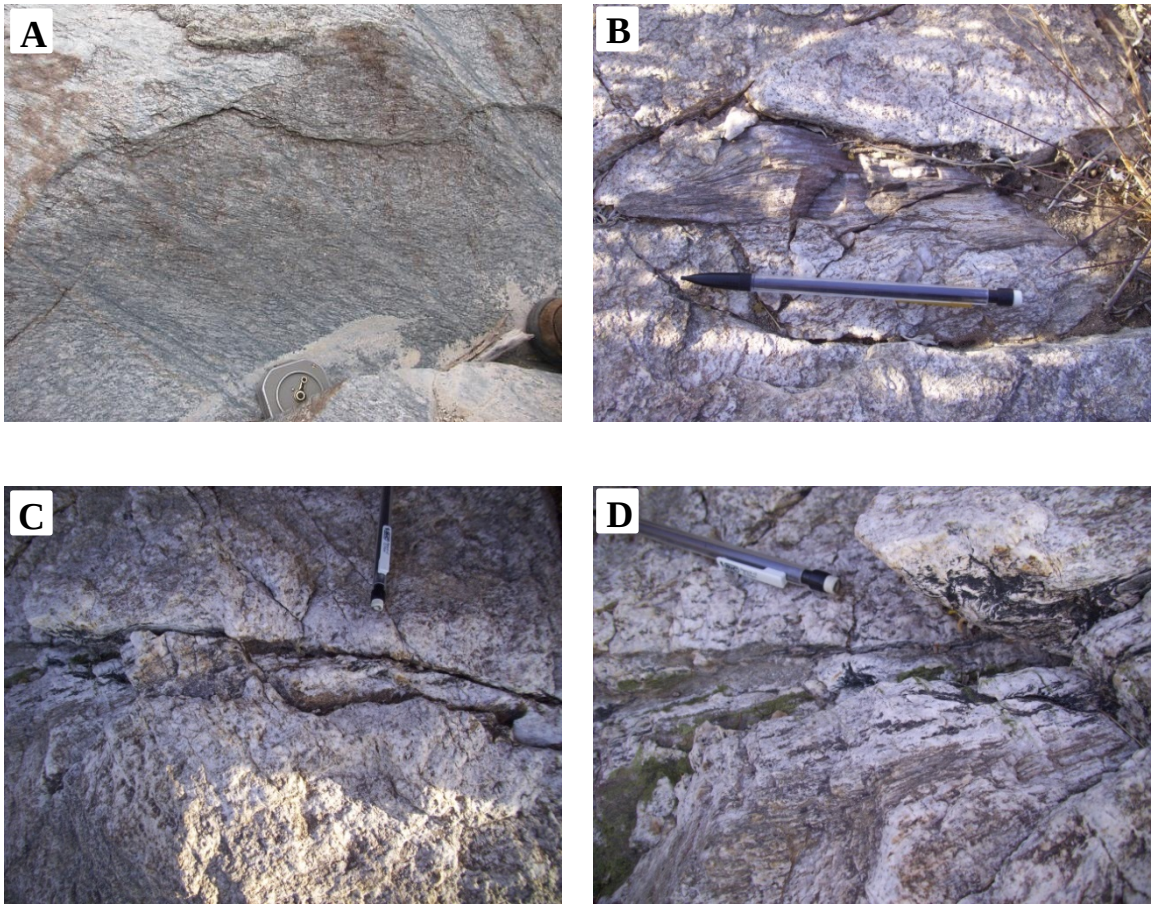

Figure 2.10: Discrete shear zones affected by bleaching with no central veins. A) A series of bleached zones with flanking paired shear zones; B-C) Sheared rocks wedged in fractures with bleached haloes; D) Sheared rock and bleached halo overlap outside a central fracture.

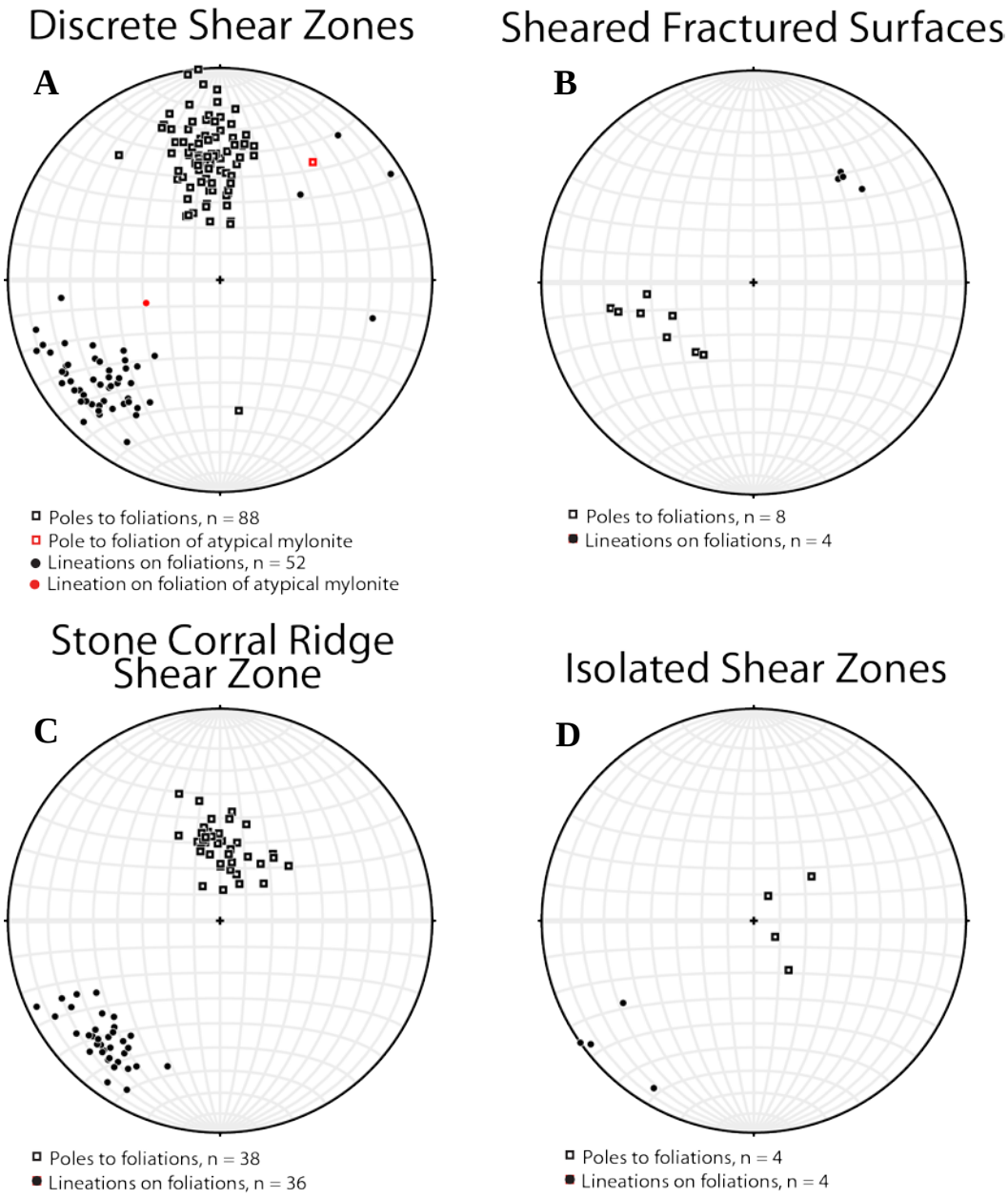

Figure 2.11: Stereograms of structural features in mylonitized rocks in the study area. Equal area, lower hemisphere projections.

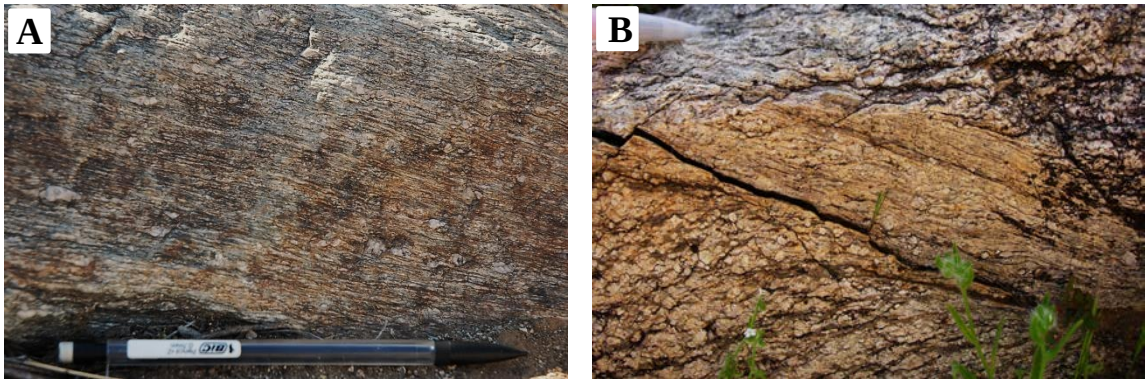

Figure 2.12: Photographs of mylonites with σ-type feldspar porphyroclasts indicating a top-to-the-right (SW) sense of shear. Note the deflection of the country rock foliation into parallelism with the shear zone boundary in B.

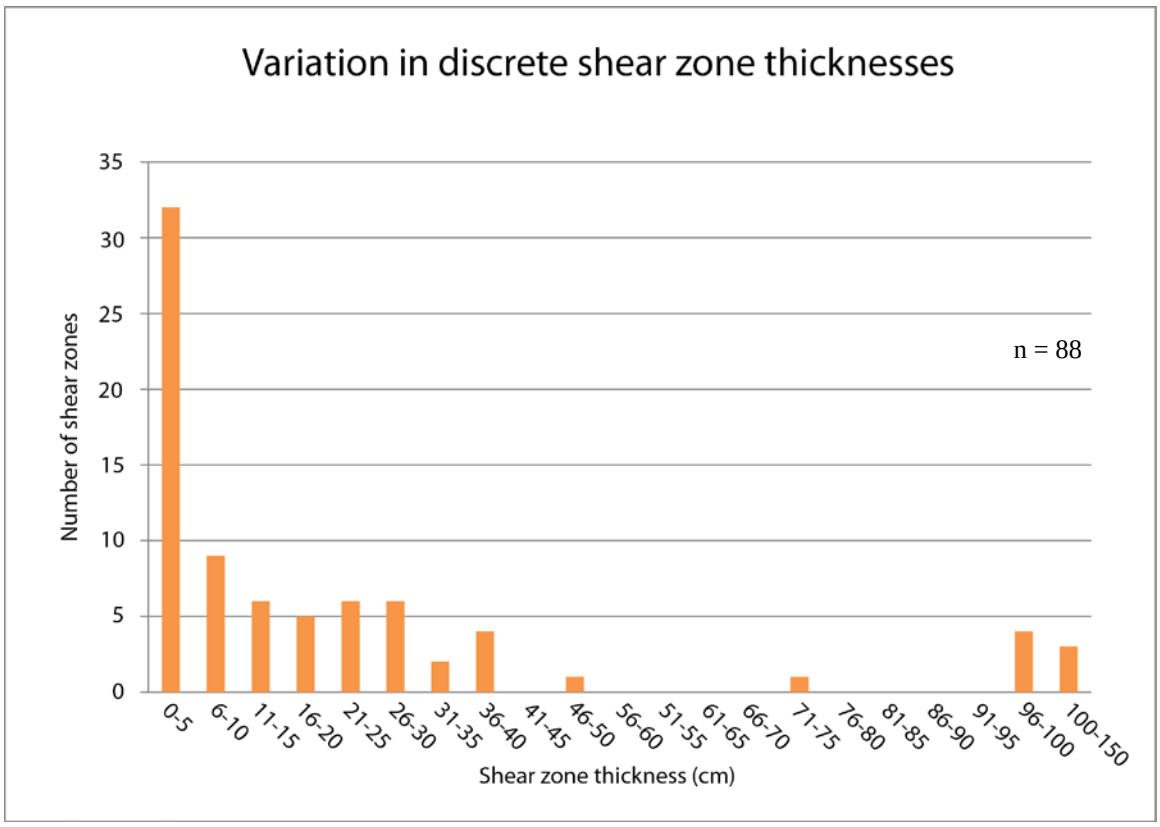

Figure 2.13: Plot of shear zone thicknesses.

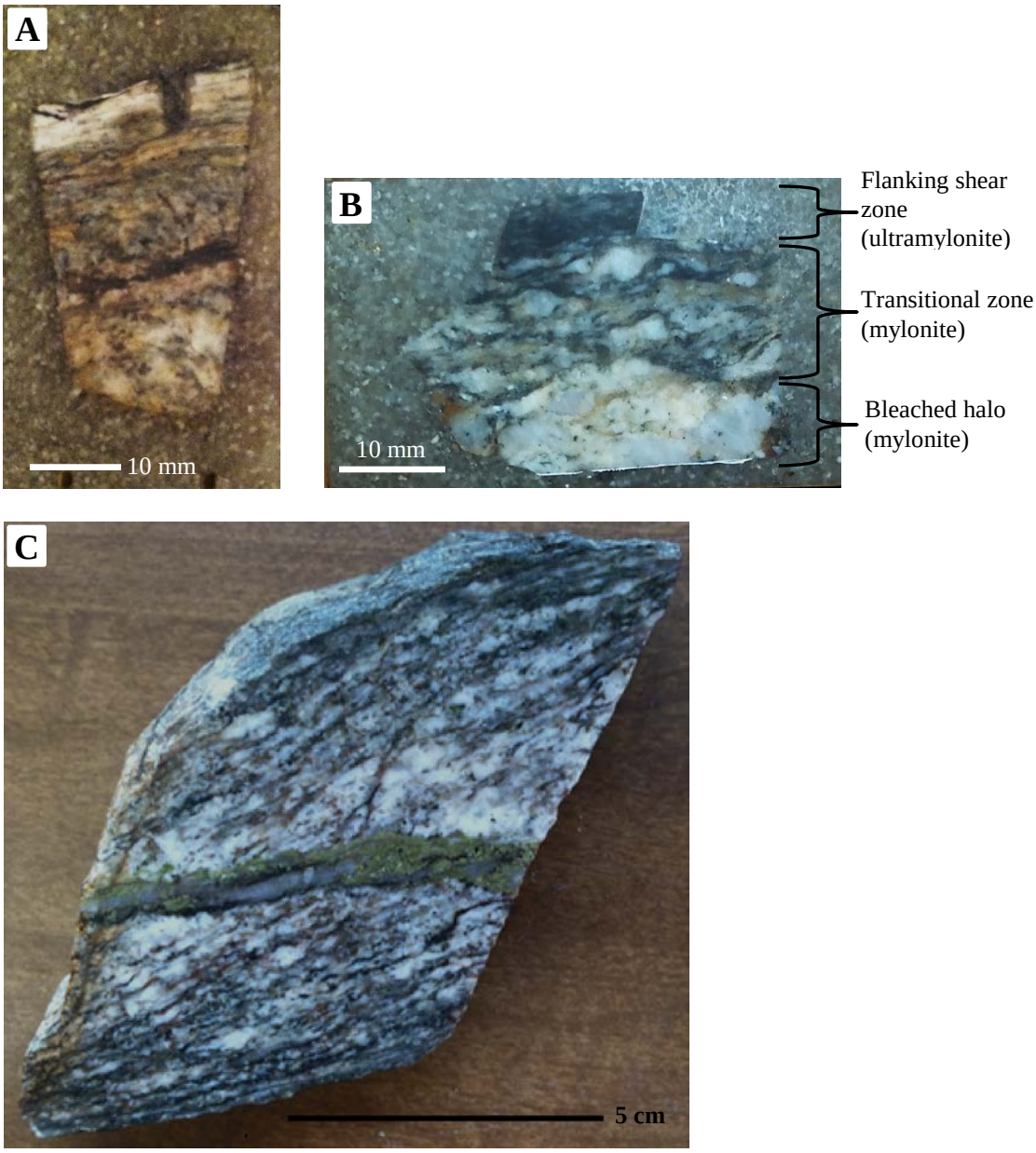

Figure 2.14: Photographs of discrete shear zone hand samples in cross section. Transition from bleached halo to flanking ultramylonite is gradual. In A-B, the veins were not preserved in the samples but were present in the field below the bleached haloes. A) A portion of the ultramylonite is also bleached; sample HAR-55 in epoxy; B) The boundary between the bleached halo and transition zone appears sharp in hand sample, but is not visible when viewed in thin section. Compare to field photograph in Figure 1.5E; sample SCM-51 in epoxy; C) The central quartz-epidote vein crosscuts a pre-existing foliation. Compare to field photograph in Figure 1.5G; sample HAR-16.

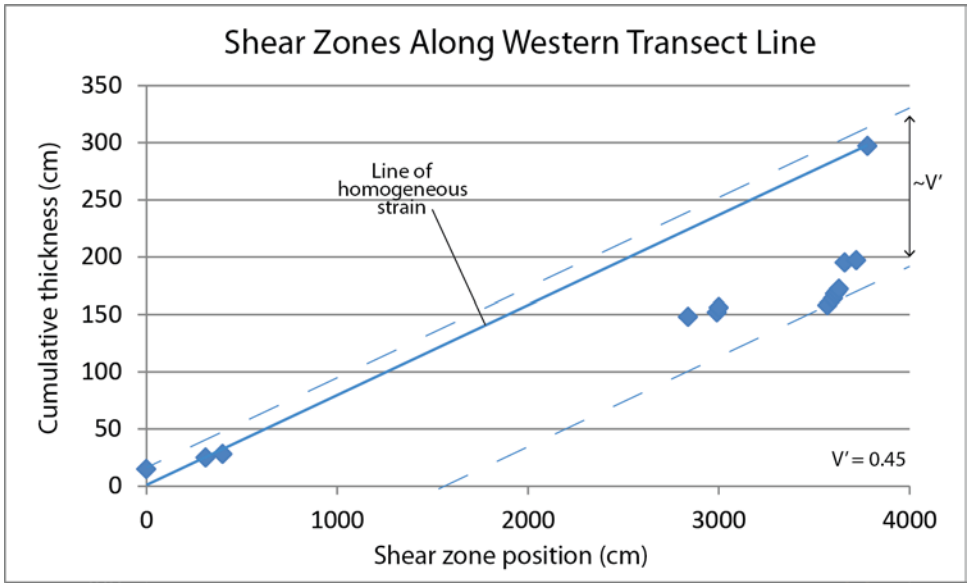

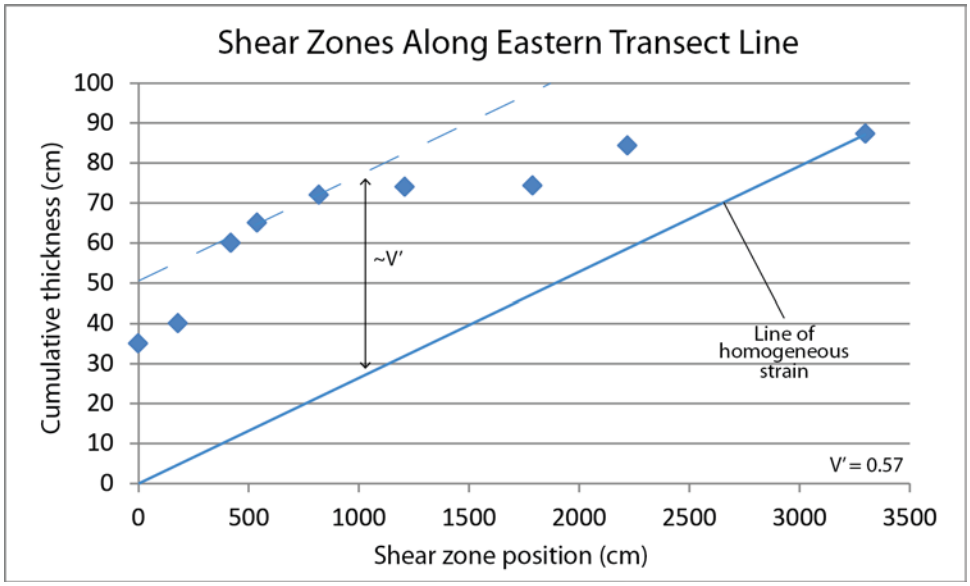

Figure 2.15: Plots of cumulative shear zone thickness vs. shear zone position for the western and eastern transect lines. The shear zone position begins with the position of the first shear zone that intersected the transect line. The solid line represents a line of homogeneous strain. The dotted lines indicate the positions of D_{max} and D_{min}. D_{min} in the eastern transect line plot is equal to the line of homogeneous shear. Plot designed after Figure 7 of Hooker et al., 2011.

Sample	GPS Northing	GPS Easting	Category
H2	297232	3749847	Northern country rock
SCM-6	296565	3749610	Northern country rock
SCM-17b	296608	3749604	Northern country rock
SCM-48-1	297232	3749849	Northern country rock
HQ-D	297249	3749861	Northern country rock
B-4	296698	3749426	Southern country rock
B-7	296729	3749350	Southern country rock
B-28	296835	3749469	Southern country rock
HAR-49	296571	3749620	Epidote-coated fractured surface
HAR-50	296569	3749615	Epidote-coated fractured surface

Table 2.1: Locations and categories of non-mylonitic samples collected from the Stone Corral study area.

Sample	GPS Northing	GPS Easting	Category
H1	297232	3749847	Discrete shear zone
SCM-12	296582	3749622	Discrete shear zone
SCM-17	296608	3749604	Discrete shear zone
HQ-A	296560	3749619	Discrete shear zone
HAR-14	297159	3749855	Discrete shear zone
HAR-53	296514	3749817	Discrete shear zone
SCM-51	296577	3749628	Discrete shear zone*
HQ-C	297249	3749861	Discrete shear zone*
HAR-16	297131	3749861	Discrete shear zone*
HAR-56	297204	3749846	Discrete shear zone*
HAR-38	296791	3749830	Discrete shear zone*
HAR-52	296578	3749632	Discrete shear zone*
HAR-55	296563	3749650	Discrete shear zone*
HQ-B	297239	3749863	Discrete shear zone
HAR-9	297239	3749863	Discrete shear zone**
SCM-4	296576	3749595	Atypical discrete shear zone
SCM-48-2	297232	3749849	Mylonitized fractured surface
SCM-19	296562	3749568	Stone Corral shear zone boundary
H3	296529	3749521	Stone Corral shear zone
SCM-20	296527	3749536	Stone Corral shear zone
B-3	296630	3749466	Stone Corral shear zone
HAR-3	296533	3749487	Stone Corral shear zone
HAR-4	296525	3749407	Stone Corral shear zone
HAR-5a	296482	3749243	Stone Corral shear zone
HAR-5b	296482	3749243	Stone Corral shear zone
HAR-6	296553	3749224	Stone Corral shear zone
B-5	296715	3749388	Isolated shear zone
B-9	296676	3749275	Isolated shear zone
HAR-7	296669	3749258	Isolated shear zone
HQ-E	298665	3752009	Detachment fault shear zone
HQ-F	298644	3751916	Detachment fault shear zone
HQ-G	298310	3751945	Detachment fault shear zone

*Sample from shear zone with central vein, bleached halo, and flanking paired shear zones morphology
**Sample from shear zone affected by bleaching but with no central vein

Table 2.2: Locations and categories of mylonitic samples collected from the Stone Corral study area and from the Eagle Eye detachment fault, Eagle Eye Mountain.

Strike	Dip	Thickness (cm)	Distance along transect (m)	Cumulative distance (m)	Spacing (m)
62°	28° SE	15	0.6	0	0
68°	34° SE	10	3.7	3.1	3.1
67°	43° SE	3	4.6	4	0.9
90°	43° S	120	29	28.4	24.4
89°	50° S	4	30.5	29.9	1.5
89°	50° S	4	30.6	30	0.1
88°	56° S	2	36.3	35.7	5.7
85°	48° S	6.2	36.6	36	0.3
85°	48° S	4	36.7	36.1	0.1
85°	48° S	2.5	36.8	36.2	0.1
85°	48° S	2	36.9	36.3	0.1
82°	40° SE	23	37.2	36.6	0.3
86°	44° S	1.5	37.8	37.2	0.6
90°	48° S	100	38.4	37.8	0.6

Table 2.3: Shear zone measurements along the western transect line.

Strike	Dip	Thickness (cm)	Distance along transect (m)	Cumulative distance (m)	Spacing (m)
80°	30° SE	35	1.9	0	0
95°	34° S	5	3.7	1.8	1.8
79°	29° SE	20	6.1	4.2	2.4
83°	35° SE	5	7.3	5.4	1.2
85°	35° S	7	10.1	8.2	2.8
72°	38° SE	2	14	12.1	3.9
76°	68° SE	0.3	19.8	17.9	5.8
72°	45° SE	10	24.1	22.2	4.3
80°	23° SE	3	34.9	33	10.8

Table 2.4: Shear zone measurements along the eastern transect line.

Transect location	Average spacing (m)	Standard deviation of spacing	C_v	Cumulative Thickness (cm)	V'
Northeastern	2.91	6.66	2.29	297.2	0.45
Northwestern	4.13	3.07	0.74	87.3	0.57

Table 2.5: Fracture spacing analysis calculations.

Chapter 3: Petrography

The granitic rocks of the northeastern Harquahala Mountains are overprinted by several different styles of deformation (see Chapter 2), but the genetic relationships between these different fabrics and conditions of deformation are difficult to discern in the field. In this chapter, the mineralogy and the microstructures are described for rocks displaying all the different styles of deformation apparent in the Stone Corral study area. First, the country rocks north and south of the Stone Corral ridge shear zone are described to establish the degree and type of deformation prior to formation of the shear zones, and to discern whether they have the same mineralogy and deformed under the same conditions.

Next, the mineralogy and microstructures among the many mylonites in the study area are described to establish the deformation conditions, senses of shear, and strain localization mechanisms, as well as to determine how the discrete zones with the central epidote vein, bleached haloes, and flanking paired shear zones formed. The different shear zones are described starting with the mm- to m-scale discrete shear zones in the northern part of the study area not affected by veins and bleaching (Figure 1.4), followed by the shear zones with a central vein, bleached halo, and flanking paired shear zones morphology (Figure 1.5), and then the unusual discrete shear zones in the northern part of the study area that display different orientations than the other more common discrete shear zones (e.g., sample SCM-4 in Figure 2.3), including the mm-scale mylonitized veneers on fractured surfaces (Figure 2.8A-C). Next, the samples collected from the few hundred meters thick Stone Corral ridge shear zone are described (Figures 2.2, 2.8D-E), followed by the isolated 0.5-1 m thick shear zones found near the crest of Stone Corral ridge (Figures 2.1, 2.2, 2.8F). Lastly, the mylonitic rocks collected from near the Eagle

Eye detachment fault on Eagle Eye Mountain (Figure 1.3) are described for comparison with the various mylonites of the Stone Corral study area, which have previously all been interpreted as forming during Miocene MCC exhumation as well.

3.1 METHODS

Standard (27x46 mm) or large (45x70 mm) thin sections were prepared for 42 samples (Tables 2.1, 2.2). Thin sections were cut parallel to lineation and perpendicular to foliation whenever possible. Mineralogical and microstructural information was recorded for all thin sections and is summarized in Tables 3.1-3.3. The mineralogy of each sample was visually estimated. In the mylonitized samples, much of the feldspar was recrystallized into very fine grains, and thus potassium feldspar was difficult to discern from plagioclase feldspar. In addition, many of the remaining feldspar porphyroclasts were very altered or showed no distinguishing characteristics and were difficult to identify as plagioclase or potassium feldspar. For this reason, the total feldspar content is estimated for the mylonites, whereas the plagioclase and potassium feldspar contents are estimated separately for the country rocks and bleached haloes.

3.2 COUNTRY ROCK

The granitic country rock located north of the Stone Corral ridge shear zone (i.e., the “northern country rock”), displays different degrees and styles of deformation than the granitic country rock located south of the shear zone near the crest of Stone Corral ridge (i.e., the “southern country rock;” Figures 2.1, 2.2). The northern country rock displays a gneissic texture that is locally protomylonitic and is characterized by feldspar porphyroclast-rich layers mixed with thinner quartz- and mica-rich layers. The southern country rock is undeformed to weakly foliated; the foliation is defined by the rough alignment of biotite and locally of quartz.

3.2.1 Northern Country Rock

3.2.1.1 Mineralogy and texture

Five samples were collected from the meta-granitic country rocks in the northern part of the study area (i.e., north of the Stone Corral ridge shear zone; Table 2.1, Figures 2.1, 2.3, 2.4). The samples have very similar modal mineralogy with 35-38% plagioclase feldspar, 30-36% potassium feldspar, 22-26% quartz, and 3-6% biotite (some of which is replaced by chlorite; Table 3.1). All the samples contain lesser amounts of epidote, titanite, apatite, amphibole, and opaque minerals. Three of the samples contain <1% garnet.

The samples are composed of large feldspar porphyroclasts, discontinuous ribbons and pods of quartz grains, numerous pockets of fine grained feldspars, scattered bands of biotite, and larger biotite that are commonly clustered (Figure 3.1A-B). Feldspar porphyroclasts average ~1-2 mm in length, although a few larger porphyroclasts up to ~5-6 mm in size are preserved in sample SCM-6, which is slightly less deformed than the other samples (Figure 3.1A). Some porphyroclasts are bordered by masses of fine, recrystallized feldspar (Figures 3.1C-D, 3.2A). Many of the potassium feldspar porphyroclasts display microcline twinning.

Minor to moderate amounts of feldspar alteration are present in all samples and affect both porphyroclast edges and interiors. Partial replacement of feldspar is most commonly by biotite and epidote (Figure 3.1C-D), and less commonly by sericite or extremely fine optically unidentifiable grains. In many samples, biotite is observed to partially replace small amphibole grains, although in some samples (e.g., SCM-6 and HQ-D), similar sized amphibole grains (up to ~350 μm) remain within the interiors and edges of some feldspar porphyroclasts. The amount of biotite replacement positively correlates with the amount of deformation the samples experienced; however, amphibole

content does not vary amongst the samples. Thus some biotite likely resulted from other processes. The majority of biotite in the samples is found in discontinuous bands and as clustered grains ~1 mm in length that are aligned in the foliation. All samples exhibit some replacement of biotite by chlorite, ranging from minor (e.g., <5% in sample H2) to moderate (e.g., ~50% in sample SCM-6).

The presence of myrmekite on the edges of feldspar porphyroclasts is widespread in all samples. The myrmekite exists as lobes on the edges of potassium feldspar (Figure 3.1A). The lobes range in size from 200 μm to 1 mm and contain quartz vermicules up to 50 μm thick. The samples also contain a minor amount of a feldspar replacement texture in which secondary feldspar replaces potassium feldspar. The texture is very subtle, visible only as a small number of irregular blebs (100-300 μm in length) in large porphyroclasts. The blebs appear as a lighter, more powdery shade of gray than the original grains in cross-polarized light. Quartz is not associated with the replacement product.

Some of the feldspar porphyroclasts are partially or fully wrapped by layers of medium grained (~250-500 μm) quartz. In the less deformed sample, SCM-6, much of the quartz is collected into isolated pods. In all samples, the quartz bands (+/- biotite bands) define a roughly sub-horizontal foliation, but this foliation undulates around larger, more rigid feldspar porphyroclasts (Figure 3.1B).

Epidote occurs as small (~250 μm) to large (1.5 μm) anhedral to subhedral grains. Some of the grains display Carlsbad twinning or complex zoning patterns. Rare grains composed of epidote rims on allanite cores are also present. Epidote also exists as a minor replacement mineral in the cores of feldspar porphyroclasts, particularly along albite twin planes. In samples SCM-17b and SCM-6, epidote also exists as veinlets that crosscut the foliation subperpendicularly (Figure 3.1A). Symplectic quartz-epidote

grains are present in all samples, and can be found on the edges of feldspar porphyroclasts or in isolation (Figures 3.2B-C, 3.3A-B). The epidote symplectites are commonly bordered by titanite, apatite, biotite, and opaque mineral grains.

Titanite occurs as subhedral to euhedral grains ~250-800 μm wide. Amphibole grains are elongate, range in length from 100 μm to 1.5 mm, and as described above, some are partially replaced by biotite (Figure 3.1B). Opaque minerals occur as anhedral to subhedral grains ~50-250 μm in width, with rare grains reaching up to ~500 μm in width. A trace amount of hexagonal garnet, up to 1 mm in size, is present in most samples and has a pink tint in plane polarized light.

Epidote, titanite, apatite, and some of the biotite, quartz and opaque minerals appear to make up a metamorphic assemblage. They are intimately associated with each other in complicated arrays that are typical of metamorphic, rather than igneous, textures (Figure 3.4A). Rare small (~100 μm) garnet grains are also present in this assemblage, and contrary to the larger (likely igneous) garnet grains, are clear in plane polarized light. Quartz is commonly found as an embayment in titanite, epidote, and amphibole, and thus is likely a metamorphic product as well.

3.2.1.2 Microstructures

In all samples, the quartz grains display undulatory extinction and have a locally strong crystallographic preferred orientation (CPO). In general, the quartz grains are elongate with sinuous, lobate boundaries (Figure 3.5). In some quartz layers, larger grains display discontinuous undulatory extinction and numerous subgrains, commonly near the edges, that grade into recrystallized new grains of similar size, shape and optical orientation. In sample SCM-6, the least deformed sample, the quartz layers and pods exhibit only very rare examples of this transition from subgrains into new grains on the

edges of quartz. However, elongate subgrains and/or discontinuous undulatory extinction are present in many of the quartz grains, and in some cases, neighboring quartz grains show sinuous, lobate boundaries.

The feldspar porphyroclasts are highly fractured and show undulose extinction (Figure 3.1). Some of the feldspar augen appear to have undergone little to no recrystallization; these porphyroclast margins are sharp or only slightly blurry and tend to border quartz or other porphyroclasts (Figure 3.1A). Many other feldspar porphyroclasts appear to have undergone partial recrystallization on their rims, indicated by very serrated and sometimes blurry boundaries and by the presence of subgrains on their boundaries that transition into new grains of similar shape and size (Figure 3.1C-D). Many small clusters of new grains have similar optical orientations, and subgrains and new grains show a gradational change in optical orientation away from the feldspar porphyroclasts. Masses of very fine grained, grungy recrystallized feldspars of similar optical orientation are also present in the samples. This type of recrystallization is commonly associated with feldspar porphyroclasts that have been greatly affected by myrmekite replacement on their rims.

All samples are affected by thin brittle-ductile shear bands that crosscut the foliation and locally cut across entire thin sections (Figure 3.2). Layers of elongate quartz are deflected into some of the shear bands and exhibit extensive localized subgrains and new recrystallized grains (Figure 3.2B). Zones of extensive fine grained, grungy recrystallized feldspars (Figure 3.2A) and occasional elongate biotite and epidote grains are present as well. A couple of the shear bands lack ductile quartz microstructures and appear to be brittle fractures. These bands have a granular, powdery appearance in plane polarized light, which also is suggestive of fractures.

A few shear sense indicators are present in the samples. The brittle-ductile quartz-rich and feldspar-rich shear bands are oriented at angles between ~30° to 40° to the overall foliation, and resemble C'-type shear bands (Figure 3.2). However, these angles may be apparent angles as a couple of the samples did not have a clear lineation and so were cut parallel to the lineation direction of rocks in nearby outcrops. Some of the shear bands also change orientation slightly when traced along their lengths. For example, one of the shear bands in sample SCM-6 is oriented at an angle of ~30° where it initiates with respect to the foliation, but when traced along its length, its orientation steepens to ~40°. This change in angle may be a result of different rheologies as the shear band tends to be at a shallower angle in feldspar-rich layers and at a steeper angle in quartz-rich layers. In the three samples cut parallel to lineation and perpendicular to foliation, the orientation of the bands imply a top-to-the-northeast sense of shear if they are C'-type shear bands. The few bands that appear to have formed solely from brittle processes also have the same orientation and thus sense of shear. The only other shear sense indicator present in the country rock samples is a slight quartz grain shape preferred orientation (GSPO) in sample SCM-17b that is also inclined in a top-to-the-northeast direction.

3.2.2 Southern Country Rock

3.2.2.1 Mineralogy and texture

Three samples were collected from the country rock in the southern part of the study area (i.e., south of the Stone Corral ridge shear zone; Table 2.1, Figures 2.1, 2.2). Sample B-7 was collected from weakly foliated granite, and sample B-28 was collected from a moderately foliated granite. The third sample, B-4, was collected from a massive granite that appeared undeformed in the field and in hand sample. The modal mineralogy

of the three samples is very similar with 34-38% plagioclase, 32-35% potassium feldspar, 25-26% quartz, and 3-8% biotite (Table 3.1). All three samples contain minor amounts of opaque minerals and rare epidote. The moderately foliated sample also contains a small amount of titanite.

Although the modal mineralogy is comparable among the three samples, the samples differ from each other in both grain size and amount of recrystallization. More deformed samples have smaller grain sizes and are more recrystallized. Feldspar porphyroclasts in the least deformed sample, B-4, range from 1-2.5 mm (Figure 3.6A). Quartz grain size tends to average ~500-750 μm, but may be as large as 1.5 mm (Figure 3.6C). Biotite is present as subhedral grains that approach a rectangular shape and average ~750 μm in the long direction and ~250 μm in the short dimension. In the weakly deformed sample, B-7, feldspar porphyroclast size averages ~250-500 μm; quartz averages ~1 mm, and biotite varies in length but averages ~100-150 μm in width. The biotite is crudely aligned and defines the foliation in this sample. In the most deformed sample, B-28, feldspar porphyroclast sizes average ~150-400 μm (Figure 3.6B); quartz averages ~500 μm (Figure 3.6D), and biotite also varies in length but averages ~50 μm in width. The crudely aligned biotite and parallel, slightly elongate quartz define the foliation. All three samples show minor to moderate sericitic alteration in some of the feldspar porphyroclasts, and minor to moderate replacement of biotite by chlorite.

3.2.2.2 Microstructures

All three samples display evidence of intracrystalline deformation and recrystallization. Although sample B-4 appeared undeformed in the field and in hand sample, the rock has clearly undergone minor but pervasive deformation and recrystallization when viewed in thin section (Figure 3.6A, C). The quartz grains in all

samples show discontinuous undulatory extinction and exhibit a weak CPO. The grains are amoeboid in shape with sinuous boundaries and finger-like protrusions into neighboring grains (Figure 3.6C). All samples also have a small number of quartz pods where a transition exists from old grains to subgrains on the edges of the old grains to neighboring new grains that are similar in size, shape, and optical orientation to the subgrains (Figure 3.6D). In the most deformed sample, many of the quartz grains contain subgrains that extend across the entire grain.

Feldspar porphyroclasts show discontinuous undulatory extinction, and many grains are fractured. Myrmekite is present in all three samples and is extensive in the two lesser deformed samples (Figure 3.6A). The sizes of the myrmekite lobes vary greatly and reach a maximum of ~1 mm in sample B-4. Quartz vermicules within the myrmekite lobes can be up to ~50 μm in thickness. Myrmekite is present both as protrusions nucleating on the edges of grains and as feathery growths lining microfractures. Most of the recrystallization seen in the feldspar grains appears to be recrystallization of the myrmekitic intergrowths (Figure 3.6A-B). Recrystallized fine grained, grungy looking feldspar is also present along some of the feldspar porphyroclast boundaries. This type of recrystallization seems to be most developed on myrmekite lobes and recrystallized myrmekite grains.

Flame perthite is also present throughout all three samples (Figure 3.6B), but is very minor in the two lesser deformed samples. Flame perthite is ubiquitous in the most deformed sample, which suggests it is deformation-related. The microstructure appears to have nucleated on grain boundaries in most cases, but, in some, it seems to have nucleated on intragranular microfractures.

3.2.3 Interpretation

The bulk mineralogy of the country rock that crops out north of the Stone Corral ridge shear zone is similar to that of the country rock that crops out south of the Stone Corral ridge shear zone, indicating that the same unit is likely present on both sides. However, the northern country rock contains a significantly greater amount of metamorphic minerals than the southern country rock. Whereas the northern country rock has common metamorphic epidote, titanite, garnet, apatite, and biotite, the southern country rock contains only trace amounts of titanite and epidote. This may suggest the northern country rocks were more affected by fluid infiltration that enhanced the breakdown of preexisting minerals to form the metamorphic assemblage. The northern country rock is also more intensely deformed and is crosscut by discrete top-to-the-northeast shear bands. All the country rocks show evidence for predominantly high temperature grain boundary migration (GBM) recrystallization of quartz and subgrain rotation (SGR) recrystallization of feldspar, and for a lesser amount of SGR recrystallization of quartz and bulging (BLG) recrystallization or neocrystallization of feldspar. Quartz and feldspar in the top-to-the-northeast shear bands that crosscut the foliation in the northern country rock are recrystallized by SGR and BLG, respectively.

3.3 DISCRETE MYLONITIC SHEAR ZONES

3.3.1 Discrete Shear Zones without Bleaching and Central Veins

3.3.1.1 Mineralogy and texture

Six samples were collected from the discrete shear zones located in the northern portion of the study area that are not associated with bleaching and epidote veins (Table 2.2, Figures 1.4, 2.1, 2.3, 2.4). The samples share a similar mineralogy but differ in the modal proportions of minerals (Table 3.2). Three of the samples, H1, SCM-17, and

HAR-14 were collected from isolated shear zones that were not in the vicinity of other shear zones with a central vein, bleached halo, and flanking paired shear zones morphology. These three samples share an almost identical modal mineralogy of ~66-67% feldspar, ~22-25% quartz, 8-9% biotite, and lesser amounts of epidote, titanite, amphibole, apatite and opaque minerals. The other three samples, SCM-12, HQ-A, and HAR-53, were collected from a meter-scale shear zone in the western part of the study area that is exposed along strike for ~25 meters (Figure 2.3). Although the three samples were not associated with bleaching, epidote veining, and flanking paired shear zones, most of the other shear zones in the vicinity do display that morphology. These three samples had similar feldspar contents (~64-68%) as the mylonites from the isolated shear zones. However, they contained higher quartz contents (~27-35%) and lower biotite contents (~1-7%) that are mostly altered to chlorite. Samples HQ-A and HAR-53 also contain small amounts of muscovite, and some of the feldspars show minor sericitic alteration. Sample SCM-12 contains minor epidote, titanite, and amphibole. The amphibole is scarce and is almost completely altered to biotite and chlorite.

The discrete shear zone samples are characterized by undulating layers of fine grained (~10-30 μm) feldspar, quartz, and biotite that are intermixed with continuous and discontinuous layers of medium-grained (~50-200 μm) quartz, some of which form long ribbons (Figure 3.8A-B). Sample HQ-A is an exception in that biotite is very rare, and in both HQ-A and HAR-53, scarce short strings of fine grained muscovite are present in the feldspar-rich matrix layers. Also, sample SCM-17 is significantly finer grained than the other samples with matrix grains on the scale of one to tens of microns and feldspar porphyroclasts on the scale of tens to hundreds of microns. In the other samples, feldspar porphyroclasts range in size from ~500 μm-3.5 mm (Figure 3.7).

In all samples, the feldspar porphyroclasts are widespread and exist most commonly as isolated grains, but more rarely may be present in trains of multiple grains. A few very elongate feldspar grains (~300-700 μm in length) are scattered throughout some samples. In most samples, the grain boundaries of the feldspar in the fine grained layers do not appear sharp because of the presence of fine grained biotite, which forms wispy bands that undulate between and through the fine feldspar grains (Figures 3.7E, 3.8B). Rare relicts of well-developed biotite grains are preserved. The quartz layers are generally thinner than the fine grained feldspar layers and are less abundant, but the grain size within the layers is larger (Figure 3.8B). The feldspar porphyroclasts display various degrees of chemical breakdown to mica.

Epidote grains in the samples tend to be subhedral and are commonly fragmented. They range in size from ~100 μm to 1 mm and are scattered throughout the samples, commonly associated with the mica-rich bands (Figure 3.9A). Quartz-epidote symplectites are present in some of the samples (Figure 3.3E). Epidote also appears to have replaced parts of feldspar porphyroclasts in some samples. The opaque mineral grains are anhedral to subhedral (and more rarely euhedral), ~10-30 μm in size, scattered throughout the samples, and can be either isolated or form trains. The titanite grains are typically subhedral to euhedral and ~250-500 μm in length. They commonly display a fish-like habit and are found either isolated or in clusters, in which case they are generally found near large epidote grains (Figure 3.9A). Some have inclusions of opaque minerals. Amphibole grains range in size from tens of microns to hundreds of microns (Figure 3.8C). The titanite, biotite, epidote, amphibole and opaque minerals are commonly associated with each other.

Myrmekite on the edges (or more rarely in the interiors) of feldspar porphyroclasts is present in all samples to various degrees (Figure 3.7A). The myrmekite

is finer grained than in the samples from the country rocks. Myrmekitic intergrowths are more abundant in samples that are less strained. A replacement texture in which feldspar porphyroclasts have been partially replaced by secondary feldspar is also present to varying degrees within all the samples. This replacement texture is similar to that visible in the country rocks but is more obvious, appearing as patches, rather than blebs, of powdery gray in cross-polarized light. Energy-dispersive X-ray Spectrometry (EDS) analysis of this texture was performed on a sample from a shear zone with the central vein, bleached halo, and flanking paired shear zones morphology (see Chapter 5). The results of the analysis indicated that the replacing feldspar was oligoclase. This replacement texture is described in detail in section 3.3.2 (see also Figures 3.14-3.16).

3.3.1.2 Microstructures

Many of the larger quartz grains in the quartz-rich layers display sweeping undulatory extinction and have a very strong CPO. Most of the quartz grains in the samples exhibit serrate/lobate boundaries (Figure 3.8A). Many of the amoboid shaped grains, particularly the larger grains, also contain elongate subgrains that extend across the length of the grains. In most cases, these quartz subgrains are not the same size as the smaller recrystallized quartz grains in the samples. Transitions from larger older grains to subgrains to new grains of similar size with a corresponding gradation in degree of lattice orientation are locally present, but not widespread. Additionally, whereas the majority of grains in the quartz layers have sinuous boundaries, not all the layers contain grains with subgrains.

The feldspar porphyroclasts are highly fractured and show continuous and locally discontinuous undulatory extinction (Figure 3.7E). In all samples, some of the feldspar porphyroclasts appear to have been either partially or fully pulled apart a short distance

(100-400 μm) with large quartz between the two halves. Many feldspar porphyroclasts appear to have undergone partial to moderate recrystallization, indicated by serrate boundaries and the presence of abundant subgrains which transition into new grains with similar lattice orientations on many boundaries (Figure 3.7). Additionally, fine grained, grungy looking recrystallized grains are present near the boundaries of some of the feldspar porphyroclasts (Figure 3.7F), and some are also present within the fine grained feldspar-rich matrix.

Within the fine grained feldspar-rich matrix layers, the intermixed quartz grains are of a similar size and shape as the feldspar grains (Figure 3.8B). The fine feldspar grains are similar in size to the subgrains and new grains associated with the feldspar porphroclasts. Large masses of these grains appear to have similar optical orientations. Additionally, some of the few slightly larger grains in the matrix layers are divided into 2-3 subgrains that are the same size as the other smaller grains.

Unequivocal shear sense indicators are ubiquitous throughout all the thin sections, and display a top-to-the-southwest sense of shear. Almost all samples contain numerous feldspar σ-type mantled porphyroclasts (Figure 3.7E). Some samples contain titanite and/or biotite fish-like grains (Figures 3.8A, 3.9A), or σ-type mantled amphibole porphyroclasts (Figure 3.8C). Inclined recrystallized quartz grains in the ribbons are common in the samples (Figure 3.8B), and clear biotite-rich C'-type shear bands at ~30-35° angles to the foliation are also widespread in several samples (Figure 3.8D).

3.3.2 Discrete Shear Zones with a Central Epidote Vein, Bleached Halo, and Flanking Paired Shear Zones Morphology

The shear zones within the study area that possess the central vein, bleached halo, and flanking paired shear zones morphology vary greatly in intensity of bleaching and shearing. Seven samples were collected from shear zones that showed all different

degrees of development from likely incipient (e.g., sample HQ-C, Figure 1.5A) to fully developed (e.g., sample SCM-51, Figures 1.5E-F, 2.9D-F, 2.14B). Mineralogical and microstructural differences exist between the least and the most developed shear zones with this morphology. The less developed discrete shear zones still preserve the subhorizontal country rock foliation in the bleached halo (although the country rock has been modified by replacement and recrystallization), and the central epidote vein crosscuts this foliation subvertically (Figure 3.10A; also see Figure 2.14C). In the less developed to moderately developed discrete zones, the flanking paired shear zones typically consist of either mylonite or ultramylonite, although the flanking paired zones in the likely incipient shear zone sample (HQ-C) do not contain mylonite, but instead consist of biotite-rich C'-type shear bands that cut through the country rock foliation or locally reorient the foliation into parallelism. In the most developed discrete shear zones, the country rock foliation is not preserved in the bleached zone or in the flanking paired shear zones, but instead the foliation parallels the vein, and the flanking paired shear zones consist of ultramylonite.

An additional two samples, HQ-B and HAR-9, were collected from the eastern mapped area (Figure 2.4) from a shear zone that had undergone extensive bleaching in its core without an associated epidote vein. Sample HAR-9 was collected from the core of the bleached part of the shear zone whereas sample HQ-B was collected from non-bleached mylonitized rock on the border of the bleached core. These samples are also discussed in this section because, despite not having a central epidote vein, their microstructures are very similar to those of the shear zones discussed in this section and likely formed from the same processes.

All of the samples collected from the shear zones with central epidote veins, bleached haloes, and flanking paired shear zones display unique changes in mineralogy

across their widths from the vein outward. The samples are described in detail from the vein outward with a particular emphasis on the end-member types, incipient shear zone sample, HQ-C, and fully developed shear zone sample, SCM-51.

3.3.2.1 Mineralogy and texture

The epidote vein in the incipient shear zone sample, HQ-C, does not have a vein-like morphology when viewed in thin section. Instead, a large cluster of epidote grains have partially overgrown feldspars on either side of a fracture (Figure 3.10A). The total width of the area replaced by epidote grains is ~4 mm. The epidote grains are scattered and range in size from ~250 μm to ~1.25 mm. The feldspar in the vein/fracture area is mostly recrystallized and/or replaced by oligoclase. Chlorite is also common along the fracture, composing about 15% of the area, and much of it is found in short, thin, discontinuous subvertical veinlets that crosscut the older fabric. Minor quartz, biotite, and garnet are also present. In this sample, sericitization of the feldspars is present to a small extent within and along the borders of the highly chloritized fracture trace, but is minor to non-existent otherwise. The opaque minerals in the sample are much more abundant adjacent to the epidote vein grains than elsewhere in the sample, and this relationship holds true in all the other samples as well.

The epidote vein in sample SCM-51, the sample from the fully developed shear zone, appears as a vein in thin section rather than as an epidote-rich replacement texture (Figure 3.11A-B). The epidote vein is ~1.25 cm thick, partially broken up, and composed of a mixture of subhedral to euhedral grains ~0.5 mm in length, and euhedral rectangular grains ~ 2 mm in length and ~0.5 mm in width. Some of the grains are zoned, and a couple exhibit faint albite-type twinning. A lesser number of grains appear

to have replaced feldspar porphyroclasts in a manner similar to that seen in sample HQ-C.

Whereas sericitization was minimal in sample HQ-C, the feldspar grains in sample SCM-51 are heavily sericitized in a ~1-1.5 mm zone directly adjacent to the vein and within the broken up parts of the vein (Figure 3.12). Outside of this zone, the degree of sericitization of the feldspars drops off dramatically and then further decreases gradually away from the vein. Chlorite, some with a radiating habit, comprises ~5% of the vein area. Quartz is also present as vein filling and recrystallized feldspar from the wall rock has been mixed in with the vein during deformation. In the strongly altered zone adjacent to the vein, metamorphic titanite, epidote, and opaque minerals are ubiquitous (Figure 3.12). The opaque minerals decrease dramatically in number away from the vein, and the titanite and epidote are almost entirely restricted to the altered area. Small biotite grains are present but very rare.

The other samples also contain vein epidote and some contain vein quartz, as well as epidote replacement of plagioclase near the veins (Figures 3.10B, 3.11C, 3.13). These samples do not contain chlorite in the veins. Biotite is present most commonly as a feldspar replacement product. In all samples, biotite content is lower in the bleached haloes than in the flanking paired shear zones, but is not systematically different than biotite content in the country rock (Tables 3.1, 3.2). Opaque minerals increase in amount near the vein in every sample, and titanite is present both near and away from the vein and is associated with epidote, quartz, and garnet (Figure 3.4C-E). Several titanite grains in multiple samples contain a single garnet inclusion. The feldspar immediately adjacent to the vein is sericitized in some samples (Figure 3.10B).

Near the central veins in all samples except for SCM-51, many large (several mm long) feldspar porphyroclasts are present, but the grain size of the porphyroclasts

progressively decreases towards the flanking paired shear zones where porphyroclasts are much less numerous and range in size from ~500 μm to ~1 mm long. Quartz grain size similarly decreases from ~1-1.5 mm adjacent to the vein to ~100-200 μm in the paired shear zones. Biotite becomes more abundant from the vein to the flanking shear zones (Figure 3.14). Biotite grains are mostly isolated near the vein and are associated with large feldspar porphyroclasts (Figure 3.15), but are more aligned away from the vein and form through-going bands in the paired shear zones (Figure 3.14E).

3.3.2.2 Microstructures

In some of the samples, the epidote veins are fractured and some grains are pulled apart (Figure 3.11), whereas in other samples, the veins remain intact (Figure 3.10B). Some grains continued growing as they were pulled apart as evidenced by the presence of optically continuous fibers that connect separate parts of the grains (Figure 3.11B). Some of the epidote vein grains are deformed into subtle fish that give a sense of shear, many display undulatory extinction, and some are folded (Figure 3.11A). In the fully developed shear zone sample, SCM-51, subgrains are evident on a few of the epidote grains, although they are isolated and extremely rare (Figure 3.11D).

The vein quartz that precipitated with the epidote is medium to coarse grained (hundreds of microns up to several millimeters in length) and exhibits lobate and sinuous boundaries (Figure 3.13). The sinuous nature of these boundaries is particularly pronounced in coarse-grained quartz found in protected pockets surrounded by large epidote grains (Figure 3.13A-B). Where the vein quartz is not protected by epidote, it has undergone complete or near complete recrystallization (Figure 3.13C-D).

Many of the quartz grains display undulose extinction both inside the veins and away from the veins. In the bleached haloes, quartz grains display a moderate CPO,

whereas in the paired shear zones, the CPO is locally very strong. Feldspar is highly fractured and also displays undulose extinction (Figures 3.16C, 3.17D).

Many of the feldspar porphryoclasts outside the veins and throughout the bleached zones contain subgrains on their boundaries and new grains of similar size and optical orientation in the surrounding matrix. In sample SCM-51, the recrystallization of feldspar porphyroclasts is complete in the thin altered zone adjacent to the vein (Figure 3.12), but in general, the recrystallization of the porphyroclasts progressively increases away from the vein (Figure 3.14). However, the feldspar porphyroclasts in all samples have been very affected by myrmekite replacement and by the non-symplectic oligoclase replacement of potassium feldspar (Figures 3.15, 3.16). Myrmekite replacement textures are known to recrystallize readily (Vernon et al., 1983; Vernon, 1991; Tsurumi et al., 2003), and possibly this is also true of the oligoclase replacement texture.

These replacement textures, which are present in minimal amounts in the non-bleached discrete shear zone samples, are extensive and striking in the samples from the bleached zones and flanking paired shear zones (Figures 3.14-3.16). Very few potassium feldspar grains in the bleached zones and paired shear zones are unaffected by the replacement, and all stages of replacement from minor to complete can be discerned. The non-symplectic oligoclase replacement texture is irregular and patchy in appearance in some places, but has square edges to it in other places (Figure 3.15). The prevalence of the square-shaped replacement pattern implies that the replacement product may have utilized cleavage planes for access to the interiors of the K-feldspar porphyroclasts.

Very rarely, tiny myrmekite lobes are found on the edges of the oligoclase replacement texture that extend into the non-replaced relict grain interiors. Very commonly the same grains affected by the oligoclase replacement texture are also affected by myrmekite replacement, but the myrmekitic plagioclase does not have the

same optical orientation as the non-symplectic oligoclase. Many of the grains with the replacement texture simultaneously show albite twinning in the powdery gray oligoclase replacement patches and microcline twinning in the darker gray potassium feldspar patches (Figure 3.16).

The oligoclase replacement texture is commonly not associated with other minerals, but can be associated in varying degrees with biotite, muscovite, and/or sericite. These minerals are present within the feldspar porphyroclasts, nearly always in the oligoclase patches rather than in the relict potassium feldspar patches (Figure 3.15). Epidote, sphene, and garnet may also be present with the replacement texture. The degree to which the micas appear with the replacement texture is generally minor near the vein. In some samples, sericite and muscovite are more common near the vein than biotite, but other samples lack white mica altogether. From the vein outward, the amount of biotite associated with the oligoclase increases significantly. In the more sheared portions of the rock, biotite is far more abundant as a replacement product than muscovite or sericite. In most samples, muscovite is absent or nearly absent in the more sheared parts of the rocks.

Biotite is not only present as a replacement texture in the interiors of the potassium feldspar grains but is also present near the rims. As recrystallization of the myrmekite and oligoclase replacement textures increase away from the vein, the biotite content increases as well, and the grains become progressively more aligned, eventually forming connected strands and through-going bands (Figure 3.14). This alignment and interconnectedness of biotite is most apparent on the rims of porphyroclasts where recrystallization of myrmekite and oligoclase is greatest. In most samples, the increase in biotite content from the vein outward to the flanking shear zones is gradual. In a sample of one of one of the less common flanking paired shear zones that also appears bleached

(Figure 2.14A), the biotite content is lower and quartz layers are thicker and more abundant.

In some of the samples, relatively thick bands of quartz are present throughout the bleached zone, some of which are strongly recrystallized and exhibit a strong CPO (Figure 3.17A). These bands are significantly thicker and more through-going than the quartz bands and pods in the country rock, and therefore likely initiated as quartz veins that were subsequently deformed. In some samples, these quartz layers have deformed much more readily than the more feldspar-rich layers, and an S-C fabric is apparent in which the quartz layers form the C-planes in the fabric and the feldspar-rich layers form the S-planes (Figure 3.17A). Both the feldspar porphyroclasts that compose the S-planes and the recrystallized quartz grains in the quartz layers that compose the C-planes are inclined in a top-to-the-southwest direction.

Many of the paired shear zone samples contain closely associated epidote, titanite, garnet, and opaque minerals. These minerals may be found wrapped in biotite folia and elongate in the direction of foliation. Many of the amphibole grains are fish-like in shape and indicate a top-to-the-southwest sense of shear. Small (100-250 μm) garnet is also found with faces adjacent to epidote or titanite grains and as inclusions in titanite, or more rarely as isolated grains (Figure 3.4C-F). Garnet is more abundant in the shear zones than it is in the bleached haloes and the surrounding country rock, and lacks the pink tint of the igneous garnet present in some of the country rock. Titanite is also commonly intimately associated with opaque minerals. It typically contains opaque inclusions, exhibits faces adjacent to opaque minerals, and sometimes appears to rim opaque minerals.

A few of the flanking paired shear zone samples are composed of mylonite (Figures 3.4F, 3.15B), and these shear zones appear very similar in thin section to the

discrete shear zones not affected by bleaching and veining (Figures 3.7, 3.8, 3.9A). The main difference is that the flanking paired shear zone mylonites contain more biotite, and the feldspars are much more replaced by myrmekite and oligoclase. The majority of the flanking paired shear zones, however, are composed of ultramylonite (Figure 3.14E). These shear zones are also very biotite rich, and the quartz and feldspar grains that compose the bulk of the matrix are similar in size (10s of μm to ~100 μm), resulting in a fairly homogeneous fabric (Figure 3.14E-F). Very fine grained, grungy looking recrystallized feldspar is also present within the matrix. Thin layers of these grains are interspersed with layers of recrystallized myrmekite and other recrystallized feldspar grains.

In the incipient shear zone sample, HQ-C, the paired shear zones are manifested as biotite-rich C'-type shear bands rather than as mylonitic or ultramylonitic shear zones (Figures 3.17C, 3.18). These thin shear bands are characterized by 1-5 μm thick through-going biotite-rich layers oriented at ~30-35° to the foliation. Fine layers of very fine grained grungy recrystallized feldspar are immediately adjacent to the biotite grains in the shear bands and in some cases make up a significant portion of the shear bands (Figures 3.17B-D, 3.18). Some of the C'-type shear bands are richer in quartz than in biotite. In these areas, the bands of quartz that are aligned with the country rock foliation, previously described as probable quartz veins, are reoriented into an S-C'-type structure (Figures 3.17C). Quartz grains in the middle of some of the reoriented layers are long and thin, and together display a strong CPO, whereas the quartz grains on the edges display numerous subgrains that transition into new grains of similar size and lattice orientation. An S-C' fabric is well developed where C'-type shear bands are farther apart (Figures 3.17B-D, 3.18A-B). The S-fabric is mostly defined by σ-type mantled feldspar porphyroclasts and inclined recrystallized quartz grains. Some of the σ-type mantled

feldspar porphyroclasts are large and elongate (Figure 3.17D). Rarely, large (~1 mm long) rectangular quartz grains comprise part of the quartz bands and contribute to the S-fabric. Where the C'-type shear bands are close together, recrystallization of intermediary quartz and feldspar is extensive, and the S-C' fabric is lost (Figure 3.18C-D). In these regions, the C'-type shear bands are no longer distinguishable from the surrounding grains which have adopted the same orientation as the shear bands, resulting in a relatively homogeneous fabric that appears similar to the ultramylonitized fabric of the better developed flanking paired shear zone samples (compare Figures 3.14E-F and 3.18D).

The same unequivocal shear sense indicators that are present in the other discrete shear zones not associated with veining and bleaching are also present in the paired shear zones that are associated with veining and bleaching. Shear sense indicators include feldspar σ-type mantled porphyroclasts (Figure 3.17B), amphibole fish, biotite fish, inclined recrystallized quartz in bands and veins (Figure 3.13C-D), S-C fabrics (Figures 3.13C-D, 3.17), and biotite-rich C'-type shear bands (Figures 3.17B-D, 3.18). In sample HQ-C, some of the feldspar porphyroclasts that are preserved between the C'-type shear bands display comma-shaped myrmekite on their rims that is deflected in the direction of shear (after Simpson, 1985; Simpson and Wintsch, 1989; Figure 3.19). All of the shear sense indicators yield a top-to-the-southwest sense of shear.

3.3.3 Atypical Discrete Mylonitic Shear Zone

As discussed in Chapter 2, one discrete shear zone was observed with an anomalous SE strike and SW dip in the northern part of the study area (Figure 2.3), and contained a 1 cm thick quartz vein on one margin.

3.3.3.1 Mineralogy and texture

A sample of this vein (SCM-4) shows most of the quartz is very fine grained (~10 μm in length) and slightly elongate. A couple of clusters of elongate porphyroclast-like quartz ribbons are present (Figure 3.20A). Ribbons may be as long as ~1 mm in length, but are more commonly hundreds of microns in length. A small number of plagioclase and potassium feldspar porphyroclasts, ranging from ~100 to 500 μm in length, exist as isolated grains or in trains of several grains. Some of the feldspars show minor to moderate alteration to sericite. A couple of grains with microcline twinning show no alteration. In all cases, the feldspar porphyroclasts are associated with seams of very fine grained feldspar and mica that contribute to the foliation in the rock. The mica is mostly biotite, but rare muscovite is present in the seams as well.

3.3.3.2 Microstructures

The porphyroclast-like quartz ribbons display undulatory extinction and show a strong CPO. Aside from these uncommon ribbons, the quartz is almost entirely recrystallized. The quartz grains are all of similar size (~10 μm) and shape, and together display a strong CPO. A transition from subgrains to new grains of the same size and shape is clearly visible on the edges of the quartz ribbons (Figure 3.20A).

Some of the feldspar porphyroclasts are fractured, and undulatory extinction is common. Some feldspars are not recrystallized; others are partially recrystallized on their boundaries. These porphyroclasts contain very fine grained grungy feldspar grains on their borders, and the boundaries between the porphyroclasts and the recrystallized grains are blurry. Subgrains are not present on the porphyroclasts that border these very fine grains. However, rare feldspars have a few subgrains on their edges and also new grains on their borders that are of similar size and crystallographic orientation as the subgrains.

Many shear sense indicators are present in the sample, and all of them indicate the same sense of shear. At high magnification, a pronounced S-C fabric is evident in which the C-type shear bands are defined by seams of mica and fine grained recrystallized feldspar, and the S-planes are defined by the slightly elongated and inclined recrystallized quartz grains that compose the bulk of the sample. Other shear sense indicators include feldspar σ-type mantled porphyroclasts, feldspar mineral fish, and σ-type quartz ribbons (Figure 3.20A). Unfortunately, the part of the sample that contained the orientation notch was lost during thin section construction, and so the direction of shear is uncertain. A small indent is found in one corner of the sample that may be a remnant of the notch, and if this is the case, the sense of shear is top-to-the-southwest.

3.3.4 Mylonitized Veneers on Fractured Surfaces

3.3.4.1 Mineralogy and texture

Sample SCM-48-2 was collected from one of the isolated fractured surfaces that are coated with thin mylonitic veneers in the northern part of the study area (Figure 2.8A-C). These veneers appear to be only ~1 mm in thickness in the field and cut across the country rock foliation. In thin section, the mylonitized veneer is only ~100-200 μm thick and is above and subparallel to a ~600-800 μm thick zone of protomylonite (Figure 3.20B). The mylonitized surface is composed of ~67% feldspar, ~24% quartz, ~8% biotite, some of which is altered to chlorite, and ~1% muscovite (Table 3.2). The majority of feldspar is extremely fine grained (μm-scale), although rare feldspar porphyroclasts ~100 μm in size are present (Figure 3.20B). A quartz layer is present with grain sizes up to ~50 μm, but the majority of the quartz is very fine grained (μm-scale) and is found intermixed with the fine grained feldspar. Biotite, chlorite, and muscovite

are present in wispy bands and are commonly associated with the fine grained feldspar layers.

In the protomylonite zone, the feldspar porphyroclasts range in size from ~100-400 μm (Figure 3.20B). One rare large clast is ~800 μm in length. Recrystallized, very fine grained feldspar is plentiful. Quartz is present in layers in which individual grain sizes are ~50-100 μm in length with fewer larger grains up to ~200 μm in length. Some titanite grains are isolated, but more commonly the grains are clustered. Titanite is diamond shaped and most grain sizes range from tens of microns to hundreds of microns. A single large titanite grain, ~500 μm in length, is also present. A trace amount of opaque minerals, anhedral to euhedral in shape and up to ~100 μm in length are present in small clusters and trains and tend to be associated with the fine grained feldspar layers.

3.3.4.2 Microstructures

Many of the quartz grains show a strong CPO, and undulose extinction is widespread. The quartz grains appear to have been entirely recrystallized. In the mylonitized veneer, the quartz is extremely fine grained, and large masses of grains share similar optical orientations (Figure 3.20B). The recrystallized feldspar is extremely grungy looking and boundaries of the grains look blurry.

In the protomylonite zone, transitions from old grains with subgrains to new grains of the same size and shape are apparent. Feldspar porphyroclasts commonly display undulose extinction, and some are fractured. A small number of the porphyroclasts have subgrains on their edges that transition to adjacent new grains of similar size and similar optical orientation. However, much of the recrystallized feldspar is extremely fine grained, very grungy in appearance, and with blurry boundaries (Figure 3.20B). Large masses of these fine grained recrystallized feldspar layers have similar

optical orientations. Some feldspar porphyroclasts display a hint of myrmekite on their edges, and some show a secondary feldspar (likely oligoclase) replacement texture similar to that seen in many of the mylonites from the more common discrete shear zones (Figures 3.14-3.16). The feldspar porphroclasts in the immediately adjacent country rock also show the replacement texture. In these grains, the texture can be striking, visible as numerous larger and typically interconnected blebs of feldspar that have replaced up to half of the original grain. The texture decreases and disappears away from the protomylonite zone.

A few shear sense indicators are present in both the mylonitic veneer and the protomylonite zone and all suggest a top-to-the-south sense of shear (Figure 3.20B). The most obvious shear sense indicator is inclined recrystallized quartz. Subtle domino feldspars and δ-type and σ-type mantled feldspar porphyroclasts are also present.

3.3.5 Interpretation

The common discrete shear zones described in sections 3.3.1 and 3.3.2 contain the same metamorphic mineral assemblage as the adjacent country rock (i.e., the northern country rock). Some of these minerals, such as titanite, epidote, and opaque minerals, are locally abundant near the central epidote veins in the discrete shear zones characterized by a central vein, bleached halo, and flanking paired shear zones morphology (Figure 3.12). Biotite, and more rarely, epidote, garnet, or titanite, are associated with the non-symplectic oligoclase replacement product, and biotite and garnet are more plentiful in the flanking paired shear zones than in the bleached haloes and the country rock. All of the more common discrete shear zones contain myrmekite and non-symplectic oligoclase replacement of feldspar, but these features are particularly widespread in the shear zones with the central vein, bleached halo, and flanking paired

shear zones morphology. These replacement products appear to be responsible for the bleached appearance of the bleached haloes.

Most of the common discrete shear zones show evidence for lattice reorientation of quartz (into long thin ribbon grains; Figure 3.8A), and a few of the samples contain evidence of lattice reorientation of feldspar (into elongate grains; Figure 3.17D). All of the samples show evidence for predominantly GBM recrystallization in quartz and SGR recrystallization in feldspar with a smaller contribution of SGR recrystallization in quartz and BLG recrystallization or neocrystallization in feldspar (Figure 3.7). The fine grained feldspar in the feldspar-rich matrix layers was likely formed primarily by SGR recrystallization. Some of these matrix grains appear to have been further recrystallized by BLG recrystallization or were neocrystallized. All of the shear zones indicate a top-to-the-southwest sense of shear (Figures 3.7E, 3.8, 3.9A).

Conversely, the sole, atypical discrete shear zone with a SE strike and a SW dip (section 3.3.3) and the mylonitized veneers on fractured surfaces (section 3.3.4) show evidence for predominantly SGR or BLG recrystallization in quartz and BLG recrystallization or neocrystallization in feldspar (Figure 3.20).

3.4 STONE CORRAL RIDGE SHEAR ZONE ROCKS

Nine samples were collected from the Stone Corral ridge shear zone, and these samples differ greatly in mineralogy, texture, and microstructure. One of the samples, SCM-19, is a protomylonite that was collected on the northern (structurally lower) boundary of the Stone Corral ridge shear zone where the subhorizontal foliated country rocks transition into the strongly mylonitized rocks of the shear zone. This sample has much in common with country rock samples, both mineralogically and microstructurally,

but also has some important differences. The other eight samples are mylonites that vary in mineralogy and degree of strain.

3.4.1 Protomylonitic Boundary Rock

3.4.1.1 Mineralogy and texture

The protomylonite sample (SCM-19) is composed of feldspar porphyroclasts displaying varying degrees of recrystallization, long layers of elongate quartz grains, discontinuous bands of biotite, and scattered titanite, epidote, amphibole, and opaque minerals. The sample is composed of ~62% feldspar, ~32% quartz, ~4% biotite (partially replaced by chlorite), ~1% epidote, and ~1% opaque minerals (Table 3.3). Feldspar porphyroclasts average ~1-2 mm in length but may occur as large as ~4 mm. Some feldspar porphyroclasts display minor alteration to sericite, biotite or fine grained optically unidentifiable products. The quartz grains display a variety of sizes, but are all on the order of hundreds of microns.

Myrmekite on potassium feldspar porphyroclasts is widespread, occurring on most grains. The degree of myrmekite consumption of the feldspar grains is, however, highly variable. Epidote occurs as subhedral to euhedral grains ranging from ~200 μm to ~1 mm in length. Some epidote exists as rims on allanite cores and some is symplectic with quartz intergrowths (Figures 3.2C, 3.3C). Titanite grains range in size from ~100-400 μm in length (Figure 3.2C; see also Figure 8.7C). Opaque minerals are anhedral to subhedral and are on the scale of hundreds of microns in length.

3.4.1.2 Microstructures

Both the quartz that composes the bands and the framework feldspar porphyroclasts display sweeping undulatory extinction. Where the quartz bands consist

of larger, less elongated grains, the grains exhibit a moderate CPO. Conversely, where the quartz grains are elongated into thin shear bands, the grains exhibit a very strong CPO. Many feldspar porphyroclasts are also highly fractured.

Quartz has very sinuous boundaries. Many grains exhibit finger-like protrusions into other grains. In some of the small C'-type shear bands that crosscut the foliation, similar to those in the country rock samples (Figure 3.2C), more highly strained, elongate quartz grains grade into subgrains and then into new grains that are similar in size to the subgrains. Titanite and epidote grains are also found along the bands or adjacent to them (Figure 3.2C).

Many of the feldspar porphyroclasts grade into subgrains on their boundaries and then into new grains on their borders that are of similar size and optical orientation as the subgrains. This recrystallization varies in degree from minor to nearly complete. In porphyroclasts where recrystallization is near complete, extensive traces of myrmekite are present, suggesting that the presence of myrmekite may have been required for such near complete recrystallization. Additionally, a smaller amount of the recrystallized feldspar forms masses of very fine grained, grungy grains of similar optical orientation. Small C'-type shear bands are comprised largely of these very fine grained feldspars (Figure 3.2C).

Many of the epidote and epidote-allanite grains have undergone brittle deformation. These grains appear to have been fractured and some were boudinaged. One of the boudinaged grains has quartz between the separated pieces.

Several shear sense indicators are present in the sample that suggest a top-to-the-northeast sense of shear, which include σ-type mantled feldspar porphyroclasts and a boudinaged epidote-allanite grain, which has an "s"-shaped form. The C'-type shear

bands are oriented at ~30-35° to the foliation and also show a top-to-the-northeast sense of shear (Figure 3.2C).

3.4.2 Mylonites

3.4.2.1 Mineralogy and texture

The modal mineralogy of the muscovite-absent and muscovite-poor samples varies from ~60-74% feldspar, ~21-33% quartz, ~3-11% biotite (some altered to chlorite), and up to ~2% opaque minerals (Table 3.3). Most of the samples contain a trace amount of some of the metamorphic minerals that are common in the northern country rocks and discrete shear zones. This assemblage is defined by epidote, titanite, apatite, biotite, opaque minerals, and garnet. The full metamorphic assemblage is only widespread in two samples (H3 and SCM-20), both of which were collected from the northern part of the shear zone (Figures 2.1, 2.2), although another sample (HAR-5a) contains abundant metamorphic titanite and biotite. One of the samples, B-3, is very different from the others because of its high muscovite content (Figure 3.21). This sample is composed of ~48% feldspar, ~30% quartz, ~17% muscovite, and ~4% biotite (Table 3.3).

Some of the samples are characterized by intermixed layers of fine grained feldspar and quartz of similar size (~10-50 μm) that alternate with layers of medium grained (~50-250 μm) quartz (Figure 3.22A). All layers contain abundant interspersed wispy, aligned biotite grains ~10-30 μm in length. Less commonly, biotite is present as larger grains ~100-200 μm in length that are partially, and in some cases almost entirely, replaced by chlorite. Large feldspar porphyroclasts (~0.5-3 mm) are present throughout the rocks (Figures 3.22A, 3.23A). In some of the other samples, the feldspars tend to be

less recrystallized, and feldspar porphyroclasts may reach larger grain sizes of up to several millimeters.

The mica-rich sample, B-3, is characterized by undulating and commonly discontinuous ribbons of medium grained (~100-600 μm) quartz, layers rich in large (~1-2 mm) muscovite grains, and layers of large (~1-2 mm) feldspar porphyroclasts separated mostly by finer grained (~10-50 μm) feldspar, and less commonly by medium sized (~100-500 μm) grains of quartz (Figure 3.21). Thin, wispy, interconnected muscovite grains are common throughout the sample. Biotite is also present as wispy bands and as subhedral grains up to ~300 μm in length. Many of the feldspar porphyroclasts in the sample are clustered or form trains. Some of the feldspar porphyroclasts are elongate in the direction of foliation (Figure 3.21A).

In some samples, the feldspar and quartz in the finer grained feldspar-rich layers are relatively uniform in both size and shape (Figure 3.22A), whereas in other samples, grain size is much more variable from both layer to layer and within each layer, and quartz matrix grains tend to be much larger than feldspar. Mica is common in all samples as an alteration product within the feldspar porphyroclasts and within the fine grained feldspar. In some of the samples, biotite is the most common mica alteration product, whereas in other samples, sericite is the most common alteration product.

In the two samples collected from the northern part of the shear zone that contain the extensive metamorphic mineral assemblage (samples SCM-20 and H3), epidote grains are up to ~0.5 mm in length, subhedral to euhedral in shape, and are commonly present in the feldspar-rich layers. Some of the grains are wrapped by mica folia and are slightly elongate in the direction of foliation. Several epidote grains display Carlsbad twinning. Other epidote grains are associated with extensively recrystallized feldspar porphyroclasts or myrmekite-rich areas. Many of these epidote grains are patchy in

appearance and are present in the cores of recrystallized porphyroclasts, suggesting they are reaction products. Epidote is occasionally found in contact with titanite and opaque minerals (Figure 3.4B). Rare symplectic quartz-epidote grains are also present (Figure 3.3D). Additionally, rare epidote veinlets ~1 mm in length crosscut the foliation at nearly right angles. Epidote is rare or absent in the other samples (i.e., those collected from the central and southern parts of the shear zone).

In all samples, subhedral to euhedral oxide minerals are well distributed throughout the rocks and are ~10-50 μm in size. In some samples, titanite grains are also distributed throughout the rock and are sometimes found near the edges of feldspar porphyroclasts that have undergone significant recrystallization. Titanite is euhedral in shape and commonly fish-shaped (Figure 3.9B; see also Figure 8.7E-F). The grains are ~0.5-1 mm in length and are commonly found clustered and in trains. The grains are elongate in the direction of foliation and wrapped by biotite folia. In B-3, rare garnet is present as subhedral grains up to ~1 mm in size. In the samples H3 and SCM-20, garnet grains are clustered and form trains; individual grains in the trains are dismembered, broken, and pulled apart. Sample H3 also contains minor fine grained (~10-50 μm) amphibole that is wrapped by biotite folia. Much of the amphibole is almost fully replaced by biotite.

3.4.2.2 Microstructures

In all samples, many of the quartz grains display undulatory extinction, and together the grains display a strong CPO (Figure 3.22). Some feldspar porphyroclasts also exhibit undulatory extinction, as well as subgrains (Figure 3.23). Most porphyroclasts contain abundant fractures, and some include planes of fluid inclusions or altered material that may indicate healed microfractures. The muscovite grains in B-3

also show undulatory extinction (Figure 3.21). The grains are aligned parallel to the foliation, but also display slight bending across their lengths and some have fine recrystallized grains on their boundaries.

In some of the samples, much of the quartz displays amoeboid textures, whereas other quartz has sharper, more polygonal boundaries (Figure 3.22). Many of these boundaries are pinned by micas that likely impeded further growth of the grains, but some grains do appear to have overgrown micas. In other samples, some of the quartz also displays amoeboid textures with sinuous grain boundaries, but a significant amount of quartz instead contains subgrains on its boundaries that grade into recrystallized new grains of similar size, shape, and optical orientation.

Some of the samples contain a small number of feldspar porphyroclasts with fairly sharp grain boundaries, continuous extinction, and with no subgrains present, but most of the feldspar porphyroclasts appear to have undergone moderate to large amounts of recrystallization, as evidenced by blurry and serrated boundaries and/or the presence of subgrains on boundaries and interiors. These porphyroclasts have small subgrains on their boundaries that transition into new grains with a simultaneous gradation in degree of lattice orientation. Figure 3.23 shows the full range of the degrees of recrystallization present in the porphryoclasts, from minimum recrystallization (e.g., the top grain in Figure 3.23A) to possibly complete recrystallization (Figure 3.23D). Masses of very fine grained, grungy looking feldspar are also present to a minor degree. In other samples, this relationship is reversed. The majority of feldspar porphyroclasts have masses of very fine grained grungy feldspar near their rims, and a lesser (but still significant) number of porphyroclasts have subgrains that transition into new grains of similar size, shape, and optical orientation. Similarly, the fine grained feldspar-rich layers contain more very fine grained grungy feldspar than do the other samples.

The abundance of myrmekite on porphyroclast boundaries may have also greatly enhanced the amount of recrystallization in many of the samples. Myrmekite is particularly extensive throughout some of the samples, such as the two samples collected from the northern part of the shear zone (samples SCM-20 and H3) and the muscovite-rich sample (B-3). Whereas myrmekite is common on the foliation-parallel edges of porphyroclasts, the lobes are also quite pervasive on non-foliation edges, particularly in sample B-3. Extensive recrystallization of myrmekite-rich parts of feldspar porphyroclasts may have led to complete or near complete recrystallization of some of the porphyroclasts (Figure 3.22B). In B-3, minor flame perthite is also present on some porphyroclasts.

Some of the fine grained feldspar layers contain characteristics reminiscent of myrmekite, such as lobe-shaped boundaries and remnants of tiny quartz vermicules, particularly in sample B-3 (Figure 3.22B). Aside from these myrmekitic vestiges, few microstructures are visible in the feldspars of the finer grained layers in most samples. These grains exhibit fairly uniform extinction overall and do not show evidence of brittle deformation, so it is likely many of these grains formed as a result of recrystallization of former feldspar porphryoclasts. In some of the samples, though, a minority of the fine grains have continuous or discontinuous undulatory extinction, suggesting some further deformation was recorded after recrystallization. In these samples, both the quartz and the feldspar grains in the fine grained layers appear to have accommodated deformation similarly as they are very similar in size and shape, and are only optically distinguishable by their degree of alteration and their difference in relief (Figures 3.22A, 3.23).

In sample H3, dilational microstructures are associated with many of the garnet grains. Grains of euhedral garnet have been broken apart in the rock, and quartz fringes have grown in their pressure shadows. In some cases, large quartz fibers that grew off

the garnet fragments can be discerned. As the garnets were pulled apart, fluids in the rock must have collected in the dilation sites between the broken grains and precipitated the quartz. Undulose extinction is apparent in some of the larger quartz grains; as the rigid garnets were pulled further apart, these quartz grains were no longer completely protected in their stress shadows, and underwent further deformation.

Kinematic indicators are evident in all samples, but a consistent sense of shear is only provided by half of the samples. In these samples, numerous feldspar porphyroclasts define subtle to obvious sigma-clasts with a top-to-the-southwest sense of shear. Two samples (SCM-20 and H3) contain titanite fish (Figure 3.9B; see also Figure 8.7E-F), and another sample (HAR-5a) contains small feldspar fish that all indicate a top-to-the-southwest sense of shear. Some of the quartz bands contain grains that are elongate and inclined in a top-to-the-southwest direction, and one sample (HAR-5b) contains quartz-rich C'-type shear bands inclined in a top-to-the-southwest direction.

In the rest of the samples, many of the microstructures are symmetric, and the microstructures that are asymmetric give both top-to-the-northeast and top-to-the-southwest senses of shear. For example, muscovite fish are common in sample B-3 but do not consistently indicate the same sense of shear (Figure 3.21B). However, the shapes of several feldspar porphyroclasts together with their recrystallized tails have a very subtle σ-type appearance that may suggest a top-to-the-southwest sense of movement.

3.4.3 Interpretation

The protomylonite sample (SCM-19) and the two mylonite samples from the northern part of the shear zone (H3 and SCM-20) contain the same metamorphic mineral assemblage as the country rocks and the discrete shear zones in the northern part of the study area. Sample HAR-5a is rich in titanite, but for the most part, the other samples

only contain trace amounts, if any, of the metamorphic minerals. The two mylonite samples (H3 and SCM-20) with the full assemblage of metamorphic minerals are also significantly more strained than most of the other samples.

The microstructures differ between the samples from the northern part of the shear zone and the samples from the central and southern parts of the shear zone as well. The quartz in the samples from the northern part of the shear zone is extensively recrystallized by GBM recrystallization, and the feldspar is extensively recrystallized by SGR recrystallization. The quartz and feldspar in the fine grained layers are similar in size and shape, which is typical of high temperatures of deformation. Conversely, in the central and southern parts of the shear zone, the quartz still shows evidence for GBM recrystallization but also shows evidence for SGR recrystallization. Similarly, the feldspar still shows some evidence for SGR recrystallization, but also shows more evidence for BLG recrystallization or neocrystallization than the samples from the northern part of the shear zone. These differences may suggest cooling occurred during deformation or more than one episode of deformation (see section 9.2.2.3 for further discussion). The samples with ambiguous senses of shear may provide evidence for two periods of shear with opposite senses, or else they may indicate a significant coaxial component to the shear during one episode of deformation (see section 9.2.3 for further discussion).

3.5 ISOLATED MYLONITIC SHEAR ZONES

3.5.1 Mineralogy and Texture

Three samples (B-5, B-9, and HAR-7) were collected from mylonitized rocks south of the Stone Corral ridge shear zone near the crest of Stone Corral ridge (Figures 2.1, 2.2, 2.8F). These samples were collected from isolated mylonitic outcrops ~0.5-1

meter thick. All surrounding outcrops were foliated but not mylonitized. The samples are composed of similar modal mineralogies, containing ~65-70% feldspar, ~25-32% quartz, and ~3-6% biotite (commonly replaced by chlorite; Table 3.3).

The samples are characterized by fine grained feldspar-rich layers (with intermixed quartz) that are intermingled with larger grained quartz ribbons (Figure 3.24). Feldspar porphyroclasts are abundant. In samples B-9 and HAR-7, the fine grained feldspar-rich layers and grains comprising the quartz ribbons are much finer grained than in B-5. In these two samples, the fine grained feldspar grains are commonly only ~25 μm in size, whereas the fine feldspar grains in B-5 are ~100 μm. The quartz grains in the quartz layers in samples B-9 and HAR-7 are elongate and ~50-100 μm in length, whereas those in B-5 are ~50-200 μm. The feldspar porphyroclasts in all samples are variable in size, ranging from ~250 μm to several mm in length, and some grains are moderately altered to sericite. Biotite exists as thin, wispy, foliation-parallel bands in samples B-9 and HAR-9, and as minor larger grains up to 400 μm in length in sample B-5. Most of the biotite grains in sample B-5 are partially or fully replaced by chlorite.

3.5.2 Microstructures

In two of the samples (B-9 and HAR-7), sweeping undulatory extinction of quartz is widespread. The quartz grains in these samples are extremely long, thin and appear attenuated (Figure 3.24B). The quartz has an extremely strong CPO. The quartz in sample B-5 also has a strong CPO, although not as pronounced as that in the other samples. Some of the feldspar grains in all samples display patchy undulatory extinction. Fracturing and microfracturing of feldspars is extensive.

The quartz grain boundaries in the samples are slightly blurry because of the finer grain size and larger number of subgrains. Most of the grains show an obvious transition

from subgrains on the edges of old grains to bordering new grains of similar size (Figure 3.24B). Most of the grains and subgrains in the samples are very elongate, although a few rare layers in sample B-5 contain recrystallized subpolygonal to polygonal grains. Although the morphology of this quartz is much different, subgrains that are similar sizes as the new surrounding grains are also plentiful in these layers.

A small number of the feldspar porphyroclasts in the samples have a few subgrains on their boundaries that transition into new grains of similar size, shape, and optical orientation as the subgrains. However, the majority of the feldspar porphyroclasts have very fine grained, grungy masses of grains present on some boundaries, and much of the feldspar in the fine grained feldspar layers also looks extremely grungy (Figure 3.24).

Myrmekite is uncommon in all samples. In sample B-9, the only myrmekite evident is almost completely enclosed within a feldspar porphyroclast. The high strain experienced by the rock may have destroyed all deformation-induced myrmekite as soon as it formed since myrmekite recrystallizes readily during deformation, or alternatively and perhaps more likely, the conditions weren't favorable for myrmekite formation. The rare myrmekite that does exist in the rock may be a remnant of an earlier fabric, and the location of the myrmekite (enclosed in porphyroclasts) protected it from destruction during subsequent deformation.

The sense of shear suggested by the microstructures in the samples is top-to-the-northeast (Figure 3.24A). The kinematic indicators in B-9 are widespread and unequivocal, whereas those in the other two samples are more subtle. In sample B-9, σ-type feldspar porphyroclasts, oblique recrystallized quartz grains, and normal microfaults all indicate a top-to-the-northeast sense of shear. The microfaults crosscut the foliation and must have occurred after the mylonitization. In the other samples, several σ-type

feldspar porphyroclasts also suggest a top-to-the-northeast sense of shear. Some broken feldspar porphyroclasts appear to have been rotated like dominos in a top-to-the-northeast direction, and in some areas in sample B-5, the recrystallized subpolygonal quartz grains are very subtly elongated and inclined in a top-to-the-northeast direction (see Figure 4.5).

3.5.3 Interpretation

The extremely long, thin, and attenuated appearance of the quartz grains in a couple of the samples suggests very high strain and significant lattice reorientation. The samples show compelling evidence that SGR recrystallization was the dominant recrystallization mechanism in quartz, and BLG recrystallization was the dominant recrystallization mechanism in feldspar. Alternatively, much of the fine grained feldspar may have been neocrystallized. The samples also show clear evidence for a top-to-the-northeast sense of shear, rather than the top-to-the-southwest sense of shear seen in the discrete shear zone mylonites in the northern part of the study area and in some of the Stone Corral ridge shear zone mylonites. These samples also lack the metamorphic mineral assemblage of the other shear zones and the northern country rocks, and they lack the extensive myrmekite seen in the other shear zones and the country rocks (including the adjacent southern country rocks that host the isolated shear zones).

3.6 MYLONITES FROM EAGLE EYE MOUNTAIN

3.6.1 Mineralogy and texture

Three mylonitic samples from near the detachment fault at Eagle Eye Mountain were collected for comparison with the mylonitic samples of the Stone Corral area (Figure 1.3). The modal mineralogy differs greatly among the three samples. Sample HQ-E contains ~35% feldspar, ~25% quartz, ~30% white mica, ~5% opaque minerals, and ~5% chlorite. Sample HQ-F contains ~79% feldspar, ~15% quartz, ~5% white mica,

and ~1% opaque minerals, and sample HQ-G contains ~59% feldspar, ~26% quartz, and ~15% white mica (Table 3.3). HQ-G contains trace amounts of opaque minerals, and all three samples contain trace amounts of epidote. The fine grained nature of the majority of the feldspar in the samples makes it difficult to estimate the amount of potassium feldspar versus plagioclase feldspar, but the majority of the larger feldspar porphyroclasts are potassium feldspar.

The grain sizes of various minerals and the overall morphology differ among the samples. Sample HQ-E is overall very fine grained. Almost all of the feldspar has been recrystallized into fairly uniform grains ~10 μm in size (Figure 3.25). A few angular clasts ~150 μm are present but are overgrown by numerous flakes of white mica. The quartz in the sample is present in discontinuous bands and isolated clast-like pods and is larger grained than the other minerals. Long ribbon grains in the bands average ~300-400 μm in length but can be as long as ~850 μm. The width of the bands is ~100-150 μm. The quartz in the pods is also elongate but to a much lesser degree (Figure 3.25A). It also averages ~300-400 μm in length but is thicker than the quartz bands at ~250 μm in width. The white mica in the rock exists as both widespread, continuous, very fine grained layers parallel to (and partly defining) the foliation, and as numerous large single grains ~400-450 μm in length (Figure 3.25B). The opaque minerals are elongate, rounded, and parallel to foliation. They range in length from ~100-350 μm. Chlorite is widespread and extensively interspersed in the fine grained recrystallized feldspar layers, forming an interconnected framework.

Sample HQ-F is coarser grained than sample HQ-E. The feldspar is present both as large, angular porphyroclasts ranging from ~150-650 μm in length, and as fine grained recrystallized masses surrounding the porphyroclasts and filling the interstices between porphyroclasts that appear to be broken apart and slightly separated. The quartz is

present as long ribbons ~500-750 μm in length and as finer grains in discontinuous bands interspersed in the fine grained feldspar masses. The white mica is very fine grained and forms continuous undulating bands.

Sample HQ-G contains abundant angular to subangular feldspar porphyroclasts ~150-500 μm in length. Many of the porphyroclasts are closely spaced with fine grained masses of recrystallized feldspar grains between them. Similar recrystallized feldspar masses also form fine grained layers in the sample. The quartz is present as fairly equant, rectangular grains in long continuous bands. The grains range from ~150-750 μm in length and are ~100-250 μm in width. The white mica is present as very fine grained specks that together form bands that appear to have grown around and through the fine grained feldspar layers.

3.6.2 Microstructures

Despite the differing modal mineralogy and textures in the three samples from near the detachment fault, the microstructures present are very similar and suggest similar deformation conditions. The quartz in all three samples displays continuous undulatory extinction and a CPO, which is moderate in samples HQ-E and HQ-G and strong in sample HQ-F. Some of the feldspars display discontinuous undulatory extinction, and many of the feldspars are highly fractured. In sample HQ-G, some of the fractured feldspars have quartz within the fractures.

Samples HQ-E and HQ-F contain old quartz grains that transition into subgrains on their boundaries and then into new neighboring grains of similar size, shape, and optical orientation, but sample HQ-G shows this feature to only a very small degree in isolated areas. All three samples also show examples of quartz grains with small bulges along their boundaries that protrude into neighboring quartz grains (Figure 3.25A). New

grains of similar size, shape, and optical orientation as the bulges are also present on the grain boundaries. The quartz layers in sample HQ-G are composed of large, rectangular grains. These grains also show small bulges on their boundaries that protrude into neighboring grains. The boundaries look finely serrated at high magnification, and adjacent new grains that are the same size as the protrusions are also present.

Many of the feldspar porphyroclasts in all three samples have boundaries that appear to blur into grungy masses of very fine grained feldspar of similar optical orientation that make up a large percentage of the samples, and that comprise almost all of the feldspar present in sample HQ-E. A small number of feldspar porphyroclasts contain flame perthite, but no myrmekite is present.

Very pronounced shear sense indicators are present in samples HQ-E and HQ-F. In sample HQ-E, mica fish (Figure 3.25B), pods of quartz grains forming σ-like clasts, isolated quartz fish, and C'-type shear bands defined by fine grained white mica imply a clear top-to-the-northeast sense of shear. In sample HQ-F, feldspar pieces rotated like dominos, pods of feldspar grains forming subtle σ-like clasts, quartz fish, and obvious C'-type shear bands defined by fine grained white mica bands also suggest a top-to-the-northeast sense of shear. Sample HQ-G does not contain any straightforward kinematic indicators.

3.6.3 Interpretation

The microstructures present in the Eagle Eye samples indicate that BLG and SGR recrystallization were both important recrystallization mechanisms in quartz, and that BLG recrystallization and/or neocrystallization were important processes affecting the feldspars. The top-to-the-northeast sense of shear in the samples is consistent with the

sense of shear displayed by the mylonites in the isolated shear zones near the crest of Stone Corral ridge (Figures 3.24A, 3.25B; see also Figure 4.5).

3.7 DISCUSSION: DEFORMATION TEMPERATURES

The mylonites of the Stone Corral study area display differing mineralogy, textures, and microstructures that suggest more than one deformation episode must have occurred. The northern country rock underwent deformation and metamorphism that resulted in the development of a poorly developed, locally protomylonitic gneissic foliation. The quartz in this foliation recrystallized predominantly by GBM recrystallization, and the feldspar recrystallized predominantly by SGR recrystallization (Figures 3.1C-D, 3.5). These recrystallization mechanisms are typical of temperatures >500 °C (Stipp et al., 2002; Tullis, 2002). The metamorphic mineral assemblage of these rocks is composed of epidote, titanite, biotite, opaque minerals, apatite, and garnet (Figure 3.4A). Myrmekite is also widespread (Figure 3.1A).

The quartz and feldspar in the discrete shear zones in the northern part of the study area and the mylonites located at the base (i.e., northern part) of the Stone Corral ridge shear zone also recrystallized predominantly by GBM and SGR recrystallization, respectively (Figures 3.7, 3.13, 3.22A, 3.23). These mylonites share the same metamorphic mineral assemblage as the northern country rocks (Figure 3.4). The mylonites also are greatly affected by myrmekite replacement textures and by a non-symplectic oligoclase replacement texture that is particularly well developed in the shear zones affected by bleaching, and is likely the main cause for the bleached appearance (Figures 3.14-3.16, 3.19). Overall, the recrystallization mechanisms of quartz and feldspar and the mineralogy of the rocks (i.e., extensive myrmekite, symplectic epidote, amphibole that is green in plane polarized light, and synkinematic growth of garnet and

biotite) suggest temperature conditions of >500 °C for both the country rocks and the mylonites, which is typical of amphibolite-facies conditions.

Conversely, the atypical discrete shear zone quartz vein sample (SCM-4) has recrystallized almost entirely by SGR recrystallization (Figure 3.20A). SGR recrystallization of quartz is typical of deformation temperatures between ~400-500 °C (Stipp et al., 2002), and therefore this shear zone may have formed at a lower temperature than the amphibolite facies shear zones. Alternatively, the SGR recrystallization may be due to a higher strain rate.

The mylonitized veneers on the fractured surfaces also appeared to have formed at lower temperature conditions because the quartz recrystallized predominantly by BLG recrystallization and feldspar recrystallized predominantly by BLG recrystallization or was neocrystallized (Figure 3.20B). Additionally, the country rock foliation is crosscut by the fabric rather than reoriented into parallelism as in the amphibolite facies discrete shear zones. These features suggest the veneers formed at greenschist-facies conditions, consistent with Miocene metamorphic core complex deformation. These shear zones, however, are found above and subparallel to a <1 mm thick protomylonite zone that likely formed at amphibolite-facies conditions. Some of the feldspar in this zone appeared to have recrystallized by SGR recrystallization, and much of the feldspar is affected by the non-symplectic oligoclase replacement texture (and less commonly by myrmekite). This texture is also extensive in the immediately adjacent country rock and decreases in intensity away from the protomylonite zone. This texture is characteristic of the amphibolite facies mylonites and is responsible for the bleached haloes found in some of the discrete shear zones. Therefore, the protomylonite zone likely developed at amphibolite-facies conditions during the Late Cretaceous and was reactivated during greenschist-facies conditions during the Miocene to form the mylonitized veneers. The

possibility that the veneers formed during amphibolite-facies conditions at very high strain rates cannot be ruled out, however, without more study.

Some of the mylonites in the Stone Corral ridge shear zone display the same quartz and feldspar recrystallization microstructures and contain the same metamorphic mineral assemblage as the country rocks and amphibolite facies discrete shear zone mylonites (Figures 3.4B, 3.22, 3.23). These mylonites thus also likely formed during amphibolite-facies conditions. Other mylonites in this shear zone, however, display slightly different quartz and feldspar recrystallization microstructures, and also lack the metamorphic mineral assemblage. The quartz in these samples still shows recrystallization by GBM but also shows more recrystallization by SGR than the other samples. The feldspar also still shows some recrystallization by SGR but has been more affected by BLG recrystallization or neocrystallization than the amphibolite facies samples. These recrystallization mechanisms suggest deformation temperatures of ~450-550 °C, typical of upper greenschist-facies or lower amphibolite-facies conditions (Stipp et al., 2002; Tullis, 2002).

The isolated mylonites south of the Stone Corral ridge shear zone show strikingly different recrystallization microstructures than the other samples. The quartz in these highly strained samples has undergone extensive SGR recrystallization, and the feldspars have undergone extensive BLG recrystallization or neocrystallization (Figure 3.24), suggestive of deformation temperatures of ~400-500 °C, typical of greenschist-facies conditions (Stipp et al., 2002; Tullis, 2002). These samples also lack the metamorphic mineral assemblage of the amphibolite facies mylonites and country rocks.

The mylonite samples of Eagle Eye Mountain contain quartz that has recrystallized by both BLG and SGR recrystallization (Figure 3.25A). The prevalence of grains recrystallized by both of these mechanisms suggests that the mylonites were at

transitional deformation conditions in which BLG was the dominant recrystallization mechanism, but SGR recrystallization was still very active, perhaps between ~350-400 °C (Stipp et al., 2002). Although BLG recrystallization of feldspars does not tend to occur below ~400°C (Tullis, 2002), neocrystallization may be active down to ~250 °C if fluid is present (Fitz Gerald and Stünitz, 1993). The very fine grained feldspar in these samples, therefore, may have been more affected by neocrystallization than BLG recrystallization (Figure 3.25). The recrystallization mechanisms and the likely temperatures of deformation are consistent with the conditions during Miocene detachment fault mylonitization. Interestingly, however, the large, rectangular quartz grains seen in sample HQ-G are typically indicative of relatively high temperatures of deformation. This feature may have developed during an earlier event that affected this sample, but the strong evidence for BLG recrystallization on the boundaries of these grains suggests they were overprinted by a lower temperature deformation event (i.e., detachment faulting).

The petrographic characteristics of the samples from the numerous shear zones throughout the study area and from Eagle Eye Mountain indicate that at least two different episodes of mylonitization are represented in the Harquahala metamorphic core complex. One episode occurred at amphibolite-facies conditions, and the other occurred at greenschist-facies conditions. The details and implications of this are discussed thoroughly in Chapter 9.

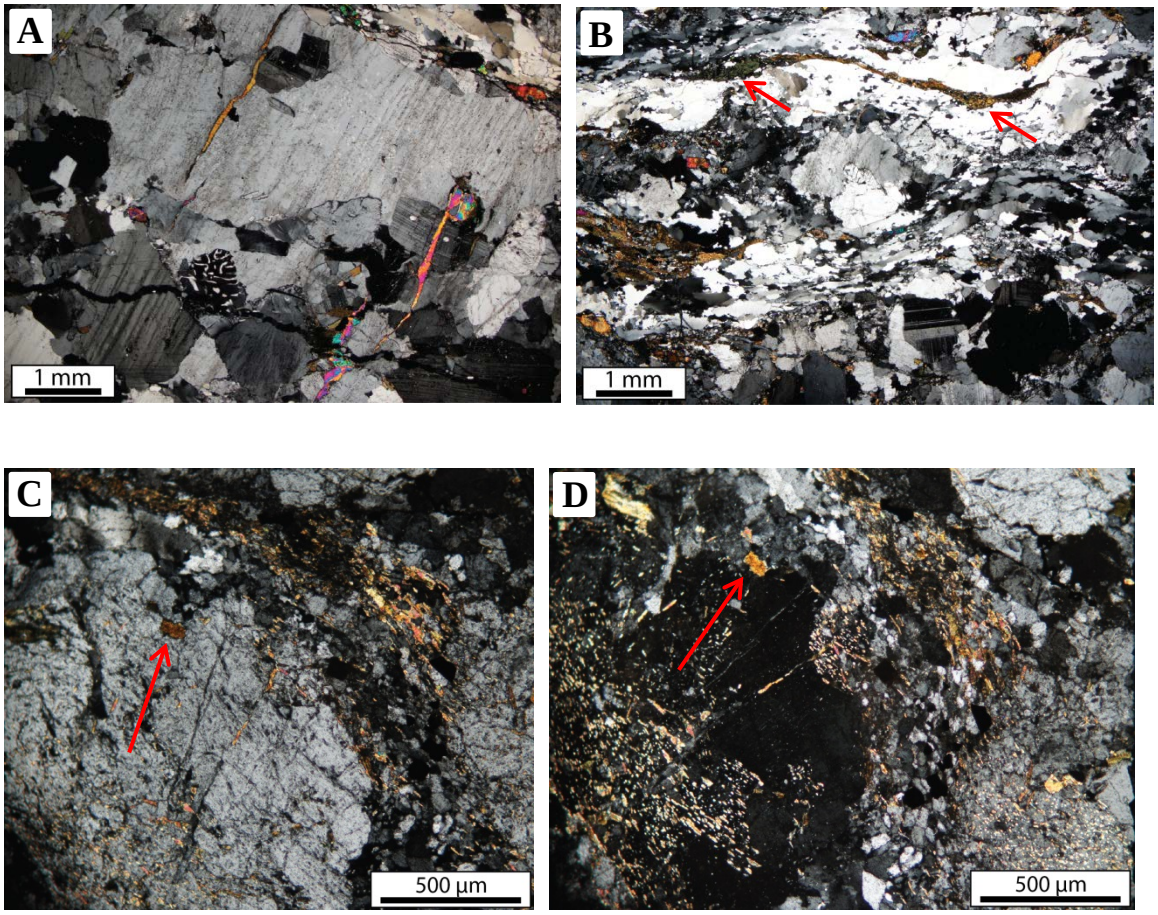

Figure 3.1: Photomicrographs of the northern country rock. A) Feldspar, some of which is rimmed by myrmekite and some of which is crosscut by epidote veinlets; sample SCM-6; B) Foliation is defined by layers rich in feldspar porphyroclasts and layers rich in quartz. Red arrows point to amphibole partially replaced by biotite; sample HQ-D; C-D) Same area, but stage is rotated in D to emphasize SGR recrystallization on the edges of the feldspar porphyroclasts. Red arrows point to a biotite grain for a reference point. Note the replacement of feldspar by biotite and the extensive fracturing of the feldspar; sample H2.

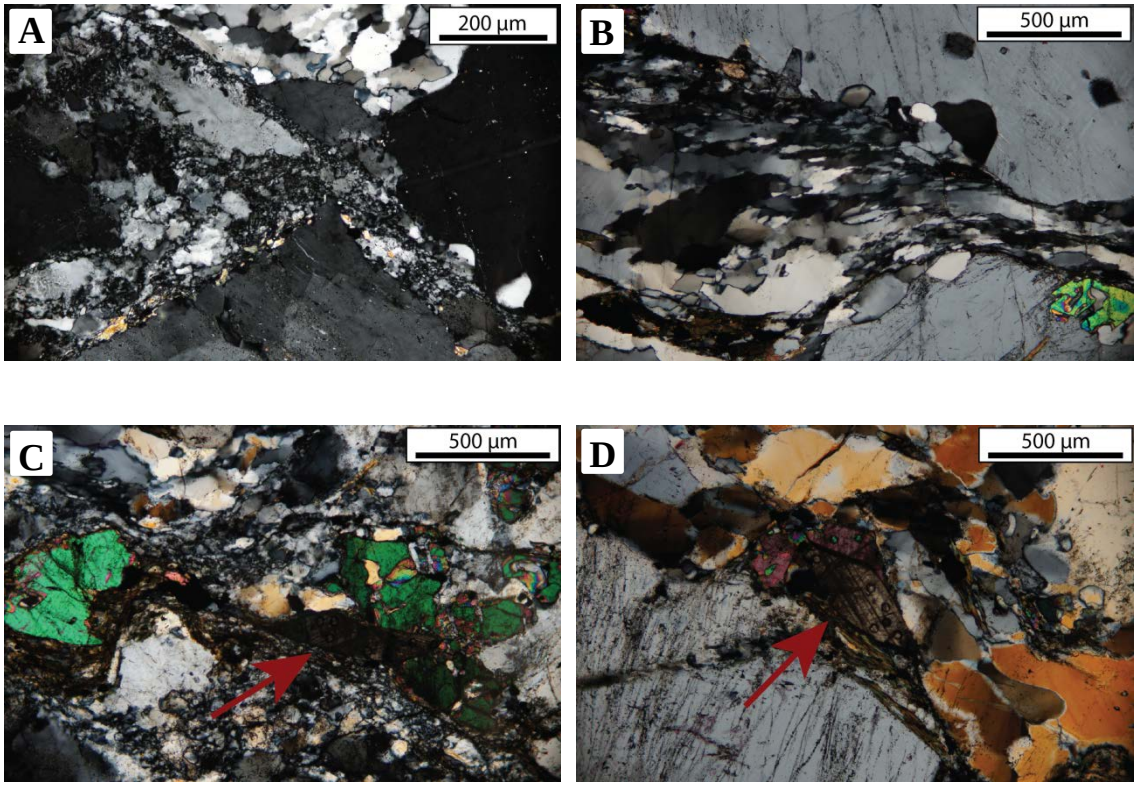

Figure 3.2: Photomicrographs of discrete shear bands in the northern country rock and the Stone Corral ridge shear zone protomylonite. Red arrows point to titanite. The small circles in the titanite grains in C, D are laser ablation pits formed during U-Pb dating. A) BLG recrystallization or neocrystallization of feldspar along narrow shear bands; sample HQ-D; B) Deflection of quartz grains into narrow shear band with SGR recrystallization of quartz. Note symplectic epidote on edge of a feldspar porphyroclast; sample SCM-6; C) Titanite and symplectic epidote along a shear band. Note BLG recrystallization or neocrystallization of feldspar along the band; sample SCM-19; D) Titanite and epidote along a shear band; sample SCM-6.

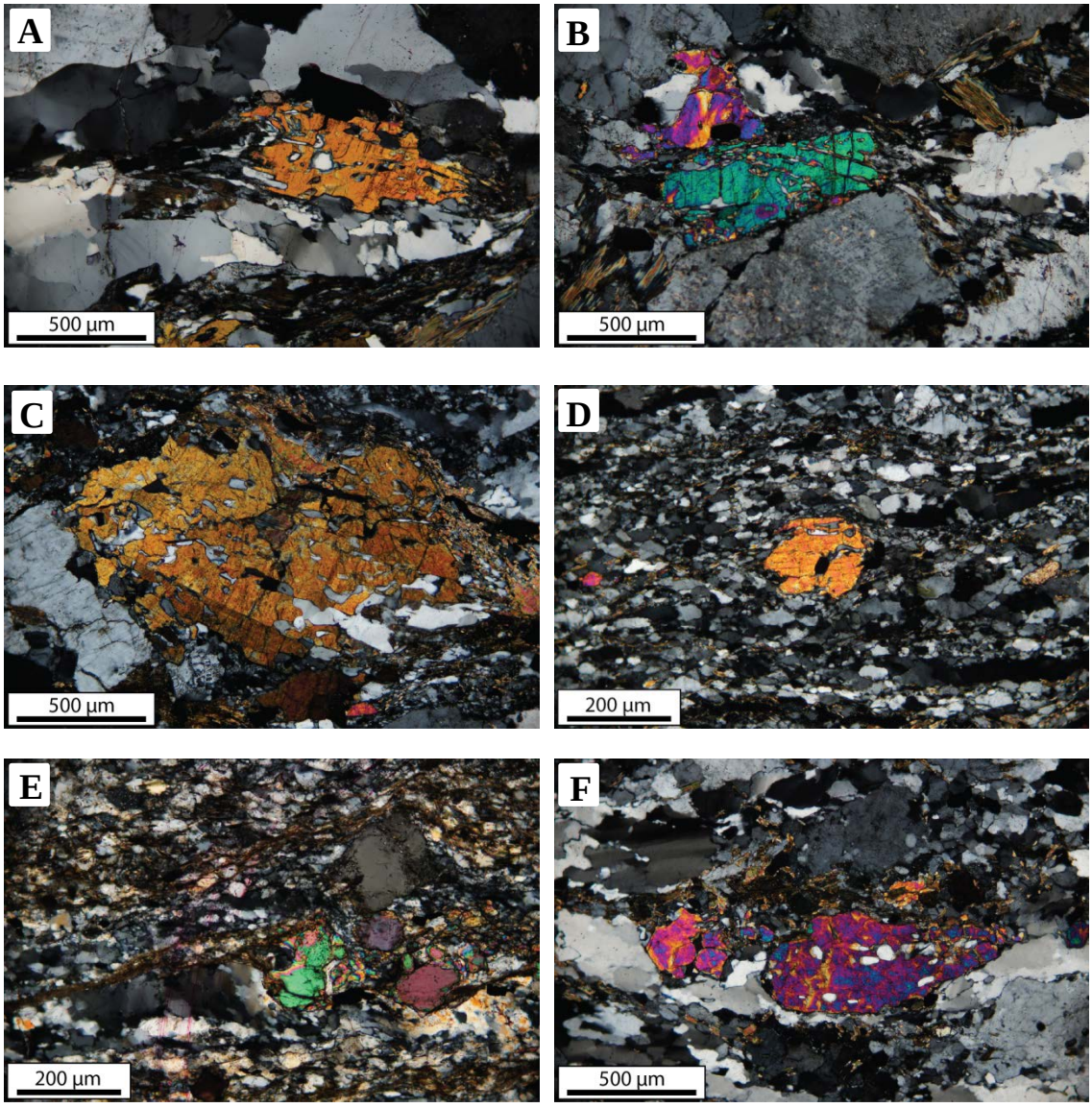

Figure 3.3: Photomicrographs of symplectic epidote. From samples: A, B) Country rock; sample SCM-6; C) Protomylonite; sample SCM-19; D) Stone Corral ridge shear zone mylonite; sample H3; E) Discrete shear zone mylonite; sample H1; F) Bleached halo of discrete shear zone; sample HAR-16.

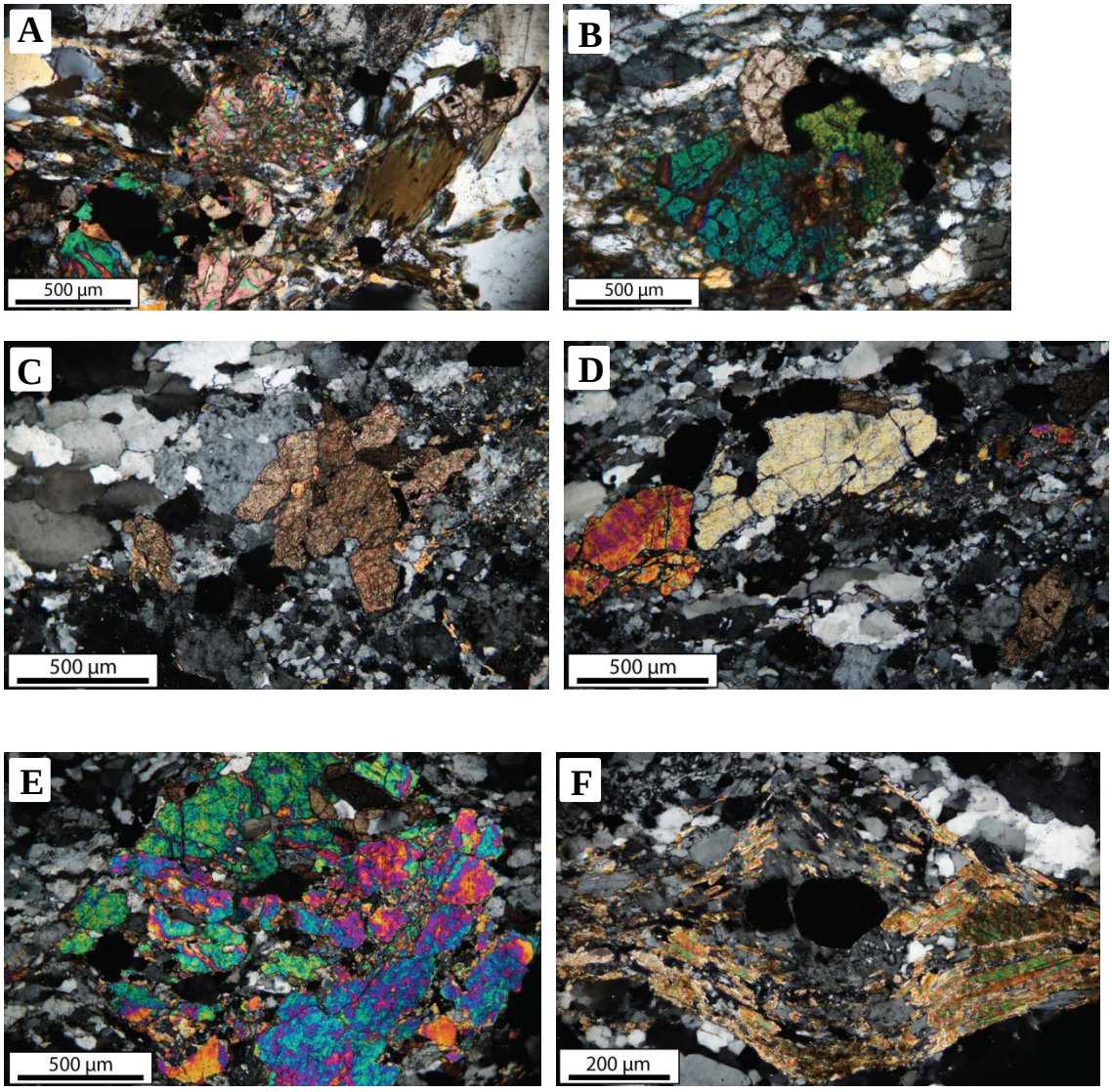

Figure 3.4: Photomicrographs of metamorphic minerals in country rock and mylonitic samples in the northern part of the study area. A) Symplectic epidote, titanite, biotite and opaque minerals in country rock; sample SCM-6; B) Epidote, titanite, and an opaque mineral in Stone Corral ridge shear zone; sample SCM-20; C-D) Epidote, titanite, garnet, and opaque minerals from discrete shear zone; sample HAR-16; E) Epidote, titanite, garnet, and opaque minerals from discrete shear zone; sample HAR-52; F) Garnet, myrmekite, and biotite from discrete shear zone; sample HQ-B.

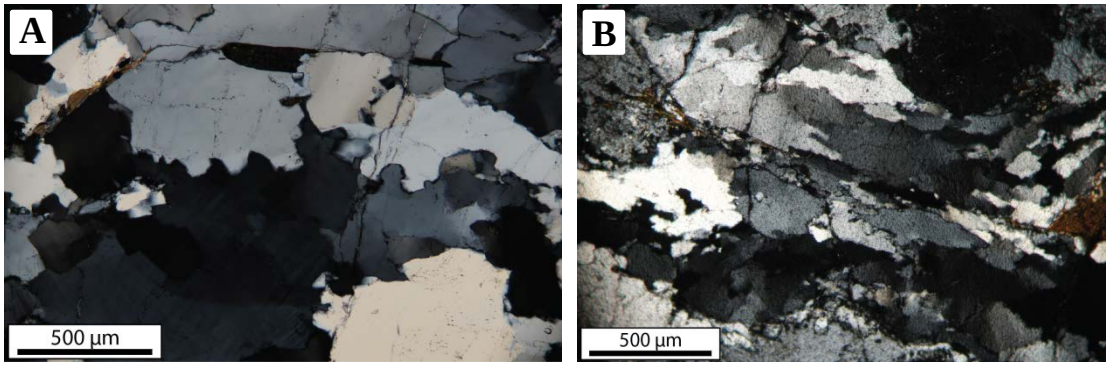

Figure 3.5: Photomicrographs of quartz in the northern country rock. The sinuous boundaries are characteristic of GBM recrystallization. Samples: A) SCM-6; B) H2.

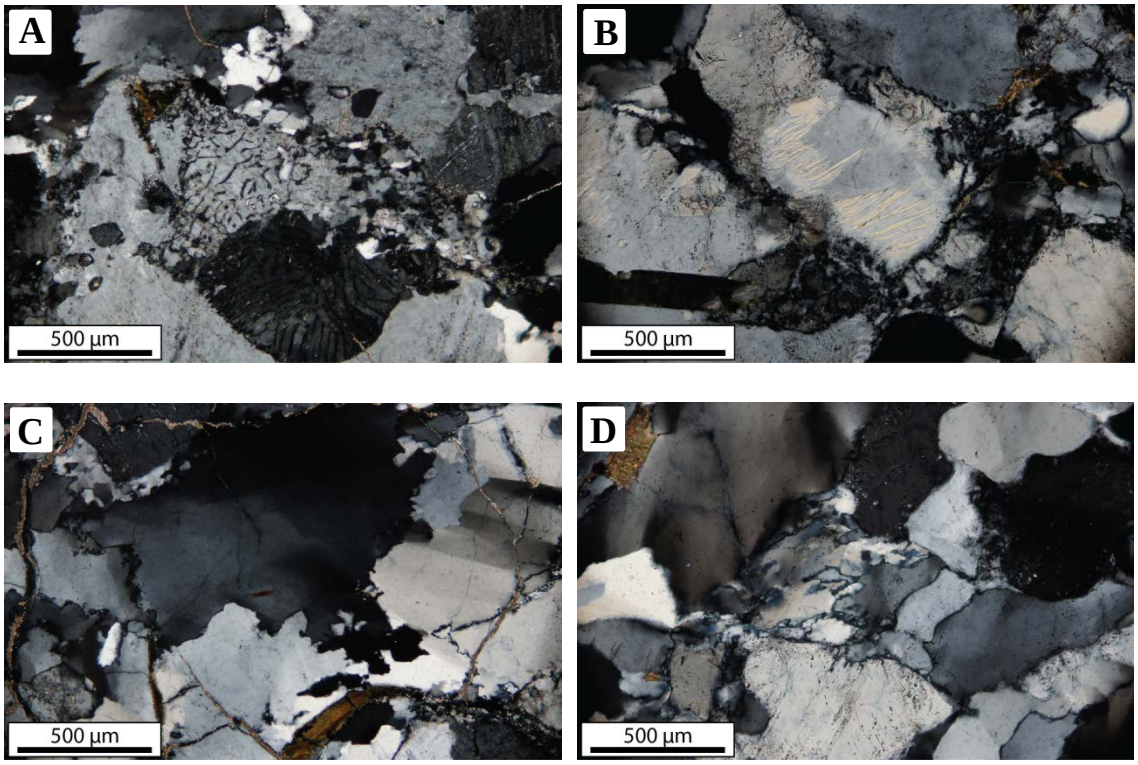

Figure 3.6: Photomicrographs of quartz and feldspar in the southern country rock. A) Feldspar with myrmekite that is partially recrystallized; sample B-4; B) Flame perthite in feldspar; sample B-28. C) GBM recrystallization in quartz; sample B-4; D) GBM and SGR recrystallization in quartz; sample B-28.

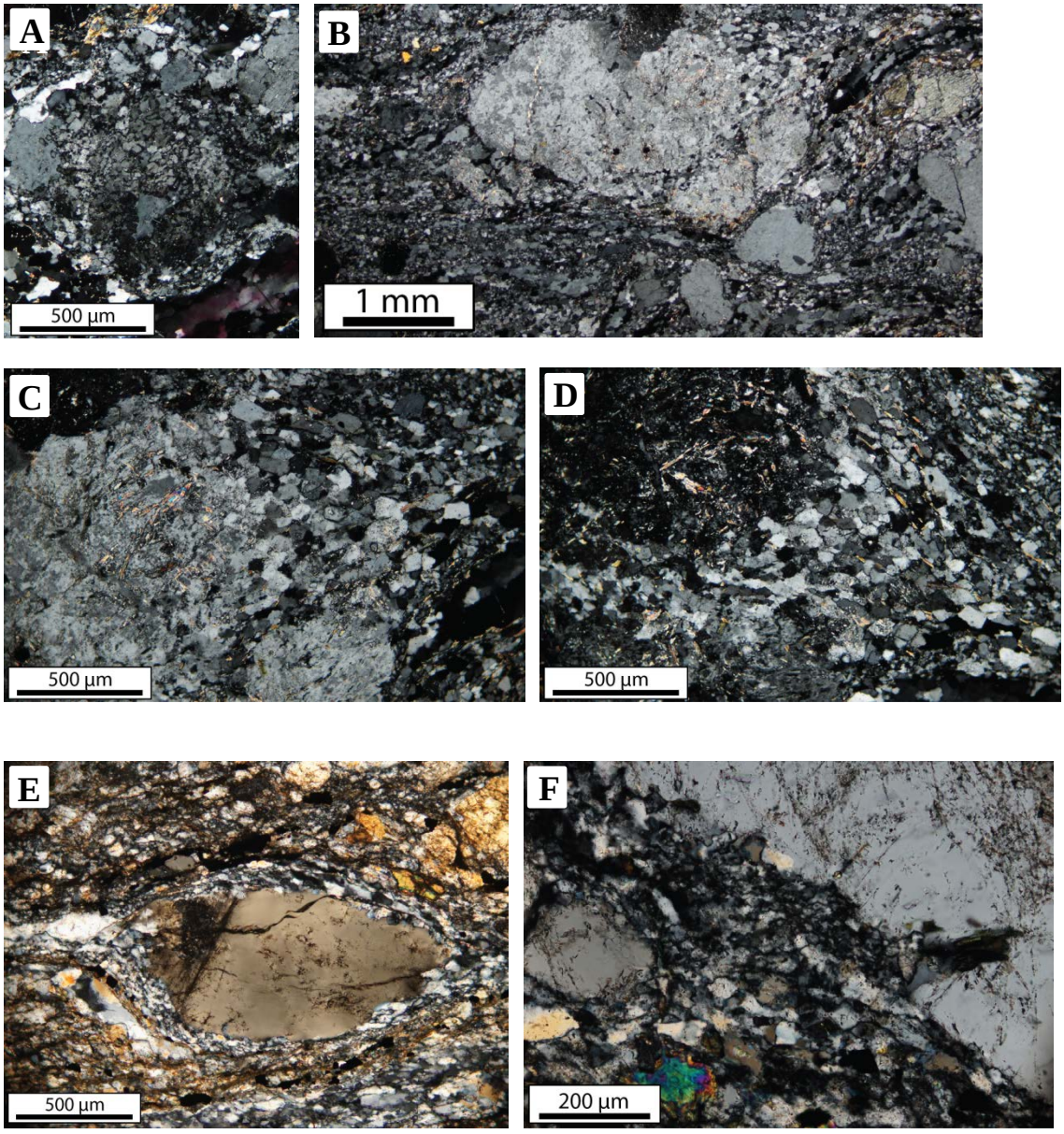

Figure 3.7: Photomicrographs of feldspar in the discrete shear zones. A) Recrystallization of myrmekite; sample HAR-53; B-D) SGR recrystallization of feldspar; sample HAR-53; E) SGR recrystallization of fractured feldspar porphyroclast with top-to-the-left (SW) sense of shear. Note abundant biotite in fine grained feldspar-rich matrix; sample H1; F) SGR recrystallization and BLG recrystallization on the edge of a feldspar porphyroclast; sample SCM-12.

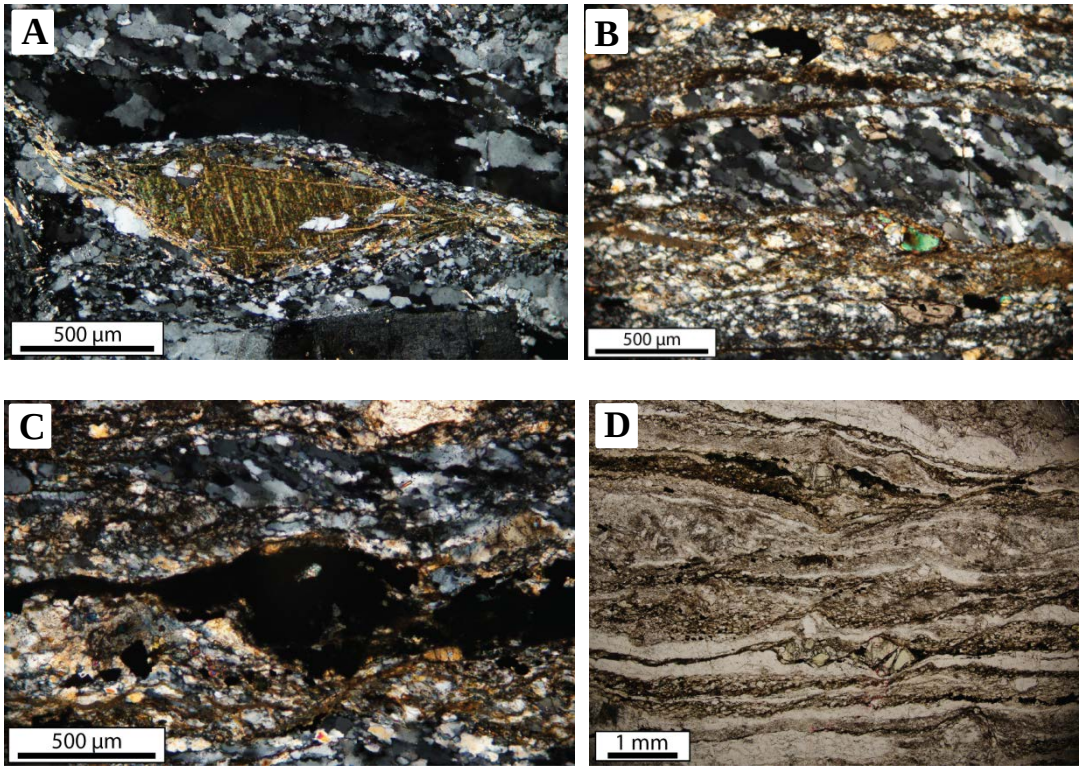

Figure 3.8: Photomicrographs of kinematic indicators in the discrete shear zones. A) Quartz ribbon grain above a biotite fish with top-to-the-left (SW) sense of shear; sample HAR-53. B) Oblique quartz grain shape fabric indicating a top-to-the-left (SW) sense of shear. Biotite is abundant, and quartz and feldspar are similar sizes in the fine grained feldspar-rich layers; sample H1; C) σ-type amphibole porphyroclast with a top-to-the-left (SW) sense of shear; sample H1; B) C'-type shear bands with a top-to-the-left (SW) sense of shear; sample H1.

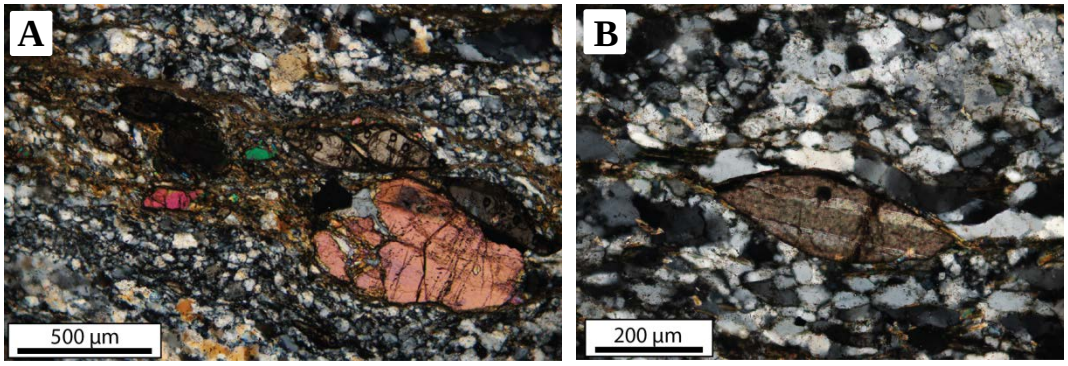

Figure 3.9: Photomicrographs of titanite fish in mylonites. Fish indicate a top-to-the-left (SW) sense of shear. A) Train of titanite fish and epidote in a biotite-rich layer in a discrete shear zone. The small circles in the titanite grains are laser ablation pits formed during U-Pb dating; sample H1; B) Stone Corral ridge shear zone; sample H3.

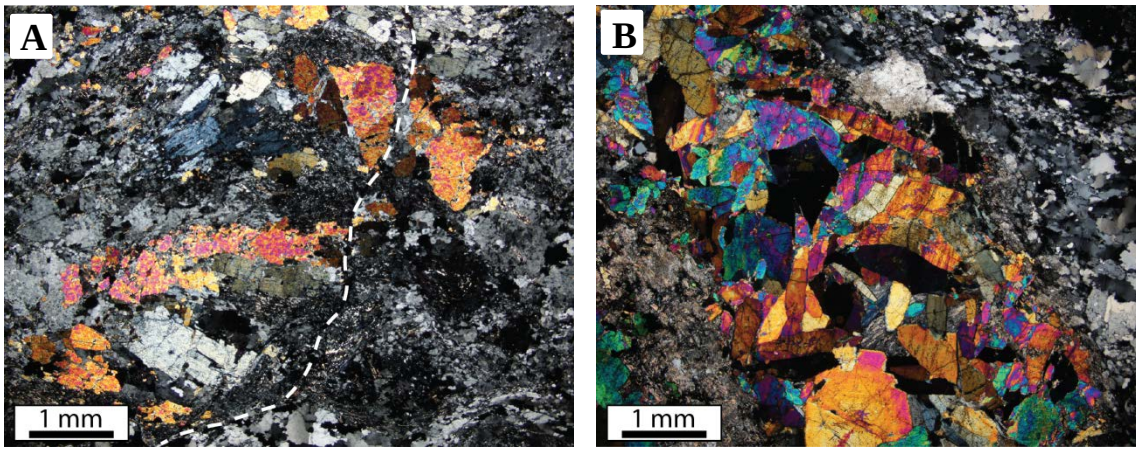

Figure 3.10: Photomicrographs of epidote in central veins in less developed discrete shear zones. A) Apparent vein comprised of epidote replacement of plagioclase along a central fracture. Fracture is traced in white dotted line. Subhorizontal country rock foliation is preserved; sample HQ-C; see field photograph Figure 1.5A; B) Nearly undeformed epidote vein with surrounding highly sericitized feldspar alteration zone; sample HAR-52.

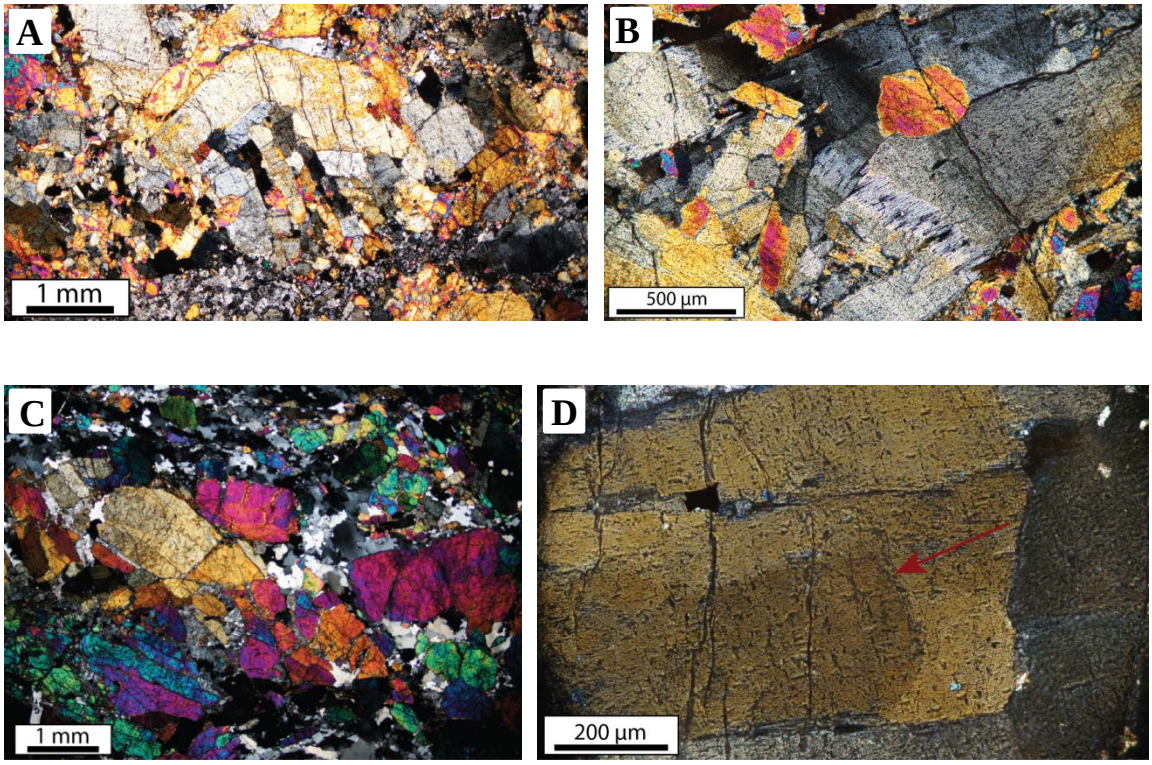

Figure 3.11: Photomicrographs of deformed epidote in central veins in well-developed discrete shear zones. A) Folded epidote grain in vein; sample SCM-51; see field photographs in Figure 2.9E-F; B) Fibers connecting pulled apart epidote grains in vein; note subgrains; sample SCM-51; see field photograph in Figure 2.9D; C) Broken epidote vein grains; sample HAR-16; see field and hand sample photographs in Figures 1.5G, 2.14C; D) Subgrains in an epidote. Arrow points to subgrain; sample SCM-51.

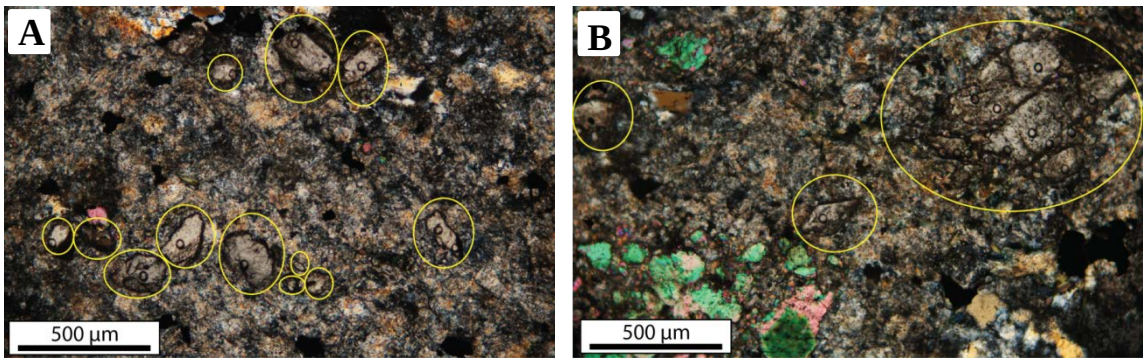

Figure 3.12: Photomicrographs of highly altered zone adjacent to the epidote vein in a discrete shear zone; sample SCM-51. Feldspar in zone is fully recrystallized and highly sericitized. Larger titanite grains are circled in yellow. The small circles in the titanite grains are laser ablation pits formed during U-Pb dating.

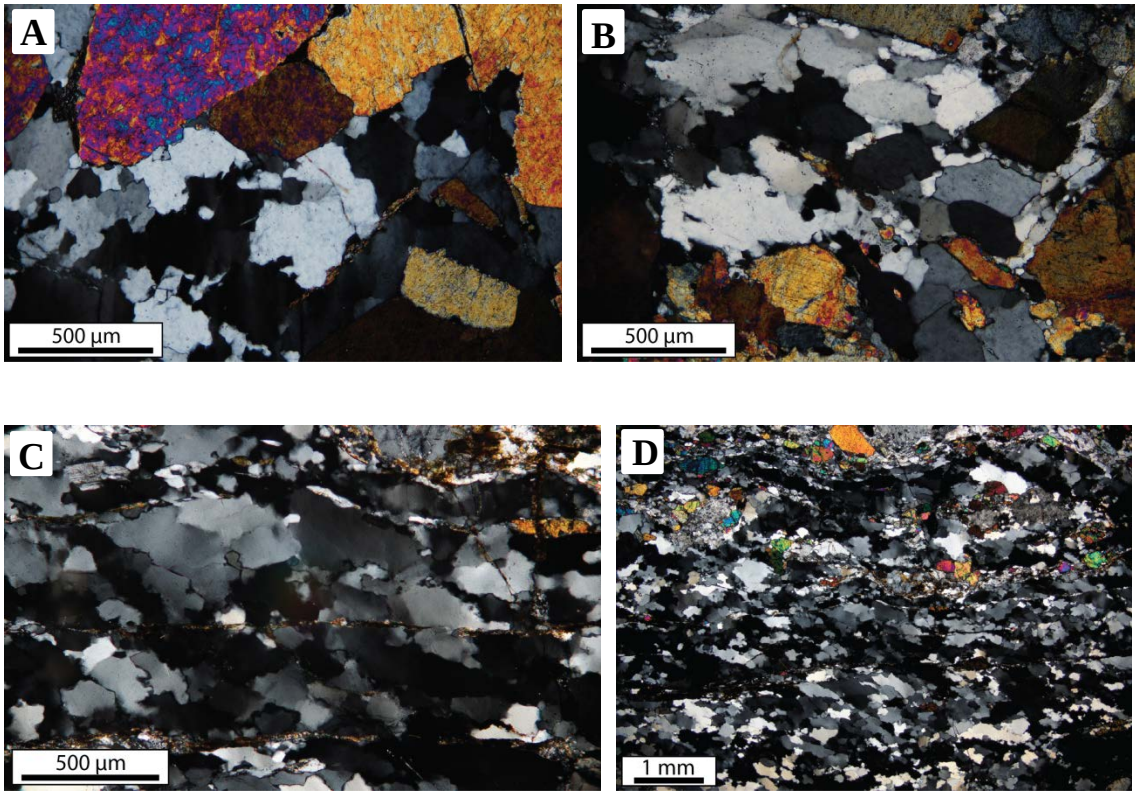

Figure 3.13: Photomicrographs of quartz in central veins in discrete shear zones. Quartz has lobate boundaries indicating GBM recrystallization. A-B) Pockets of vein quartz in epidote-rich vein have undergone minor recrystallization; samples HAR-16, HAR-52; C-D) Elongate recrystallized vein quartz and thin aligned layers of mica comprise an S-C fabric with a top-to-the-left (SW) sense of shear; sample HAR-16.

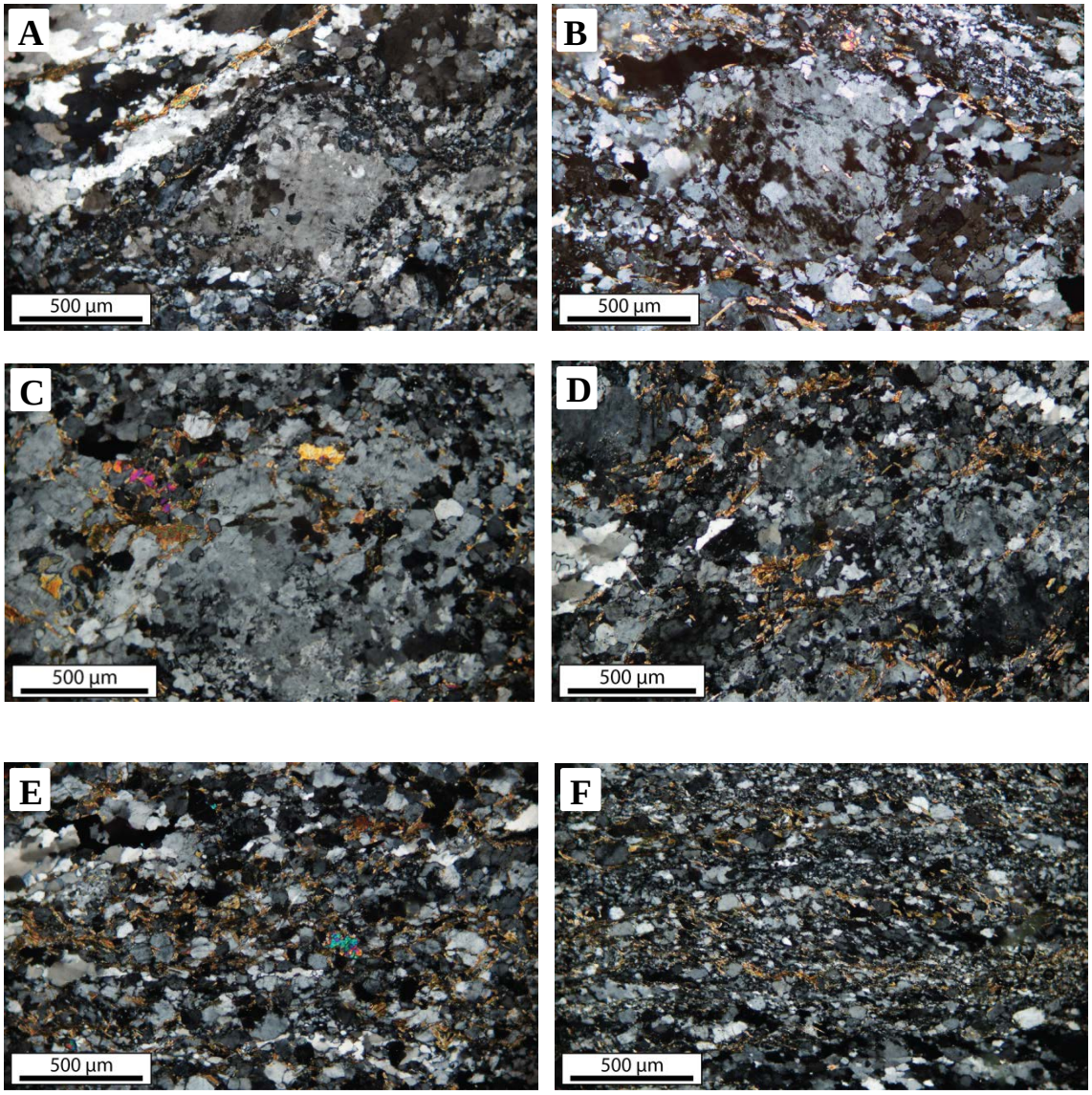

Figure 3.14: Photomicrographs of progressive increases in recrystallization and biotite content across the transition from bleached haloes to flanking paired shear zones. Note the extensive recrystallization of the feldspar grains affected by myrmekite and non-symplectic oligoclase replacement. A-B) Partially recrystallized feldspar porphyroclasts in a bleached halo; sample HQ-C; C-D) Recrystallization in the transition zone between the bleached halo and flanking shear zone; sample HAR-16; E-F) Extensively recrystallized feldspar and through-going biotite bands in flanking shear zones; samples HAR-16, HAR-38.

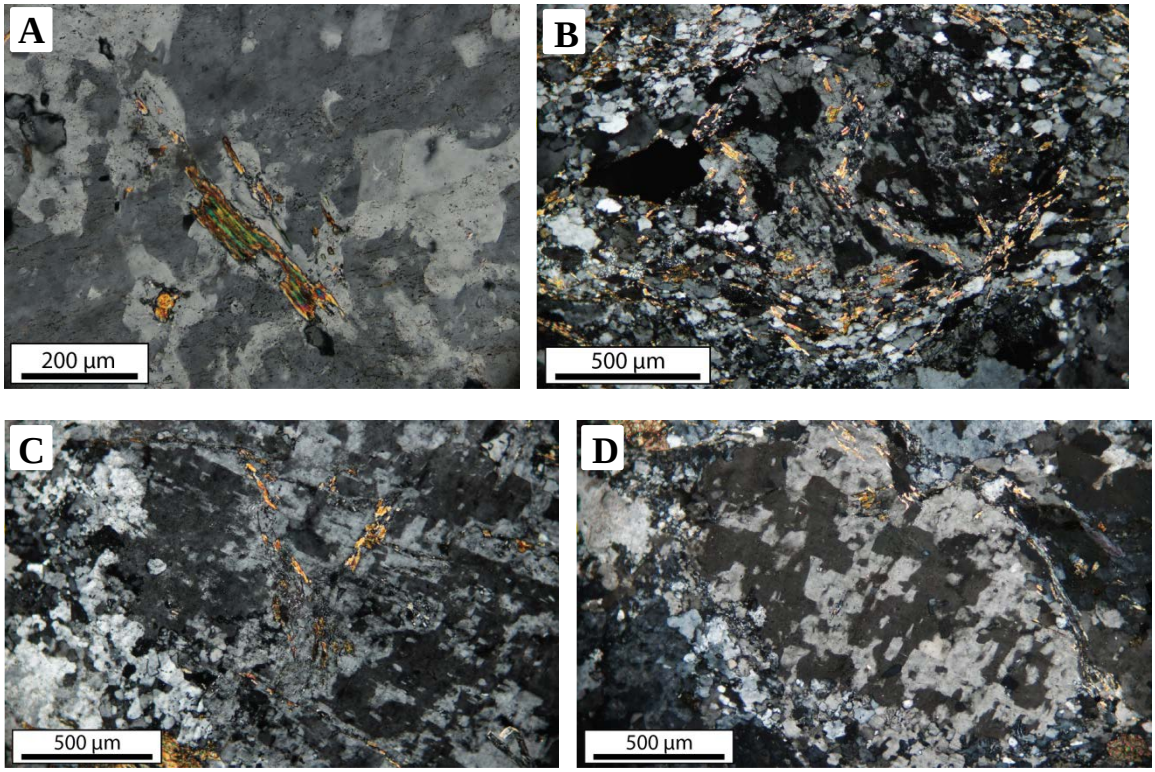

Figure 3.15: Photomicrographs of myrmekite and non-symplectic oligoclase replacement of potassium feldspar. Darker gray interference colors are potassium feldspar and lighter gray colors are oligoclase. Biotite is commonly found within the oligoclase patches. A-B) Oligoclase has a patchy replacement pattern in potassium feldspar; samples HAR-16, HQ-B; C-D) Oligoclase has an angular replacement pattern in potassium feldspar; samples HAR-16, HQ-C.

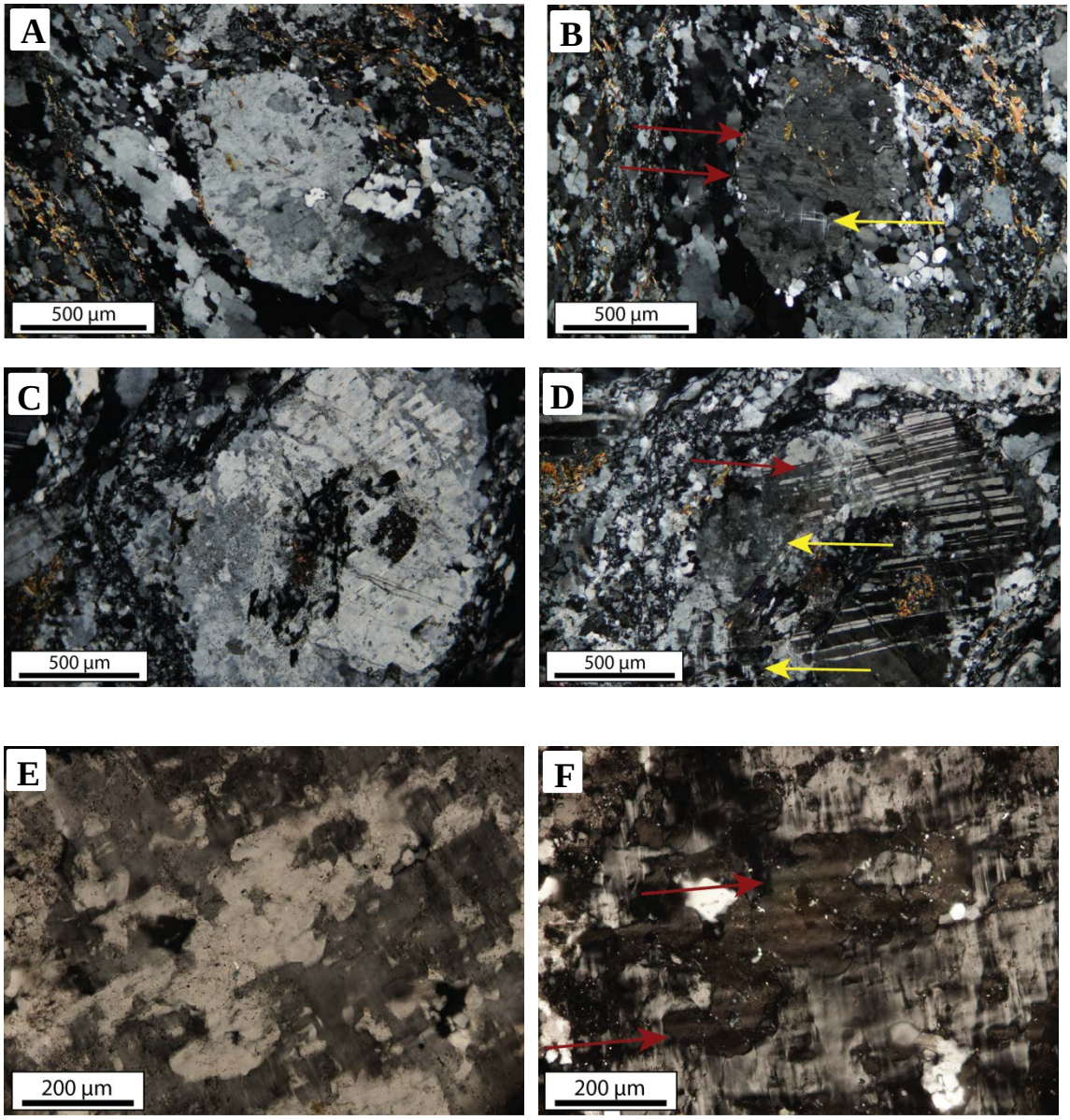

Figure 3.16: Photomicrographs of albite and microcline twinning in potassium feldspar grains that are partially replaced by oligoclase. In A, C, and E, oligoclase displays a lighter gray interference color, whereas K-feldspar displays a darker gray interference color. B, D, and F show the same grains as A, C, and E, respectively, but are rotated to show twinning. Red arrows point to albite twinning and yellow arrows point to microcline twinning. Note fractures in C. Samples: A-B) HQ-C, C-D) HAR-52, E-F) HQ-C.

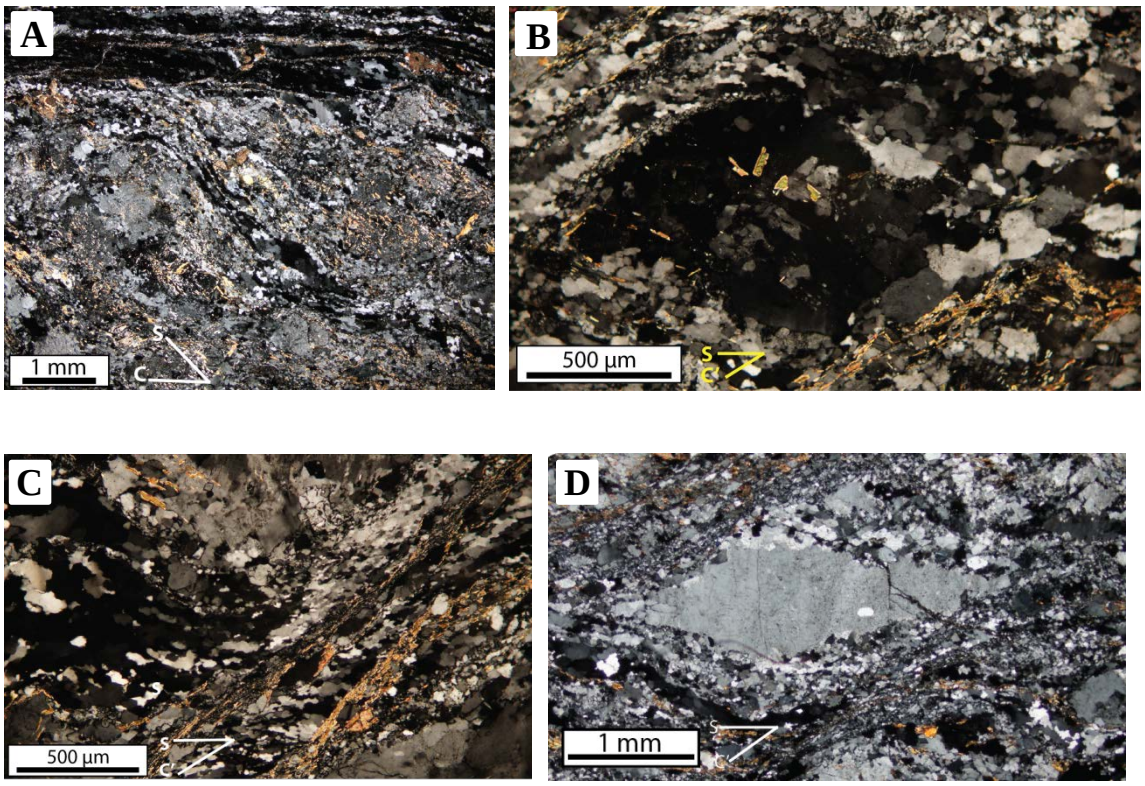

Figure 3.17: Photomicrographs of S-C and S-C' fabrics in discrete shear zones. The fabrics indicate a top-to-the-left (SW) sense of shear. A) S-C fabric in the bleached portion of a shear zone; sample HAR-55; B-D) S-C' fabric in the sheared portion of an incipient shear zone. Feldspar σ-type porphyroclast in B indicates a top-to-the-left (SW) sense of shear. Fractured feldspar porpyroclast in D is very elongate, suggestive of lattice reorientation; sample HQ-C.

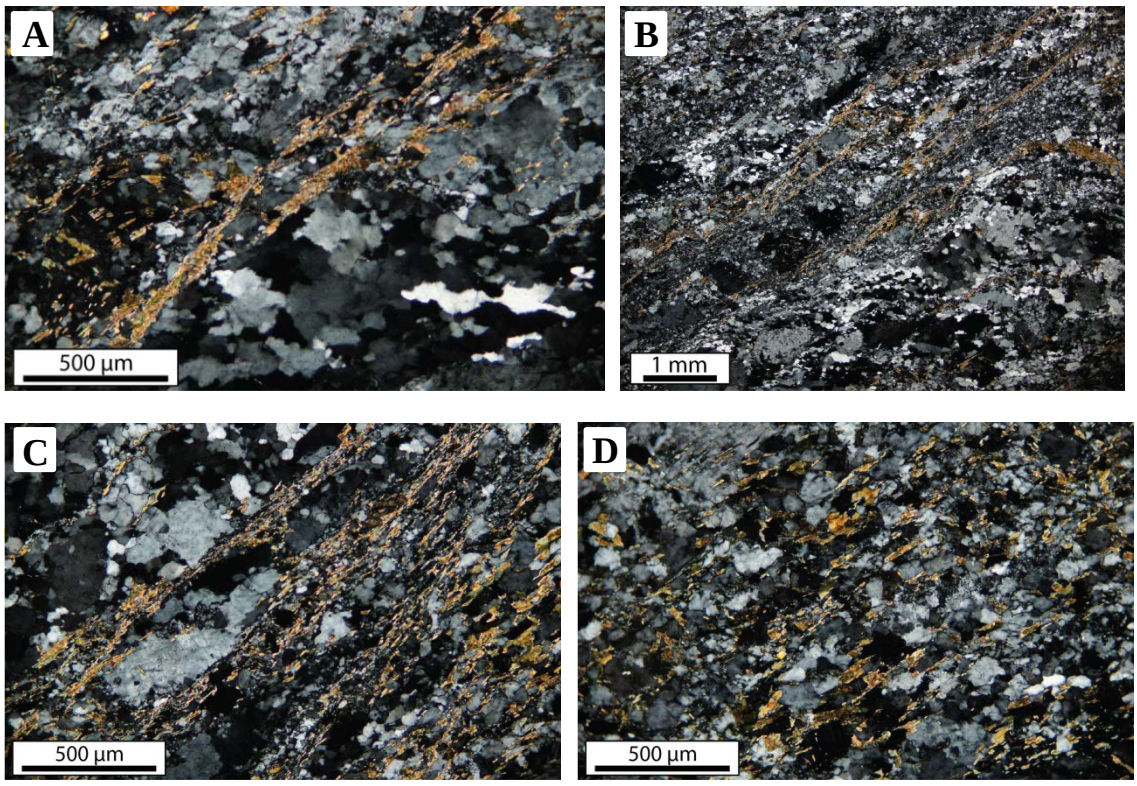

Figure 3.18: Photomicrographs of various stages of biotite-rich C'-type shear band development in an incipient shear zone; sample HQ-C. Southwest is to the top-left. Note BLG recrystallization of feldspar adjacent to biotite-rich bands. A) C'-type shear bands crosscut sub-horizontal quartz layers in the country rock foliation where the shear bands are few in number and widely spaced. Compare to Figure 3.17C where shear bands are closely spaced and the subhorizontal quartz in the country rock foliation is reoriented to parallel the shear bands. B) C'-type shear bands crosscutting subhorizontal country rock foliation (lower right). Where bands are closely spaced, the interstitial fabric is much more recrystallized; C) The S-C' fabric is lost where shear bands are numerous and closely spaced and recrystallization of the intermediary rock is pervasive; D) In the most deformed part of the discrete shear zone, biotite is abundant, recrystallization of all minerals is extensive, and a new fabric is developed. Compare to well-developed flanking paired shear zones, Figure 3.14E-F.

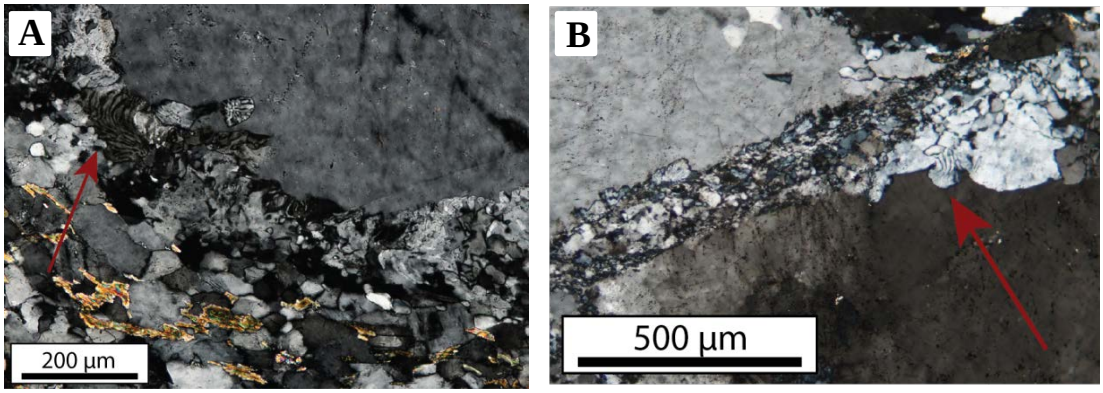

Figure 3.19: Photomicrographs of deflected myrmekite on the edges of feldspar porphyroclasts. Myrmekite is deflected in a top-to-the-left (SW) sense. Arrows point to lobes with clearly bent quartz vermicules; sample HQ-C.

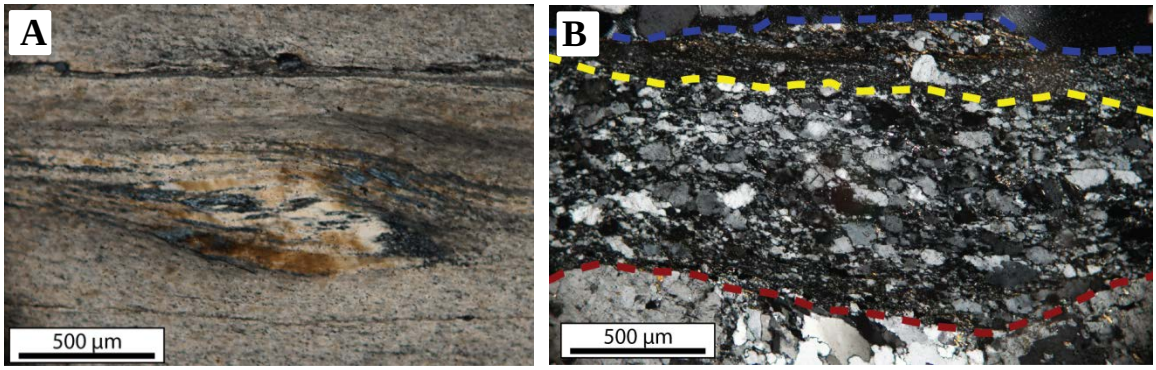

Figure 3.20: Photomicrographs of mylonites from uncharacteristic discrete shear zones in the northern part of the study area. A) Mylonitized quartz vein from the atypical shear zone in an unusual orientation. Quartz has undergone extensive SGR recrystallization. Ribbons indicate a top-to-the-left (SW?) sense of shear; sample SCM-4; B) Sharp boundaries between country rock and protomylonite zone (dashed red line), and between protomylonite zone and a mm-scale mylonitized veneer found on a fractured surface (dashed yellow line). The dashed blue line is the boundary of the sample. Very fine grained feldspar in the mylonitized shear zone is grungy looking, and likely recrystallized from BLG recrystallization or was neocrystallized. Note feldspar σ-type porphyroclasts indicating an apparent top-to-the-left (S) sense of shear; sample SCM-48-2.

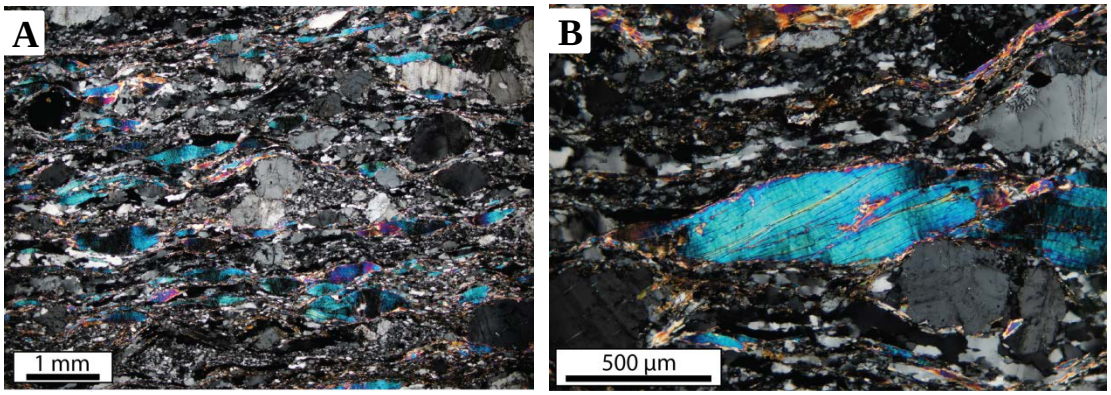

Figure 3.21: Photomicrographs of muscovite-rich mylonite from the Stone Corral ridge shear zone; sample B-3. Muscovite displays undulatory extinction and is bent. Muscovite fish in B indicates a top-to-the-right (NE) sense of shear, although its orientation may be affected by the feldspar porphyroclast. Note some feldspar porphyroclasts in A are elongate parallel to foliation.

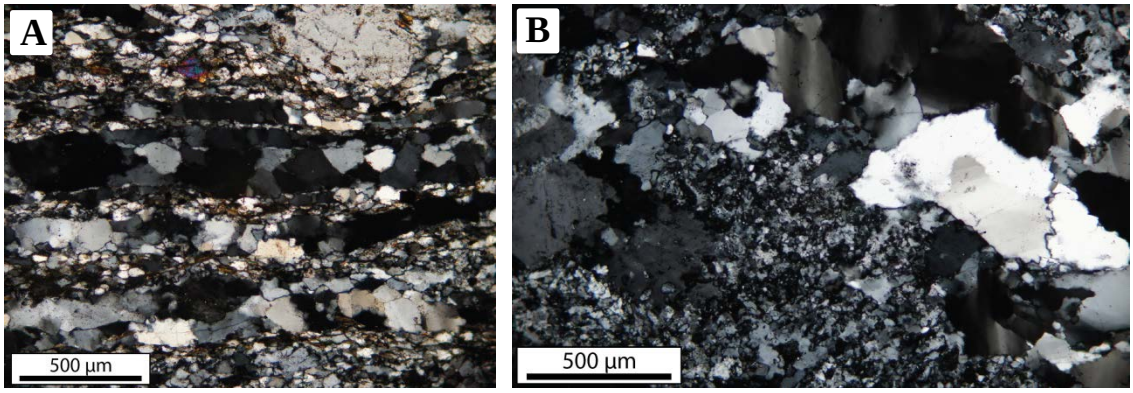

Figure 3.22: Photomicrographs of quartz and feldspar in the Stone Corral ridge shear zone. A) Quartz grains in the bands display lobate boundaries typical of GBM recrystallization or straight boundaries typical of normal grain growth. Quartz grains in the fine grained feldspar-rich layers are similar in size to the feldspar grains; sample H3; B) Quartz grains display discontinuous undulatory extinction and lobate boundaries typical of GBM recrystallization. Much of the fine grained feldspar is recrystallized myrmekite; sample B-3.

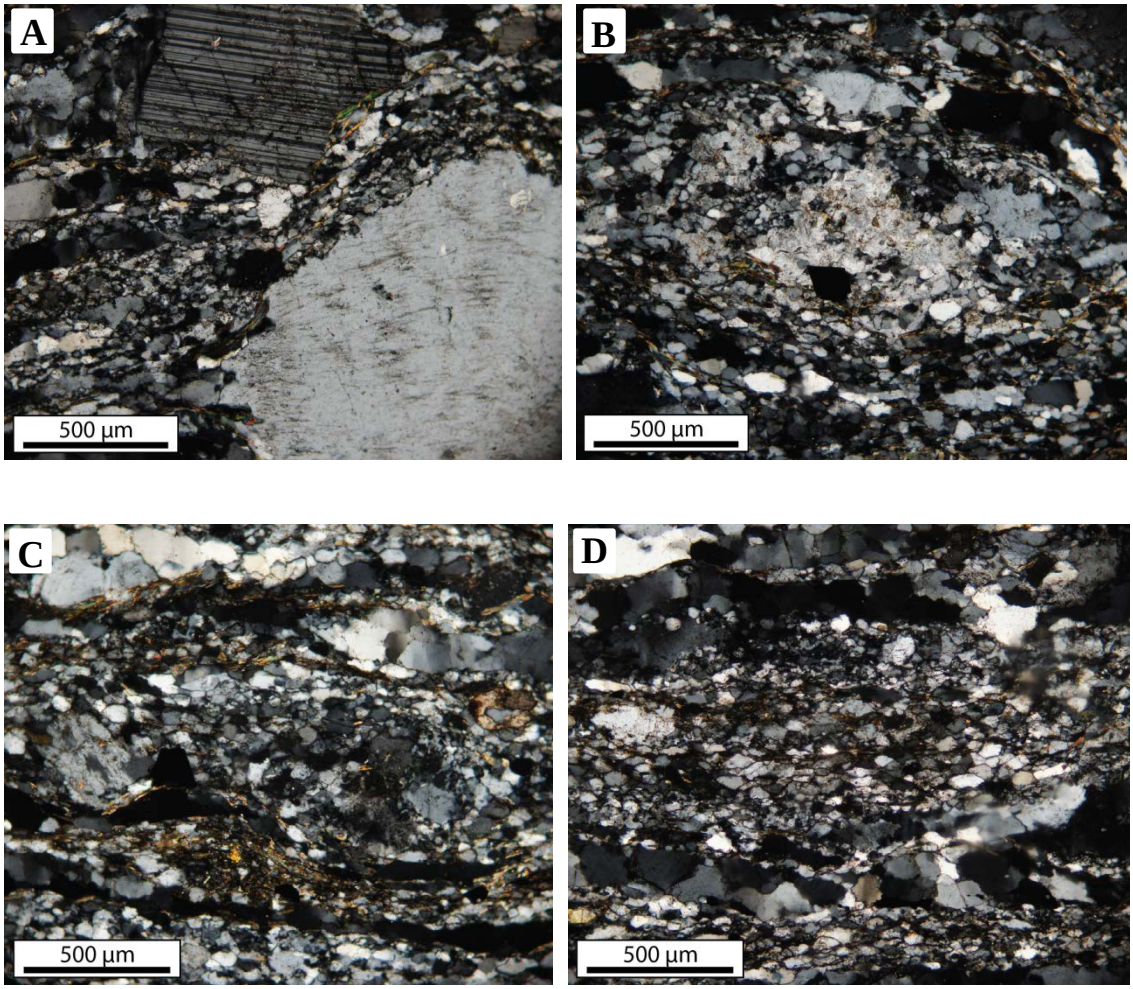

Figure 3.23: Photomicrographs of various degrees of feldspar recrystallization in mylonite from the Stone Corral ridge shear zone; sample H3. Note that quartz and feldspar grains in the fine grained layers are similar in shape and size. A) Minor SGR recrystallization on the edge of a feldspar porphyroclast; B) Moderate SGR recrystallization of a feldspar porphyrclast; C) Near complete SGR recrystallization of a feldspar porphyroclast; D) Fine grained feldspar of similar size, shape, and optical orientation that may represent complete SGR recrystallization of a feldspar porphyroclast.

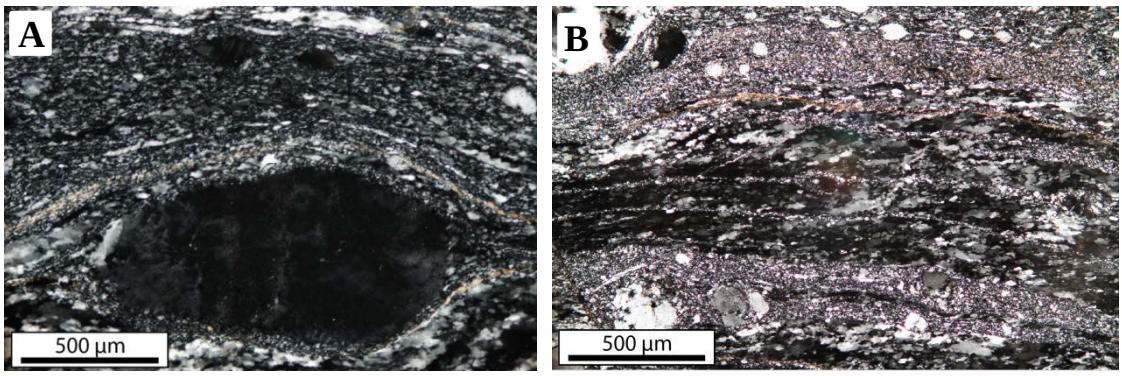

Figure 3.24: Photomicrographs of quartz and feldspar in the isolated shear zones near the crest of Stone Corral ridge. Finer grained layers are characterized by SGR recrystallization of quartz and BLG recrystallization or neocrystallization of feldspar; sample B-9. A) Large feldspar σ-type mantled porphyroclast indicates a top-to-the-right (northeast) sense of shear; B) Quartz bands are characterized by elongate grains with a strong CPO. Grains contain subgrains that are similar size as new grains, indicating SGR recrystallization.

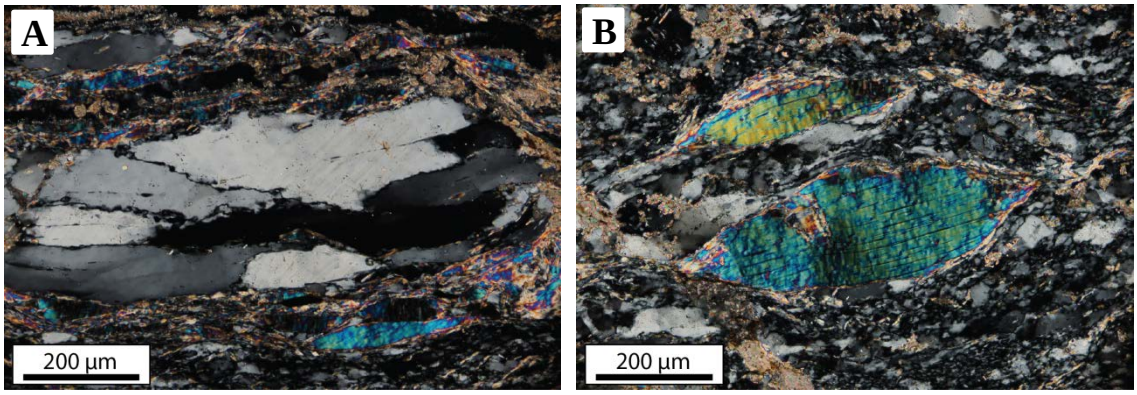

Figure 3.25: Photomicrographs of microstructures in mylonite from the Eagle Eye detachment fault. Note the very fine grained grungy looking feldspar matrix grains; sample HQ-E. A) BLG recrystallization of quartz in which grain boundaries are finely serrated and adjacent new grains are the same size as the serrations. B) Mica fish indicate a top-to-the-right (NE) sense of shear.

Country rock sample name	Mineralogy (mode %)[1]	Sense of shear	Quartz recrystallization[2]	Feldspar recrystallization[3]	Additional microstructures[4]	Probable peak deformation T (°C)
H2	plag (38), kspar(30), qtz (22), biot (6), epi (2), op (2), ti, amph, gar, ap	top-NE	GBM, minor SGR	SGR, BLG	C' s.b., boud. epi, myrm, symp. epi	>500
SCM-6	plag (35), kspar (34), qtz (24), biot(+chl) (5), epi (2), op, amph, ti, gar, ap	top-NE	GBM, minor SGR	SGR, BLG	C' s.b., myrm, symp. epi	>500
SCM-17b	plag (35), kspar (36), qtz (24), biot(+chl) (3), epid (2), op, amph, ti, gar, ap	top-NE	GBM, minor SGR	SGR, BLG	C' s.b., obl. qtz GSPO, myrm, symp. epi	>500
SCM-48-1	plag (37), kspar (30), qtz (26), biot (6), epi (1), op, ti, amph, ap	top-NE	GBM, minor SGR	SGR, BLG	C' s.b., myrm, symp. epi	>500
HQ-D	plag (35), kspar (32), qtz (25), biot (6), epi (1), amph (1), op, ti, ap		GBM, minor SGR	SGR, BLG	C' s.b., myrm, symp. epi	>500
B-4	plag (38), kspar (35), qtz (25), biot(+chl) (2), op, epi		GBM, minor SGR	SGR, BLG	myrm, fl. perthite	>500
B-7	plag (36), kspar (35), qtz (26), biot(+chl) (3), op, epi		GBM, minor SGR	SGR, BLG	myrm, fl. perthite	>500
B-28	plag (34), kspar (32), qtz (26), bio(+chl) (8), op, ti, epi		GBM, minor SGR	SGR, BLG	myrm, fl. perthite	>500

[1] determined by visual estimation

[2,3] GBM=high T grain boundary migration recrystallization; SGR=subgrain rotation recrystallization; BLG=bulging recrystallization

[4] C' s.b.: top-to-NE C' shear bands; boud. epi.: boudinaged epidote; myrm: myrmekite; symp. epi: symplectic epidote; obl. qtz GSPO: oblique quartz grain shape preferred orientation; fl. perthite: flame perthite

Table 3.1: Mineralogical and microstructural data table for country rock samples.

Sample	Mineralogy (mode %)[1]	Sense of shear	Quartz recrystallization[2]	Feldspar recrystallization[3]	Additional microstructures[4]	Probable peak deformation T (°C)
H1	feld (66), qtz (22), biot (9), epi (1) ti (1), amph (1), op, ap	top-SW	GBM, minor SGR	SGR, BLG	C' s.b., myrm, symp. epi, obl. qtz GSPO, ti/amph fish, feld/epi σ-clasts	>500
SCM-17	feld (66), qtz (24), biot (8), amph (1), epi (1), ti, op	top-SW	GBM, SGR	SGR, BLG	myrm, obl. qtz GSPO, ti/amph fish, feld/amph σ-clasts	>500
HAR-14	feld (67), qtz (25), biot (8), epi, ti, amph, op, ap	top-SW	GBM, minor SGR	SGR, BLG	myrm, obl. qtz GSPO, ti fish, feld σ-clasts	>500
SCM-12	feld (68) qtz (27), biot(+chl) (5), op, epi, ti, amph	top-SW	GBM, SGR	SGR, BLG	C' s.b., myrm, feld σ-clasts	>500
HQ-A	feld (63), qtz (35), biot(+chl) (1), musc (1), op	top-SW	GBM, minor SGR	SGR, BLG	C' s.b., myrm, obl. Qtz GSPO, feld σ-clasts	>500
HAR-53	feld (64), qtz (28), biot(+chl) (7), musc (1), epid, ti, op, gar, ap	top-SW	GBM, minor SGR	SGR, BLG	myrm, obl. qtz GSPO, feld σ-clasts, biot fish, ti fish	>500
SCM-51*	sz: feld (63), qtz (22), biot(+chl) (15), op, epi, ti bh: plag (40), kspar (18), qtz (35), ser (4), ti (2), biot(+chl) (1), op, ap, epi		GBM, SGR	SGR, BLG	myrm, obl. qtz GSPO, obl. ti/epi, feld σ-clasts, folded epi, fibrous epi	>500
HQ-C*	sz: feld (65), qtz (25), biot (10), epi, ti, ap, gar bh: plag (34), kspar (28), qtz (27), biot(8), ep (1), ti (1), op, ap, gar	top-SW	GBM, minor SGR	SGR, BLG	C' s.b., def myrm, obl. qtz GSPO, feld σ-clasts	>500
HAR-16*	sz: feld (63), qtz (22), biot (15), op, gar, epid, ap, ti bh: plag (36), kspar (27), qtz (27), biot (8), ep (1), ti (1), op, ap	top-SW	GBM, minor SGR	SGR, BLG	myrm, symp. epi, obl. Qtz GSPO, epi fish	>500
HAR-56*	sz: feld (63), qtz (25), biot (12), op (2), epi, ti, amph gar, ap, musc bh: plag (31), kspar (24), qtz (40), biot (2), ep (2), ti (1),op, ap	top-SW	GBM, minor SGR	SGR, BLG	myrm, obl. qtz GSPO, feld σ-clasts	>500
HAR-38*	sz: feld (60), qtz (20), biot (18), op (2), epi, ti, amph gar, ap, musc bh: plag (34), kspar (25), qtz (35), biot (4), ep (2)	top-SW	GBM, minor SGR	SGR, BLG	C' s.b., myrm, obl. qtz GSPO, feld σ-clasts, amph fish	>500
HAR-52*	sz: feld (64), qtz (20), biot (12), epid (2), op (1), ti (1), gar, ap bh: plag (36), kspar (27), qtz (28), biot (5), ep (3), op (1)	top-SW	GBM, minor SGR	SGR, BLG	C' s.b., myrm, symp. epi	>500
HAR-55*	sz: feld (58), qtz (30), biot (12), op, amph, epid, ti, ap bh: plag (37), kspar (28), qtz (25), biot (10), ep, ti, op	top-SW	GBM, minor SGR	SGR, BLG	S-C fab, myrm, obl. qtz GSPO, feld σ-clasts	>500
HQ-B	feld (63), qtz (27), biot (8), epi (2), ti, op, amph, gar	top-SW	GBM, minor SGR	SGR, BLG	C' s.b., myrm, ti fish, ep fish, amph fish, feld σ-clasts	>500
HAR-9	feld (65), qtz (27), biot (6), epi (2), ti, op, gar	top-SW	GBM, minor SGR	SGR, BLG	myrm, obl. qtz GSPO, feld σ-clasts	>500
SCM-4	qtz (100), feld, biot, musc	top-SW?	SGR	BLG	S-C fabric, feld/qtz fish, feld σ-clasts	400-500
SCM-48-2	feld (67), qtz (24), biot(+chl) (8), musc (1), ti, op	top-S	BLG	BLG	myrm, obl. qtz GSPO, obl. ti, feld σ-clasts, feld δ-clasts, inclined feld	350-400

[1] determined by visual estimation

[2,3] GBM=high T grain boundary migration recrystallization; SGR=subgrain rotation recrystallization; BLG=bulging recrystallization

[4] C' s.b.: C' shear bands; boud epi.: boudinaged epidote; myrm: myrmekite; def myrm = deflected myrmekite; symp. epi: symplectic epidote; obl. qtz GSPO: oblique quartz grain shape preferred orientation

* sample collected from zones with a central epidote vein, bleached halo, and flanking paired shear zones; sz = flanking shear zone, bh = bleached halo

Table 3.2: Mineralogical and microstructural data table for discrete mylonitic shear zone samples.

Sample	Mineralogy (mode %)[1]	Sense of shear	Quartz recrystallization[2]	Feldspar recrystallization[3]	Additional microstructures[4]	Probable peak deformation T (°C)
SCM-19	feld (66), qtz (28), bio(+chl) (4), epi (1), op (1), amph, ti, ap	top-NE	GBM, minor SGR	SGR, BLG	C' s.b., myrm, symp. epi, obl. qtz GSPO, feld σ-clasts, boud epi	>500
H3	feld (60), qtz (26), biot(+chl) (11), op (2), epi (1), gar (1), ti, amph, ap	top-SW	GBM, minor SGR	SGR, BLG	myrm, symp. epi, obl. qtz GSPO, feld σ-clasts, ti fish	>500
SCM-20	feld (64), qtz (23), biot(+chl) (11), op (2), epi, gar, ti, amph, ap	top-SW	GBM, minor SGR	SGR, BLG	myrm, symp. epi, obl. qtz GSPO, feld σ-clasts, ti fish	>500
B-3	feld (49), qtz (30), musc (17), biot (4), op, gar		GBM, minor SGR	SGR, BLG	myrm, musc fish, feld σ-clasts	>500
HAR-3	feld (68), qtz (21), biot (6), ser (5), op, epi		GBM, SGR	BLG, SGR	myrm	>450
HAR-4	feld (64), qtz (33), biot (3), musc, op, epi		SGR, GBM	BLG, SGR	myrm	>450
HAR-5a	feld (62), qtz (22), biot (16), ti, op, ap, musc, ser	top-SW	GBM, SGR	BLG, SGR	mrym, feld fish, feld σ-clasts	>450
HAR-5b	feld (74), qtz (22), biot (4)	top-SW	GBM, SGR	BLG, SGR	C' s.b., myrm, feld σ-clasts	>450
HAR-6	amphibole (48), plagioclase (52), ti, op			BLG, SGR	amph fish	>450
B-5	feld (65), qtz (32), biot (3)	top-NE	SGR	BLG	obl. qtz GSPO	400-500
B-9	feld (70), qtz (25), biot(+chl) (5)	top-NE	SGR	BLG	obl. qtz GSPO, feld σ-clasts, normal microfaults	400-500
HAR-7	feld (68), qtz (26), biot(+chl) (6), ser	top-NE	SGR	BLG	obl. qtz GSPO, feld σ-clasts	400-500
HQ-E	feld (35), qtz (25), musc (30), op (5), chl (5)	top-NE	BLG, SGR	BLG	C' s.b., musc fish, qtz σ-clasts, qtz fish	350-400
HQ-F	feld (79), qtz (15), musc (5), op (1)	top-NE	BLG, SGR	BLG	C' s.b., feld σ-clast, qtz σ-clasts, qtz fish, inclined feld	350-400
HQ-G	feld (59), qtz (26), musc (15)		BLG, SGR	BLG		350-400

[1] determined by visual estimation

[2,3] GBM=high T grain boundary migration recrystallization; SGR=subgrain rotation recrystallization; BLG=bulging recrystallization

[4] C' s.b.: C' shear bands; boud epi.: boudinaged epidote; myrm: myrmekite; def myrm = deflected myrmekite; symp. epi: symplectic epidote; obl. qtz GSPO: oblique quartz grain shape preferred orientation

Table 3.3: Mineralogical and microstructural data table for non-discrete mylonitic shear zone samples. Samples were collected from the Stone Corral ridge shear zone, isolated shear zones on the crest of Stone Corral ridge, and shear zones near the detachment fault on Eagle Eye Mountain.

Chapter 4: Electron Backscatter Diffraction Analysis

Electron backscatter diffraction (EBSD) analysis of quartz was performed on ten samples from throughout the study area, including the country rock and different types of shear zones (see Chapters 1 and 2). The analyses were performed to collect crystallographic preferred orientation (CPO) data to better understand the conditions of deformation experienced by the rocks in the study area, and to compare those conditions among samples. Specifically, the analyses were performed to identify the active slip systems, senses of shear, types of strain (coaxial vs. non-coaxial), and magnitudes of strain experienced by the rocks during deformation. A major goal of the analyses was to determine if the different types of shear zones in the study area deformed under the same or different conditions.

4.1 METHODS

4.1.1 Sample Selection

Nine of the ten samples analyzed by EBSD were collected from the Stone Corral study area (Figure 4.1). One sample, HQ-F, was collected from below the Eagle Eye detachment fault on Eagle Eye Mountain (Figure 1.3). Of the nine samples analyzed from the Stone Corral study area, two of the samples (H2 and SCM-17b; Figure 1.4D) were collected from the crudely deformed country rock in the northern part of the study area. Two samples (H1 and SCM-12; Figure 1.4D) were collected from the abundant discrete shear zones in the northern part of the study area, and a third sample (SCM-4) was collected from the mylonitized quartz vein from the atypical (SE-striking, SW-dipping) discrete shear zone in the northern part of the study area. Two samples (H3 and B-3) were collected from the Stone Corral ridge shear zone, and another two samples (B-

5 and B-9) were collected from the isolated shear zones on the crest of Stone Corral ridge in the southern part of the study area.

4.1.2 Analytical techniques

The quartz CPO data was collected by conducting EBSD analyses using a Phillips XL30 Environmental Scanning Electron Microscope (ESEM) and an HKL Nordlys EBSD detector in the Department of Geological Sciences at the University of Texas at Austin. Data was collected from several quartz-rich areas of X-Z thin sections where quartz is present as recrystallized grains. More than 500 quartz grains (and up to 1263 quartz grains) were analyzed in each sample (Table 4.1). The ESEM operating conditions used were a 20 kV accelerating voltage, 250x magnification, 6 μm spot size, and a working distance of 18-24 mm. Index diffraction patterns were automatically indexed at a step size of 25 μm by Channel 5 Flamenco software and Aztec software.

4.1.3 Data Analysis

The quartz CPO data was modified from points to grains using a 10° misorientation angle to define grain boundaries. Two of the samples (discrete shear zone sample, H1, and isolated shear zone sample, B-9) were mounted at an angle to the x-direction and so the data had to be rotated (-20° and +25°, respectively) in the x direction to correct for that error before further analysis. The software program PFch5 (Mainprice, 2005) was used to construct the pole figures of c-axis and a-axis data and also to gather statistics on the data. The program discarded all diffraction pattern data that was obtained with a mean angular deviation (MAD) $\geq$ 1.3°. The pole figures constructed were contoured by multiples of uniform distribution and data was plotted as one point per grain.

The statistical data calculated for each c-axis plot included the J-, P-, G-, and R-indices. The indices are used as a semi-quantitative means of evaluating fabric strength and distribution. The CPO fabric strength is described by the J-index (Bunge, 1982) with higher J-indices associated with more intensely developed fabrics. The distribution of the data is evaluated by determining the degree to which the data represent a point (P-index), girdle (G-index), or random distribution (R-index; Vollmer, 1990). P-, G-, and R-indices are described by numerical values between 0 and 1 whose summation is equal to 1. P- and G-indices were also normalized to detach the effects of the random distribution element of the data (after Barth et al., 2010). The normalized point and girdle values were calculated as $P_n = P/(P+G)$ and $G_n = G/(P+G)$, respectively. This normalization serves to better illuminate the degree of different lattice slip system activation during deformation. The activity of basal <a> and rhomb <a> (± prism <a>) slip is manifested as a girdle on a pole figure (and therefore is defined by a high G-index), whereas the activity of predominantly prism <a> slip is manifested as a point located at the y-maxima on a pole figure (and therefore is defined by a high P-index; Figure 4.2).

The determination of the slip systems that were active during deformation by examination of the c-axis pole figure geometry and P_n and G_n values is significant for constraining deformation conditions because slip system activity occurs partly as a function of temperature. Low temperature deformation is typically accommodated by basal <a> slip system activity (with possible contributions from rhomb <a> and prism <a> slip system activity), whereas higher temperature deformation (≥500 °C) is accommodated primarily by prism <a> slip system activity (with very little contribution from basal <a> slip; Bouchez, 1977; Schmid and Casey, 1986; Stipp et al., 2002; Figure 4.2). At even higher temperatures (>550-600 °C), deformation is accommodated predominantly by prism <c> slip (Lister and Dornseipen, 1982; Okudaira et al., 1995).

The pole figures were also examined for asymmetry with respect to the rock foliation and lineation. The degree of asymmetry may be used to qualitatively evaluate the type of strain accommodated during deformation. Symmetric pole figures are typical of coaxial deformation, whereas asymmetric pole figures are typical of progressive non-coaxial deformation (Schmid and Casey, 1986). Asymmetry was also examined to determine the sense of shear in the samples that experienced non-coaxial deformation (Schmid and Casey, 1986). However, the degree of pole figure symmetry/asymmetry may also be controlled by pre-existing fabrics, changes in kinematics during deformation, and the effects of later deformation, and therefore caution must be exercised during fabric symmetry/asymmetry interpretations (Lister and Williams, 1979).

4.2 RESULTS

Pole figures for all samples are plotted in Figures 4.3 and 4.4. The data for each sample are presented as scatter plots and as pole figures contoured with multiples of uniform distribution. The scatter plots for most of the samples display all the data points analyzed, whereas the pole figures contoured with multiples of uniform distribution display the data converted to one point per grain. The clustering of the data in some of the scatter plots and contoured pole figures suggests that the software may have overestimated the number of grains in some samples when converting points to grains (e.g., sample SCM-4).

4.2.1 Northern Country Rock

Pole figures for the two northern country rock samples (H2 and SCM-17b) are presented in Figure 4.3. The lineations in the country rock outcrops were extremely subtle, and although each individual lineation trended in the same general direction, their specific orientations were non-consistent along their lengths. Even on the scale of the

hand sample, the trends of the lineations gently swung ~15° along the length of the sample. Because of this change in orientation and because of the general subtlety of the lineations, the country rock samples were difficult to cut parallel to lineation, which may explain why the pole figures are off-centered.

The data for sample H2 suggest a moderate quartz CPO fabric (J-index of 2.64; Table 4.1). The fabric is better represented as a girdle (G = 0.52 and G_n = 0.68) than as a point (P = 0.24 and P_n = 0.32), and the pattern of grain distribution in the c-axis pole figure suggests dominantly rhomb <a> and prism <a> slip with a smaller contribution of basal <a> slip. The c-axis pole figure is ambiguous in terms of sense of shear, but the a-axis maxima are rotated clockwise to the x-axis, and therefore suggest that some of the deformation was non-coaxial with a top-to-the-northeast sense of shear.

The data for sample SCM-17b suggest a weak quartz CPO fabric (J-index of 1.71; Table 4.1) and are largely randomly distributed (R = 0.55). The pole figures are difficult to interpret because they are off-centered without obvious patterns, possibly because the lineation was not consistent, and therefore the pole figure data may represent grains that are not oriented parallel to lineation direction. Regardless, the c-axis maxima is clearly clockwise of the z-axis which suggests some component of the strain was non-coaxial with an apparent top-to-the-northeast sense of shear.

4.2.2 Discrete Shear Zone Mylonites

The statistics for the data collected from the discrete shear zone mylonite samples (H1 and SCM-12) indicate that the quartz CPO fabrics are strong (J-index of 5.43 and 5.14, respectively; Table 4.1), and the data distribution for these samples is better described by a point geometry than by a girdle or random geometry with P = 0.63, 0.64 and P_n = 0.72, 0.72 for H1 and SCM-12, respectively. The c-axis pole figures illustrate

the data as mostly situated in the center of the diagram at the Y-maxima (Figure 4.3). This distribution suggests that prism <a> slip was the dominant slip system active during deformation. Minor amounts of rhomb <a> slip are also evident. Whereas the c-axis data are fairly symmetrical in H1, the data in SCM-12 are slightly tilted counterclockwise to the z-axis, which suggests a top-to-the-southwest sense of shear for the sample. The a-axis maxima in both samples are shifted counterclockwise to the x-axis, which also suggests a top-to-the-southwest sense of shear.

4.2.3 Atypical Discrete Shear Zone Mylonite

The statistical data for the atypical discrete shear zone mylonite sample (SCM-4) suggest a very strong quartz CPO fabric (J-index of 8.08; Table 4.1) that is very well described by a point distribution ($P = 0.76$, $P_n = 0.90$). The c-axis pole figure displays the data as consolidated near the Y-maxima, suggesting prism <a> slip was the dominant active slip system with no evidence for rhomb <a> slip or basal <a> slip (Figure 4.3). The orientation notch in the sample was destroyed during thin section construction, so the sense of shear is not determinable. A small indent was found on one side of the sample, which may be a remnant of the notch. Regardless, the c-axis pole figure appears symmetric and the symmetry/asymmetry of the a-axis pole figure is somewhat ambiguous. The a-axis maximum plots near the x-axis, and the data are shifted away from the perimeter of the circle, so the determination of a clockwise or anti-clockwise rotation of the a-axis maxima from the x-axis is difficult. Additionally, the a-axis pole figure displays several a-axis maxima that are nearly equally populated with data suggesting the shear had a large coaxial component.

4.2.4 Stone Corral Ridge Shear Zone Mylonites

The pole figures and statistical calculations for the two samples from the Stone Corral ridge shear zone (H3 and B-3) differ from each other. The quartz CPO fabric is moderate for sample H3 (J-index of 3.87; Table 4.1) and fairly weak for sample B-3 (J-index of 1.69). The data distribution for H3 is better described by a point geometry (P = 0.47, P_n = 0.63) than it is by a girdle or randomly distributed geometry. Conversely, the data for B-3 is largely randomly distributed (R = 0.49), and when the data are normalized, they are better represented by a girdle geometry (G_n = 0.57) than a point geometry (P_n = 0.43).

The c-axis pole figure for sample H3 suggests that both prism <a> and rhomb <a> slip were active with hints of basal <a> slip activity (Figure 4.4). The c-axis pole figure for B-3 also suggests that prism <a> and rhomb <a> slip were active, but displays a stronger component of basal <a> slip than the pole figure for sample H3 (Figure 4.4). The pole figure for B-3 exhibits the beginning of four limbs extending out from the Y-maxima which hint at a basal <a>-type girdle.

Additionally, the sense of shear suggested by the data differs for the two samples. The c-axis pole figure for sample H3 is rotated anti-clockwise from the z-axis, indicating a non-coaxial contribution to the strain and a top-to-the-southwest sense of shear. Similarly, the a-axis maxima display an anti-clockwise rotation from the x-axis which also suggests a top-to-the-southwest sense of shear. The presence of many a-axis maxima with a similar intensity and an almost symmetric distribution imply a significant coaxial component to the strain as well. Conversely, the c-axis pole figure for sample B-3 is ambiguously asymmetric (i.e., not symmetric but the data are not clearly rotated clockwise or anti-clockwise from the z-axis), and the a-axis maxima are rotated

clockwise to the x-axis, suggesting a non-coaxial strain contribution and a top-to-the-northeast sense of shear.

4.2.5 Isolated Shear Zone Mylonites

The data for the two mylonites from the isolated shear zones on the crest of Stone Corral ridge, B-5 and B-9, yield moderate quartz CPO fabrics (J-indices of 3.42 and 2.68, respectively; Table 4.1). The distribution of the data for sample B-5 is best represented by a point geometry (P = 0.55, P_n = 0.72). The distribution of the data for sample B-9 is also better described by a point geometry (P = 0.38, P_n = 0.54), but it also has a significant girdle geometry component (G = 0.33, G_n = 0. 46). The c-axis pole figure for sample B-5 indicates the activity of dominantly prism <a> slip with a significant component of rhomb <a> slip (Figure 4.4). The c-axis pole figure for sample B-9 also suggests significant prism <a> and rhomb <a> slip, but also displays data points that extend to both poles, which is particularly evident in the scatter plot pole figure, which suggests basal <a> slip was also active during deformation (Figure 4.4).

The c-axis pole figure for sample B-5 looks fairly symmetric, but the a-axis pole figure displays a counterclockwise rotation of the a-maxima from the x-axis. This rotation suggests the strain accommodated by this sample was at least partly non-coaxial and implies a top-to-the-southwest sense of shear. The nearly equal intensity of a-axis point maxima on the left and right sides of the pole figure, and the otherwise wide spread of the a-axis data around the pole figure suggest an important coaxial component as well. Conversely, the c-axis and a-axis pole figures for sample B-9 both suggest a top-to-the-northeast sense of shear as the c-axis data are rotated clockwise from the z-axis and the a-axis maxima are rotated clockwise from the x-axis.

4.2.6 Eagle Eye Mountain Detachment Fault Mylonite

The data for the detachment fault sample, HQ-F, yield a weak to moderate quartz CPO fabric (J-index of 1.98; Table 4.1) with the data best represented by a girdle geometry (G = 0.42; G_n = 0.70). The contoured data in the c-axis pole figure extend across the stereogram from top right to bottom left (Figure 4.4), indicating that basal <a>, rhomb <a>, and prism <a> slip were all active during deformation. The c-axis pole figure is rotated clockwise to the z-axis, and the a-axis maxima are rotated clockwise to the x-axis, which implies the sample experienced a top-to-the-northeast sense of shear during deformation.

4.3 Summary and Brief Discussion

The EBSD data for the country rock samples (H2 and SCM-17b) and one of the Stone Corral ridge shear zone samples (B-3) indicate prism <a>, rhomb <a>, and basal <a> slip systems were active during deformation, which may suggest that low to medium temperatures prevailed (Figure 4.2). However, this interpretation is not consistent with the microstructures and mineralogy of these three samples, which suggest deformation temperatures of >500 °C (see Section 3.11). The simple model of deformation temperature estimation based on the slip systems that were employed to accommodate deformation does not take into account the effects of preexisting fabrics, strain rates, changes in strain during deformation, or subsequent deformation. The slip systems active during deformation in the study area samples may have been affected by any of these other processes.

The c-axis data for the discrete shear zone samples (H1 and SCM-12) and for one of the Stone Corral ridge shear zone samples (H3) form single girdle pole figure geometries defined by predominantly prism <a> slip and rhomb <a> slip. This geometry (which suggests deformation temperatures ≤500 °C in the model in Figure 4.2) has been

recognized in the quartz CPOs of other rocks that deformed at amphibolite-facies conditions and so does not necessarily indicate a lower temperature of deformation (Toy et al., 2008).

The pole figure for the atypical discrete shear zone mylonite sample (SCM-4) displays a strong clustering of the data at the y-maxima. If temperature was the greatest control on c-axis orientation during the deformation of this sample, the data would imply deformation temperatures of ≥500 °C (Stipp et al., 2002). However, in the thin section of the sample, the quartz is highly recrystallized by SGR recrystallization (Figure 3.20A). The small number of feldspar porphyroclasts that are present are not strongly recrystallized, but some of the fine-grained feldspar likely recrystallized by BLG recrystallization or was neocrystallized (see Section 3.3.3). These structures are more characteristic of temperatures below 500°C, although strain rates and the presence of fluids also exert a control on microstructure development. The pole figure pattern for this sample, which is highly dominated by prism <a> slip, may be a function of a preexisting fabric in which quartz was oriented in such a way that that prism <a> slip was favored during deformation. Because the vein was composed almost entirely of quartz, the quartz may have deformed very readily because the grains were not impeded by large feldspar porphyroclasts or other rigid minerals. Additionally, this deformation may have been aided by hydrolytic weakening (see Chapter 6).

The contoured pole figures for the samples collected from the isolated shear zones on the crest of Stone Corral ridge (B-5 and B-9) do not look significantly different than those from the other mylonites. The c-axis pole figures of these samples also form single girdles defined by predominantly prism <a> and rhomb <a> slip activity with a smaller contribution of basal <a> slip in sample B-9, and no evidence for basal <a> slip in sample B-5. However, in contrast to the c-axis scatter plot pole figures for the discrete shear

zone samples, the scatter plot pole figure for sample B-9 shows that a significant amount of the data extends to the poles, suggesting basal <a> slip was likely very active during deformation.

In thin section, these samples looked very different than the other mylonites as they had undergone pervasive SGR recrystallization of quartz and BLG recrystallization or neocrystallization of feldspar (see Section 3.5; Figures 3.24, 4.5). These microstructures suggest deformation likely occurred during greenschist-facies conditions. The significant degree of basal <a> slip suggested by the c-axis scatter plot pole figure for Sample B-9 is consistent with temperatures typical of greenschist facies deformation (Figure 4.4). The similarity of the pole figures for sample B-5 to the pole figures of the other (relatively higher temperature) mylonites and country rock may be due to inheritance of a pre-existing fabric rather than to similar deformation conditions (Toy et al., 2008), although a pre-existing fabric is not evident in thin section.

The c-axis pole figure for the detachment fault mylonite, HQ-F, is defined by a girdle, although the type of girdle (single girdle or cross-girdle) is difficult to tell with the patchy distribution of the data in the figure. However, the pole figure differs greatly from all the others in that the girdle reveals a significant contribution of basal <a> slip. The c-axis maximum plots near the y-maxima, but two other maxima are present at both poles. This distribution strongly suggests lower temperature deformation and is consistent with the greenschist-facies conditions that prevailed during detachment faulting.

The senses of shear provided by the pole figures for most of the samples that were analyzed are consistent with the microstructural shear sense indicators discussed in Chapter 3. The top-to-the-northeast sense of shear suggested by the a-axis pole figure for the Stone Corral ridge shear zone sample (B-3) may be a result of coaxial deformation as the shear sense indicators seen in thin section give both top-to-the-northeast and top-to-

the-southwest senses of shear. A strong coaxial contribution to the Stone Corral ridge shear zone would explain the inconsistency between the top-to-the-northeast sense of shear indicated by the pole figure for B-3 and the top-to-the-southwest sense of shear indicted by the pole figure for the other Stone Corral ridge shear zone sample (H3). Additionally, whereas the sense of shear is ambiguous in thin section in a few of the other Stone Corral ridge shear zone samples, the sense of shear is clearly top-to-the-southwest in some of the samples (Figure 3.9B; Table 3.3). Alternatively, the top-to-the-northeast sense of shear given by the a-axis pole figure for B-3 may be the result of changing kinematic conditions during deformation or of more than one episode of deformation (Lister and Williams, 1979).

The a-axis pole figure for one of the isolated shear zone samples (B-5) implies a top-to-the-southwest sense of shear that is not consistent with the microstructures seen in thin section (Figures 4.4, 4.5). In thin section, sample B-5 is characterized by broken up feldspar porphyroclasts that are incined in a top-to-the-northeast direction and by a few feldspar σ-type porphyroclasts that also indicate a top-to-the-northeast sense of shear (Figure 4.5A-B). Additionally, recrystallized quartz grains are subtly elongated and inclined in a top-to-the-northeast direction in some areas of the thin section, although the quartz grains appear polygonal in other areas (Figure 4.5C-D). The EBSD analyses were conducted on these larger polygonal grains.

Although the quartz and feldspar in the sample from the isolated shear zone (B-5) appear to have deformed and recrystallized under the same conditions as the other samples from the isolated shear zones on the crest of Stone Corral ridge, this sample was less deformed and recrystallized than the others (compare figures 3.24 and 4.4). The top-to-the-southwest sense of shear suggested by the quartz a-axis pole figure may be a record of a previous foliation, may reflect the effects of changing kinematics during

deformation, or may be the result of the the superimposed effects of more than one stage of deformation (Lister and Williams, 1979). Additionally, the strain may have had a significant coaxial component that could have resulted in the two different apparent senses of shear in the thin section and in the EBSD pole figures. More samples would need to be collected and analyzed to ascertain why the sense of shear suggested by the pole figure differs from that suggested by the microstructures, and also to truly ascertain the kinematics.

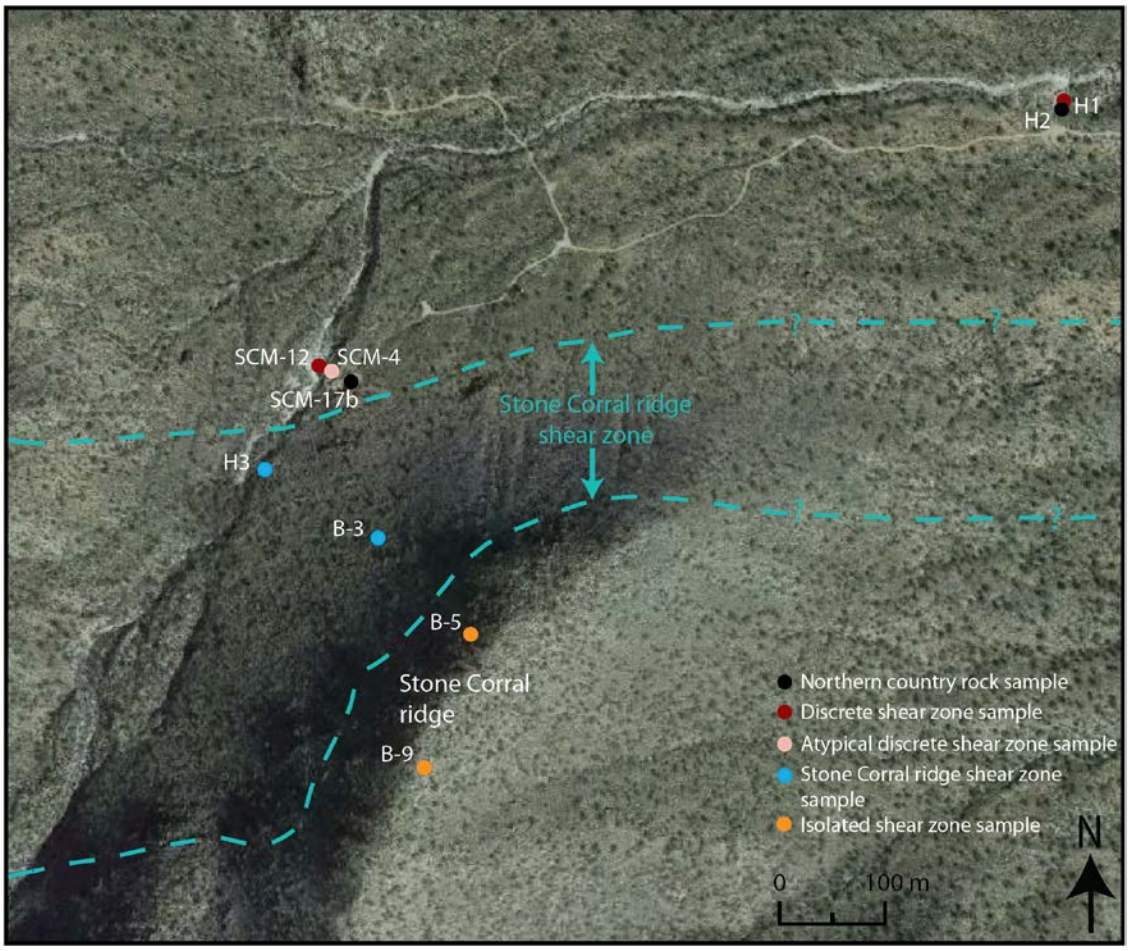

Figure 4.1: Areal photograph of the Stone Corral study area with locations of samples plotted that were used for EBSD analysis (photograph from Google Earth).

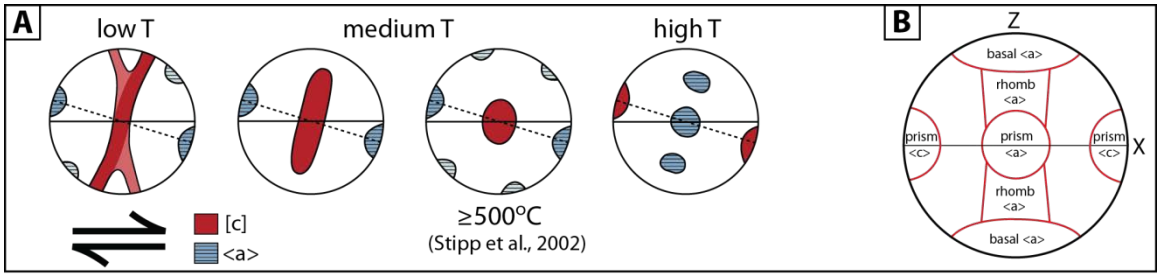

Figure 4.2: Generalized quartz CPO patterns. A) Generalized patterns with increasing temperature during non-coaxial progressive deformation (modified from Passchier and Trouw, 2005); B) Illustration of quartz c-axis patterns and the specific slip system activities they may record (modified from Toy et al., 2008; based on Schmid and Casey, 1986). Figure from Singleton and Mosher, 2012.

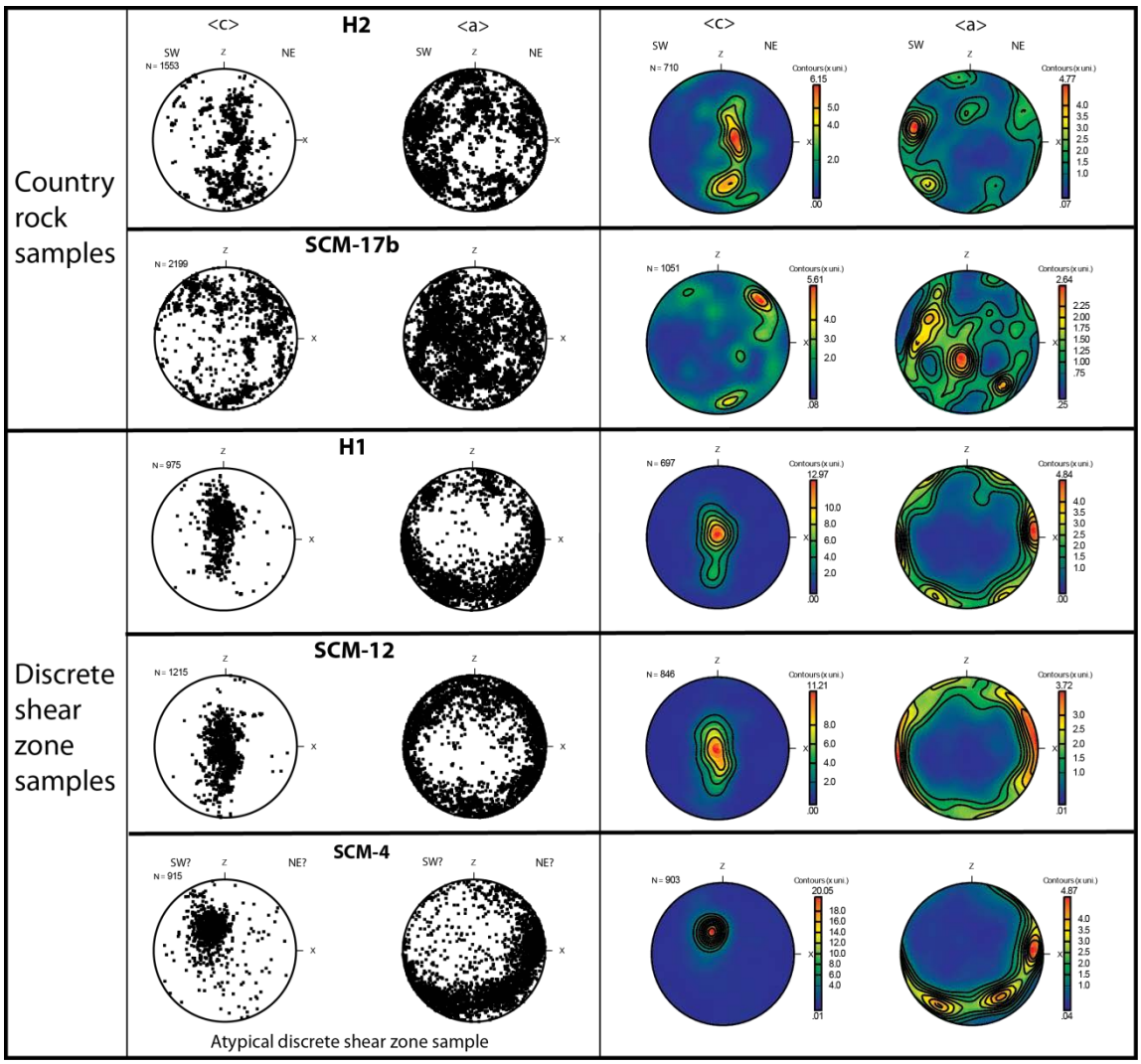

Figure 4.3: Lower hemisphere pole figures of quartz <c> and <a> axes in samples from the discrete shear zones and country rocks north of Stone Corral ridge. Raw data are shown in scatter plots in the left column and include all analyzed points. Data plotted as one point per grain and contoured with multiples of uniform distribution are shown in the right column. Northeast is to the top right of each sample. Pole figures were constructed using PFch5 (Mainprice, 2005).

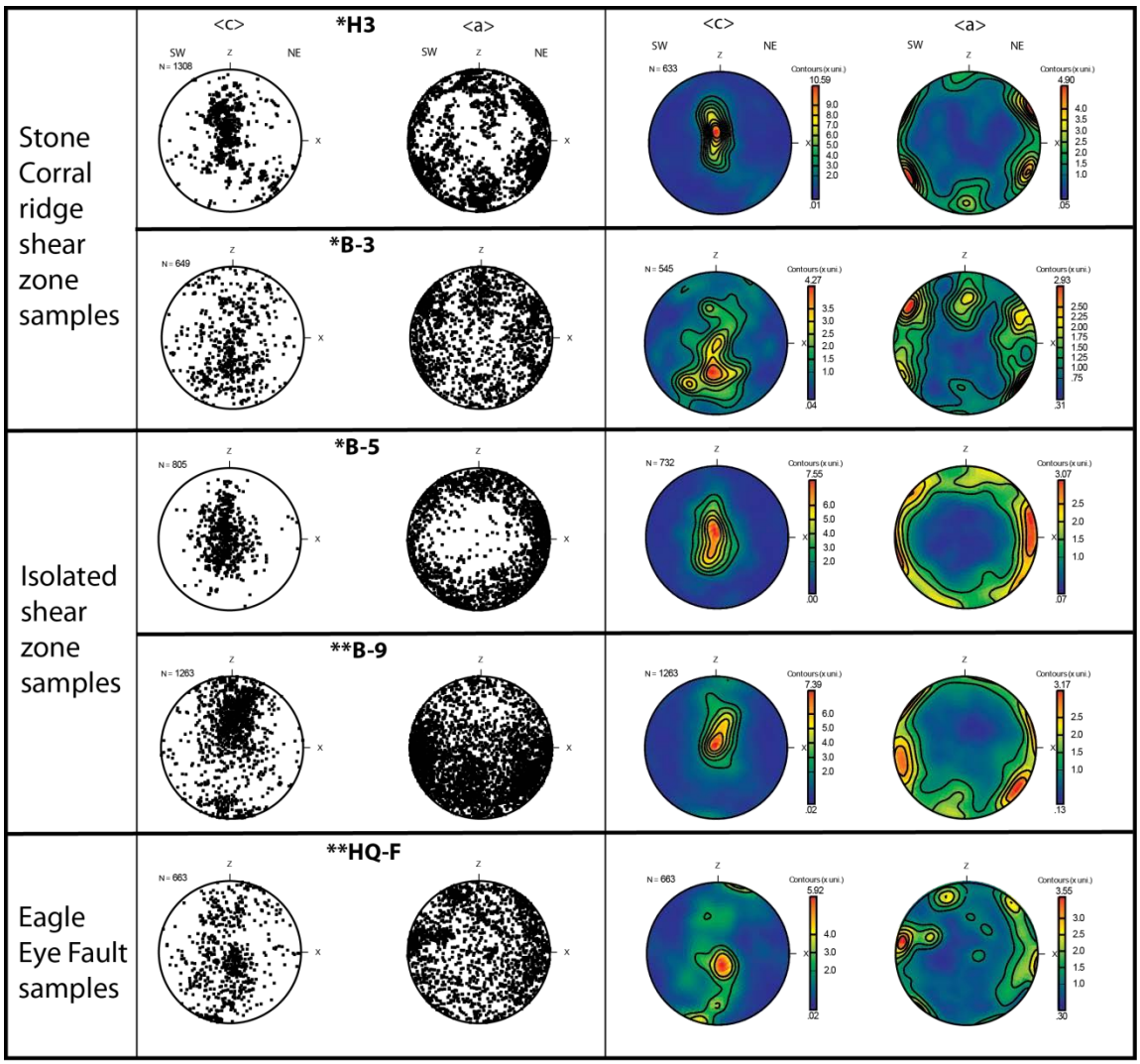

*Scatter plot data plotted as all points analyzed.
**Scatter plot data plotted as one point per grain.

Figure 4.4: Lower hemisphere pole figures of quartz <c> and <a> axes in samples from the Stone Corral study area and Eagle Eye Mountain. Raw data are shown in scatter plots in the left column. Data contoured with multiples of uniform distribution are shown in the right column. Northeast is to the top right of each sample. Pole figures were constructed using PFch5 (Mainprice, 2005).

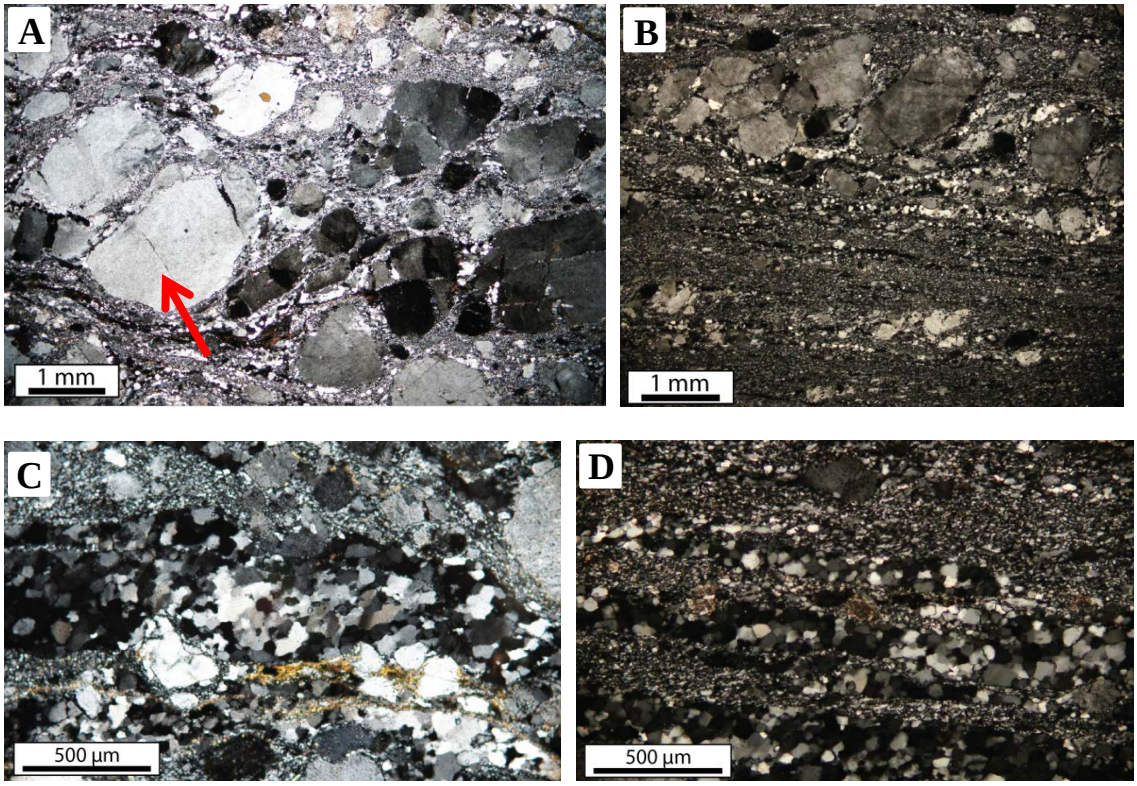

Figure 4.5: Feldspar and quartz microstructures in the isolated shear zone sample, B-5. Note the very fine grained, grungy-looking feldspar typical of BLG recrystallization or neocrystallization. A-B) Feldspar porphyroclasts are inclined in a top-to-the-right (NE) direction. Red arrow in A points to a feldspar σ-type mantled porphyroclast indicating a top-to-the-right (NE) sense of shear; C-D) Quartz layers with polygonal shaped grains that were analyzed with EBSD. Quartz in C appears subtly inclined in a top-to-the-right (NE) direction

	H2	SCM-17b	H1	SCM-12	SCM-4	H3	B-3	B-5	B-9	HQ-F
J	2.64	1.71	5.43	5.14	8.08	3.87	1.69	3.42	2.68	1.98
P	0.24	0.08	0.63	0.64	0.76	0.47	0.22	0.55	0.38	0.18
G	0.52	0.37	0.24	0.25	0.08	0.28	0.29	0.21	0.33	0.42
R	0.24	0.55	0.13	0.11	0.16	0.25	0.49	0.24	0.29	0.4
P_n	0.32	0.18	0.72	0.72	0.9	0.63	0.43	0.72	0.54	0.3
G_n	0.68	0.82	0.28	0.28	0.1	0.37	0.57	0.28	0.46	0.7
# grains	710	1051	697	846	903	633	545	732	1263	733
Rotation (on x)			-20°						25°	
Sense of Shear	Top-NE	Top-NE	Top-SW	Top-SW	Top-SW?	Top-SW	Top-NE	Top-SW	Top-NE	Top-NE

Table 4.1: Summary of pole figure data and statistics for all samples.

Chapter 5: Energy-dispersive X-ray Spectrometry

Energy-dispersive X-ray spectrometry (EDS) point analyses were conducted on two thin sections of sample SCM-51, which was collected from one of the discrete shear zones with a central epidote vein, bleached halo, and flanking paired shear zones morphology (Figures 1.5E-F, 2.9D-F; 2.14B). One of the thin sections analyzed included a piece of the central epidote vein and the adjacent ~1-1.5 mm-thick highly sericitized, feldspar-rich alteration zone (Figures 3.11A-B, 3.12). The other thin section analyzed included part of the bleached halo, one of the flanking ultramylonite zones, and the transitional boundary between them (Figure 2.14B).

The EDS analyses were undertaken to determine how the composition of plagioclase feldspar varies as a function of distance from the central epidote vein. Spectral maps were obtained to determine and compare the compositions of the secondary feldspar replacement products (i.e., myrmekitic plagioclase and the non-symplectic plagioclase; Figures 3.14-3.16, 3.19). Both of these products are extensive in the shear zones and are responsible for the bleached appearance of the bleached haloes (see Chapter 3; Figures 3.14-3.16). The presence of albite twinning in the non-symplectic secondary feldspar in thin section indicates this replacement product is plagioclase (Figure 3.16), but the composition of the plagioclase is unknown. The country rock granite that hosts the shear zones is composed of ~35-38% plagioclase feldspar and ~30-36% potassium feldspar, but in the disrete shear zones, much of the feldspar has been almost entirely replaced by the secondary plagioclase.

5.1 METHODS

EDS was used to collect numerous semi-quantitative point X-ray spectra and elemental X-ray map data from sample SCM-51. The analyses were performed on two

carbon coated thin sections using a Phillips XL30 Environmental Scanning Electron Microscope (ESEM) equipped with an X-max 50 mm large area silicon drift EDS detector in the Department of Geological Sciences at the University of Texas at Austin. All data were collected under high vacuum with an accelerating voltage of 20 kV, spot size of 6 μm, and working distance of 13-20 mm. For analysis of the epidote vein and the adjacent highly altered feldspar-rich zone, a magnification of 100 was used. For analysis of the bleached halo and the flanking ultramylonite zone, a magnification of 200 was used. For analysis of myrmekite and the widespread non-symplectic secondary feldspar replacement product, magnifications of 60 and 100 were used, respectively. The replacement textures were imaged using secondary electron imaging. Atomic percentages were calculated from the weight percent data and were used to determine the anorthite percentages of the plagioclase feldspars.

5.2 RESULTS

5.2.1 Composition of the Epidote Vein and the Adjacent Highly Altered Zone

Spectra were obtained on epidote from four points within the epidote vein, and the compositional data from all points are in good agreement with each other with oxygen values of ~53-54 weight percent (wt. %), silicon values of ~16-18 wt. %, calcium values of ~12-12.5 wt. %, aluminum values of ~10-12 wt. %, and iron values of ~6-7 wt. % (Table 5.1). Spectra were also obtained from feldspar grains in several areas within the highly altered zone adjacent to the epidote vein (Figure 3.12). All the spectra yielded sodium-rich compositions with some spectra also containing a small amount of calcium and/or potassium (Table 5.2). However, because the feldspar grains are so highly sericitized, the potassium is likely hosted within this alteration product rather than within the feldspar grains. With this assumption, the anorthite percent (Ca/(Ca+Na)x100) was

calculated for each spectrum using the atomic percentages of sodium and calcium, which yielded anorthite values of 0-4%. The feldspar in the altered zone, therefore, is nearly pure albite (Table 5.3).

5.2.2 Composition of the Bleached Halo

The plagioclase feldspar grains in the bleached zone are very coarse grained (up to several mm), and only two large grains were analyzed. Numerous spectral point data were obtained from the two grains which share similar compositions (Table 5.4). Sodium contents range from 6.6 to 7.4 wt. %; calcium contents range from 2.5-3.9 wt. %, and potassium contents are all less than half a weight percent. The anorthite percentages calculated for the data range from 19-26% (Table 5.3), which is significantly higher than the anorthite percentages of the feldspar-rich altered zone adjacent to the vein. This compositional data indicate the large feldspar porphyroclasts in the bleached zone are oligoclase.

5.2.3 Composition of the Flanking Ultramylonite Zone

Point spectra were obtained from numerous plagioclase grains in the flanking ultramylonite zone. These spectra also indicate high sodium contents relative to calcium contents with 5.1-7.0 wt. % sodium and 2.4-3.4 wt. % calcium (Table 5.5). Some of the spectra also contain potassium contents up to 1.5 wt. %. The anorthite percentages calculated for the points range from 18-23%. Therefore, the plagioclase feldspar in the utramylonite zone is also oligoclase.

5.2.4 Replacement Products: Myrmekite and the Non-symplectic Secondary Feldspar

Point spectra were obtained from several points on myrmekitic plagioclase lobes on the edges of two potassium feldspar grains in the bleached halo. These analyses

yielded sodium contents of 6.0-7.5 wt. % and calcium contents of 2.3-3.8 wt. % (Table 5.6). Anorthite percentages range from 15-25% (Table 5.3), which indicates the myrmekitic plagioclase is oligoclase rather than albite. Elemental maps for one of the analyzed grains are presented in Figure 5.1.

A potassium feldspar grain that had undergone partial replacement by the non-symplectic feldspar product was analyzed in the transitional zone between the bleached halo and the flanking ultramylonite zone (Figure 5.2). Similar to the analyses of the other plagioclase grains in the sample, the point spectra indicate a composition rich in sodium with a lesser amount of calcium. Sodium contents range from 4.7 to 6.1 wt. % and calcium contents range from 1.8 to 2.5 wt. % (Table 5.7). However, the potassium contents are also very high at 1.3 to 4.4 wt. %. The anorthite percentage was only calculated for the one spectrum that did not have a significant contribution of potassium (Table 5.3). The result for the spectrum is 20% anorthite, which indicates that the non-symplectic replacement product is oligoclase.

5.3 Summary and Brief Discussion

5.3.1 Fluid-rock Interaction

The EDS analyses of large plagioclase porphyroclasts in the bleached halo, small recrystallized plagioclase grains in the flanking ultramylonite zone, myrmekitic plagioclase in the bleached halo, and the non-symplectic feldspar replacement product in the transitional area between the bleached halo and the ultramylonite zone indicate that all of the feldspar is oligoclase. The only plagioclase in the sample that is not oligoclase is the plagioclase in the ~1-1.5 mm alteration zone directly adjacent to the epidote vein. This alteration zone is nearly pure albite.

The restriction of albite to this thin, highly altered zone may be related both to the higher degree of fluid-rock interaction that occurred in the zone and to the high abundance of the calcium-rich minerals in the vein and altered area that would have acted as sinks for calcium but not for sodium. The fluids that were present in the antecedent fracture, which is now filled with the epidote vein, were likely sodium-rich because the widespread feldspar replacement products that are largely responsible for the bleached appearance of the bleached haloes are oligoclase. The rock directly adjacent to the fracture, i.e., the thin alteration zone in sample SCM-51, would have experienced more interaction with these sodium-rich fluids than the rest of the rock in the bleached zone because of the high permeability offered by the fracture. This alteration zone, therefore, would be more readily replaced.

In addition, the growth of the vein epidote, as well as the metamorphic epidote and titanite in the altered zone, would have acted as sinks for calcium, which would have left less calcium available for the secondary feldspars to utilize during consumption of older grains. If conditions were such that the fluids near the fracture could leach calcium from the plagioclase feldspar grains in the adjacent rock to aid in the nucleation and growth of epidote and titanite, then a significant amount of sodium would have remained behind. This sodium would be available for the growth of the albitic feldspar at the expense of the older plagioclase and potassium feldspar porphyroclasts. Some of the potassium that would have been released from the consumption of the potassium feldspar grains by the albite could have contributed to the development of the abundant sericitic alteration. Potassium may also have been transported by the fluid further into the rock where it could be utilized in mineral growth elsewhere, such as in the production of the abundant biotite present in the flanking shear zones.

5.3.2 Significance of the Potassium Content in Ultramylonitic Plagioclase Grains

The composition of the plagioclase grains in the flanking ultramylonite zone differs from that of the plagioclase grains in the bleached halo and the myrmekite in one important way. The plagioclase grains in the ultramylonite zone contain a minor amount of potassium (<1 atomic percent) that may be significant, considering that the calcium contents of the grains are all <2 atomic percent.

The potassium in the grains may have two possible sources. Because of the fine-grained nature of the ultramylonite zone, the point spectra may have slightly overlapped grain boundaries and included a small amount of neighboring potassium feldspar grains. Because the analyses were performed using secondary electron imaging rather than backscatter electron imaging, grain boundaries were not always easy to discern. However, the ultramylonite zone contains abundant fine-grained biotite that wraps around the feldspar grains, so if point spectra overlapped boundaries, biotite should have also been included in some of the analyses, but no magnesium or iron were detected in any of the spectral data. Additionally, a small spot size of 6 μm was used for the analyses so that grain boundaries would be more easily avoided.

Perhaps a more likely source for the potassium would be from within the feldspar grains themselves. If the potassium feldspar grains in the ultramylonite zone had undergone significant but incomplete replacement by the non-symplectic oligoclase and myrmekite replacement products, patches of potassium feldspar in the grains may still remain. This possibility is supported by thin section observations of the bleached haloes and flanking mylonite zones in several samples. In the thin sections, the progressively more intense recrystallization of the highly replaced feldspar grains from the bleached haloes into the shear zones is clearly evident. Many (if not most) of the fine grains in the

flanking shear zones appear to be recrystallized myrmekite and non-symplectic oligoclase.

Further evidence is provided to support this idea by the data collected from the non-symplectic oligoclase replacement product. The extremely patchy nature of oligoclase replacement in the potassium feldspar grains is clearly evident in the composite and elemental maps that were obtained from one of these partially replaced grains (Figure 5.2). All of the spectral data collected from the oligoclase-rich areas of this grain included significant portions of potassium as well, except for one spectrum (Table 5.7). The plagioclase grains in the ultramylonitic zone contain lesser amounts of potassium than the oligoclase in this partially replaced grain, but still contain much more potassium than the grains in the bleached halo. This small amount of potassium may be a vestige of an earlier composition that has been almost entirely replaced by the metamorphic oligoclase.

5.3.3 Comparison of Mean Anorthite Percentages

The mean anorthite percentages of all the plagioclase grains analyzed are provided in Table 5.3. The mean anorthite percentages of the bleached halo grains, flanking ultramylonite zone grains, myrmekitic plagioclase, and the non-symplectic oligoclase replacement product are very similar at ~20-22%. The similarity in the chemistry of the grains analyzed in the bleached haloes to the other feldspar grains is significant because these bleached halo grains do not show clear evidence for replacement by secondary feldspars, but yet they share the same composition as the replacement products. This similarity may indicate that the grains underwent complete replacement by the secondary feldspar product.

The bleached halo in this particular shear zone (sample SCM-51) is unique because the large grains do not show the extensive patchy non-symplectic replacement texture in thin section that is so striking in all of the other bleached halo samples. This shear zone is also one of the largest and the best developed of all the shear zones in the study area, and therefore the grains in the bleached halo may have experienced more fluid-rock interaction than many of the grains in the smaller and less developed shear zones. The larger degree of fluid-rock interaction may have resulted in the more complete replacement of the feldspars by the secondary oligoclase. Conversely, the grains in the bleached halo may be original preserved plagioclase grains with a similar composition to the secondary oligoclase. However, this seems unlikely considering that the non-symplectic oligoclase replacement of the original feldspar grains in all of the other samples is so extensive that it seems to have affected all or nearly all of the grains in the bleached haloes. Additionally, this very replacement process seems to be most responsible for the bleached appearance of the rock.

5.3.4 Development of the Non-symplectic Oligoclase Replacement Product

In thin section, the non-symplectic oligoclase replacement product forms angular patches in some of the potassium feldspar grains, suggesting the replacement may have initiated along cleavage planes (Figure 3.15C-D). Microfractures along cleavage planes may have allowed fluids to gain access to the interiors of the porphyroclasts. The fluids could have transported ions to the reaction sites and removed ions released during the replacement reactions.

Although the anorthite percentage could only be meaningfully calculated for one of the EDS point spectra obtained from the non-symplectic oligoclase replacement product, the similarity in the composition of this spectrum to the myrmekitic plagioclase

spectra is intriguing. Because these two replacement products also formed during the same deformation event and under the same fluid-rich metamorphic conditions, this compositional similarity suggests the products likely formed from similar processes and reactions. The question then arises as to why the non-symplectic plagioclase is present at all. Why did the replacement reaction simply not produce additional myrmekite?

In the myrmekite-forming reaction, a potassium feldspar grain reacts with sodium and calcium ions in a fluid to form myrmekite and to release potassium into the fluid. Simpson and Wintsch (1989) and Tsurumi et al. (2003) provide the following reaction:

$$(1 + x)KAlSi_3O_8 + (1 - x)Na^+ + xCa^{2+} = Na_{1-x}Ca_xAl_{1+x}Si_{3-x}O_8 + 4xSiO_2 + (1 + x)K^+$$

where x is a compositionally dependent variable that will be equal to the anorthite component ($Ca^{2+}/ (Ca^{2+} + Na^+)$) of the plagioclase in the myrmekite formed. In the case of sample SCM-51, the mean anorthite content of the myrmekitic plagioclase is ~0.2 (Table 5.3), and so the appropriate reaction is:

$$1.2KAlSi_3O_8 + 0.8Na^+ + 0.2Ca^{2+} = Na_{0.8}Ca_{0.2}Al_{1.2}Si_{2.8}O_8 + 0.8SiO_2 + 1.2K^+$$

The non-symplectic oligoclase product likely resulted from a similar reaction because it formed synchronously with the myrmekite and is of a nearly identical composition. However, during the formation of the non-symplectic oligoclase, the silica did not precipitate as quartz vermicules and so must have been utilized by an additional mineral-forming reaction or was transported elsewhere. The mineralogy and microstructures of the numerous samples collected from the shear zones with the central vein, bleached halo, and flanking paired shear zones morphology provide evidence for a couple of possible sinks for the silica product.

In the thin sections of all of the samples collected from shear zones with the central vein, bleached halo, and flanking paired shear zones morphology, partially replaced potassium feldspar grains are present in which biotite is associated with the non-

symplectic oligoclase replacement product. The biotite is present within the oligoclase patches and is elongate in the same direction as the host patches, which strongly suggests that it either also is a reaction product or that it formed in the oligoclase patches later (Figure 3.15). For the biotite to have formed during the non-symplectic oligoclase-producing reaction, the presence of Mg^{2+} or $Fe^{2+,\ 3+}$ would have been required. These ions would need to have been introduced by fluids during the reaction as they are not significant components of feldspar. The abundance of metamorphic epidote, vein epidote, and opaque minerals (particularly near the vein), some of which are iron oxides (Figure 5.1), suggest that the metamorphic fluids may have been iron-rich. Fluids may have introduced Na^{+}, Ca^{2+}, and $Fe^{2+,\ 3+}$ to the reacting potassium feldspar to form the oligoclase and biotite, which would provide an explanation for why quartz is absent. The silica would have been used in the production of biotite rather than in the production of myrmekitic quartz vermicules.

Although all the samples contain some potassium feldspar grains with the intimately related biotite and oligoclase replacement patches, only a couple of the samples exhibit this relationship extensively. These samples were collected from the flanking shear zones that have undergone only moderate mylonitization (Figure 3.15B). If this relationship existed in the more intensely mylonitized and ultramylonitized flanking shear zones, the evidence has been obliterated by the extreme amount of recrystallization and grain-size reduction of the feldspar and biotite.

In the bleached haloes, on the other hand, potassium feldspar is extensively replaced by the non-symplectic oligoclase product, but the majority of these replaced grains are biotite-absent. In these grains, the silica that would have been released during the replacement reaction must have been transported out of the feldspar grain by the fluid. This silica may have been used in any of the metamorphic reactions that were

occurring simultaneously to form minerals such as epidote and titanite. Some of the silica may also have precipitated into pore spaces, either into fractures or into the transient pore spaces that are created and destroyed during deformation. The long quartz layers and thick pods that are present in the bleached zones of many of the samples may have in part precipitated from this source (e.g., Figures 3.17A, 3.18A).

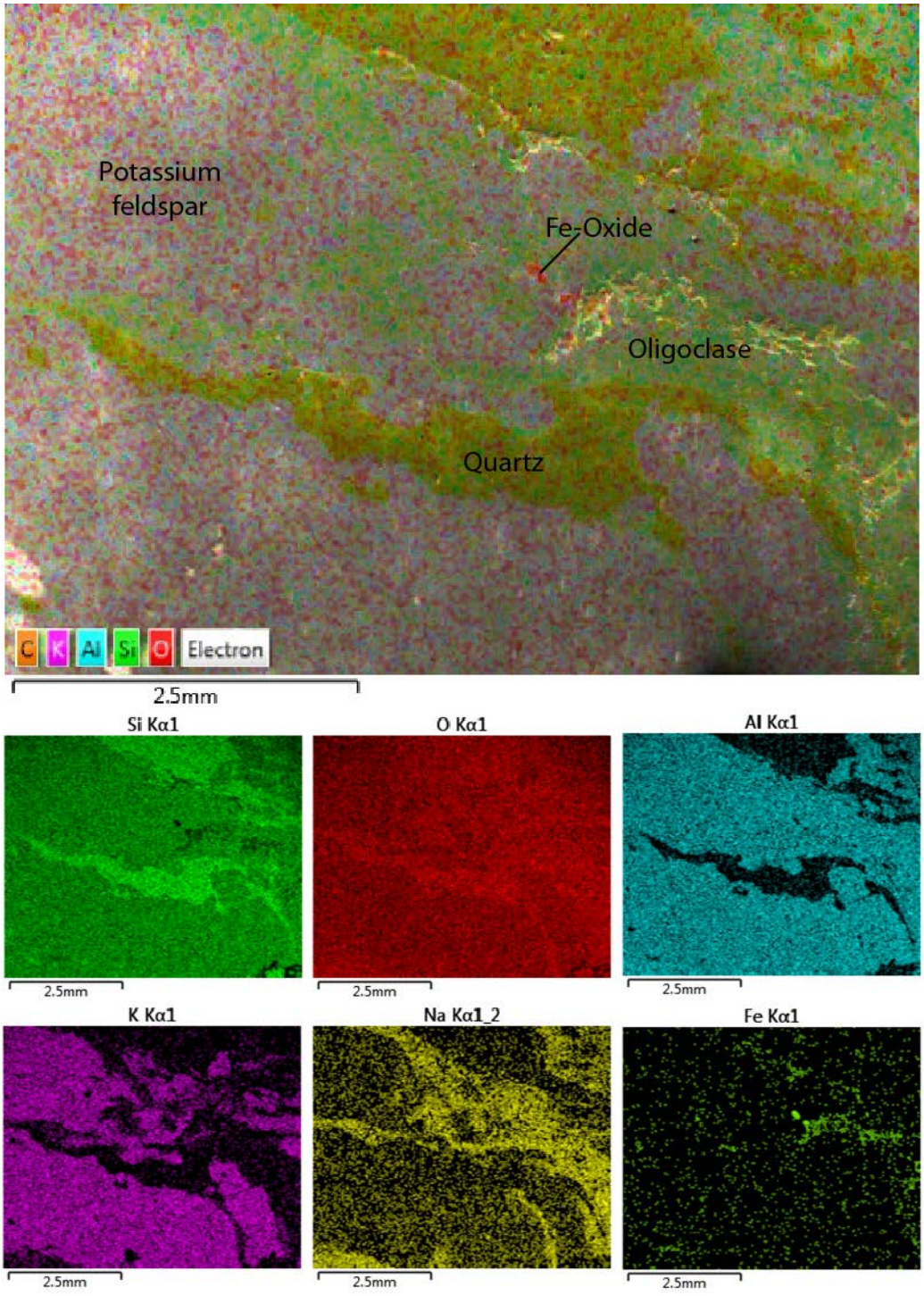

Figure 5.1: Composite and elemental maps of myrmekite replacement of potassium feldspar. In the composite map, pink is potassium feldspar, light green is oligoclase, dark yellow-green is quartz, and red is iron oxide.

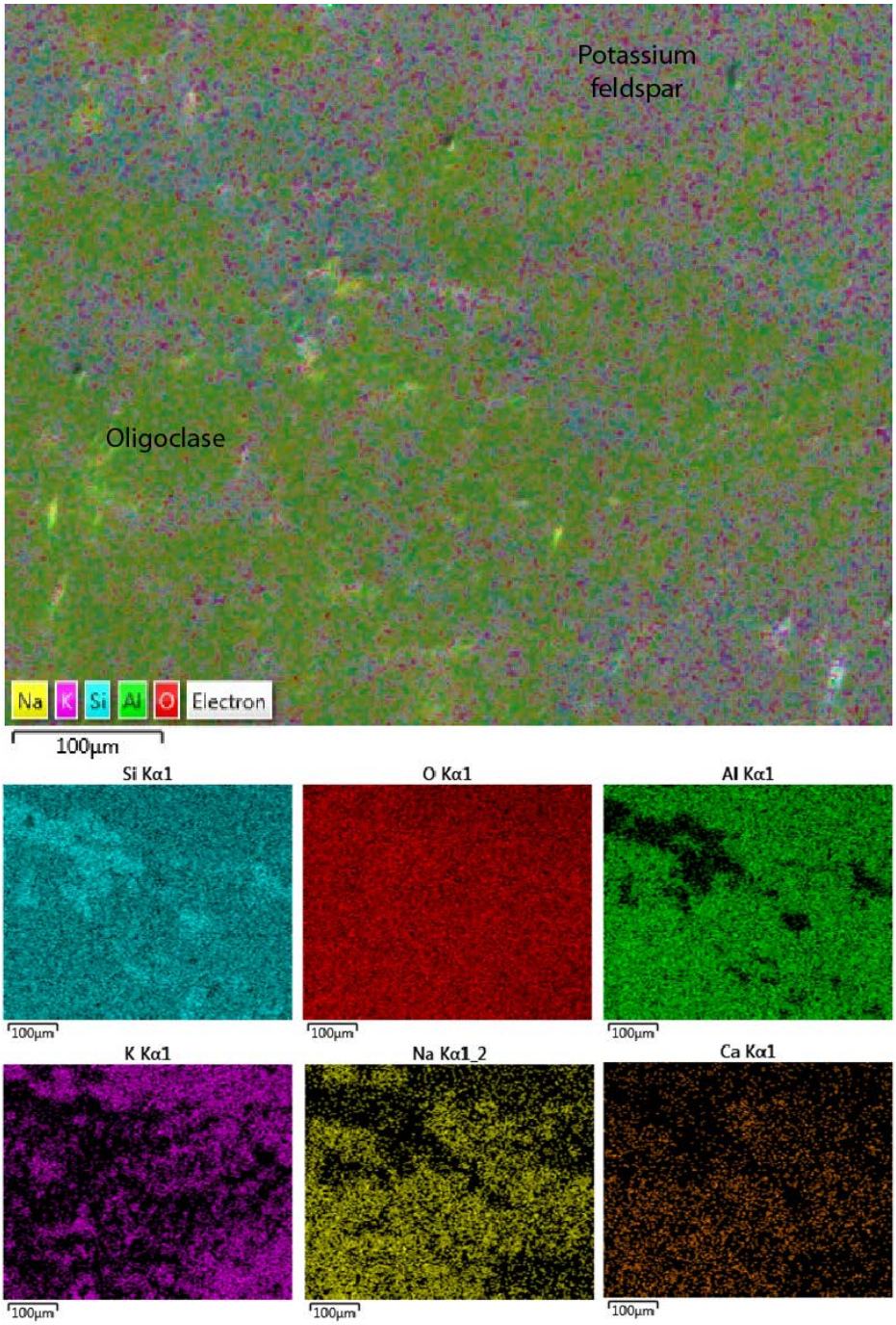

Figure 5.2: Composite and elemental maps of non-symplectic oligoclase replacement of potassium feldspar. In the composite map, pink is potassium feldspar and green is oligoclase. Although the elemental map of silicon shows quartz strands in this particular case, quartz is not typically associated with the replacement texture.

	Spectrum	Ca	Fe	Al	Si	O
Epidote	1	12.6	6.3	11.7	15.7	53.7
	2	11.1	7.5	10.3	17.5	53.7
	3	11.3	6.1	11.0	17.9	53.7
	4	12.5	5.6	12.5	16.5	52.8

Table 5.1: Elemental point analyses of the central epidote vein in weight percentages.

	Spectrum	O	Si	Al	Na	Ca	K	Fe
Altered Zone Adjacent to Vein	5	53.4	27.2	10.4	9.0	0.0	0.0	0.0
	6	55.3	25.6	10.8	7.4	0.0	0.8	0.0
	7	54.8	25.5	10.7	7.2	0.0	1.5	0.3
	8	53.9	25.3	10.8	8.4	0.7	0.7	0.3
	9	54.4	26.1	10.5	7.8	0.0	1.0	0.2
	10	53.8	27.0	9.7	9.5	0.0	0.0	0.1
	11	54.8	26.5	9.7	8.4	0.6	0.0	0.0
	12	54.5	26.4	9.6	8.4	0.5	0.5	0.1
	13	54.1	26.4	10.5	8.3	0.6	0.0	0.2
	14	52.2	27.1	10.4	9.3	0.4	0.4	0.2
	15	54.6	26.5	9.5	8.8	0.4	0.0	0.3
	16	54.7	24.3	12.2	5.9	0.0	2.6	0.3

Table 5.2: Elemental point analyses of feldspar grains in the highly altered zone adjacent to the epidote vein. Data are presented in weight percentages.

	Spectrum	Na	Ca	An %
Altered Zone Adjacent to Vein μ = 1.7 An %	**5**	7.7	0.0	0
	6	6.3	0.0	0
	7	6.2	0.0	0
	8	7.2	0.3	4
	9	6.7	0.0	0
	10	8.1	0.0	0
	11	7.2	0.3	4
	12	7.2	0.2	3
	13	7.1	0.3	4
	14	8.0	0.2	2
	15	7.5	0.2	3
	16	5.1	0.0	0
Flanking Ultramylonite μ = 20.8 An %	**34**	4.7	1.3	22
	35	5.9	1.6	21
	36	5.8	1.6	22
	37	5.4	1.3	19
	38	6.0	1.8	23
	39	5.4	1.4	21
	40	6.4	1.6	20
	41	6.2	1.4	18
	42	5.9	1.6	21
***Repl.**	**53**	4.4	1.1	20

*Repl. = non-symplectic replacement product. Only one spectrum is presented because all other spectra included a significant component of potassium.

	Spectrum	Na	Ca	An %
Bleached Halo μ = 22.3 An %	**17**	6.1	1.8	23
	18	6.0	2.1	26
	19	6.5	1.6	20
	20	6.3	1.7	21
	21	6.2	1.8	23
	22	6.0	1.9	24
	23	6.7	1.3	16
	24	6.1	1.9	24
	25	6.0	2.1	26
	26	6.1	2.0	25
	27	6.5	1.5	19
	28	6.1	2.0	25
	29	6.2	1.9	23
	30	6.3	1.7	21
	31	6.1	1.9	24
	32	6.4	1.6	20
	33	6.4	1.5	19
Myrmekite μ = 21 An %	**43**	5.7	1.4	20
	44	5.5	1.4	21
	45	6.8	1.2	15
	46	5.1	1.4	21
	47	6.3	1.6	20
	48	6.1	2.0	25
	49	5.9	1.9	24

Table 5.3: Sodium and calcium atomic percentages and anorthite percentages for all analyzed plagioclase feldspar grains. Anorthite content is calculated from the atomic percentages of Na and Ca, using the formula: Ca/(Ca+Na)x100.

Plagioclase in Bleached Halo	Spectrum	O	Si	Al	Na	Ca	K	Cu
	17	43.3	32.3	13.2	6.6	3.5	0.4	0.5
	18	43.4	32.1	13.5	6.6	3.9	0.0	0.4
	19	43.6	32.7	13.0	7.1	3.0	0.2	0.4
	20	44.2	32.5	13.0	6.9	3.2	0.2	0.0
	21	43.6	32.2	13.3	6.8	3.5	0.2	0.4
	22	43.8	31.9	13.5	6.6	3.7	0.0	0.5
	23	43.9	33.0	12.8	7.4	2.5	0.0	0.5
	24	43.6	31.9	13.4	6.7	3.6	0.2	0.5
	25	43.5	32.0	13.4	6.5	3.9	0.2	0.4
	26	43.8	32.1	13.5	6.7	3.8	0.2	0.0
	27	44.0	32.9	12.9	7.2	2.8	0.2	0.0
	28	43.7	32.0	13.6	6.7	3.8	0.2	0.0
	29	43.8	32.1	13.4	6.8	3.7	0.2	0.0
	30	43.8	32.5	13.3	6.9	3.3	0.2	0.0
	31	43.9	32.2	13.4	6.7	3.6	0.2	0.0
	32	43.8	32.4	13.3	7.0	3.1	0.3	0.0
	33	43.9	32.4	13.0	7.0	2.9	0.2	0.6

Table 5.4: Elemental point analyses of feldspar grains in the bleached halo. Data are presented in weight percentages.

Flanking Ultramylonite	Spectrum	O	Si	Al	Na	Ca	K
	34	44.2	36.5	10.4	5.1	2.4	1.3
	35	43.7	32.4	12.9	6.5	3.1	1.5
	36	43.6	33.4	12.5	6.4	3.1	1.0
	37	44.2	35.2	11.2	6.0	2.4	1.0
	38	43.2	33.4	13.0	6.6	3.4	0.4
	39	43.5	34.7	11.9	5.9	2.6	1.3
	40	43.7	32.6	13.0	7.0	3.0	0.8
	41	43.6	33.2	12.8	6.8	2.6	0.9
	42	43.4	33.1	12.9	6.5	3.1	1.0

Table 5.5: Elemental point analyses of feldspar grains in the flanking ultramylonite zone. Data are presented in weight percentages.

	Spectrum	O	Si	Al	Na	Ca	K	Cu
Myrmekite	**43**	44.7	35	11.3	6.3	2.6	0.2	0.0
	44	44.9	35	10.8	6	2.6	0.2	0.7
	45	44.1	33.5	12.3	7.5	2.3	0.2	0.0
	46	44.3	37	10.3	5.6	2.6	0.2	0.0
	47	43.4	32.7	13	6.9	3.1	0.6	0.0
	48	43.6	32.1	13.6	6.7	3.8	0.3	0.0
	49	43.9	32	13.6	6.5	3.7	0.3	0.0

Table 5.6: Elemental point analyses of myrmekitic plagioclase. Data are presented in weight percentages.

	Spectrum	O	Si	Al	Na	Ca	K	Fe	Mg
Non-symplectic replacement	**50**	43.0	33.1	11.5	4.7	2	4.4	0.9	0.3
	51	43.2	33.7	12.0	5.3	2.5	3.3	0.0	0.0
	52	43.5	35.1	11.1	5.7	1.8	2.8	0.0	0.0
	53	44.5	37.7	9.6	4.8	2.2	1.3	0.0	0.0
	54	43.2	33.2	12.5	6.1	2.5	2.2	0.0	0.0

Table 5.7: Elemental point analyses of the non-symplectic secondary feldspar replacement product. Data are presented in weight percentages.

Chapter 6: Fourier Transform Infrared Spectroscopy

The water content of intragranular quartz was analyzed in numerous samples from throughout the study area by Fourier Transform Infrared (FTIR) Spectroscopy to examine the relationship between water content and strain and to test a number of hypotheses dealing with the origin of the discrete shear zones. Specifically, the following hypotheses were tested: 1) the discrete shear zones initiated on pre-existing fractures, 2) hydrolytic weakening of quartz was an important mechanism for shear zone localization, and 3) the degree of fluid rock interaction was an important factor for morphology development. If the discrete shear zones initiated on pre-existing fractures, water content is expected to be higher in these mylonites than in the country rocks and the mylonites from the other (non-discrete) shear zones because the fractures would have provided permeability for fluid flow. Similarly, if hydrolytic weakening of quartz was an important mechanism for strain accommodation in the discrete shear zones, water content should be higher in the quartz in the discrete shear zone mylonites than in the other samples. If higher fluid-rock interaction resulted in the development of discrete shear zones with a central epidote vein, bleached halo, and flanking paired shear zones morphology, then the quartz in the discrete shear zones with this morphology should contain more water than in the discrete shear zones without this morphology.

6.1 METHODS

6.1.1 Sample Selection

A total of twelve samples from across the field area were selected for FTIR spectroscopy analysis (Figure 6.1). Four of the samples analyzed were collected from the country rocks outside of the numerous shear zones. Three of the country rock samples were collected from the northern part of the study area (samples HQ-D, SCM-

17b, and SCM-6) and the fourth was collected from the southern part of the study area near the crest of Stone Corral ridge (sample B-4). Four samples were collected from the discrete mylonitic shear zones in the northern part of the study area, two of which were collected from shear zones that displayed the central epidote vein, bleached halo, and flanking paired shear zones morphology (samples SCM-51 and HQ-C; Figure 1.5A, E-F) and two of which did not display this morphology (samples H1 and SCM-17; Figure 1.4B, D). Another two samples were collected from the Stone Corral ridge shear zone (samples H3 and B-3), and the remaining two samples were collected from the isolated shear zones on the crest of Stone Corral ridge (samples B-5 and B-9).

6.1.2 Sample Preparation

Thick sections were prepared for all twelve samples for FTIR spectroscopy analysis. One thick section was made per sample with the exception of sample HQ-C for which two thick sections were prepared to include both the bleached zone and a flanking shear zone. The samples were cut into blocks with long dimensions that were only slightly shorter than a standard 27x36 mm glass slide to maximize the amount of sample available for analysis. The sample blocks were ground on one side to obtain flat surfaces and then were fastened to standard glass slides with Crystalbond adhesive. The exposed sides of the samples were grounded and polished to acquire flat surfaces and to remove visible blemishes. The samples were then removed from the glass slides, flipped over to expose the other sides, and reattached to the slides with Crystalbond adhesive. The samples were cut and ground until quartz became transparent, which occurred at different thicknesses for each sample because of the wide variation in grain sizes (Tables 6.1-6.6). The sections were then grounded and polished to eradicate visible blemishes, removed from the glass slides in an acetone bath, and thoroughly cleaned with ethanol.

6.1.3 Spectral Analysis

All twelve samples were analyzed with a ThermoElectron Nicolet 6700 spectrometer and Continuμm IR microscope located in the Department of Geological Sciences at the University of Texas at Austin. The OMNIC software program was used for IR data collection and analysis. IR analyses were conducted at a spectral resolution of 4 cm^{-1} using 60 scans per spectra. A 50 by 50 μm aperture size was used and spectra were collected in the range of 4000 to 650 cm^{-1} with the use of a KBr beamsplitter and globular IR source. Background spectral measurements were collected outside of the sample on a salt window after each sample spectra was collected to normalize the data.

The number of spectra collected from each sample ranged from 7 to 37. Grain boundaries and fluid inclusions were avoided in analyses. In the mylonitic samples, matrix grains were smaller than the thicknesses of the samples, and thus only the less common larger grains in quartz ribbons were analyzed. Photomicrograph photomosaics were made for the first few analyzed samples to better orient the sample under the IR microscope and to easily document the location of the sample points analyzed. However, the samples were so thin that they disassembled into numerous small pieces following the acetone baths for removal from the glass slides, and the photomosaics could not be used. The OMNIC software was then used to obtain photomicrographs of every area analyzed and to plot the location of sample points on the photomicrographs directly so sample locations were clearly documented. Thickness was determined for each sample point by the use of a petrographic microscope furnished with a Heidenhain focus drive linear encoder. The thickness was measured by focusing on the top and bottom of the sample at each point, and the displacement was recorded by the encoder.

Following the step-by-step methods of Gleason and DeSisto (2008), the integral area of the broad peak from 2800 to 3800 cm^{-1} was used to determine the concentration

of the hydroxyl and molecular water species within the quartz grains. The concentrations were calculated using a modified Beer-Lambert Law:

$$C(H{:}10^6\ Si) = (0.812 \times A_i \times t)$$

where $C(H{:}10^6\ Si)$ is the concentration of water at the point analyzed, A_i is the integrated absorbance under the broad peak from 2800 to 3800 cm^{-1} at the point analyzed, t is the thickness of the sample at the point analyzed (cm), and 0.812 is a calibration factor for quartz (Kats, 1962). Finally, the water concentrations were converted to ppm by weight using the conversion equation: $ppm = C(H{:}10^6\ Si) / 6.67$.

6.2 RESULTS

6.2.1 Spectral Profiles

The thicknesses of the sections at the points analyzed, the integrated absorbances, and the calculated water concentrations for all spectral analyses are reported in Tables 6.1-6.6, and the spectra are provided in Appendix A. Average water contents are summarized for all samples and sample categories in Table 6.7. Whereas some of the sample spectra show the fairly smooth broad bell-curve peak associated with molecular water, particularly those in the country rock samples, many of the spectra are superimposed with jagged or lumpy peaks (Figure 6.2). Similar superimposed peaks have been reported in the literature, and commonly appear in the IR spectral analyses of many different rock types, including both deformed and non-deformed igneous and metamorphic rocks (Kronenberg and Wolf, 1990; Kronenberg et al., 1990). Most of the individual peaks are associated with different hydrogen point defects in the crystal lattice, typically related to chemical impurities such as the substitution of aluminum, lithium, and/or hydrogen for silicon (Kats, 1962; Niimi et al., 1999; see Paterson, 1989 and Kronenberg, 1994 for thorough reviews; Figure 6.2B). One common superimposed peak

at wavelength 3620 cm^{-1} may also be related to the presence of very fine-grained mica flakes within the quartz grains (Kronenberg and Wolf, 1990; Figure 6.2C). Because much of the quartz in the analyzed samples recrystallized by GBM recrystallization, extremely small, sub-optical mica flakes may have been overgrown by the migrating quartz boundaries. Many of the spectra exhibit steeply sloping backgrounds because of internal defects in the quartz grains and scattering losses at the surface of the samples (Kronenberg et al., 1990; Figure 6.2D).

6.2.2 Water Contents

The quartz in the country rock samples yielded average water concentrations of 830-1200 H:10^6 Si, or 150-180 ppm (Table 6.1). The ranges of water concentrations vary largely within each sample at 320-4050 H:10^6 Si (50-610 ppm) for HQ-D, 450-2310 H:10^6 Si (70-350 ppm) for B-4, 0-2740 H:10^6 Si (0-410 ppm) for SCM-17b, and 150-1790 H:10^6 Si (20-270 ppm) for sample SCM-6. Importantly, sample B-4 contained similar quartz water contents as the other samples despite its difference in location (i.e., south of the Stone Corral ridge shear zone), orientation, and deformation style (see Chapters 2 and 3).

The quartz in the two mylonite samples collected from the discrete shear zones without the central epidote vein, bleached halo, and flanking paired shear zones morphology yielded average water contents of 1780 and 2260 H:10^6 Si, or 260 and 340 ppm, for SCM-17 and H1, respectively (Table 6.2). The ranges of water concentrations within each sample also varied widely from 240-2720 H:10^6 Si (40-410 ppm) for sample SCM-17 and 500-5080 H:10^6 Si (70-760 ppm) for sample H1. The quartz in the two mylonites from the discrete shear zones with the central epidote vein, bleached halo, and flanking paired shear zones morphology yielded higher average water contents of 4530

and 2540 H:10^6 Si, or 680 and 510 ppm, for samples SCM-51 and HQ-C, respectively (Table 6.3). The water concentrations ranged from 1000-11,930 H:10^6 Si (150-1790 ppm) for sample SCM-51 and from 0-8960 H:10^6 Si (0-1340 ppm) for sample HQ-C.

The water contents of the quartz in the two mylonites from the Stone Corral ridge shear zone averaged 660 and 900 H:10^6 Si (130 and 100 ppm) for samples B-3 and H3, respectively (Table 6.4). Water contents ranged from 30-1570 H:10^6 Si (<10-240 ppm) in sample B-3 and from 20-2870 H:10^6 Si (<10-430 ppm) in sample H3. The two mylonitic samples from the isolated shear zone south of the Stone Corral ridge shear zone yielded similar intragranular quartz water contents with averages of 670 and 830 H:10^6 S, or 100 and 120 ppm, for samples B-5 and B-9, respectively (Table 6.5). Water contents range from 70-1020 H:10^6 Si (10-150 ppm) for sample B-5 and from 80-2940 H:10^6 Si (10-440 ppm) for sample B-9.

6.2.3 Correlation between Water Content and Strain

The thick section of the discrete shear zone mylonite sample SCM-17 was cut perpendicular to the shear zone boundary and is composed of a <1 cm thick shear zone and the surrounding country rock. The country rock foliation is transposed to sub-parallel the shear zone within a couple of millimeters of the shear zone boundary. Spectra from numerous points were obtained throughout this sample, including from the shear zone and the surrounding country rock. The spectra can therefore be subdivided into categories based on the relative degree of strain exhibited in the rock at the points from where the data was collected. The data for the shear zone portion of the sample are divided into two categories, intermediate strain and high strain (Table 6.6). The data gathered on the intermediate strained portion of the shear zone were derived from quartz grains within the upper and lower boundaries of the shear zone where country rock

foliation was transposed to sub-parallel the shear zone foliation. These boundary layers contain ribbon grains on the scale of ~1 mm. The data gathered on the high strained portion of the shear zone were derived from the grains comprising the more central part of the shear zone, which contains highly stretched and thinned ribbon grains, the largest of which are a few hundred microns thick. Only five grains were identified that were large enough for analysis in this portion of the shear zone. The majority of the grains are significantly finer grained than the thickness of the thick section, and therefore the intragranular water contents could not be measured. The less strained portion of the sample is composed of the country rock outside of the shear zone which maintains its original foliation (i.e., it is not transposed or partially transposed to parallel the shear zone boundary).

The combined results of the shear zone analyses (from both the intermediate and high strained portions) are displayed in Table 6.2 and discussed in section 6.2.2. The results are divided into categories (intermediate and high strain) in Table 6.6. The water contents in the high strained portion of the sample average 2610 H:10^6 Si, or 390 ppm, and range from 1130-5530 H:10^6 Si (170-830 ppm), whereas the water contents in the intermediate strained portion of the sample average 1490 H:10^6 Si, or 220 ppm, and range from 240-2550 H:10^6 Si (40-380 ppm). The water contents in the low strained portion of the sample outside of the shear zone are lower, averaging 1310 H:10^6 Si, or 200 ppm, and range from 190-3000 H:10^6 Si (30-450 ppm). These results may be compared to the results from the country rock sample SCM-17b which yielded even lower average water contents of 830 H:10^6 Si, or 150 ppm (Table 6.1; see section 6.2.2). This sample was collected from the country rock within a meter of sample SCM-17 (Figure 6.1).

6.3 Brief Summary and Discussion

The water content data for individual spectral analyses fluctuate widely within each sample, yielding large standard deviations (Tables 6.1-6.6). This high variability in data values is not unusual for FTIR spectral analyses of deformed rocks (e.g., Gleason and DeSisto, 2008). Quartz grains in deformed rocks contain substantial internal defects (including water) that are unevenly dispersed within the crystal lattices. Muto et al. (2005) demonstrated through micro-IR mapping and cathodoluminescence imaging that even in mylonites that are only weakly deformed, molecular water and hydroxyl species are heterogeneously distributed. They also demonstrated over a scale of hundreds of microns that water content is lower in the dynamically recrystallized quartz portion of a single quartz aggregate than in the more deformed portion. Because of this phenomenon of heterogeneous water distribution in deformed and recrystallized quartz, the data for the rocks of the Stone Corral study area are discussed for their importance in discerning relative, rather than absolute, differences in water content among the various samples. Important systematic differences do exist among the different categories of samples, and the relative differences in average water contents among the categories are very useful for providing a general understanding of the fluid-deformation interactions that may have occurred across the study area.

6.3.1 Hydrolytic Weakening and Shear Localization

Infrared spectroscopy has served as one of the most utilized techniques for studying the effects of hydrolytic weakening of quartz in both naturally and experimentally deformed samples as it directly measures the water contents of individual grains and grain aggregates (Griggs and Blacic, 1965; Kronenberg and Wolf, 1990; Post and Tullis, 1998). These studies have demonstrated a strong correlation between increasing intragranular water content and decreasing ductile yield strength of quartz.

Experimental studies have also demonstrated that the IR absorption spectra of "dry" quartz (i.e., without molecular water) and "wet" quartz exhibit easily distinguishable characteristics (see Kronenberg et al., 1990 for a review). Dry quartz spectra are characterized by small, jagged wavenumber profiles between ~3600 cm^{-1} to 3200 cm^{-1}, whereas wet quartz spectra are characterized by a large and broad wavenumber profile with a midpoint near ~3400 cm^{-1}. These varying absorption profile characteristics are attributed to differences in the amounts and types of species of water (hydroxyl and molecular H_2O) present in the grains. Dry quartz spectra provide a measurement of the IR light absorbed by stretching vibrations of hydroxyl species, whereas wet quartz spectra provide a measurement of the IR light absorbed both by stretching vibrations of hydroxyl species and by molecular H_2O species, which most likely exist as sub-microscopic fluid inclusions (Kronenberg et al., 1990; Gleason and DeSisto, 2008).

The majority of the spectra from the analyzed quartz in all of the samples from the Stone Corral study area exhibit the broad peak characteristic of wet quartz rather than the small jagged peaks characteristic of dry quartz, including the quartz in the country rock samples. This result indicates that the rocks were wet before shear zone mylonitization commenced. Country rock sample B-4, which appears non-deformed in the field and hand sample, but exhibits weak deformation and recrystallization in thin section (Figure 3.6A, C), yielded similar water contents to the other more deformed country rock samples (HQ-D, SCM-6, and SCM-17b; Tables 6.1, 6.7). This similarity suggests water in the country rocks was present before initiation of the country rock deformation because water content does not correlate with the degree of deformation in these samples. Regardless, the water contents measured in the country rocks provide a starting point for determining external fluid interactions during shearing and inferring the role of hydrolytic weakening in the shear zone mylonites.

The mylonite samples from the large (few hundred meters thick) Stone Corral ridge shear zone (samples H3 and B-3) and from the isolated shear zones on the crest of Stone Corral ridge (samples B-5 and B-9) yielded very similar average water contents of 100-130 ppm and 100-120 ppm, respectively (Table 6.7). These water contents are slightly lower than the average water contents measured in the country rock samples, which ranged from 150-180 ppm, which implies that water was not significantly more abundant during mylonitization of these rocks. In thin section, the Stone Corral ridge shear zone samples exhibit abundant syn-deformational myrmekite which suggests fluids must have been present during deformation and likely played an important role in the microstructures present. However, myrmekite is also widespread in the country rock samples, present as much larger plagioclase lobes with much thicker quartz vermicules. Much of the myrmekite in the country rock is present on the foliation-parallel edges of the feldspar porphyroclasts, which suggests that at least some of it was also syn-deformational, and therefore fluids were likely also present during the country rock deformation. The similarity in the mineralogy and microstructures of the some of the Stone Corral ridge shear zone samples (such as H3) to the country rock samples suggests that mylonitization and country rock deformation occurred under similar (likely amphibolite-facies) deformation conditions (see section 3.7). The similarity in water contents between the Stone Corral ridge shear zone samples and the country rock samples would be expected if both deformation phases occurred under similar conditions and were closely spaced in time.

The thin sections of the isolated shear zones do not contain evidence for abundant fluids, and these shear zones appear to have deformed under lower temperature conditions (see section 3.7). The similarity in fluid content between these mylonites and the higher temperature mylonites and country rocks suggests that additional fluid was not

introduced during the lower temperature mylonitization event. This supposition is consistent with the hypothesis that the isolated mylonitic shear zones deformed at greenschist-facies conditions during exhumation of the metamorphic core complex footwall when the fluid:rock ratio was likely very low, considering no fluid sources are known to have been available at this time (see Chapter 7).

In contrast, the samples from the discrete shear zone mylonites of the northern study area (samples H1, SCM-17, SCM-51, and HQ-C) all exhibited significantly higher water contents than their host rock samples with sample averages of 260-680 ppm (Table 6.7). The average water content for all of the discrete shear zone samples is 450 ppm, which is significantly higher than the average for all the country rock samples at 160 ppm, the Stone Corral ridge shear zone samples at 120 ppm, and the isolated shear zone samples near the crest of Stone Corral ridge at 110 ppm. These results imply that significantly more water was present in the discrete shear zone rocks during deformation, and therefore that hydrolytic weakening may have played a significant role in the localization of strain into these thin zones.

The plethora of data collected from sample SCM-17 indicate that water content correlates well with the degree of strain exhibited by the rock as examined at the scale of a thin section (Table 6.6). The highly strained central portion of the shear zone contained the highest water contents with an average of 390 ppm. The coarser grained, less intensely sheared boundaries of the shear zone contained lower water contents with an average of 220 ppm, and the much lower strained country rock immediately adjacent to the shear zone contained the lowest water contents of the sample with an average of 200 ppm. A separate sample of the country rock (sample SCM-17b) that was collected less than a meter away from sample SCM-17, but still in the same outcrop, yielded the lowest water contents with an average of 150 ppm.

The 37 spectra collected from the quartz grains within sample SCM-17 may be the largest FTIR study conducted on the relationship between strain and water contents in quartz on the scale of a thin section. The results suggest that the water content and the degree of strain correlate well when averages are considered, and these results are in agreement with the results of a handful of other FTIR spectroscopy studies that have been conducted on naturally deformed rocks at a broad range of scales, including the micron scale (Muto et al., 2005), the meter scale (Kronenberg et al., 1990; Gleason and DeSisto, 2008), and even the kilometer scale (Nakashima et al., 1995). The results of this study provide an example of this relationship on the thin section (millimeter-centimeter) scale.

The FTIR spectroscopy results are consistent with the hypothesis that the discrete shear zones initiated on antecedent fractures. Fluids would have preferentially migrated through fractures which provided more porosity and permeability than the surrounding rock. The rock adjacent to the fractures, and therefore adjacent to the fluid flow paths, would have undergone more interaction with the penetrating fluid than the rock further away, a relationship that seems to be very well exemplified in the data from sample SCM-17. The quartz present in the rock adjacent to the fractures consequently would have undergone a greater degree of hydrolytic weakening, and strain would likely have been preferentially accommodated by this weakened phase. Hydrolytic weakening of quartz, therefore, likely played a key role in the localization of strain into the discrete zones.

6.3.2 The Role of Fluid-rock Interaction on Shear Zone Morphology

The discrete shear zones with the central epidote vein, bleached halo, and flanking paired shear zones morphology yield a significantly greater average water content (600 ppm) than the discrete shear zones without this morphology (310 ppm), indicating that

more water was present in these shear zones during deformation (Table 6.7). This result provides strong evidence that the degree of fluid-rock interaction experienced by the rocks in the shear zones was an important variable in the development of the two different discrete shear zone morphologies. This assertion is consistent with the findings of Mancktelow and Pennacchioni (2005) in their study of similar shear zones in the Alps. These authors concluded that the degree of fluid-rock interaction was the determining factor for whether the discrete shear zones would develop a central vein and bleached halo morphology or whether the shear zones would simply develop symmetrically on both sides of fracture traces. The FTIR data provided here for the samples from the Stone Corral study area indicate quantitatively that greater quantities of fluid were indeed present in the shear zones with the central vein and bleached halo morphology and therefore were likely a requirement for their development. The possibility also exists that differences in fluid chemistry may have played a significant role in the development of the two different shear zone morphologies. However, the metamorphic minerals associated with the shear zones with veins and bleaching (i.e., epidote, titanite, apatite, and non-symplectic oligoclase and myrmekite replacement products) are also present in the other discrete shear zones, but to a much lesser degree. This observation also suggests that the amount of fluid may have been more responsible for the differing morphologies than a difference in the chemistry of the fluids.

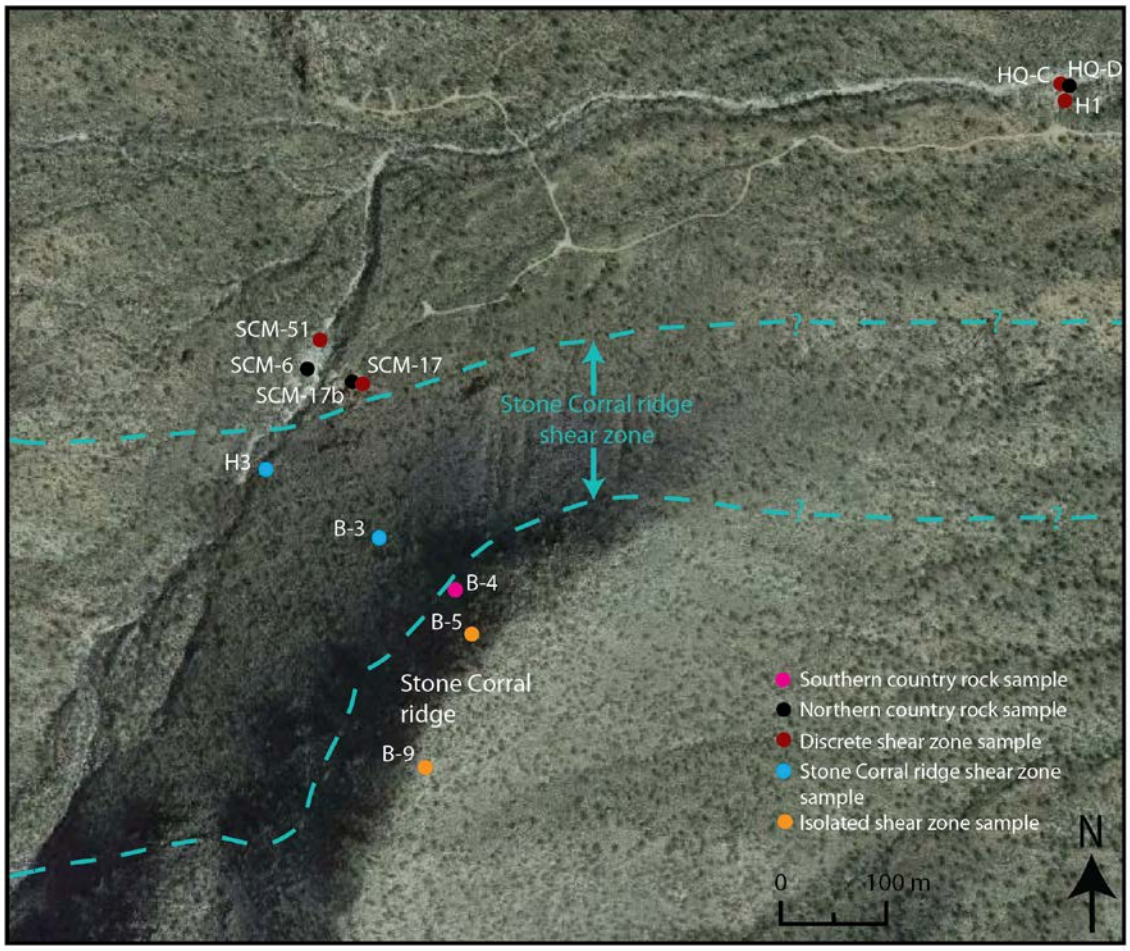

Figure 6.1: Areal photograph of the Stone Corral study area with locations of samples plotted that were used for FTIR spectroscopy (photograph from Google Earth).

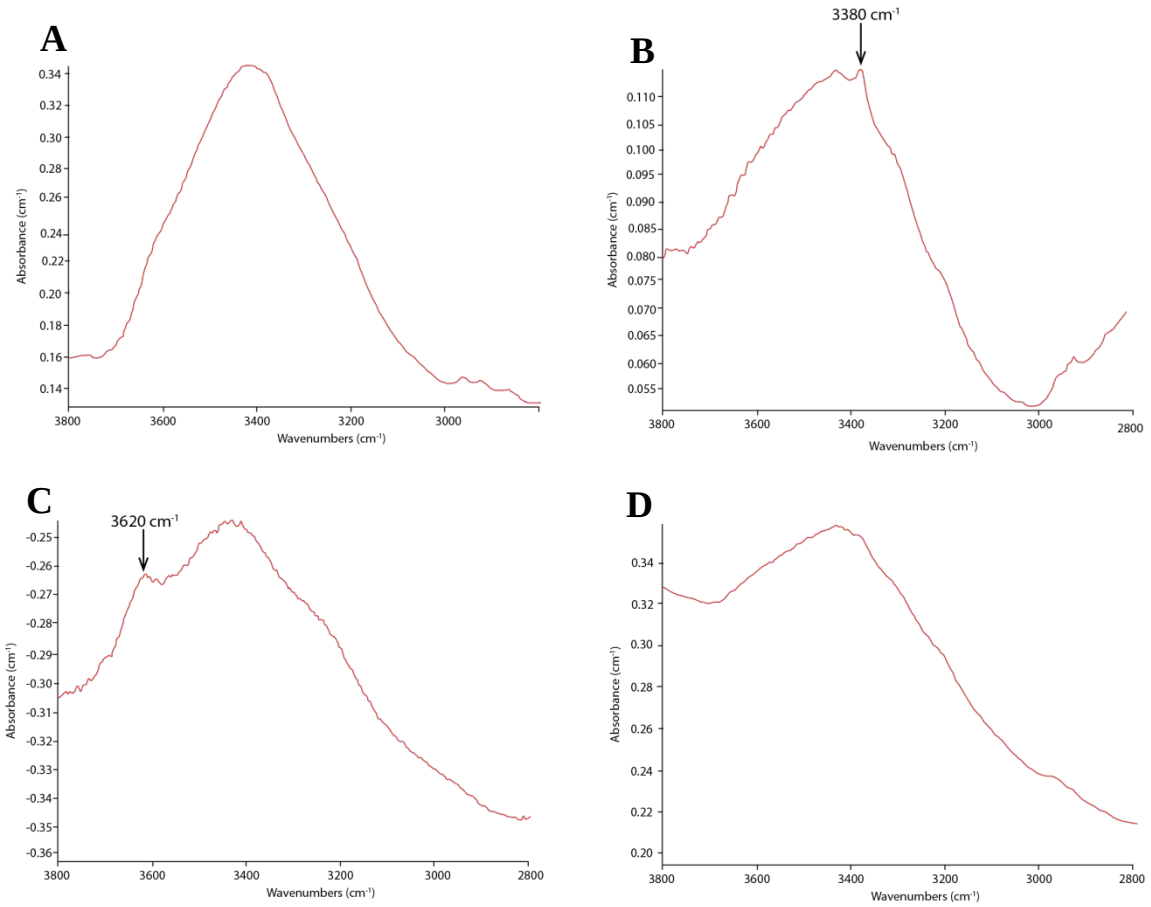

Figure 6.2: Features of FTIR spectral peaks. Absorbances have not been normalized for sample point thicknesses. See Appendix A for all spectral peaks. A) Smooth, broad bell-shaped curve with a mid-point around 3400 cm^{-1}, typical of molecular water; country rock sample B-4; B) A smaller peak at 3380 cm^{-1} is superimposed on the larger, molecular water peak, and may be related to aluminum substitution (Kronenberg, 1994 and references therein); Stone Corral ridge shear zone sample B-3; C) A smaller peak at 3620 cm^{-1} is superimposed on the larger, molecular water peak, and may be related to the presence of fine grained mica; discrete shear zone sample H1; D) Spectrum has a sloping background due to internal defects in the quartz grain and/or scattering losses at the surface of the sample; country rock sample SCM-6.

Sample	Spectrum	Thickness (cm)	Peak Integrated Absorbance (cm^{-1})	Water Concentration ($H:10^6$ Si)	Water Content (ppm)	Sample	Spectrum	Thickness (cm)	Peak Integrated Absorbance (cm^{-1})	Water Concentration ($H:10^6$ Si)	Water Content (ppm)
HQ-D μ = 1200 H:10^6 Si (180 ppm), σ = 1100	1	0.019	48.929	2090	310	SCM-17b μ = 830 H:10^6 Si (150 ppm), σ = 890	1	0.015	9.728	530	80
	2	0.018	51.009	2300	340		2	0.010	33.802	2740	410
	3	0.016	7.594	390	60		3	0.017	9.178	440	70
	4	0.017	7.918	380	60		4	0.015	0.000	0	0
	5	0.018	13.097	590	90		5	0.020	19.156	780	120
	6	0.017	16.812	800	120		6	0.022	46.815	1730	260
	7	0.013	15.292	960	140		7	0.006	13.641	1850	280
	8	0.009	8.167	730	110		8	0.014	1.067	60	10
	9	0.009	44.922	4050	610		9	0.015	3.679	200	30
	10	0.006	5.366	730	110		10	0.011	8.736	640	100
	11	0.012	40.809	2760	410		11	0.012	2.051	140	20
	12	0.017	7.286	350	50	SCM-6 μ = 1090 H:10^6 Si (160 ppm), σ = 470	1	0.027	34.415	1030	150
	13	0.013	19.208	1200	180		2	0.028	49.935	150	20
	14	0.014	5.532	320	50		3	0.027	27.004	810	120
	15	0.016	7.583	380	60		4	0.029	27.269	760	110
B-4 μ = 1080 H:10^6 Si (160 ppm), σ = 670	1	0.028	53.564	1550	230		5	0.029	35.599	1000	150
	2	0.019	11.7808	500	75		6	0.029	57.115	1600	240
	3	0.021	51.4566	1990	300		7	0.027	43.784	1320	200
	4	0.027	15.274	460	70		8	0.027	20.9568	630	90
	5	0.025	19.6112	640	100		9	0.027	21.7594	650	100
	6	0.027	51.137	1540	230		10	0.028	50.802	1470	220
	7	0.028	15.561	450	70		11	0.020	32.221	1310	200
	8	0.028	16.9395	490	70		12	0.026	57.359	1790	270
	9	0.025	19.4117	630	90		13	0.029	23.1737	650	100
	10	0.025	26.197	850	130		14	0.029	56.670	1590	240
	11	0.026	74.026	2310	350		15	0.025	46.864	1520	230
	12	0.026	51.276	1600	240						

Table 6.1: FTIR spectroscopy point absorbance measurements, thickness measurements, and calculated water contents for the interiors of quartz grains in the country rock samples. The mean water concentration (μ) and standard deviation (σ) are reported for each sample.

Sample	Spectrum	Thickness (cm)	Peak integrated absorbance (cm^{-1})	Water concentration ($H:10^6$ Si)	Water content (ppm)
*SCM-17 μ = 1780 $H:10^6$ Si (270 ppm), σ = 1110	1	0.008	23.940	2430	360
	2	0.006	8.3425	1130	170
	3	0.007	47.643	5530	830
	4	0.008	12.4411	1260	190
	5	0.008	26.7661	2720	410
	6	0.010	17.7934	1440	220
	7	0.012	22.6637	1530	230
	8	0.012	31.7517	2150	300
	9	0.012	25.8643	1750	260
	10	0.010	19.8522	1610	240
	11	0.011	14.8359	1100	160
	12	0.008	25.0791	2550	380
	13	0.006	1.7691	240	40
	14	0.008	11.4995	1170	180
	15	0.013	11.628	730	110
	16	0.012	13.4883	910	140
	17	0.014	32.2305	1870	280
	18	0.019	48.087	2060	310
	19	0.014	29.4257	1710	260
H1 μ = 2260 $H:10^6$ Si (340 ppm), σ = 1630	1	0.011	20.588	1520	230
	2	0.012	43.910	2970	450
	3	0.013	13.105	820	120
	4	0.013	16.167	1010	150
	5	0.006	32.116	4350	650
	6	0.014	31.744	1840	280
	7	0.006	13.209	1790	270
	8	0.006	37.526	5080	760
	9	0.014	11.642	680	100
	10	0.007	40.440	4690	700
	11	0.012	7.398	500	70
	12	0.014	31.865	1850	280

*A categorization of these values and additional values for sample SCM-17 are listed in Table 6.6.

Table 6.2: FTIR spectroscopy point absorbance measurements, thickness measurements, and calculated water contents for the interiors of quartz grains in mylonites from the discrete shear zones without the central vein, bleached halo, and flanking paired shear zones morphology. The mean water concentration (μ) and standard deviation (σ) are reported for each sample.

Sample	Spectrum	Thickness (cm)	Peak integrated absorbance (cm-1)	Water concentration (H:10^6 Si)	Water content (ppm)
SCM-51 μ = 4530 H:10^6 Si (680 ppm), σ = 3440	1	0.012	32.821	2220	330
	2	0.006	59.757	8090	1210
	3	0.008	87.546	8890	1330
	4	0.014	39.332	2280	340
	5	0.017	38.571	1840	280
	6	0.006	88.128	11930	1790
	7	0.014	17.283	1000	150
	8	0.009	73.302	6610	990
	9	0.013	33.435	2090	310
	10	0.010	93.137	7560	1130
	11	0.012	43.452	2940	440
	12	0.011	57.554	4250	640
	13	0.011	14.483	1070	160
	14	0.014	45.614	2650	400
HQ-C μ = 3410 H:10^6 Si (510 ppm), σ = 2540	1	0.007	11.841	1370	210
	2	0.010	8.633	700	100
	3	0.010	0.000	0	0
	4	0.010	16.404	1330	200
	5	0.012	25.752	1740	260
	6	0.008	34.435	3500	520
	7	0.007	22.469	2610	390
	8	0.014	90.287	5240	790
	9	0.012	114.772	7770	1160
	10	0.010	59.414	4820	720
	11	0.010	28.287	2300	340
	12	0.013	13.496	840	130
	13	0.011	121.316	8960	1340
	14	0.015	24.330	1320	200
	15	0.008	23.637	2400	360
	16	0.008	46.963	4770	720
	17	0.008	12.635	1280	190
	18	0.015	28.741	1560	230
	19	0.014	19.851	1150	170
	20	0.006	48.708	6590	990
	21	0.005	17.503	2840	430
	22	0.007	63.316	7340	1100
	23	0.007	51.423	5970	900
	24	0.009	68.479	6180	930
	25	0.012	40.676	2750	410

Table 6.3: FTIR spectroscopy point absorbance measurements, thickness measurements, and calculated water contents for the interiors of quartz grains in mylonites from the discrete shear zones with the central vein, bleached halo, and flanking paired shear zones morphology. The mean water concentration (μ) and standard deviation (σ) are reported for each sample.

Sample	Spectrum	Thickness (cm)	Peak integrated absorbance (cm-1)	Water concentration (H:10^6 Si)	Water content (ppm)
H3 μ = 900 H:10^6 Si (130 ppm), σ = 830	1	0.011	2.2109	160	20
	2	0.011	1.7838	130	20
	3	0.010	5.9699	480	70
	4	0.010	5.7404	470	70
	5	0.012	11.470	780	120
	6	0.011	38.905	2870	430
	7	0.011	23.0258	1700	250
	8	0.012	11.1919	760	110
	9	0.010	14.7598	1200	180
	10	0.010	23.3184	1890	280
	11	0.009	3.799	340	50
	12	0.009	0.2461	20	<10
	13	0.011	12.5834	930	140
B-3 μ = 660 H:10^6 Si (100 ppm), σ = 510	1	0.120	13.379	90	10
	2	0.150	6.133	30	<10
	3	0.009	5.392	490	70
	4	0.007	4.683	540	80
	5	0.010	11.498	930	140
	6	0.012	5.205	350	50
	7	0.011	11.817	870	130
	8	0.009	17.423	1570	240
	9	0.007	13.363	1550	230
	10	0.009	5.021	450	70
	11	0.011	10.028	740	110
	12	0.010	3.202	260	40

Table 6.4: FTIR spectroscopy point absorbance measurements, thickness measurements, and calculated water contents for the interiors of quartz grains in the mylonites from the Stone Corral ridge shear zone. The mean water concentration (μ) and standard deviation (σ) are reported for each sample.

Sample	Spectrum	Thickness (cm)	Peak integrated absorbance (cm-1)	Water concentration (H:10^6 Si)	Water content (ppm)
B-5 μ = 670 (100 ppm), σ = 330	1	0.011	11.5192	850	130
	2	0.012	15.1321	1020	150
	3	0.016	1.3936	70	10
	4	0.016	13.049	660	100
	5	0.016	10.2423	520	80
	6	0.015	10.913	590	90
	7	0.018	22.396	1010	150
B-9 μ = 830 (120 ppm), σ = 760	1	0.040	39.975	810	120
	2	0.041	10.3595	210	30
	3	0.038	34.269	730	110
	4	0.032	30.659	780	120
	5	0.032	34.783	880	130
	6	0.041	12.707	250	40
	7	0.037	3.6941	80	10
	8	0.054	107.241	1610	240
	9	0.049	177.165	2940	440
	10	0.049	43.200	720	110
	11	0.051	19.685	310	50
	12	0.048	11.750	200	30
	13	0.048	89.081	1510	230
	14	0.049	8.0448	130	20
	15	0.049	73.362	1220	180

Table 6.5: FTIR spectroscopy point absorbance measurements, thickness measurements, and calculated water contents for the interiors of quartz grains in the mylonites from the isolated shear zones. The mean water concentration (μ) and standard deviation (σ) are reported for each sample.

Relative strain	Spectrum	Thickness (cm)	Peak integrated absorbance (cm-1)	Water concentration (H:10^6 Si)	Water content (ppm)
*High μ = 2610 H:10^6 Si, (390 ppm) σ = 1770	1	0.008	23.940	2430	360
	2	0.006	8.3425	1130	170
	3	0.007	47.643	5530	830
	4	0.008	12.4411	1260	190
	5	0.008	26.7661	2720	410
*Intermediate μ = 1490 H:10^6 Si (220 ppm), σ = 610	6	0.010	17.7934	1440	220
	7	0.012	22.6637	1530	230
	8	0.012	31.7517	2150	300
	9	0.012	25.8643	1750	260
	10	0.010	19.8522	1610	240
	11	0.011	14.8359	1100	160
	12	0.008	25.0791	2550	380
	13	0.006	1.7691	240	40
	14	0.008	11.4995	1170	180
	15	0.013	11.628	730	110
	16	0.012	13.4883	910	140
	17	0.014	32.2305	1870	280
	18	0.019	48.087	2060	310
	19	0.014	29.4257	1710	260
Low μ = 1310 H:10^6 Si (200 ppm), σ = 930	20	0.010	21.469	1740	260
	21	0.020	59.581	2420	360
	22	0.018	6.342	290	40
	23	0.008	5.8841	600	90
	24	0.023	64.028	2260	340
	25	0.022	66.564	2460	370
	26	0.008	1.9675	200	30
	27	0.009	33.2717	3000	450
	28	0.011	26.6925	190	30
	29	0.010	24.531	1990	300
	30	0.009	3.1662	290	40
	31	0.021	16.2701	630	90
	32	0.022	22.8658	840	130
	33	0.022	33.5649	1240	190
	34	0.013	4.434	280	40
	35	0.014	29.6669	1720	260
	36	0.018	26.7543	1210	180
	37	0.016	42.694	2170	330

*These values are also listed in Table 6.2.

Table 6.6: FTIR spectroscopy point absorbance measurements, thickness measurements, and calculated water contents for quartz grain interiors in sample SCM-17. The data are categorized by relatively high strain (grains in the central part of the shear zone), intermediate strain (grains in the boundary area of the shear zone), and low strain (country rock foliation immediately adjacent to the shear zone). The mean water concentration (μ) and standard deviation (σ) are reported for each category.

Sample Category	Sample Name	Average water content (ppm)	Average water content for category (ppm)
Country rock	B-4	160	160 ppm
	HQ-D	180	
	SCM-6	160	
	SCM-17b	150	
Discrete shear zone (without central vein and bleached halo morphology)	H1	340	310 ppm
	SCM-17	270	
Discrete shear zone (with central vein and bleached halo morphology)	SCM-51	680	600 ppm
	HQ-C	510	
Stone Corral ridge shear zone	H3	130	120 ppm
	B-3	100	
Isolated shear zone	B-5	100	110 ppm
	B-9	120	

Total discrete shear zone average: 450 ppm

Table 6.7: Summary of average intragranular quartz water contents in individual samples and sample categories. Water content is much higher in quartz in the discrete shear zone mylonites than in the other sample categories. The discrete shear zones with the central vein, bleached halo, and flanking paired shear zones morphology have more water in quartz than the discrete shear zones without this morphology.

Chapter 7: Stable Isotope Analysis

Oxygen isotope analysis was conducted on quartz and feldspar in many samples throughout the study area, including samples from the country rocks, the discrete shear zones, the Stone Corral ridge shear zone, and the isolated shear zones on the crest of Stone Corral ridge. Oxygen stable isotope analysis was also conducted on epidote from the central epidote vein in the discrete shear zone sample, SCM-51 (Figures 2.9D-F; 3.11A-B, D), and on metamorphic epidote in the country rock sample, SCM-6 (Figures 3.3A-B, 3.4A). The analyses were conducted to determine 1) which rocks in the study area had undergone fluid infiltration, 2) the source(s) of the fluid(s) affecting the rocks, 3) any isotopic variations among the rocks, and 4) the nature of fluid flow in the area (i.e., channelized or pervasive flow).

An understanding of the fluid flow history in the study area is important for a number of reasons. Because the samples in the study area are all composed of granite, any significant isotopic depletion in only some of the samples (e.g., the greenschist facies mylonites from the isolated shear zones on the crest of Stone Corral ridge) would indicate that those samples likely underwent deformation at a different time than the others. In addition, determining the source of the shear zone fluid is helpful in testing the hypothesis that the shear zones formed during metamorphic core complex (MCC) deformation. A meteoric source of fluid would provide evidence for MCC deformation, whereas an igneous and/or metamorphic source of fluid would provide evidence for Late Cretaceous deformation (see section 7.3.2). The isotopic analyses of the discrete shear zones affected by veining and/or bleaching, therefore, are especially important because these shear zones were clearly infiltrated with a significant amount of fluid that likely affected the isotopic compositions of the minerals.

Additionally, quartz-feldspar and quartz-epidote geothermometry were performed on a couple of discrete shear zone samples in an effort to obtain an estimate of the mylonitization temperature. The temperatures yielded by the analyses, however, are likely quartz closure temperatures rather than deformation temperatures. The geothermometry methods and data are presented and further discussed in Appendix B.

7.1 METHODS

7.1.1 Sample Selection

Oxygen isotope analysis was performed on quartz and feldspar in eight samples from the Stone Corral study area (Figure 7.1). Three of the samples were collected from the country rock, two of which (H2 and SCM-6; Figure 1.4D) were collected from the northern part of the study area, and one of which (B-4) was collected from the southern part of the study area near the crest of Stone Corral ridge. Three of the samples were collected from discrete shear zones in the northern part of the study area. One of these samples (H1; Figure 1.4D) was collected from a shear zone without the central vein, bleached halo, and flanking paired shear zones morphology, whereas another sample (SCM-51; Figures 1.5E-F; 2.9D-F) was collected from the bleached halo portion of a shear zone with this unique morphology. The third sample (HQ-B) was collected from the mylonitic portion of a shear zone that displayed a less deformed bleached section flanked by a mylonite zone, but did not contain any veins. One sample (B-3) was collected from the Stone Corral ridge shear zone, and another sample (B-9) was collected from one of the isolated shear zones on the crest of Stone Corral ridge in the southern part of the study area. Oxygen isotope analysis was also performed on epidote from two of the samples. The epidote grains analyzed were collected from the central epidote vein of sample SCM-51 and from the scattered epidote grains in sample SCM-6, which was

the least deformed of the country rock samples collected in the northern part of the study area.

7.1.2. Sample Preparation and Analytical Methods

The samples were cut into hand-sized slabs, crushed with a mortar and pestle, and run through sieves with grid sizes of 2 mm, 1 mm, 710 μm, 500 μm, 355 μm, and 125 μm. Mineral separates were then handpicked under a binocular stereo microscope. Most grains picked ranged in size from 355 μm to 710 μm. Grains were immersed in a petri dish filled with ethanol, and were broken apart and scraped clean by hand with a tungsten needle until all visible mineral coatings and inclusions were removed.

The sample grains were then analyzed in a ThermoElectron MAT 253 stable isotope mass spectrometer located in the Department of Geological Sciences at the University of Texas at Austin. The spectrometer is equipped with a laser fluorination oxygen extraction line, a BrF_5 vacuum extraction system, and a series of NaCl and liquid nitrogen traps. The sample was heated by an infrared laser in a chamber with purified BrF_5 which resulted in the liberation of the oxygen in the sample in a gaseous form. The gas was then filtered through the NaCl and liquid nitrogen traps for purification, amassed onto a 5 angstrom molecular sieve, and measured with a precision of ±0.05-0.06‰. Quartz and garnet standards were analyzed both before and after the sample analyses to confirm the analyses were valid. The $\delta^{18}O$ values were calculated relative to V-SMOW.

7.2 RESULTS

7.2.1 Quartz and Feldspar Oxygen Isotopes

The oxygen isotope results for the quartz and feldspar grains in all the samples are listed in Tables 7.1 and 7.2 and plotted in Figure 7.2. In three of the samples (country rock sample, SCM-6, and discrete shear zone samples, SCM-51 and HQ-B), feldspar

grains underwent an unknown reaction within the chamber and turned a banana yellow color. These samples were analyzed first, and the error associated with them has been increased to ±0.25‰ to compensate for the uncertainties associated with the causes and effects of this reaction. The quartz grains in two of the samples (discrete shear zone sample, H1, and Stone Corral ridge shear zone sample, B-3) left behind a residual white powder after heating, which indicates that the grains were contaminated, possibly by internal small inclusions of a separate mineral. The existence of a small peak at 3620 cm^{-1} in many of the FTIR spectral peaks obtained from the quartz in the mylonitic samples suggests that sub-optical mica flakes may have been present in the quartz (see Section 6.2.1). If mica inclusions were unknowingly incorporated in the quartz stable isotope analyses, the resulting isotopic values would be lowered. One of the two contaminated samples did provide the lowest quartz $\delta^{18}O$ values, but the other sample provided the highest value.

The oxygen $\delta^{18}O$ values of the quartz in the samples range from 8.51±0.05 to 9.68±0.05‰, whereas the values of the feldspars range from 6.48±0.25‰ to 8.15±0.05‰. The isotopic values for the country rock samples overlap with those from the mylonitic samples; no discernible difference exists between the two groups (Figure 7.2). Although the quartz $\delta^{18}O$ values of the two contaminated samples, HQ-B and H1, are slightly lower and slightly higher than the other samples, respectively, no significant differences are apparent among the mylonitic samples collected from the discrete shear zones, the Stone Corral ridge shear zone, and the isolated shear zones near the crest of the mountain (Figure 7.1).

7.2.2 Epidote Oxygen Isotopes

The $\delta^{18}O$ values of the epidote mineral separates from the country rock sample (SCM-6) and the discrete shear zone mylonite sample (SCM-51) are radically different (Table 7.2). For sample SCM-51, in which the separates analyzed were acquired from the central deformed epidote vein, the $\delta^{18}O$ value was 4.83±0.06‰. For sample SCM-6, in which the separates analyzed were isolated grains scattered throughout the sample, the $\delta^{18}O$ value was 2.57±0.06‰.

7.3 FLUID HISTORY

All of the $\delta^{18}O$ values, even those from the contaminated samples, are within the ranges of values expected for quartz and feldspar in igneous rocks (~5-15‰; Taylor, 1968; Taylor and Sheppard, 1986). Igneous rocks, however, rarely preserve the magmatic crystallization values, but instead record other geologic phenomena that affected the rocks. Original oxygen isotopic crystallization values are preserved only if the initial isotopic equilibrium among the phases is maintained through cooling, which is extremely unlikely to occur unless the rock is quenched (Giletti, 1986). Additionally, this equilibrium must be maintained through all subsequent processes that act on the rock, including any metamorphism and deformation. Thus, the $\delta^{18}O$ values of plutonic rocks more likely will provide information on the compositions of infiltrating fluids (Taylor, 1973; Taylor, 1990; Wickham and Taylor, 1990), temperatures of deformation (O'Hara et al., 1997), cooling rates of plutons (Crowley and Giletti, 1983), or rates of denudation and uplift (Giletti, 1986). The oxygen stable isotope analyses in this study were conducted to gain information on these types of secondary processes.

7.3.1 Isotopic Evidence for Fluid Infiltration

7.3.1.1 Subvertical Distribution of Quartz and Feldspar Isotopic Data in δ-δ Space

The data for quartz-feldspar mineral pairs have been plotted in Figure 7.2 with the $\delta^{18}O$ of quartz, the lower exchange rate mineral, on the x-axis and the $\delta^{18}O$ of feldspar, the higher exchange rate mineral, on the y-axis. The distribution of the data points in δ-δ space may be viewed as a function of the processes that operated during the setting of the oxygen isotopes. If closed system cooling occurred, isotopic exchange among minerals would have continued until closure temperatures were reached without further disruption. In this case, a line fit to the points in δ-δ space would have a negative slope (Gregory and Criss, 1986). Conversely, if open system hydrothermal alteration occurred, the isotopic systematics would have been disrupted, and a line fit to the points in δ-δ space would be steep with a positive slope, indicative of disequilibrium (Gregory et al., 1989). In the case of hydrothermal alteration, the line may be near-vertical during the initial fluid influx, whereas if the event is very long lasting, the slope of the line would gradually rotate to shallower values and approach 45° when equilibrium was reached.

The δ-δ plot of the quartz and feldspar values from the Harquahala country rock samples (H2, SCM-6, and B-4) reveals steep, near vertical slopes (Fig. 7.2). The slopes for the discrete shear zone mylonitic samples from the northern part of the study area (H1, HQ-B, and SCM-51) are similarly steep. The contaminated sample, H1, is plotted further left than the others, but this is likely an artifact of the contamination; quartz is the isotopically heaviest mineral in the granites, so any contamination would shift the isotope composition to lower values. A shift to the right of the data for sample H1 would only better define the steep, subvertical trend of the data points. The other two mylonite samples (Stone Corral ridge shear zone sample, B-3, and isolated shear zone sample, B-9) also plot in the subvertical array, although the value of the quartz in the contaminated

sample, B-3, would likely plot further to the right if the contaminating particles were absent. The subvertical trends of the quartz and feldspar data in δ-δ space for both the mylonitic samples and the country rock samples suggest that the rocks were affected by open system hydrothermal alteration, either by meteoric waters (Gregory et al., 1989) or by deeper metamorphic or igneous waters (Žák et al., 2005).

The disequilibrium conditions produced during fluid influx in granitic rocks commonly result in variations in $\Delta_{Qtz\text{-}Fsp}$ oxygen isotope values among samples. These variations are characterized by relatively similar $\delta^{18}O$ quartz values among the samples and by wider variation in $\delta^{18}O$ feldspar values among the samples (Gregory et al., 1989). In the Harquahala samples, if the outlier $\Delta_{Qtz\text{-}Fsp}$ value of 0.36‰ from the contaminated sample, H1, is ignored, the $\Delta_{Qtz\text{-}Fsp}$ values display a wide range from 1.35‰ to 2.62‰ (Table 7.2). A 1.7‰ difference exists between the highest and lowest feldspar $\delta^{18}O$ values, whereas only a 0.45‰ difference exists between the highest and lowest $\delta^{18}O$ quartz values if the two contaminated quartz samples are ignored. These variations are significant, and suggest that the feldspar in the samples underwent oxygen isotopic exchange with another phase at a temperature that was low enough that quartz was closed to exchange. The feldspar may have exchanged with another mineral phase (e.g., biotite), but likely also exchanged with a fluid phase.

The quartz $\delta^{18}O$ values of the Stone Corral samples, which range from 8.51-9.68‰, are lower than the values typically reported for unaltered S-type granites, which range from 9.5-11.4‰ (Harris et al., 1997). This departure from normal values further indicates that post-magmatic crystallization fluids likely had an influence on isotopic exchanges. Furthermore, the overlapping quartz and feldspar $\delta^{18}O$ arrays in δ-δ space for the mylonitic samples and the country rock samples suggest that this exchange occurred pervasively, both inside and outside of the shear zones. Thus, both the deformed country

rock and the cross-cutting shear zones were likely infiltrated by fluids from similar sources.

7.3.1.2 Discrepancies in Epidote Oxygen Isotope Data

Metamorphic epidote was analyzed in a country rock sample (SCM-6) and vein epidote was analyzed in a discrete shear zone sample (SCM-51) to compare the chemistry of these two different forms of epidote and thus determine whether they formed in the presence of fluids from the same or different sources. The large difference in epidote oxygen isotope values between the two samples is significant if accurate. Unfortunately, the analysis of the epidote from sample SCM-6 may have been contaminated. The epidote in this sample was very fine grained and because much of the epidote was symplectic in nature, the grains were intertwined with other minerals. Some of the grains had a thin coating of hematite as well. Great care was taken to remove any trace of the other minerals, but once this removal was complete, the grain size of the epidote was so small it could hardly be seen by the naked eye, which introduces the possibility that remnants of other minerals that were too small to be visible may have been present during analysis. Remnants of quartz and feldspar would have raised the $\delta^{18}O$ epidote value and reduced the Δquartz-epidote value, whereas remnants of hematite would have lowered the $\delta^{18}O$ epidote value and increased the Δquartz-epidote value.

On the other hand, the $\delta^{18}O$ value of the feldspar was also lower in sample SCM-6 than in all of the other samples analyzed. This result may suggest that the sample was out of isotopic equilibrium. The subvertical array of the quartz and feldspar $\delta^{18}O$ data in δ-δ space for the three country rock samples also suggests the country rock oxygen isotope system was out of equilibrium, likely as a result of fluid infiltration. In this case, the

lower epidote $\delta^{18}O$ value would not be as unusual. Unfortunately, not enough data was collected to test these two hypotheses.

7.3.2 Source of the Fluid

The quartz and feldspar oxygen isotope data imply that hydrothermal alteration affected both the country rocks and the mylonites. The presence of fluid during mylonitization of the discrete shear zones is also strongly suggested by the morphology of the mylonites with central veins and bleached haloes, the petrographic characteristics of the mylonites (e.g., the presence of synkinematic myrmekite and non-symplectic oligoclase replacement products, and the widespread BLG recrystallization or neocrystallization of feldspar), and the FTIR water content analyses. The quartz and feldspar oxygen isotope data indicate that the source of the fluid present during deformation must have been igneous or metamorphic water as meteoric water is isotopically light. Meteoric water would have depleted the isotopic values of the feldspar, particularly in the heavily fluid-infiltrated grains of the discrete shear zones with the central veins and bleached haloes which clearly underwent significant interaction with the fluids. The oxygen isotope value of the vein epidote in sample SCM-51 is within the range of values for magmatic and metamorphic epidote in plutonic rocks (Keane and Morrison, 1997; Ferreira et al., 2003; Morrison, 2004), and is therefore also consistent with an igneous or metamorphic source for the parent fluid.

The identification of an igneous or metamorphic source of the fluids is significant as it helps to constrain the structural and metamorphic setting that may have been responsible for the formation of the shear zones. In particular, the data help to determine if a metamorphic core complex setting is an appropriate interpretation for the formation of the shear zones. Two different models have been proposed for the nature of fluid-rock

interaction during MCC extension and unroofing. Fricke et al. (1992) proposed a model in which meteoric water penetrates both the upper and the lower plate of the MCC, potentially percolating to depths of greater than 10 kilometers during deformation by the mechanisms of seismic pumping and dilatancy pumping. The isotope data of the present study, however, exclude the possibility of syn-kinematic meteoric water penetration in the Harquahala rocks during development of the discrete shear zones.

Reynolds and Lister (1987) proposed an alternative two-fluid system model, in which the upper plate (i.e., hanging wall) of a core complex interacts with meteoric and connate fluids at near-hydrostatic conditions during deformation while the lower plate (i.e., footwall) of a MCC is affected by deep-seated igneous fluids at high fluid pressure conditions during deformation. In this model, the deep-seated igneous fluids are sourced from plutons and travel up the lower plate shear zone into the upper plate detachment fault to lower pressure, lower temperature, and more porous conditions, whereas the upper plate fluids do not travel down the fault or infiltrate the lower plate ductile shear zones. Other MCCs in California and Arizona provide examples of this model, including the Whipple Mountains, Picacho Mountains, and South Mountains MCCs (Kerrich et al., 1984; Smith and Reynolds, 1985; Kerrich and Rehrig, 1987, Smith et al., 1991; Morrison, 1994). However, deformation in these MCCs occurred shortly after the intrusion of Tertiary plutons, which would have provided a source for the magmatic fluids that have been inferred to have been present during footwall deformation. Conversely, in the Harquahala MCC, no Tertiary plutons are exposed. Unless a pluton is unexposed at depth, no magmatic fluid source would have been available to interact with the shear zones during MCC deformation.

The other possible source for the fluids, metamorphism, also would not be compatible with the shear zones forming during MCC deformation as the rocks in the

MCCs of the Whipple detachment system and the other detachment systems in Arizona experienced prograde metamorphism during the Late Cretaceous and/or Early Tertiary, and therefore the fluids that would have been released through metamorphism would have dissipated substantially earlier than the initiation of Miocene MCC mylonitization. Additionally, because retrograde metamorphism is prevalent during MCC deformation, fluid is absorbed in hydration reactions rather than released (Reynolds and Lister, 1988). Therefore, no metamorphic fluid source would have been available during the deformation of the Harquahala MCC.

If the shear zones instead formed during the Late Cretaceous (also see Chapter 8) then both an igneous and a metamorphic fluid source may have been available. The extensive Late Cretaceous plutonism in the northeastern portion of the range could have provided the source for igneous waters, whereas prograde metamorphism at deeper levels may have provided the source for metamorphic waters. The Brown's Canyon granite, which hosts many of the shear zones in the study area, yielded a zircon crystallization age of ~75.5 Ma (see Chapter 8). A sample of the granite ~1.5 km to the southwest of the study area yielded a younger zircon crystallization age of ~65 Ma, and a sample another ~5.5 km further to the southwest yielded an age of ~67 Ma (Michael Prior, unpublished data). These ages suggest that the Late Cretaceous plutonism in the Harquahala Mountains was a protracted event. The crystallization of the nearby younger bodies of Late Cretaceous granite could have provided the fluids that facilitated the metamorphism in the study area.

Conversely, the fluids may have had a metamorphic origin and been sourced from rocks at greater depth. Although the fluid-rich metamorphic event that affected the granite in the study area occurred shortly after peak metamorphism (Richard, 1988), the fluid-rich metamorphism may have been synchronous with peak metamorphism of rocks

at depth. In a region affected by crustal thickening, such as the Maria Fold and Thrust Belt, deeper levels of the crust commonly experience peak metamorphism later than do shallower levels of the crust if uplift occurs synchronously with or shortly succeeds the thickening (Stüwe, 1998). Volatiles released by dehydration reactions during peak metamorphism in the deeper crust will migrate to shallower levels, and therefore a post-peak metamorphic fluid infiltration event may be recorded in the rocks. This infiltration event, which may leave a retrograde metamorphic overprint on the rocks, is simply a later stage of one protracted metamorphic event. In actively deforming structural settings undergoing this history, the fluids will likely be channelized along shear zones (Clark et al., 2005).

7.3.3 Pervasive vs. Channelized Fluid Flow

In the nearby Little Harquahala Mountains (Figure 1.1), a Late Cretaceous fluid-rich metamorphic event has also been recognized. The Rb-Sr whole rock isochron ages of early Cretaceous (166 ± 11 Ma) volcanic rocks of various compositions were reset at 70 ± 3 Ma (Asmerom et al., 1991). The homogeneous resetting of the ages in all of the samples implies that fluid-rich metamorphic conditions must have prevailed at ~70 Ma, and that fluid flow must have been pervasive. This timing is identical to the timing of the fluid-assisted metamorphism of the Stone Corral study area (Richard, 1988; Chapter 8 of this study), and the isotopic resetting of the rocks in the Little Harquahala Mountains may be a shallower level expression of the same event as the fluids continued to travel upwards to lower temperatures and pressures.

The discrete shear zones in the northern part of the study area clearly underwent greater fluid-rock interaction than the country rock and the Stone Corral ridge shear zone as is indicated by the higher water contents measured by FTIR spectroscopy and the

presence of central veins and bleached haloes in some of the shear zones. However, the overlapping vertical arrays of quartz and feldspar $\delta^{18}O$ values in δ-δ space for the country rocks and the shear zones (Figure 7.2), as well as the hydrous metamorphic mineral assemblages (e.g., biotite, epidote, apatite, and myrmekite) in all the amphibolite-facies samples (i.e., country rock and mylonite) suggest that fluid flow was quite extensive. In conjunction, the available data suggest that fluid flow may have been pervasive during the metamorphism as was the case in the adjacent Little Harquahala Mountains, but that significantly greater volumes of fluid were channelized through the discrete shear zones. If the discrete shear zones reactivated antecedent fractures, the increased porosity and permeability provided by the fractures would easily explain how and why the fluids were channelized.

7.3.4 Summary

The stable isotope data indicate that all the rocks in the study area were infiltrated by fluids from the same source or similar sources as significant isotopic variations are not present among the different types of samples. The fluids affecting the rocks were isotopically heavy, and therefore must have been igneous or metamorphic, rather than meteoric, and likely infiltrated during the Late Cretaceous. Although fluid flow was pervasive in the study area, it was mainly channelized along the discrete shear zones.

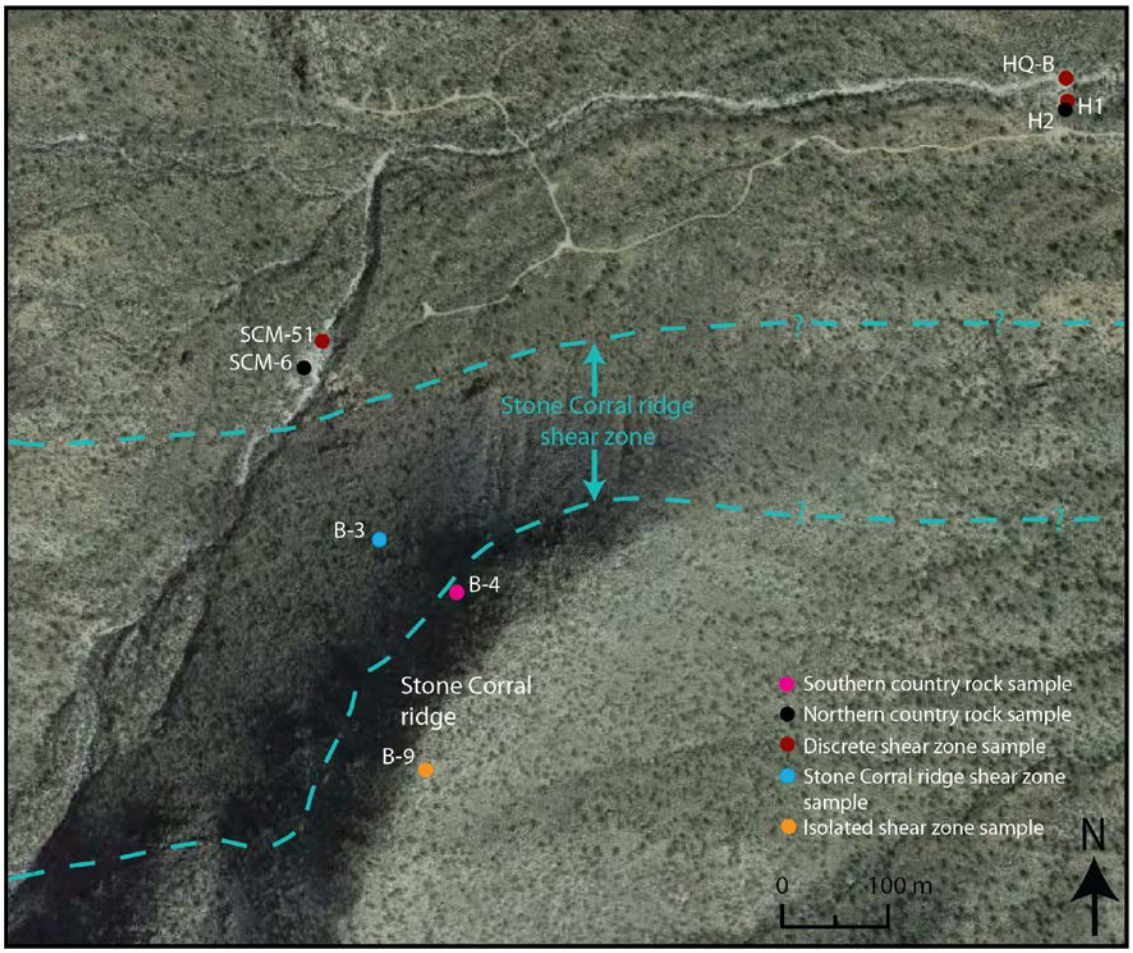

Figure 7.1: Areal photograph of the Stone Corral study area with locations of samples plotted that were used for stable isotope analyses (photograph from Google Earth).

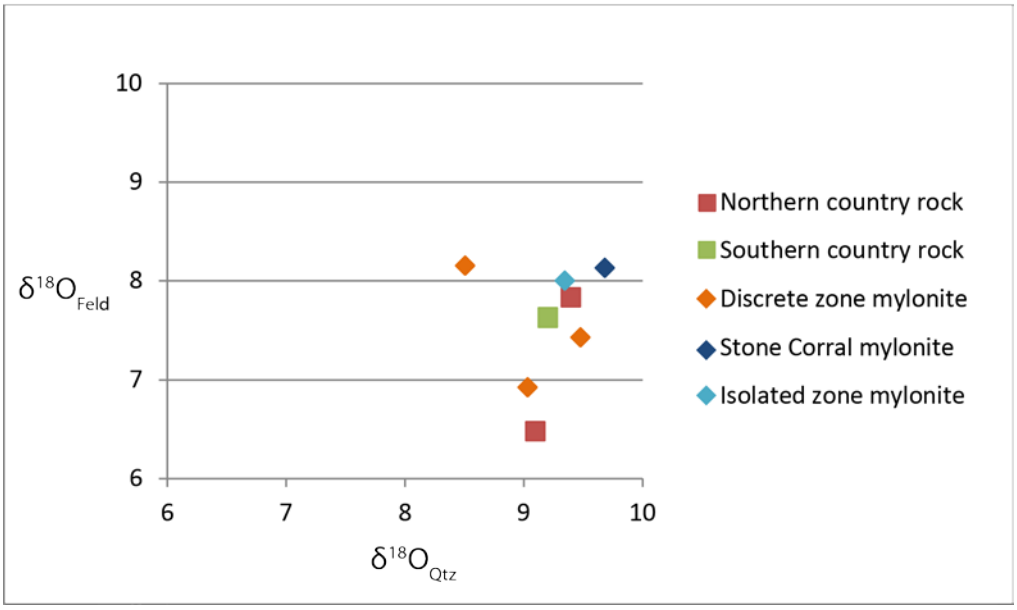

Figure 7.2: Plot of $\delta^{18}O$ quartz and feldspar values for all samples. Both the country rocks and mylonites form subvertical arrays that overlap. The lower quartz value of the outlier discrete shear zone sample is likely in error as it was contaminated, most likely by an isotopically lighter mineral (see text).

Date Analyzed	Sample ID	Type	$\delta^{18}O$-raw (‰)	$\delta^{17}O$-raw (‰)	$\delta^{17}O/d^{18}O$	$\delta^{18}O$ calibrated (‰)	$\delta^{18}O$ error (‰)	Calibrated against
5/14/2012	lausanne-qtz	standard	17.522	9.076	0.5179774	17.908	0.25	UWG-2=5.82‰
5/14/2012	lausanne-qtz	standard	17.551	9.08	0.517349439	17.937	0.25	UWG-2=5.82‰
5/14/2012	lausanne-qtz	standard	17.642	9.134	0.517741753	18.028	0.25	UWG-2=5.82‰
5/14/2012	Gee Whiz-qtz	standard	11.903	6.15	0.516676468	12.289	0.25	UWG-2=5.82‰
5/14/2012	UWG-gt	standard	5.069	2.545	0.502071414	5.455	0.25	UWG-2=5.82‰
5/14/2012	SCM-6-feld	sample	6.092	3.12	0.512147078	6.478	0.25	UWG-2=5.82‰
5/14/2012	SCM-51 feld	sample	6.535	3.333	0.510022953	6.921	0.25	UWG-2=5.82‰
5/14/2012	HQ-B-feld	sample	7.044	3.632	0.515616127	7.43	0.25	UWG-2=5.82‰
5/14/2012	SCM-6-qtz	sample	8.713	4.508	0.517387811	9.099	0.06	UWG-2=5.82‰
5/14/2012	SCM-51 qtz	sample	8.648	4.45	0.514569843	9.034	0.06	UWG-2=5.82‰
5/14/2012	HQ-B qtz	sample	9.093	4.693	0.516111294	9.479	0.06	UWG-2=5.82‰
5/14/2012	SCM-6-epid	sample	2.18	1.121	0.514220183	2.566	0.06	UWG-2=5.82‰
5/14/2012	SCM-51 epid	sample	4.443	2.226	0.501012829	4.829	0.06	UWG-2=5.82‰
5/14/2012	UWG-gt	standard	5.434	2.748	0.505704821	5.82	0.06	UWG-2=5.82‰
12/18/2012	Lausanne-qtz	standard	17.504	9.069	0.518110146	17.672	0.05	UWG-2=5.82‰
12/18/2012	Lausanne-qtz	standard	17.427	9.053	0.519481265	17.595	0.05	UWG-2=5.82‰
12/18/2012	Lausanne-qtz	standard	17.901	9.392	0.524663427	18.069	0.05	UWG-2=5.82‰
12/18/2012	UWG-gt	standard	5.652	2.938	0.519815994	5.82	0.05	UWG-2=5.82‰
12/18/2012	H1-qtz	sample	8.339	4.415	0.529439981	8.507	0.05	UWG-2=5.82‰
12/18/2012	H1-feld	sample	7.981	4.229	0.529883473	8.149	0.05	UWG-2=5.82‰
12/18/2012	H2-qtz	sample	9.229	4.862	0.52681764	9.397	0.05	UWG-2=5.82‰
12/18/2012	H2-feld	sample	7.659	4.072	0.531662097	7.827	0.05	UWG-2=5.82‰
12/18/2012	B3-qtz	sample	9.516	5.025	0.528058008	9.684	0.05	UWG-2=5.82‰
12/18/2012	B3-feld	sample	7.959	4.198	0.527453198	8.127	0.05	UWG-2=5.82‰
12/18/2012	B4-qtz	sample	9.035	4.68	0.517985612	9.203	0.05	UWG-2=5.82‰
12/18/2012	B4-feld	sample	7.458	3.992	0.535264146	7.626	0.05	UWG-2=5.82‰
12/18/2012	B9-qtz	sample	9.178	4.865	0.530071911	9.346	0.05	UWG-2=5.82‰
12/18/2012	B9-feld	sample	7.829	4.192	0.53544514	7.997	0.05	UWG-2=5.82‰
12/18/2012	UWG-gt	standard	5.712	3.021	0.528886555	5.88	0.05	UWG-2=5.82‰

Table 7.1: Raw and calibrated oxygen isotope data for all samples and standards. Key: qtz = quartz, gt = garnet, feld = feldspar, epid = epidote.

Sample	Quartz $\delta^{18}O$ (‰)	Feldspar $\delta^{18}O$ (‰)	Epidote $\delta^{18}O$ (‰)	$\Delta_{Qtz\text{-}Fsp}$ (‰)	$\Delta_{Qtz\text{-}Epid}$ (‰)
H2	9.40±0.05‰	7.83±0.05	-	1.57	-
SCM-6	9.10±0.06‰	6.48±0.25	2.57±0.06	2.62	6.53
B-4	9.20±0.05‰	7.63±0.05	-	1.57	-
H1	8.51±0.05‰	8.15±0.05	-	0.36	-
SCM-51	9.03±0.06‰	6.92±0.25	4.83±0.06	2.11	4.2
HQ-B	9.48±0.06‰	7.43±0.25	-	2.05	-
B-3	9.68±0.05‰	8.13±0.05	-	1.55	-
B-9	9.35±0.05‰	8.00±0.05	-	1.35	-

Table 7.2: Summary table of oxygen isotope data.

Chapter 8: U-Pb Geochronology

U-Pb isotope analysis using a Laser Ablation Inductively Coupled Plasma Mass Spectrometer (LA-ICP-MS) was performed on titanite grains in samples from the country rock in the northern part of the study area, the discrete shear zones, and the Stone Corral ridge shear zone (Figure 8.1). The dating was executed to determine the timing of metamorphism and deformation in each of these categories of rocks. Both cores and rims of the grains were analyzed to document different generations of titanite growth, if present. Additionally, both deformed and undeformed or less deformed grains were analyzed to search for different generations of nucleation and growth of titanite grains. U-Pb isotope analysis was performed on zircon grains in one sample from undeformed granite near the crest of Stone Corral ridge to determine the crystallization age of the granite (Figure 8.1).

8.1 METHODS

8.1.1 Sample Selection

U-Pb isotope analysis of titanite was performed on nine samples from the northern portion of the study area (Figure 8.1). Three of the samples analyzed (SCM-6, SCM-48-2, and HQ-D) were collected from the deformed country rock. Six of the samples analyzed were collected from mylonitic shear zones. Three of these (H1, SCM-12, and SCM-17) come from discrete shear zones without central veins or bleaching (Figure 1.4). Another one of these samples (SCM-51) comes from the bleached halo of a well-developed shear zone with the central vein, bleached halo, and flanking paired shear zones morphology (Figure 1.5E-F). The remaining two samples, a mylonite (H3) and a protomylonite (SCM-19), come from the Stone Corral ridge shear zone. The protomylonite was collected from the gradational northern boundary of the shear zone.

An additional sample (AZSC-6) was collected from the country rock in the southern part of the study area for U-Pb isotope analysis of zircons.

8.1.2 U-Pb Isotopic Analysis

Titanite and zircon grains were analyzed at the University of Texas at Austin using a 193nm ArF Excimer laser ablation system with a Helex cell coupled to an Element 2 high resolution inductively coupled plasma mass spectrometer. Standard titanites (OLT?) and zircons (GJ1) were measured under identical operating conditions, bracketing the samples to correct for instrument drift and downhole elemental fractionation. The titanite grains were analyzed in situ in ~40 micron thick sections. Both cores and rims of grains were analyzed in all samples and multiple points were obtained from many of the grains. The ablation pits measured 30 μm in diameter and ~16 μm deep. Additional analyses were performed with a 20 μm pit size on the rims of many of the grains in three of the samples (H1, H3, and SCM-19). Titanite grain sizes ranged from <100 μm to several mm.

The zircon grains were separated from a crushed rock sample and were mounted on double-sided tape. One 30 μm spot was analyzed per grain. Ablating the unpolished grain surface perpendicular to growth zoning makes it possible to date even thin rims which would be inaccessible on polished grains. Mike Prior prepped this sample and helped with the analyses. Zircon and titanite data were reduced using the program Iolite on an IGOR Pro platform, and ages were calculated and plotted on Tera-Wasserberg diagrams.

8.2 RESULTS

U-Pb isotope data for individual spots from all samples are presented in Tables 8.1-8.10. Ages and other critical information for each sample are summarized in Tables

8.11 and 8.12, and Tera-Wasserburg diagrams are provided in Figures 8.2-8.5. The ages yielded by zircon and titanite U-Pb dating are not concordant due to variable incorporation of common Pb, but the data for most of the samples do yield very linear trends with minimal spread on the Tera-Wasserburg plots.

The ages used in this study are the lower intercept ages in the Tera-Wasserburg diagrams. These diagrams graphically correct for the common lead contribution to the raw data. The lower intercept ages, therefore, provide the radiogenic $^{206}Pb/^{238}U$ ages of the grains, rather than the ages resulting from the combined contributions of both radiogenic lead and differential amounts of common lead incorporated in the grains from a common lead reservoir. These lower intercept ages are interpreted as the ages of crystallization or the ages of the systems' closures to lead (see section 8.3.2).

Importantly, the mean square of the weighted deviates (MSWD) values for the data are >1 for all samples (and in some cases, significantly >1), which indicates the data are over-dispersed. Several possibilities may explain the scatter in the data. The grains may not all be cogenetic. The data may not represent a simple two component mixture of common and radiogenic lead, but may instead include a component of lead inheritance or loss. Lastly, the data spread may be the result of analytical errors. For example, analyses may have incorporated a small amount of material from other phases at depth. Regardless, the data in this study were treated very conservatively and were not filtered.

8.2.1 Whole Sample Ages

The analyses performed on titanite grains produced Late Cretaceous ages with dates that range from ~68-75 Ma. Two of the country rock samples, HQ-D and SCM-6, provided similar ages of 71.0±2.1 Ma (n=20) and 72.0±1.7 Ma (n=12), respectively (Figure 8.2; Table 8.11). The third country rock sample, SCM-48-2, provided an older

age than the other two samples at 75.6±4.0 Ma (n=6), although this age is within the error of the younger ages. The older age and the larger error associated with this sample may be the result of the small number of grains analyzed within the sample (Table 8.11).

The titanite analyses of the discrete shear zone mylonites also yielded Late Cretaceous ages (Figure 8.3; Table 8.11). Three of the samples, H1, SCM-17, and SCM-51, yielded similar ages of 69.1±2.5 Ma (n=28), 67.9±2.4 Ma (n=15), and 70.7±1.7 Ma (n=22), respectively. The fourth sample, SCM-12, yielded an older age of 74.7±2.4 (n=8). The older age may be a result of larger error associated with the small number of grains analyzed. Additionally the MSWD is very large for sample SCM-12 at 17. The MSWD values calculated from the data for the other samples are <10. The larger MSWD for sample SCM-12 indicates that the error is not well explained by analytical uncertainties, and therefore the error may in part be the result of the small number of analyzed grains.

The mylonite sample from the Stone Corral ridge shear zone, H3, yielded an age of 69.4±2.2 Ma (n=27), which is very similar to the ages yielded by the discrete shear zone rocks (Figure 8.4; Table 8.11). The protomylonite sample, SCM-19, collected from the boundary of the Stone Corral ridge shear zone yielded an age of 71.6±3.0 (n=15), which is very similar to the ages yielded by the country rock samples. However, the Tera-Wasserburg diagram for this sample reveals a significant amount of spread in the data points, and the MSWD value for the sample is very high at 33. In this sample, 60 point analyses were conducted on 15 grains, so the high MSWD cannot be explained by too small of a dataset as it can be for sample SCM-12.

The analyses performed on the zircon grains of the Brown's Canyon granite sample AZSC-6, which was collected from the crest of Stone Corral ridge, provided a

lower intercept date of 75.5±1.3 Ma and an an upper intercept date of 1672±22 Ma (Figure 8.5).

8.2.2 Rim vs. Core Ages

The U-Pb titanite data points for all the samples were divided into groups based on whether they were obtained from inside the cores of the grains or on the rims of the grains (Tables 8.1-8.9; Figure 8.7F). Only the data from one sample, SCM-19, yielded a significant difference in rim and core ages. In this sample, the cores of the grains yielded an age of 75.3±2.4 Ma (n=15; MSWD=16) and the rims yielded an age of 53.9±3.7 Ma (n=10; MSWD=12; Figure 8.6; Table 8.11). The MSWD values for the rim and core data are higher than the values for most of the other samples, but are significantly lower than the MSWD value of 33 for the combined rim and core data for this sample.

The dates for the separated rim and core data within all the other samples are within error of each other. No systematic difference between rim and core ages exists among the samples. Some samples yielded slightly older core ages, whereas others yielded slightly older rim ages.

8.2.3 Microstructural Controls on Grain Ages

The data for each sample were also separated into groups on the basis of microstructural qualities exhibited by the analyzed grains (Tables 8.1-8.9). The data for the country rock samples were divided into two groups with titanite grains located: 1) within and parallel to the country rock foliation (Figure 8.7A), or 2) within and parallel to the top-to-the-northeast shear bands that crosscut the country rock foliation (Figures 3.2D, 8.7B). The data for the protomylonite sample from the boundary of the Stone Corral ridge shear zone was similarly separated into two groups with titanite grains located: 1) within and parallel to the protomylonitic foliation, or 2) within and parallel to

the top-to-the-northeast shear bands that crosscut the protomylonitic foliation (Figures 3.2C, 8.7C).

The data for the mylonites were also divided into two groups with titanite grains: 1) clearly deformed during mylonitization, or 2) with a more ambiguous relationship to the deformation. None of the samples of mylonites are characterized by a foliation crosscut by through-going, top-to-the-northeast C'-type shear bands as in the country rocks and protomylonite. Grains clearly deformed during mylonitization have a fish-like shape that provides a distinct top-to-the-southwest sense of shear and some display undulatory extinction and/or deformation twins (Figures 3.9; 8.7D-E).

In all cases, the ages yielded by the grains in the different microstructural data categories within each sample are within error of each other. No systematic age differences are apparent within the country rock and protomylonite samples regardless of the grains' associations with the country rock foliation or with the crosscutting top-to-the-northeast shear bands. Similarly, no systematic age differences are apparent within the mylonite samples exhibiting differing degrees of grain deformation.

8.3 DISCUSSION

8.3.1 Titanite Closure Temperature and Reactivity

The mineral titanite has been demonstrated to be a very effective U-Pb geochronometer for dating metamorphism, deformation, and fluid infiltration of rocks in a variety of settings because of its high closure temperature and its ease of reaction during metamorphism (Frost et al., 2000). The closure temperature for titanite varies depending on the cooling rate of the rock and the grain sizes of the minerals, but a minimum closure temperature is estimated at ~650-700 °C (e.g., Scott and St-Onge, 1995; Pidgeon et al., 1996; Frost et al., 2000). Under certain conditions, titanite grains

may survive extremely high temperatures for extended periods of time without disturbance to the U-Pb system. Titanite grains with Precambrian ages have been preserved during fluid- and deformation-absent Phanerozoic subduction to mantle depths at temperatures up to 750 °C and pressures of 1.5-2.0 GPa, despite not being stable at these conditions (Spencer et al., 2013). The U-Pb system in titanite, therefore, is not easily reset by high temperature alone, and closure temperatures are in the range of upper amphibolite-facies to granulite-facies conditions.

In the Stone Corral study area in the Harquahala Mountains, the rocks have clearly undergone fluid-assisted metamorphism and deformation at temperatures that are lower than the closure temperature of titanite. Therefore, U-Pb dating of titanite is an ideal technique for determining the timing of these events in this area. Additionally, because titanite may grow in a variety of temperature and pressure conditions that are typical of greenschist and amphibolite facies metamorphism (Frost et al., 2000), the amphibolite-facies conditions that prevailed during deformation of the country rocks and shear zones in the study area would have been conducive to titanite growth.

8.3.2 Titanite U-Pb Dating of Metamorphism and Deformation

Despite the resistance of the U-Pb system in titanite to being reset solely by thermally activated volume diffusion at high temperature, titanite is an extremely reactive mineral during metamorphism and is therefore ideal for dating post-crystallization events, such as deformation and fluid infiltration (Frost et al., 2000). Because of this reactivity, U-Pb dating of titanite has been used extensively to determine the timing of such processes as hydrothermal activity (Corfu and Muir, 1989), contact metamorphism (Verts et al., 1996), shear zone deformation (Resor et al., 1996), and regional metamorphism

associated with large scale tectonic events, such as arc-continent collision (Scott and St-Onge, 1995) and the exhumation of UHP terranes (Gao et al., 2012; Spencer et al., 2013).

To use the U-Pb system in titanite as a means of dating deformation and metamorphism, the mineral must have either grown or reacted during the particular event (Frost et al., 2000). Several ways of demonstrating growth during deformation include titanite grains: 1) oriented parallel to foliations or lineations that have not been mechanically rotated into parallelism with the fabric during deformation, 2) associated with mineral reactions that occurred during metamorphism or deformation, and 3) in deformed or metamorphosed rock with a protolith that does not include titanite as one of its phases (Frost et al., 2000).

Microstructural evidence suggests that the titanite in the Stone Corral study area shear zones, which is oriented parallel to the mylonitic fabric, may have grown during mylonitization, but this evidence is not conclusive (section 8.3.2.1). However, the mylonitic titanite is clearly associated with metamorphic mineral reactions that occurred during fluid infiltration, and this metamorphism and fluid infiltration can be demonstrated to have occurred during mylonitic deformation (section 8.3.2.2). Thus, a compelling case is made for the syn-mylonitic growth of titanite in the shear zones.

The titanite in the country rock is plentiful in the very deformed country rock in the northern part of the study area that is dated in this study, and is rare in the undeformed and little deformed country rock in the southern part of the study area. The degree of metamorphism and the amount of titanite in the country rock samples are positively correlated to the degree of deformation experienced by each sample. This association implies the metamorphism (and thus the titanite growth) occurred synchronously with the deformation (section 8.3.2.3). Therefore, the dating of the titanite grains in the country rock samples provides a date for the country rock deformation

8.3.2.1 Relationship of titanite to the mylonitic fabric

The titanite in the Stone Corral mylonites are elongate parallel to the foliation, but direct evidence indicating whether the titanite grew during the development of the foliation or grew earlier and then rotated into parallelism with the foliation is lacking. The titanite in the mylonites exhibit very different habits than the titanite in the country rocks, but some of these differences may be attributed to the effects of mylonitization on the grains, which are evident in the fish-like and sigmoidal shapes of many grains, and the presence of twinning, undulose extinction, and, more rarely, gentle bending of grains (Figure 8.7C). Additionally, some of the titanite have an extremely long aspect ratio of up to ~7:1, which may indicate growth during shear zone deformation, or may indicate extreme stretching of pre-existing grains during deformation. However, because of the high reactivity of titanite, in conjunction with the high amount of strain experienced by the rocks and the presence of fluids during mylonitization, these grains would likely provide the age of mylonitization (at least on their rims, if not pervasively) regardless of whether they formed during the deformation or existed prior to it (Frost et al., 2000).

8.3.2.2 Growth of metamorphic titanite during fluid infiltration and mylonitization

Importantly, indirect evidence does imply that the titanite grew during mylonitization rather than prior to it, because most, if not all, of the titanite is metamorphic, and metamorphism, fluid infiltration, and mylonitization can be demonstrated to have occurred synchronously. Ample petrographic evidence shows that titanite in both the country rocks and the mylonites clearly formed as a reaction product of the fluid-assisted metamorphism. The titanite is closely associated with other metamorphic minerals in the rocks, including epidote, biotite, quartz, garnet, apatite, and opaque minerals (see Chapter 3; Figure 3.4). Titanite is commonly found clumped or

intertwined with these other minerals, with faces adjacent to metamorphic epidote, or forming trains of small grains near trains of epidote grains (Figure 3.9A).

In sample SCM-51 (dated in this study), which was collected from a discrete shear zone with central epidote veins, a bleached halo, and flanking paired ultramylonite zones, titanite is pervasive within the highly altered portion of the bleached halo near the central vein, and is associated with abundant epidote grains (Figure 3.12). These two minerals decrease in abundance dramatically from the vein outwards toward the flanking paired shear zones, which indicates they formed during metamorphism related to the infiltration of the fluids that caused the bleaching and the precipitation of the central epidote vein. Additionally, in many of the other discrete shear zones with the central epidote vein, bleached halo, and flanking paired shear zones morphology, some titanite appears to be a reaction product associated with the replacement of feldspar by oligoclase during the bleaching process (see Section 3.3.2).

Significant evidence exists that indicates that the fluid-assisted metamorphism responsible for the bleaching in the shear zones (including the titanite-rich alteration zones) occurred at the same time as the shear zone deformation, and this evidence is summarized in detail in section 9.1.2. The evidence includes the significantly higher water content of intragranular quartz in the shear zones than in the country rocks (see also Chapter 6), the formation of synkinematic myrmekite (which is seen in thin section by the presence of myrmekitic lobes and vermicules deflected in the direction of shear, and also by the dependence of the size of the lobes and vermicules on the degree of strain; Figure 3.19), and the presence of optically continuous fibers that connect pulled apart epidote grains in the central veins of the shear zones with the central vein, bleached halo, and flanking paired shear zones morphology (Figure 3.11B). Therefore, the titanite in the shear zones (particularly in those associated with the bleached halo metamorphism), may

clearly be used to date not only the fluid-assisted metamorphism, but also the deformation of the shear zones.

8.3.2.3 Growth of metamorphic titanite during country rock deformation

Just as the titanite in the shear zones can be used to date bleaching and mylonitization, the titanite in the country rocks that host the shear zones can be used to date the gneissic country rock deformation, because metamorphism of these rocks (and thus titanite growth) can also be demonstrated to have occurred during this deformation. The non-deformed and faintly foliated country rocks in the southern part of the study area may provide examples of the protolithic rock of the more intensely deformed country rocks in the northern part of the study area that were dated in this study. Although titanite is not entirely absent in these undeformed or little deformed rocks, it is very rare. Three samples were collected from these rocks for thin section observations (see section 3.2.2), and titanite is notably absent from the two least deformed of these samples (B-4 and B-7). The third sample (B-28) was slightly more deformed, and contained rare small titanite grains that were neither plentiful enough nor large enough to date in situ in thick sections. Other metamorphic minerals in these samples, such as epidote, follow a similar trend in which fewer grains and smaller grain sizes correlate to lesser degrees of deformation. In the northern country rock samples that are more intensely deformed and were dated in this study, the titanite grains are both large in size and abundant. These observations suggest that the titanite grains are associated with the deformation and likely grew synchronously. Additionally, if any pre-existing igneous titanite was present, the fluid-rich conditions that prevailed during metamorphism and deformation would have aided in the resetting of the U-Pb titanite system, especially on the rims.

In conclusion, the petrographic evidence indicates that titanite likely grew during one protracted fluid-assisted metamorphic event that was synchronous with the country rock and shear zone deformations. These two different styles of deformation were closely spaced in time.

8.3.3 Testing for Different Generations of Titanite Growth

Many studies have indicated that the cores of titanite grains may preserve relict igneous or metamorphic material that retains U-Pb crystallization ages, whereas the rims contain material that has either been isotopically reset during metamorphism and deformation or that has developed by new growth during these events, and therefore provide younger U-Pb ages that date those events (e.g., Verts et al, 1996; Corfu and Stone, 1998; Gao et al., 2013; Spencer et al., 2013). However, the data collected on the cores and rims of the titanite grains (including in the "heads" and "tails" of the titanite fish) in the Stone Corral study area samples yielded similar ages, which implies that the grains within each sample experienced only one stage of growth during Late Cretaceous metamorphism and deformation, with only one exception, sample SCM-19 (Table 8.11). Similarly, the more deformed grains and the less deformed grains in the samples also all yielded similar ages, which also suggests that the nucleation and growth of all the titanite grains occurred during the same event within each individual sample, or that the U-Pb isotopic system was completely reset in the grains during the same event.

The one exception to a single stage of titanite growth in the samples is the protomylonite sample SCM-19, in which the core ages of the grains are significantly older than the rim ages (~75 Ma and ~54 Ma, respectively; Figure 8.6). The data in this sample may be reflecting a more complex geologic history than the other samples, but in the Tera-Wasserburg diagram of the combined data, the data points that diverge from the

isochron are much larger than the others, indicating more error is associated with them (Figure 8.4). The more precise data points, which form the majority of the data, conform well to the isochron, which may mean the age of 71.6±3.0 that's provided by the combined data is a reliable age. This age is the same as the ages provided by the country rock samples, and is within error of the ages provided by the mylonite samples (Table 8.11).

The two slightly older ages of ~74.5-75.5 Ma yielded by the country rock sample SCM-48-2 and the discrete shear zone sample SCM-12 are less reliable than the other ages because only a small number of grains were analyzed (Table 8.11). These older ages, therefore, may not be meaningful. With the exception of sample SCM-12, the titanite ages of the mylonites are slightly younger (~68-70.5 Ma) than the ages of the country rock (~71-72 Ma; Table 8.11), which is consistent with mylonitization occurring soon after country rock deformation. However, the ages of the country rock and mylonite samples are within error of each other, and so the U-Pb data taken independently cannot absolutely demonstrate that the mylonites are younger. Regardless, the data indicate that these mylonitic shear zones did not form during Miocene core complex development.

8.3.4 Crystallization Age of the Brown's Canyon granite

The lower intercept date of ~75.5 Ma yielded by the zircons from the undeformed Brown's Canyon granite is interpreted as the crystallization age of the pluton. The upper intercept date of ~1670 Ma is likely an older inherited age from the Proterozoic rocks that were melted to form the Brown's Canyon pluton. Previous U-Pb zircon age dates from the Brown's Canyon granite body provided a U-Pb zircon age of 77 ± 7 Ma (Isachsen et al., 1999), and therefore the date yielded by sample AZSC-6 in this study is within error of the previously determined age. The date of the Brown's Canyon granite is significant

in that it gives an age of crystallization for the protoliths of at least some of the mylonites. Although both the deformed country rocks and the mylonites in the northern part of the study area are likely part of the Stone Corral granite, genetically related to the Brown's Canyon granite, the possibility remains that some or all of these rocks may be Precambrian granite that was intruded by the Brown's Canyon and Stone Corral plutons (Richard, 1988; Richard et al., 1990). Regardless, the zircon crystallization age of the Brown's Canyon granite is only slightly older than the titanite ages for the metamorphism and deformation of the rocks in the northern part of the study area, which indicates the metamorphic and deformation events occurred during the cooling of the pluton.

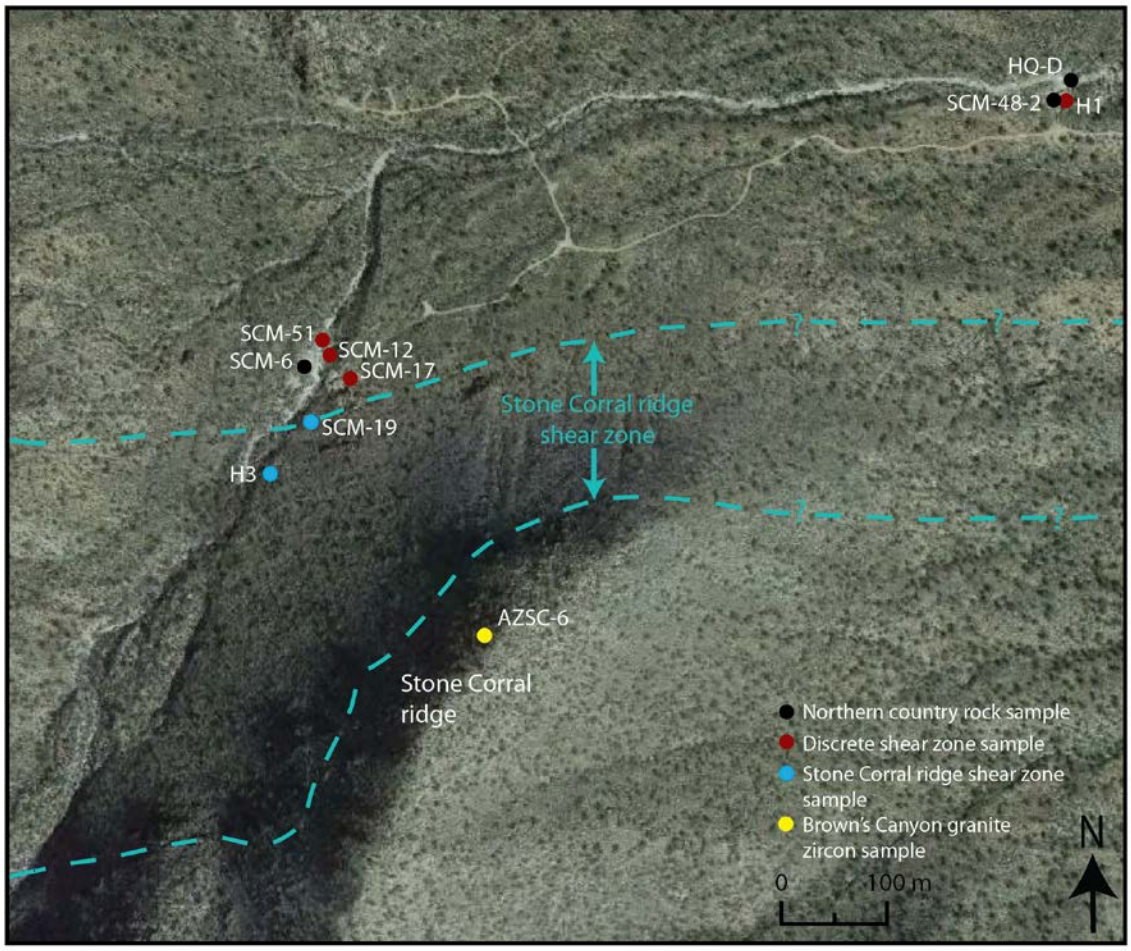

Figure 8.1: Areal photograph of the Stone Corral study area with locations of samples plotted that were used for U-Pb isotope analyses (photograph from Google Earth).

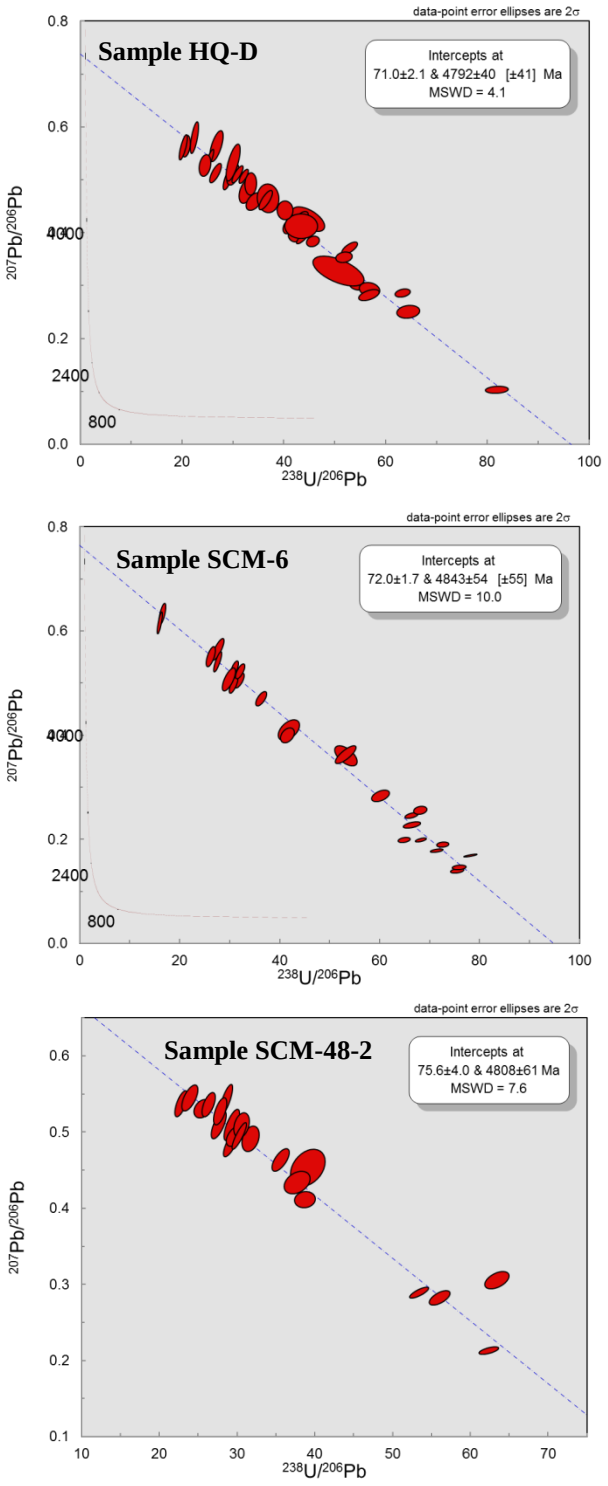

Figure 8.2: Tera-Wasserburg diagrams for titanite analyses in the country rock samples.

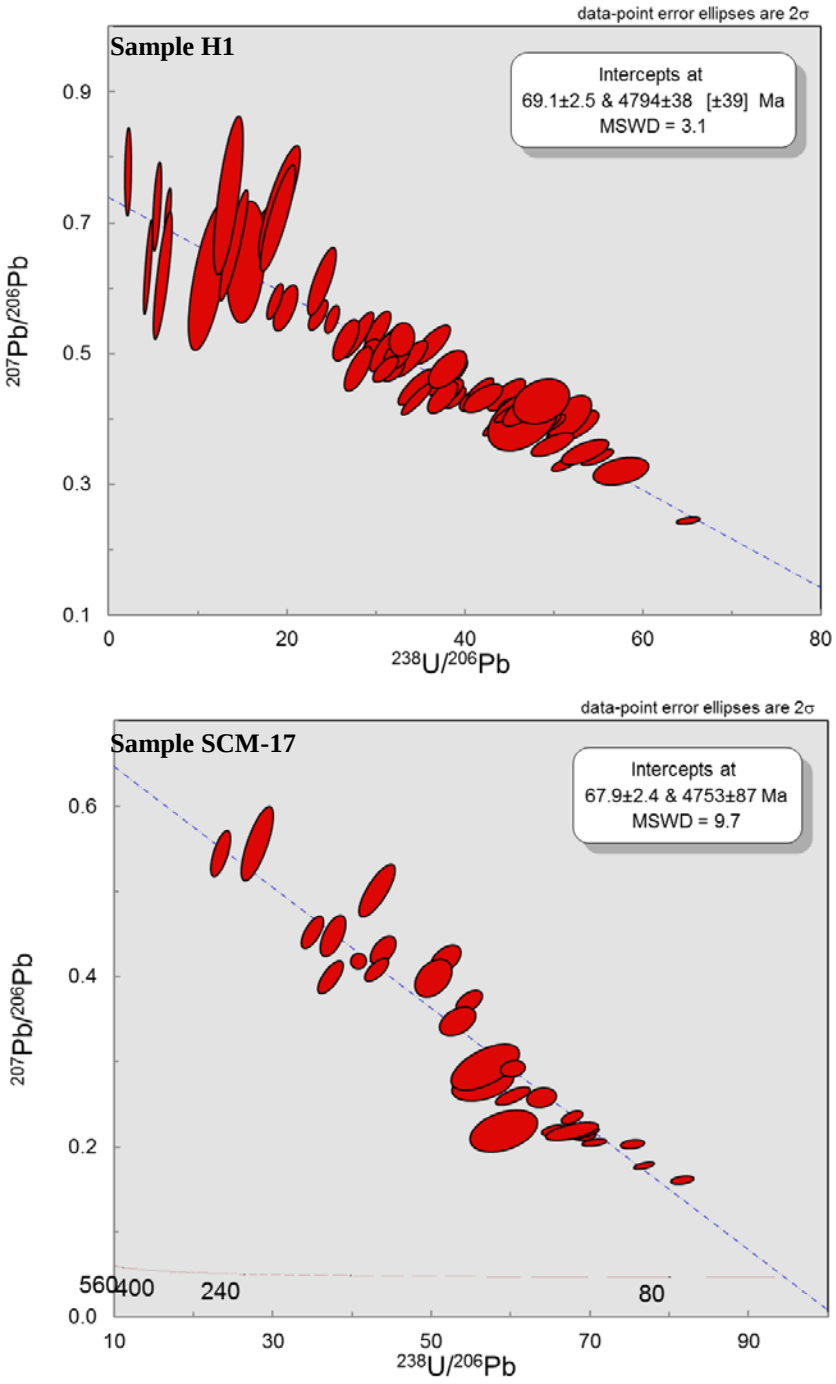

Figure 8.3: Tera-Wasserburg diagrams for titanite analyses in the discrete shear zone samples (continued on next page).

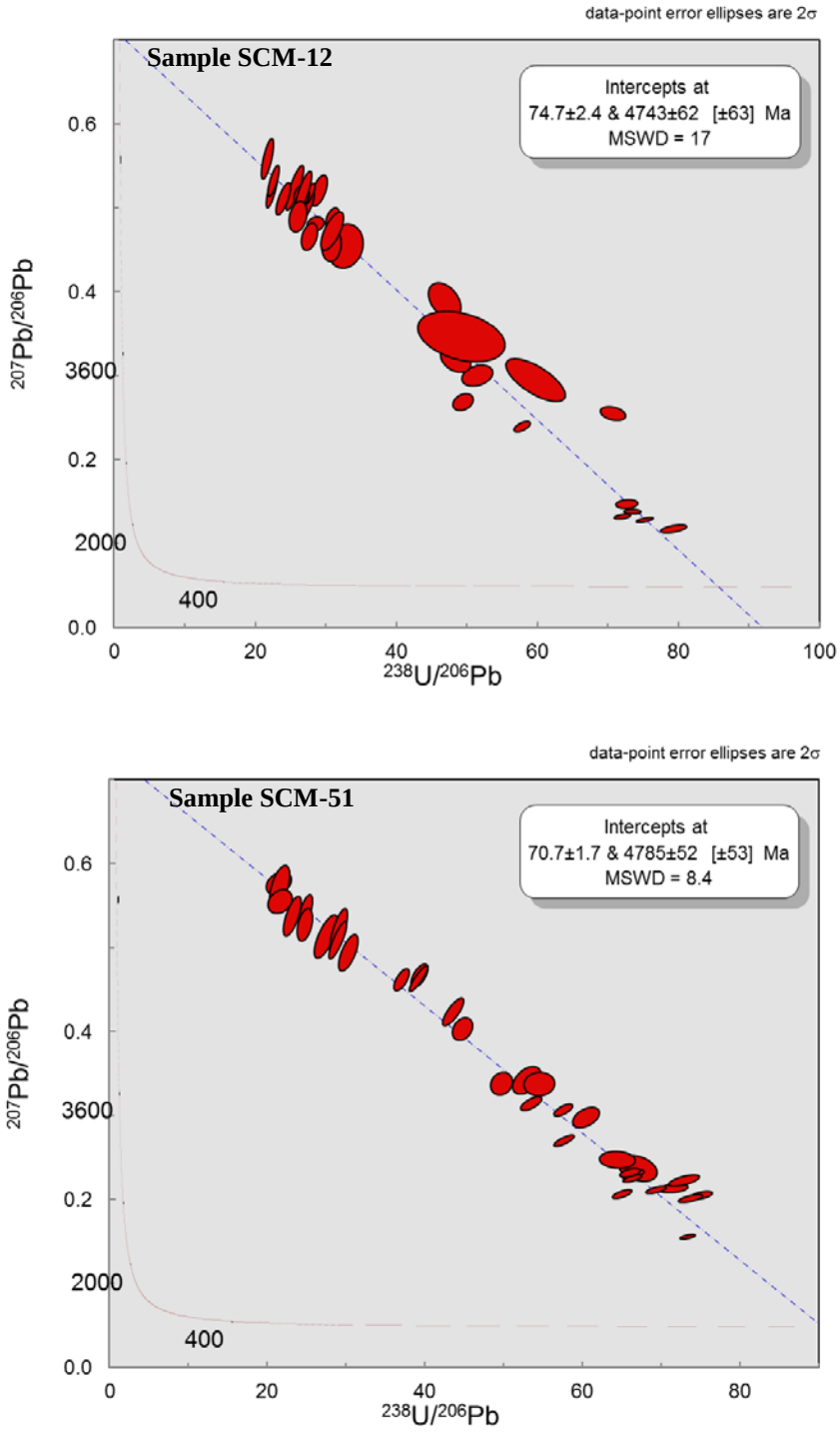

Figure 8.3: (continued from previous page).

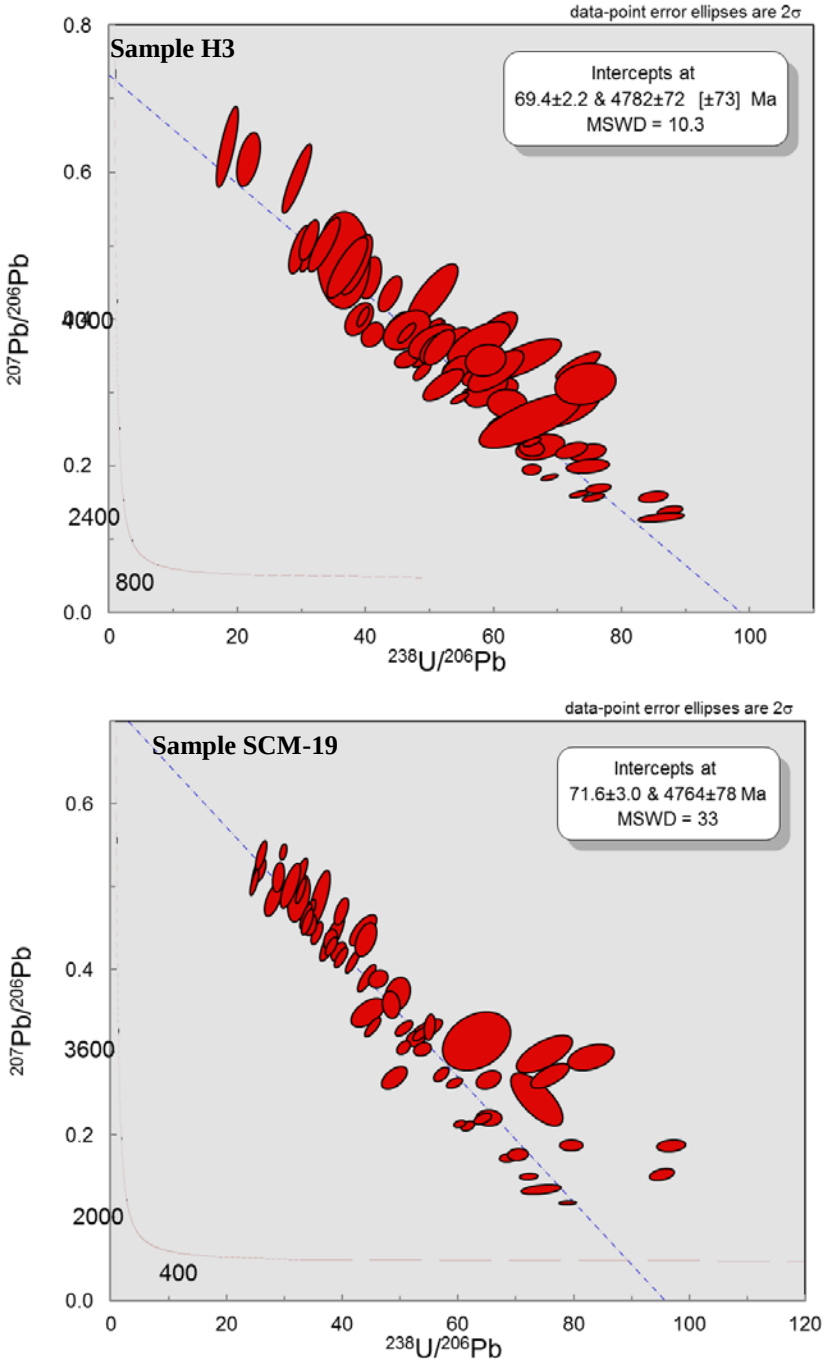

Figure 8.4: Tera-Wasserburg diagrams for titanite analyses in the Stone Corral ridge shear zone samples.

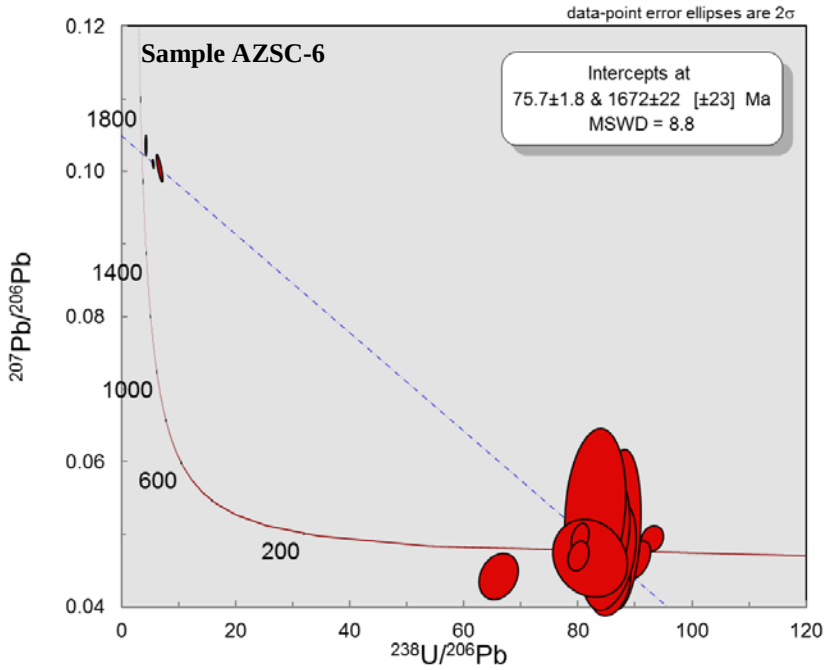

Figure 8.5: Tera-Wasserburg diagram for zircon analyses in the Brown's Canyon granite.

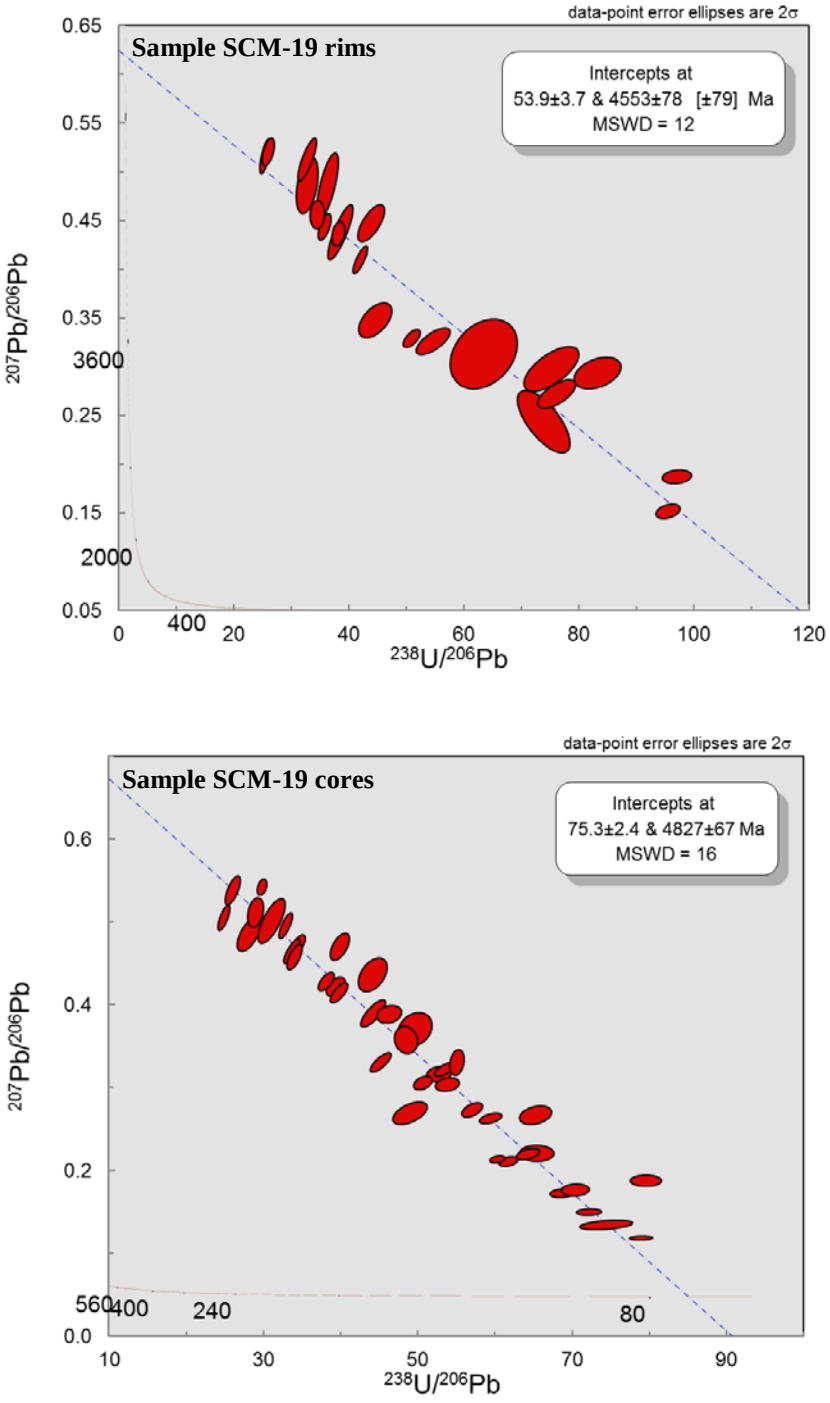

Figure 8.6: Tera-Wasserburg diagrams for titanite analyses on the rims of grains and within the cores of grains in sample SCM-19.

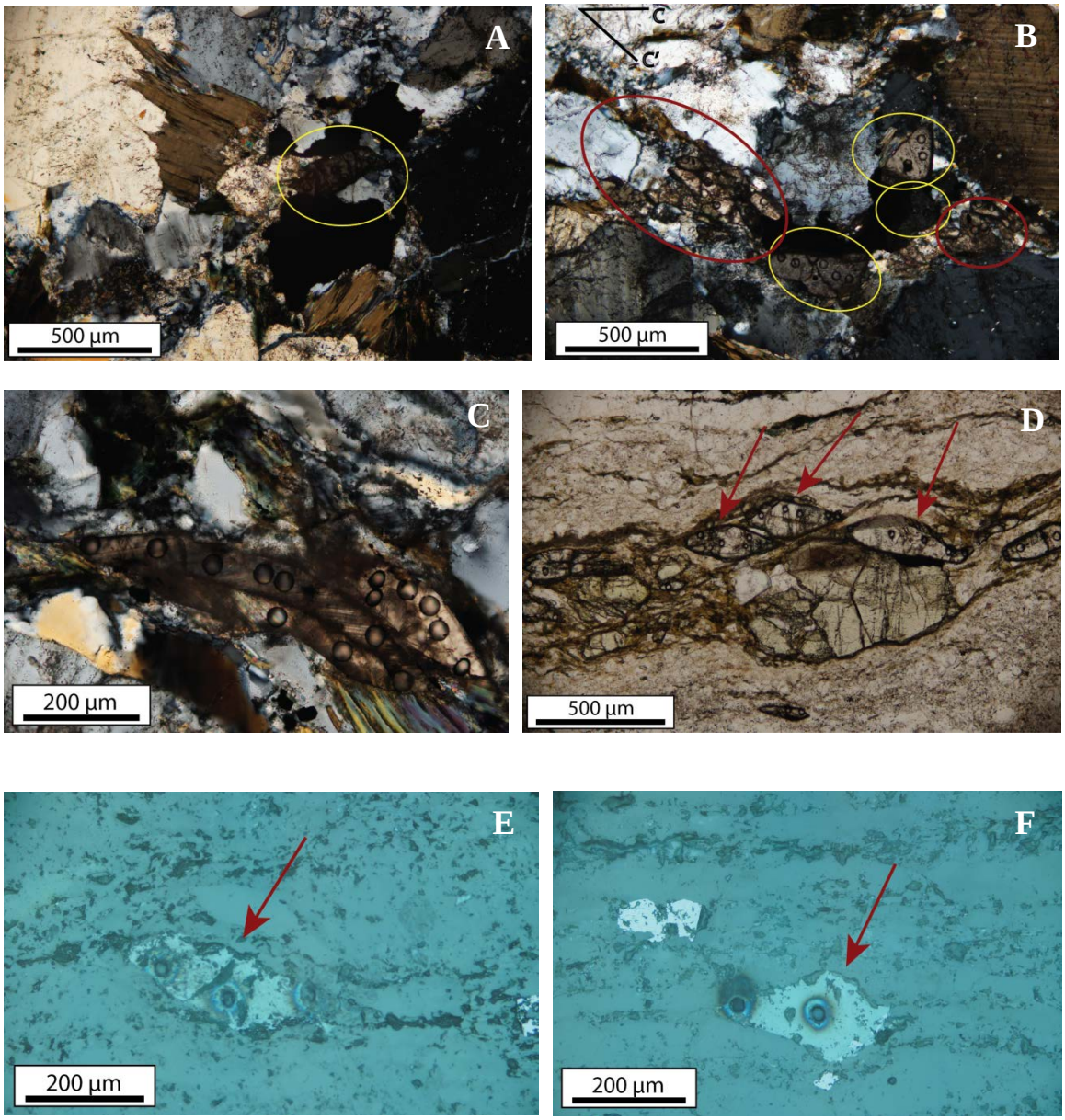

Figure 8.7: (caption continued on next page). Photomicrographs of different types of titanite grains that were used for dating of samples. Yellow circles indicate individual titanite grains. Red circles indicate clusters of titanite grains. Red arrows point to titanite fish. The small circles are laser ablation pits formed during U-Pb dating. Northeast is to the top right. A) Titanite grain parallel to the country rock foliation; sample SCM-6; B) Titanite grains at the bottom of a C'-type shear band. The train of grains are within the shear band and then wrap around a porphyroclast to parallel the country rock foliation; sample HQ-D.

Figure 8.7: (continued from previous page). C) Deformed titanite grains gently wrapped into a C'-type shear band. Note the presence of undulatory extinction and twins; sample SCM-19; D) Titanite fish in a discrete shear zone mylonite; sample H1; E) Titanite fish visible in reflected light; sample H3; F) Deformed titanite grain in reflected light. The laser ablation pit in the nose of the grain is classified as a "rim" point, whereas the pit in the center of the grain is classified as a "core" point; sample H3.

[1]Grain	~U (ppm)	+2σ	~Pb (ppm)	+2σ	$^{207}Pb/^{235}U$	+2σ	$^{206}Pb/^{238}U$	+2σ	[2]Error Correlation	$^{206}Pb/^{238}U$ Age	+2σ	Core/ Rim	[3]s.b.
1A	48.1	1.5	4.59	0.18	1.743	0.049	0.02706	0.00054	0.14255	172.1	3.4	Core	
2A	101.4	3.9	6.67	0.21	0.916	0.02	0.01961	0.00046	0.12568	125.2	2.9	Core	
2B	29.5	1.5	4.77	0.14	2.66	0.062	0.0376	0.0013	0.54494	238	7.8	Core	
2C	25.18	0.89	3.71	0.092	2.386	0.057	0.03439	0.00094	0.05626	217.9	5.9	Rim	
3A	96.8	3.7	5.16	0.16	0.966	0.019	0.01887	0.00046	0.33551	120.5	2.9	Core	
3B	606	47	3.92	0.14	0.174	0.01	0.0122	0.00027	0.23338	78.2	1.7	Core	
3C	23.27	0.89	4.11	0.15	2.91	0.1	0.0374	0.0015	0.36809	236.3	9.6	Core	
4A	86	3.6	5	0.19	0.98	0.015	0.02065	0.00042	0.081696	131.7	2.7	Core	
4B	56.77	0.77	4.41	0.13	1.317	0.039	0.02349	0.00054	0.51564	149.7	3.4	Core	
4C	21.15	0.73	3.85	0.14	2.93	0.049	0.0395	0.0011	0.13415	249.8	6.7	Core	
5A	199.6	5.4	5.66	0.32	0.536	0.024	0.0155	0.00044	0.49456	99.2	2.8	Core	
5B	20.1	0.47	4.46	0.18	3.57	0.11	0.0446	0.0013	0.027263	281.2	8.1	Core	
5C	69.9	4.9	5.08	0.15	1.289	0.057	0.02342	0.00082	0.64992	149.2	5.2	Core	
6A	63.1	1.9	4.67	0.14	1.233	0.017	0.02288	0.00052	0.28618	145.8	3.3	Core	
6B	74	2.8	5.19	0.14	1.157	0.032	0.02185	0.0005	0.65205	139.3	3.1	Core	
7A	130.1	4.7	6.49	0.37	0.88	0.038	0.01933	0.00051	0.8138	123.4	3.2	Core	X
7B	114.2	3.6	5.09	0.27	0.764	0.031	0.01834	0.00046	0.74272	117.2	2.9	Core	X
7C	28.41	0.45	4.08	0.14	2.353	0.083	0.0334	0.0011	0.55174	211.7	6.6	Core	X
8A	133.8	8.4	6.41	0.65	0.89	0.12	0.0197	0.0016	0.90652	126	10	Core	X
8B	61.5	3.3	5.18	0.18	1.387	0.039	0.0244	0.00056	0.46063	155.4	3.6	Core	X
9A	31.81	0.42	3.99	0.17	2.021	0.082	0.0306	0.0011	0.49914	194.5	7	Rim	X
9B	90	8.4	6.3	0.23	1.31	0.12	0.0223	0.0013	0.91732	142.2	8.1	Core	X
10A	165.7	9.2	7.1	0.22	0.711	0.036	0.01758	0.00051	0.7046	112.3	3.2	Rim	X
10B	116	5.5	6.63	0.41	0.942	0.029	0.01928	0.00048	0.67321	123.1	3	Core	X
11A	39.4	3.1	4.26	0.18	1.856	0.066	0.0293	0.0011	0.65996	186	6.6	Rim	X
11B	72	2.3	5.45	0.2	1.24	0.033	0.02239	0.00041	0.50655	142.7	2.6	Core	X
11C	28.8	2.4	6.21	0.43	3.75	0.14	0.0482	0.0016	0.64273	303.2	9.9	Core	X
11D	45.1	1.5	5.57	0.22	2.026	0.087	0.02985	0.00081	0.58402	189.6	5.1	Core	X
11E	19.73	0.99	4.77	0.27	3.838	0.089	0.0495	0.0016	0.25903	311.5	9.7	Core	X
12A	69	1.7	5.85	0.19	1.358	0.03	0.02294	0.00053	0.5554	146.2	3.3	Core	X
13A	73.1	3.7	7.45	0.32	1.74	0.12	0.0271	0.0013	0.72517	172.1	8.3	Core	X
14A	170.1	7.8	6.2	0.24	0.623	0.015	0.01576	0.0003	0.49706	100.8	1.9	Core	X
15A	113.2	6.7	8.32	0.41	1.31	0.1	0.023	0.0014	0.80023	146.8	8.6	Core	X
16A	22.55	0.4	3.62	0.14	2.447	0.095	0.0333	0.0013	0.049084	211.4	8.3	Core	X
17A	107.9	3.2	4.28	0.18	0.687	0.02	0.01761	0.0005	0.4239	112.6	3.1	Core	X
18A	40.5	2.1	5.43	0.31	2.177	0.034	0.03114	0.0007	0.40174	197.6	4.4	Core	X
18B	50.5	1.2	5.29	0.16	1.748	0.037	0.02745	0.00081	0.20624	174.6	5.1	Core	X
18C	33.7	1.2	6.12	0.35	2.97	0.13	0.0408	0.0016	0.70599	259.5	9.5	Core	X
19A	34.8	1.7	4.72	0.19	2.278	0.039	0.03234	0.00091	0.41241	205.1	5.7	Core	X
20A	46.3	4	4.03	0.19	1.515	0.069	0.02481	0.00079	0.7016	157.9	5	Rim	X

[1] Grain is numbered, points within grains are lettered.
[2] $^{206}Pb/^{238}U$ vs. $^{207}Pb/^{235}U$
[3] s.b. = grain is within a shear band that crosscuts the country rock foliation

Table 8.1: U-Pb titanite data from the country rock sample HQ-D. The table also includes the locations of analyzed points (i.e., core or rim of grain) and denotes which grains were located within shear bands that crosscut the foliation.

[1]Grain	~U (ppm)	+2σ	~Pb (ppm)	+2σ	$^{207}Pb/^{235}U$	+2σ	$^{206}Pb/^{238}U$	+2σ	[2]Error Correlation	$^{206}Pb/^{238}U$ Age	+2σ	Core/ Rim	[3]s.b.
1A	278.8	8.5	8.41	0.14	0.4016	0.0053	0.01464	0.0002	0.24991	93.7	1.3	Core	
2A	269.3	8.6	6.08	0.26	0.4219	0.0089	0.01539	0.00023	0.37208	98.4	1.5	Core	
2B	84.4	4.6	6.61	0.52	1.327	0.042	0.02405	0.00065	0.5185	153.2	4.1	Rim	
3A	387.1	8.4	11.55	0.3	0.3609	0.0082	0.01375	0.00019	0.43458	88.1	1.2	Core	
4A	33.6	1.3	4.8	0.15	2.354	0.042	0.03232	0.00068	0.28759	205	4.2	Core	
4B	234.3	6.2	7.03	0.32	0.4733	0.0098	0.01503	0.00032	0.45761	96.2	2	Core	
4C	313	12	7.85	0.21	0.3441	0.0049	0.01399	0.0002	0.42957	89.6	1.3	Core	
5A	511.9	7.8	7.31	0.15	0.255	0.0057	0.01323	0.00019	0.25685	84.7	1.2	Core	
5B	366.7	5.6	5.3	0.15	0.2654	0.0068	0.01316	0.00019	0.35709	84.3	1.2	Core	
6A	96.4	4.4	5.36	0.21	0.933	0.066	0.01875	0.00065	0.85537	119.7	4.1	Core	
7A	393	11	7.67	0.16	0.2974	0.0024	0.01278	0.00018	0.34849	81.9	1.1	Core	
8A	30.7	1.1	5.05	0.18	2.822	0.062	0.0362	0.0013	0.52099	229.2	8.2	Rim	X
8B	72.4	1.6	4.05	0.15	0.94	0.022	0.01878	0.00061	0.073989	119.9	3.9	Core	X
8C	39	1.2	5.39	0.18	2.335	0.05	0.0331	0.00082	0.33108	209.9	5.1	Core	X.
8D	13.25	0.69	4.37	0.13	5.29	0.13	0.0606	0.002	0.61965	379	12	Rim	X
8E	13.35	0.39	4.48	0.13	5.303	0.094	0.0624	0.0016	0.21812	390.3	9.5	Rim	X
9A	40.5	1.6	5.28	0.13	2.187	0.043	0.03136	0.00079	0.48626	199	4.9	Core	X
9B	25.3	1.1	4.23	0.19	2.704	0.045	0.03623	0.00091	0.085893	229.4	5.7	Core	X
9C	29.7	1.1	4.02	0.14	2.225	0.04	0.03247	0.00072	0.17702	205.9	4.5	Core	X
9D	19.73	0.68	2.839	0.092	2.344	0.065	0.0335	0.0012	0.38085	212.4	7.5	Core	X
9E	35.6	1.5	4.65	0.18	2.248	0.041	0.03116	0.00075	0.46188	197.8	4.7	Rim	X
9F	24.5	1.2	4.21	0.18	2.897	0.07	0.0381	0.0011	0.43236	240.7	6.9	Rim	X
10A	55.6	2.3	4.36	0.11	1.351	0.056	0.0239	0.001	0.55203	152.1	6.3	Core	
10B	47.9	2.8	5.02	0.2	1.787	0.036	0.02755	0.00067	0.39819	175.2	4.2	Core	
11A	220.5	7.8	8.26	0.26	0.5112	0.0081	0.01505	0.00024	0.40978	96.3	1.6	Core	
11B	211.4	3.8	6.74	0.31	0.518	0.014	0.01466	0.00024	0.40505	93.8	1.5	Rim	
12A	174.9	9.3	6.61	0.17	0.65	0.019	0.01661	0.0004	0.31487	106.2	2.5	Core	

[1] Grain is numbered, points within grains are lettered.
[2] $^{206}Pb/^{238}U$ vs. $^{207}Pb/^{235}U$
[3] s.b. = grain is within a shear band that crosscuts the country rock foliation

Table 8.2: U-Pb titanite data from the country rock sample SCM-6. The table also includes the locations of analyzed points (i.e., core or rim of grain) and denotes which grains were located within shear bands that crosscut the foliation.

[1]Grain	~U (ppm)	+2σ	~Pb (ppm)	+2σ	$^{207}Pb/^{235}U$	+2σ	$^{206}Pb/^{238}U$	+2σ	[2]Error Correlation	$^{206}Pb/^{238}U$ Age	+2σ	Core/ Rim
1A	66.2	3.3	5.93	0.32	1.467	0.05	0.02584	0.00074	0.78565	164.4	4.7	Core
1B	50.5	2.7	4.69	0.18	1.602	0.084	0.0256	0.0012	0.61536	163.2	7.8	Rim
2A	26.6	1.1	3.85	0.17	2.401	0.055	0.03415	0.00096	0.17858	216.4	6	Core
2B	28.3	1.3	4.59	0.18	2.618	0.051	0.03501	0.00088	0.018086	221.8	5.5	Core
2C	30.59	0.98	4.31	0.13	2.293	0.045	0.0342	0.001	0.28453	216.6	6.4	Core
2D	28.1	1.5	4.9	0.27	2.87	0.1	0.0392	0.0014	0.85884	247.9	8.4	Core
3A	133	1.2	5.53	0.15	0.695	0.015	0.01785	0.00034	0.099087	114.1	2.1	Core
3B	39.63	0.88	5.26	0.13	2.139	0.071	0.03154	0.00091	0.60563	200.1	5.7	Core
3C	43.4	1.7	6.05	0.26	2.3	0.062	0.0337	0.001	0.70246	213.9	6.2	Core
3D	19.4	1.2	3.78	0.16	3.253	0.074	0.0439	0.0013	0.52508	276.9	8	Core
4A	25.3	1	3.99	0.11	2.545	0.056	0.0362	0.001	0.34867	229.2	6.4	Rim
4B	35.9	1.7	4.95	0.13	2.298	0.073	0.03272	0.0009	0.61007	207.5	5.6	Core
4C	36.4	1.1	4.89	0.12	2.259	0.032	0.03307	0.00083	0.040725	209.7	5.2	Core
4D	40.4	2.4	3.83	0.19	1.588	0.06	0.02653	0.00098	0.72447	168.8	6.1	Core
4E	25.07	0.79	4.19	0.2	2.811	0.064	0.038	0.001	0.49561	240.4	6.3	Core
5A	202.1	8.1	5.68	0.18	0.4719	0.007	0.01604	0.00026	0.30268	102.6	1.7	Rim
5B	112.7	4.7	4.73	0.17	0.7479	0.0096	0.01873	0.00036	0.22158	119.6	2.3	Core
6A	22.51	0.92	4.29	0.18	3.142	0.088	0.0418	0.0015	0.70102	264.1	9.1	Core
6B	27.22	0.63	4.29	0.15	2.614	0.061	0.03594	0.0009	0.34606	227.6	5.6	Core
6C	42.5	2.4	4.5	0.16	1.798	0.038	0.02811	0.0007	0.36031	178.7	4.4	Core
6D	95	2.7	5.02	0.15	0.666	0.018	0.01578	0.00032	0.19669	100.9	2	Core

[1] Grain is numbered, points within grains are lettered.
[2] $^{206}Pb/^{238}U$ vs. $^{207}Pb/^{235}U$

Table 8.3: U-Pb titanite data from the country rock sample SCM-48-2. The table also includes the locations of analyzed points (i.e., core or rim of grain).

[1]Grain	~U (ppm)	+2σ	~Pb (ppm)	+2σ	$^{207}Pb/^{235}U$	+2σ	$^{206}Pb/^{238}U$	+2σ	[2]Error Correlation	$^{206}Pb/^{238}U$ Age	+2σ	Core/ Rim	[3]Fish
1A	83.3	4.6	5.86	0.33	1.176	0.044	0.02164	0.0008	0.37275	138	5.1	Core	
2A	48.5	3.8	4.7	0.34	1.597	0.058	0.0267	0.001	0.20581	169.6	6.5	Rim	
3A	80.9	9.3	3.4	0.19	0.768	0.044	0.01738	0.00077	0.43359	111.1	4.9	Core	
3B	45.9	1.7	3.1	0.15	1.214	0.089	0.0206	0.0011	0.49084	131.6	6.8	Rim	
4A	3.5	0.22	4.06	0.31	18.5	1.3	0.185	0.015	0.49447	1087	82	Rim	X
4B	2.29	0.34	4.66	0.41	49.7	7.1	0.463	0.064	0.87249	2410	280	Core	X
5A	10.13	0.23	9.39	0.59	14.97	0.6	0.1507	0.0076	0.66026	904	43	Rim	X
5B	38.5	2.6	4.5	0.21	1.955	0.064	0.0276	0.0013	0.32499	175.4	7.9	Core	X
6A	6.08	0.22	1.94	0.14	5.27	0.29	0.0522	0.0052	0.3199	331	32	Rim	X
6B	5.77	0.3	1.84	0.15	5.38	0.34	0.0596	0.005	0.30053	376	31	Core	X
7A	65.9	3.9	9.06	0.76	2.19	0.11	0.0304	0.0011	0.60465	192.7	6.8	Rim	X
7B	8.3	1	3.11	0.36	5.73	0.82	0.0649	0.0074	0.59368	405	45	Core	X
8A	7.77	0.33	2.38	0.15	5.15	0.25	0.0528	0.0045	0.095671	335	29	Rim	X
8B	5.09	0.2	2.24	0.16	6.57	0.31	0.0715	0.0067	0.011826	453	42	Rim	X
8C	64.2	3.3	5.23	0.27	1.349	0.042	0.0224	0.00089	0.19634	142.8	5.6	Core	X
8D	42.3	2.4	4.45	0.25	1.796	0.055	0.029	0.0014	0.29687	184.4	8.9	Core	X
8E	7.37	0.37	2.84	0.16	7.63	0.72	0.0745	0.0074	0.049261	461	44	Rim	X
9A	2.15	0.17	2.23	0.18	14.1	1.2	0.165	0.023	0.42783	970	130	Rim	X
9B	71.2	4.1	4.62	0.22	1.119	0.047	0.02059	0.0008	0.2943	131.4	5	Core	X
9C	64.8	1.5	3.82	0.22	1.028	0.042	0.0192	0.00089	0.25628	122.6	5.6	Core	X
9D	69	4.1	3.67	0.22	0.902	0.032	0.01871	0.00076	0.32087	119.4	4.8	Rim	X
10A	19.5	1.1	4.34	0.36	3.52	0.15	0.0418	0.0023	0.025408	264	14	Rim	X
10B	67.4	3.8	4.06	0.2	1.076	0.06	0.01934	0.00075	0.054439	123.4	4.7	Core	X
10C	43.4	3	5.13	0.22	2.009	0.064	0.0296	0.0014	0.34503	188.1	8.7	Core	X
10D	46.4	3.5	4.59	0.21	1.729	0.077	0.0263	0.0012	0.40181	167.2	7.5	Rim	X
11A	34.3	1.9	5.84	0.27	2.7	0.11	0.0376	0.0017	0.31379	238	10	Rim	X
11B	73.9	5.5	5.22	0.2	1.175	0.051	0.02108	0.00088	0.60509	134.5	5.6	Core	X
12A	44.5	2.2	4.92	0.28	1.679	0.047	0.02597	0.00096	0.21464	165.2	6	Core	X
13A	4.76	0.26	2.35	0.27	7.59	0.99	0.089	0.015	0.52861	546	87	Rim	
14A	64.2	4.2	3.82	0.16	1.001	0.032	0.02009	0.00078	0.35722	128.2	4.9	Rim	
14B	1.7	0.096	2.1	0.14	19.8	1.2	0.227	0.021	0.31486	1310	120	Rim	
14C	58	2.4	3.93	0.16	1.092	0.024	0.02013	0.00054	0.24396	128.5	3.4	Core	
14D	61.2	1.6	4.63	0.15	1.235	0.024	0.023	0.00063	0.088369	146.6	3.9	Core	
14E	43.4	2	3.78	0.13	1.474	0.03	0.02396	0.00069	0.2359	152.6	4.4	Core	
15A	32.8	1	4.51	0.18	2.257	0.071	0.0326	0.0012	0.025793	206.9	7.3	Rim	X
15B	49	2.5	3.64	0.16	1.235	0.046	0.02141	0.00095	0.050809	136.5	6	Rim	X
15C	49.2	1.4	4.55	0.18	1.538	0.039	0.02574	0.00069	0.26001	163.8	4.3	Core	X
16A	34.3	1.4	5.1	0.3	2.35	0.099	0.0357	0.0016	0.087663	226	10	Rim	
16B	29.2	1.8	4.14	0.2	2.244	0.078	0.0316	0.0015	0.33801	200.2	9.1	Core	
17A	27.4	1.3	4.04	0.23	2.447	0.076	0.0331	0.0013	0.22959	210.1	8.4	Core	
17B	28.3	1.3	4.68	0.28	2.603	0.078	0.0357	0.0018	0.174	228	11	Core	
18A	43.8	1	3.95	0.17	1.446	0.046	0.02444	0.00076	0.4307	155.6	4.8	Core	
18B	31.46	0.55	4.53	0.17	2.337	0.068	0.0349	0.0012	0.16734	221.1	7.7	Core	
18C	31.46	0.44	3.99	0.16	2.124	0.085	0.0309	0.0012	0.53749	196	7.2	Rim	
19A	45.7	2.5	3.81	0.16	1.418	0.05	0.0238	0.001	0.45399	151.7	6.3	Core	
20A	232.2	7.5	7.18	0.18	0.5205	0.0097	0.01537	0.00026	0.43626	98.3	1.7	Core	
20B	60.4	2.7	4.03	0.14	1.102	0.023	0.0204	0.00059	0.16285	130.2	3.7	Core	
20C	72.8	3.4	3.7	0.14	0.86	0.018	0.01823	0.00049	0.25425	116.5	3.1	Core	
21A	65.6	2.9	4.82	0.18	1.258	0.054	0.02198	0.00071	0.62011	140.1	4.5	Core	
22A	31.8	2.8	3.76	0.16	2.081	0.086	0.0315	0.0012	0.59917	200.1	7.7	Core	
22B	72.1	2.2	3.92	0.14	0.893	0.018	0.01951	0.00048	0.15782	124.6	3	Rim	
23A	41.4	1.3	5.91	0.22	2.117	0.059	0.0322	0.0012	0.49913	204.2	7.3	Rim	X
23B	50.8	3.6	5.31	0.22	1.6	0.049	0.0263	0.001	0.40962	167.2	6.5	Core	X
23C	45.6	1.2	7.15	0.29	2.356	0.087	0.0339	0.0011	0.63305	214.7	6.8	Core	X
24A	20.59	0.99	5.12	0.23	3.96	0.18	0.0504	0.0028	0.52101	317	17	Core	X
25A	43.1	3.4	3.99	0.31	1.18	0.11	0.0215	0.0015	0.33726	136.9	9.7	Core	X
25B	20.69	0.91	4.51	0.23	3.277	0.094	0.0425	0.0016	0.50615	268.3	9.7	Core	X
25C	16.74	0.72	4.61	0.3	4.29	0.12	0.0536	0.0021	0.36497	339	12	Core	X
26A	19.53	0.78	3.87	0.13	3.039	0.081	0.0399	0.0011	0.32788	252.1	7.1	Core	X
27A	62.6	2.1	4.82	0.13	1.26	0.018	0.02242	0.00052	0.17085	142.9	3.3	Core	X
28A	41.6	1.4	4.5	0.16	1.689	0.037	0.02686	0.00074	0.013382	170.8	4.7	Core	X
28B	35.85	0.76	4.14	0.14	1.717	0.037	0.0289	0.0012	0.016346	183.6	7.7	Core	X

[1] Grain is numbered, points within grains are lettered.
[2] $^{207}Pb/^{235}U$ vs. $^{206}Pb/^{238}U$
[3] Grain is fish-shaped and indicates a top-to-the-southwest sense of shear

Table 8.4: U-Pb titanite data from the discrete shear zone sample H1. The table also includes the locations of analyzed points (i.e., core or rim of grain) and denotes which grains have been deformed into fish that indicate a top-to-the-SW sense of shear.

[1]Grain	~U (ppm)	+2σ	~Pb (ppm)	+2σ	$^{207}Pb/^{235}U$	+2σ	$^{206}Pb/^{238}U$	+2σ	[2]Error Correlation	$^{206}Pb/^{238}U$ Age	+2σ	Core/ Rim	[3]Fish
1A	188.5	7.9	5.13	0.2	0.463	0.01	0.01528	0.00029	0.38013	97.7	1.9	Rim	X
1B	200.4	2.1	4.78	0.15	0.428	0.014	0.01445	0.00027	0.52869	92.5	1.7	Core	X
2A	290.4	4.6	5	0.15	0.3192	0.0055	0.01301	0.00018	0.085413	83.3	1.1	Core	
2B	201.2	6.3	4.75	0.13	0.4278	0.007	0.01439	0.0003	0.17425	92.1	1.9	Core	
3A	360	18	5.02	0.13	0.2721	0.0062	0.01224	0.00018	0.28441	78.4	1.2	Rim	X
3B	81.7	4	5.37	0.18	1.121	0.036	0.0193	0.00059	0.48515	123.2	3.8	Core	X
4A	262.6	9.8	4.99	0.14	0.3715	0.0083	0.01326	0.00022	0.49251	84.9	1.4	Rim	X
4B	220	11	4.71	0.16	0.4002	0.0077	0.01416	0.00026	0.55142	90.9	1.7	Core	X
5A	140.4	7.7	5.53	0.29	0.669	0.043	0.0177	0.001	0.53888	113.1	6.6	Core	X
5B	165.8	3.5	6.77	0.22	0.595	0.015	0.01658	0.00049	0.24034	106	3.1	Rim	X
6A	88.6	2.2	4.84	0.17	0.934	0.025	0.01826	0.00045	0.37447	116.6	2.9	Core	
6B	36.85	0.75	3.62	0.16	1.603	0.051	0.02318	0.00099	0.10942	147.7	6.2	Core	
7A	36.9	1.3	3.59	0.11	1.477	0.042	0.0268	0.00095	0.26686	170.5	6	Core	X
8A	72.4	3.7	4.54	0.12	1.093	0.052	0.0199	0.00075	0.43481	127	4.8	Core	
9A	41.52	0.45	4.21	0.14	1.642	0.06	0.02658	0.00094	0.26278	169.1	5.9	Core	X
9B	86.9	5.2	4.49	0.18	0.899	0.037	0.01876	0.00066	0.47177	119.8	4.2	Core	X
10A	79	3.4	4.17	0.15	0.714	0.046	0.0176	0.0011	0.29539	112.5	6.8	Core	X
10B	10.53	0.58	2.137	0.089	3.21	0.11	0.0427	0.0018	0.4507	269	11	Core	X
11A	136.4	6.6	5.5	0.14	0.668	0.021	0.01658	0.00036	0.54566	106	2.3	Rim	X
11B	122.9	2.7	10.38	0.3	1.415	0.037	0.0245	0.00048	0.72783	156	3	Core	X
12A	66	3.2	4.91	0.19	1.353	0.043	0.02276	0.0007	0.46131	145	4.4	Rim	X
12B	210.4	3.9	6.45	0.16	0.478	0.011	0.01476	0.00024	0.10171	94.4	1.5	Core	X
12C	156	10	4.93	0.15	0.556	0.023	0.01563	0.00037	0.42876	100	2.4	Core	X
13A	160.8	2.7	4.25	0.17	0.444	0.016	0.01474	0.00059	0.44297	94.3	3.8	Core	
13B	57.8	1.9	4.62	0.11	1.305	0.03	0.02318	0.00066	0.44005	147.7	4.1	Core	
14A	131.3	7.2	4.19	0.31	0.509	0.045	0.0169	0.001	0.27288	108	6.4	Core	
15A	39.28	0.62	4.31	0.13	1.782	0.049	0.02857	0.00092	0.34301	182.3	5.7	Rim	
15B	19.06	0.61	3.26	0.14	2.74	0.12	0.0357	0.0021	0.24949	226	13	Core	

[1] Grain is numbered, points within grains are lettered.
[2] $^{206}Pb/^{238}U$ vs. $^{207}Pb/^{235}U$
[3] Grain is fish-shaped and indicates a top-to-the-southwest sense of shear

Table 8.5: U-Pb titanite data from the discrete shear zone sample SCM-17. The table also includes the locations of analyzed points (i.e., core or rim of grain) and denotes which grains have been deformed into fish that indicate a top-to-the-SW sense of shear.

[1]Grain	~U (ppm)	±2σ	~Pb (ppm)	±2σ	$^{207}Pb/^{235}U$	±2σ	$^{206}Pb/^{238}U$	±2σ	[2]Error Correlation	$^{206}Pb/^{238}U$ Age	±2σ	Core/ Rim	[3]Fish
1A	33.4	1.3	5.01	0.2	2.502	0.04	0.0362	0.001	0.35995	229	6.3	Core	
1B	37.8	1.5	5.78	0.17	2.577	0.045	0.0363	0.001	0.62079	229.6	6.5	Core	
1C	46.7	2.1	5.4	0.33	1.91	0.14	0.0305	0.0019	0.76554	194	12	Core	
1D	203.1	3.3	13.12	0.74	1.041	0.04	0.02134	0.00048	0.71577	136.1	3	Core	
1E	67.6	2	8.68	0.25	2.15	0.057	0.03207	0.00085	0.67528	203.5	5.3	Core	
1F	100.1	6	6.57	0.3	1.144	0.081	0.02131	0.00085	0.80997	135.9	5.4	Core	
1G	31.99	0.8	5.26	0.2	2.663	0.096	0.0376	0.0013	0.84063	237.9	8	Core	
1H	41	1.6	6.11	0.25	2.466	0.07	0.0344	0.0011	0.53261	218.2	6.9	Rim	
2A	126	12	6.56	0.42	0.91	0.056	0.02064	0.00075	0.80658	131.7	4.8	Core	
2B	34.9	3	4.23	0.21	2.04	0.1	0.0325	0.0012	0.68779	206	7.3	Core	
3A	147	21	4.97	0.18	0.681	0.081	0.01672	0.00096	0.90246	106.8	6.1	Rim	
3B	386	20	6.19	0.26	0.2808	0.0088	0.01375	0.00024	0.41401	88.1	1.6	Core	
3C	402	15	5.71	0.17	0.2534	0.004	0.01386	0.00018	0.32432	88.7	1.1	Core	
4A	83.2	4.1	4.2	0.14	0.805	0.034	0.01941	0.00069	0.59888	123.9	4.3	Rim	X
4B	32.13	0.89	4.74	0.21	2.318	0.08	0.035	0.0012	0.90431	221.7	7.2	Rim	X
4C	159.7	4.2	5.47	0.2	0.5713	0.0098	0.01728	0.00029	0.2389	110.4	1.8	Core	X
4D	15.1	1.1	2.8	0.19	2.823	0.068	0.0391	0.0016	0.26506	246.9	9.8	Core	X
4E	10.79	0.41	2.341	0.095	3.21	0.071	0.0447	0.0014	0.24747	281.7	8.8	Core	X
4F	15.07	0.6	3.24	0.13	3.223	0.065	0.044	0.0013	0.40646	277.7	8.2	Core	X
4G	10.49	0.32	2.374	0.068	3.515	0.09	0.0457	0.0015	0.29914	288.1	9.5	Core	X
4H	27.9	1.8	3.44	0.15	2.102	0.07	0.0323	0.0014	0.48143	204.7	8.6	Core	X
4I	15.9	1.1	2.9	0.12	2.918	0.073	0.0415	0.0015	0.53948	261.9	9.5	Core	X
4J	14.15	0.57	2.33	0.11	2.646	0.062	0.0371	0.0013	0.12423	235	8	Core	X
5A	117.9	3.8	5.82	0.14	0.75	0.024	0.02021	0.00047	0.44875	129	3	Core	X
5B	19.58	0.4	3.16	0.11	2.58	0.11	0.0383	0.0015	0.72263	242.1	9.4	Core	X
5C	73	12	4.25	0.23	0.97	0.14	0.0203	0.0021	0.88463	129	13	Core	X
5D	22.14	0.98	3.46	0.11	2.315	0.081	0.0361	0.0012	0.6719	229.7	7.6	Core	X
6A	408	23	6.28	0.24	0.2595	0.0061	0.0136	0.00018	0.62125	87.1	1.2	Rim	
6B	464	10	7	0.24	0.2354	0.0033	0.01328	0.00017	0.03981	85	1.1	Core	
7A	417	12	4.4	0.2	0.2058	0.0059	0.01259	0.00024	0.026218	80.7	1.5	Core	
8A	320	14	11.68	0.7	0.498	0.019	0.01413	0.0003	0.77738	90.4	1.9	Core	

[1] Grain is numbered, points within grains are lettered.
[2] $^{206}Pb/^{238}U$ vs. $^{207}Pb/^{235}U$
[3] Grain is fish-shaped and indicates a top-to-the-southwest sense of shear

Table 8.6: U-Pb titanite data from the discrete shear zone sample SCM-12. The table also includes the locations of analyzed points (i.e., core or rim of grain) and denotes which grains have been deformed into fish that indicate a top-to-the-southwest sense of shear.

[1]Grain	~U (ppm)	+2σ	~Pb (ppm)	+2σ	$^{207}Pb/^{235}U$	+2σ	$^{206}Pb/^{238}U$	+2σ	[2]Error Correlation	$^{206}Pb/^{238}U$ Age	+2σ	Core/ Rim
1A	205.3	5.9	8.05	0.23	0.68	0.021	0.01654	0.00038	0.25983	105.8	2.4	Rim
1B	138.5	3.8	7.95	0.33	0.936	0.034	0.02011	0.00046	0.4837	128.4	2.9	Rim
2A	237.1	6.8	7.11	0.16	0.4389	0.0064	0.01539	0.00024	0.12839	98.5	1.5	Core
2B	204	17	5.78	0.17	0.49	0.034	0.01494	0.00045	0.6847	95.6	2.8	Core
3A	100.5	2.9	4.83	0.17	0.81	0.014	0.01871	0.00038	0.31223	119.5	2.4	Core
4A	17.53	0.27	2.74	0.12	2.581	0.083	0.0365	0.0016	0.45517	230.8	9.7	Core
4B	10.55	0.29	2.48	0.15	3.7	0.21	0.0466	0.0028	0.94878	293	17	Rim
4C	15.04	0.87	3.48	0.18	3.66	0.15	0.0464	0.0022	0.6657	292	14	Core
5A	18.93	0.74	3.61	0.14	3.002	0.077	0.0401	0.0012	0.4611	253.3	7.3	Core
5B	17.9	0.87	2.48	0.11	2.25	0.064	0.0331	0.0011	0.33272	209.8	6.9	Rim
5C	16.07	0.55	2.86	0.12	2.916	0.099	0.0402	0.0013	0.58598	253.7	7.9	Core
5D	14.82	0.56	3.34	0.23	3.54	0.2	0.0463	0.0027	0.93537	291	16	Core
5E	13.96	0.47	2.793	0.091	3.197	0.095	0.0432	0.0017	0.50072	273	10	Core
5F	32.72	0.75	4.66	0.27	2.469	0.073	0.0345	0.0011	0.011893	218.4	6.5	Core
5G	21.39	0.43	3.175	0.07	2.424	0.048	0.0346	0.0011	0.10061	219.4	6.9	Core
6A	122	6	6.68	0.16	0.89	0.032	0.0189	0.00052	0.28495	120.7	3.3	Core
7A	177.7	8.3	4.97	0.18	0.478	0.0074	0.01507	0.00026	0.32764	96.4	1.7	Core
8A	123.6	3.5	4.72	0.11	0.6477	0.0082	0.01736	0.00031	0.17524	111	1.9	Core
8B	258	10	5.63	0.18	0.412	0.01	0.01399	0.0003	0.61513	89.5	1.9	Core
8C	42.5	1.6	4.31	0.13	1.717	0.032	0.02701	0.00059	0.35469	171.8	3.7	Core
9A	201.4	8.6	5.5	0.17	0.4858	0.0085	0.01515	0.00024	0.38535	96.9	1.6	Rim
10A	219.9	7.8	5.16	0.15	0.4218	0.0059	0.01443	0.00022	0.30357	92.4	1.4	Core
11A	154	5.3	4.95	0.17	0.531	0.025	0.01554	0.00045	0.685	99.4	2.9	Core
12A	107.2	1.3	5.45	0.24	0.852	0.038	0.01834	0.00054	0.62588	117.1	3.4	Core
13A	228.3	3.9	5.29	0.17	0.4218	0.0085	0.01373	0.0003	0.25883	87.9	1.9	Core
14A	217.5	7	5.86	0.16	0.4692	0.0059	0.01509	0.00022	0.28267	96.6	1.4	Core
15A	45.6	2	4.84	0.17	1.638	0.034	0.02548	0.00058	0.33943	162.2	3.6	Core
16A	47	1.7	4.87	0.15	1.628	0.02	0.02552	0.00064	0.10814	162.4	4	Rim
17A	60.65	0.7	4.71	0.1	1.242	0.038	0.02235	0.00052	0.49647	142.5	3.2	Rim
18A	425	16	7.88	0.26	0.2934	0.0033	0.01365	0.00015	0.21688	87.39	0.94	Rim
19A	118.3	4.7	5.29	0.17	0.736	0.011	0.01739	0.0003	0.25136	111.1	1.9	Rim
20A	244.7	6.4	5.19	0.2	0.3776	0.0062	0.01332	0.0002	0.32762	85.3	1.3	Core
21A	252.4	9.6	5.34	0.21	0.3777	0.0059	0.01358	0.00023	0.24819	86.9	1.4	Rim
22A	56.6	1.9	4.63	0.17	1.339	0.026	0.02294	0.00058	0.011518	146.2	3.6	Core

[1] Grain is numbered, points within grains are lettered.
[2] $^{206}Pb/^{238}U$ vs. $^{207}Pb/^{235}U$

Table 8.7: U-Pb titanite data from the discrete shear zone sample SCM-51. The table also includes the locations of analyzed points (i.e., core or rim of grain). The data was obtained from the highly metamorphosed bleached halo portion of the shear zone.

[1]Grain	~U (ppm)	+2σ	~Pb (ppm)	+2σ	$^{207}Pb/^{235}U$	+2σ	$^{206}Pb/^{238}U$	+2σ	[2]Error Correlation	$^{206}Pb/^{238}U$ Age	+2σ	Core/ Rim	[3]Fish
1A	330	24	4.94	0.34	0.3063	0.0092	0.01308	0.00028	0.4035	83.8	1.8	Rim	
1B	65.1	2.8	4.98	0.28	1.27	0.053	0.0243	0.00084	0.57155	154.7	5.3	Core	
2A	91.7	7.6	5.56	0.31	1.141	0.077	0.0215	0.0014	0.6234	136.8	9	Rim	
2B	56.5	1.5	5.19	0.26	1.413	0.069	0.0256	0.0012	0.53263	163.8	7.6	Core	
2C	145	15	5.73	0.78	0.738	0.04	0.0155	0.0012	0.54322	99	7.5	Rim	
3A	100	11	4.63	0.35	0.873	0.039	0.0166	0.00081	0.1381	106.1	5.1	Rim	
3B	150.1	7	4.68	0.25	0.572	0.016	0.01552	0.00038	0.12443	99.6	2.3	Core	
3C	222	12	6.11	0.33	0.537	0.034	0.01393	0.00078	0.22402	89.2	5	Rim	
4A	138.4	8.6	5.33	0.3	0.72	0.028	0.01748	0.00056	0.6043	111.7	3.6	Core	
4B	115.4	5.4	4.92	0.32	0.752	0.039	0.01655	0.00099	0.19985	105.8	6.3	Rim	
5A	71	11	6.47	0.49	1.81	0.26	0.0273	0.0025	0.62764	173	16	Rim	X
5B	25.2	1.1	3.56	0.2	2.294	0.097	0.0336	0.0016	0.29329	213.2	9.7	Core	X
5C	54.2	4.5	5.17	0.23	1.696	0.084	0.0259	0.0014	0.076511	164.6	8.8	Rim	X
6A	210	23	5.21	0.37	0.463	0.03	0.01485	0.00069	0.40124	95	4.4	Core	X
6B	99.1	8.5	6.15	0.33	1.009	0.058	0.0198	0.0012	0.61222	126.3	7.5	Rim	X
7A	604	40	5.12	0.29	0.2077	0.0076	0.01159	0.0004	0.43328	74.3	2.6	Rim	X
7B	130.3	5.5	5.46	0.27	0.693	0.038	0.01651	0.00076	0.57687	105.5	4.8	Core	X
7C	80.6	5.4	4.68	0.21	0.954	0.035	0.01868	0.00081	0.44414	119.3	5.1	Rim	X
8A	126	10	6.51	0.36	0.876	0.051	0.0173	0.0012	0.47827	110.8	7.9	Rim	
8B	18.2	2.7	5.8	0.82	4.74	0.23	0.0541	0.0041	0.42207	339	25	Rim	
8C	42.8	3	4.77	0.24	1.834	0.05	0.0283	0.0011	0.17094	180	7.1	Core	
8D	92.9	6.5	5.59	0.31	0.977	0.042	0.01966	0.00075	0.29202	125.5	4.8	Rim	
9A	102.9	3.1	4.74	0.37	0.712	0.042	0.01696	0.00077	0.2471	108.4	4.9	Core	
9B	87.7	1.6	4.95	0.28	0.841	0.035	0.01844	0.00065	0.21539	117.7	4.1	Rim	
10A	345	19	7.18	0.32	0.2864	0.0069	0.01321	0.00024	0.092778	84.6	1.5	Core	X
10B	331.1	4.5	4.52	0.14	0.256	0.01	0.01176	0.00026	0.24708	75.4	1.6	Rim	X
11A	42.2	1.5	4.05	0.17	1.591	0.042	0.02584	0.00098	0.17678	165.2	6.1	Core	X
11B	81.4	2.1	4.01	0.21	0.821	0.034	0.01915	0.00095	0.21654	122.2	6	Rim	X
11C	28.7	1.8	3.94	0.24	2.241	0.08	0.032	0.0013	0.32477	203.1	8	Rim	X
11D	38.8	3.3	4.24	0.48	1.745	0.078	0.0269	0.0019	0.27489	171	12	Rim	
12A	84.6	3.4	3.47	0.38	0.549	0.045	0.0152	0.0015	0.18097	97.4	9.5	Rim	
12B	124.7	9.8	4.67	0.35	0.581	0.021	0.01641	0.00044	0.081975	104.9	2.8	Core	
13A	32.7	1.3	3.86	0.2	2.063	0.074	0.0298	0.0018	0.28404	189	11	Rim	X
14A	79	1.9	4.74	0.24	0.982	0.03	0.02005	0.00087	0.23746	127.9	5.5	Core	
14B	108.5	2.3	4.11	0.26	0.634	0.017	0.01365	0.00053	0.084686	87.4	3.3	Rim	
14C	40.8	0.48	6.84	0.36	2.782	0.089	0.0341	0.0022	0.22723	216	14	Rim	
15A	61.3	1.2	4.77	0.37	1.183	0.059	0.0198	0.0013	0.072859	126.1	8.1	Core	
16A	192.1	9.2	4.09	0.2	0.403	0.018	0.01338	0.00043	0.40873	85.7	2.7	Core	
16B	93	3.6	3.22	0.22	0.578	0.048	0.01343	0.0007	0.47917	86	4.5	Core	
17A	86.5	5.7	3.86	0.19	0.806	0.051	0.01698	0.00075	0.59075	108.5	4.7	Rim	
17B	176	12	3.93	0.22	0.423	0.016	0.01385	0.00039	0.22084	88.7	2.5	Core	
18A	226.7	9.5	4.4	0.24	0.368	0.017	0.01337	0.0005	0.58553	85.6	3.2	Core	
19A	80.6	2.1	4.46	0.16	0.929	0.021	0.02044	0.00048	0.12624	130.4	3	Core	
19B	110.8	4.8	4.55	0.19	0.737	0.011	0.01826	0.00038	0.32739	116.6	2.4	Core	
19C	66.9	1.8	3.94	0.15	1.032	0.029	0.0196	0.00045	0.1391	125.1	2.8	Core	
20A	182.8	3.7	4.11	0.13	0.408	0.014	0.01514	0.00028	0.45848	96.9	1.8	Core	
20B	150.1	3.1	3.73	0.12	0.469	0.022	0.01514	0.00037	0.58473	96.9	2.3	Core	
20C	59	2.2	3.04	0.1	0.864	0.015	0.01779	0.00054	0.16329	113.6	3.4	Core	
20D	32.5	4.9	6.56	0.75	3.91	0.25	0.0459	0.0032	0.74197	289	20	Rim	
20E	163.4	7.1	7.27	0.36	0.776	0.028	0.0174	0.00057	0.44153	111.6	3.5	Rim	
21A	295.8	9.3	4.69	0.16	0.3034	0.0064	0.01359	0.00024	0.075495	87	1.5	Core	
21B	61.6	2.6	4.25	0.12	1.172	0.027	0.02167	0.0006	0.40476	138.2	3.8	Core	
21C	78.7	5.9	4.54	0.17	1.025	0.036	0.02149	0.00072	0.64218	137	4.5	Core	
22A	48	3.2	3.78	0.14	1.366	0.051	0.02279	0.00077	0.15332	145.2	4.9	Rim	X
22B	137	19	4.37	0.18	0.633	0.044	0.01609	0.00066	0.6207	102.9	4.2	Core	X
22C	62.9	2.9	3.17	0.16	0.86	0.025	0.01828	0.00071	0.31308	116.8	4.5	Core	X
22D	59.3	3.4	3.55	0.15	1.045	0.024	0.01955	0.00043	0.24153	124.8	2.7	Core	X
23A	128.4	4.8	6.82	0.4	0.967	0.041	0.01938	0.00073	0.11519	123.8	4.6	Rim	X
23B	204	12	6.35	0.23	0.4868	0.0084	0.01513	0.00026	0.11355	96.8	1.7	Core	X
23C	65.3	5.6	5.55	0.28	1.546	0.078	0.02454	0.00088	0.31669	156.3	5.6	Core	X
24A	77.89	0.9	4.49	0.15	0.956	0.026	0.01969	0.00047	0.22677	125.7	3	Core	X
24B	55	1.4	4.67	0.16	1.401	0.028	0.02518	0.00051	0.050395	160.3	3.2	Core	X
25A	37.82	0.58	4.04	0.19	1.702	0.054	0.027	0.0012	0.27698	171.8	7.6	Core	
25B	36.1	1.3	4.76	0.23	2.138	0.049	0.0319	0.0013	0.48261	202.6	7.9	Core	
25C	66.3	4.1	4.55	0.17	1.206	0.032	0.02227	0.00077	0.32546	142	4.8	Core	
26A	412.5	8.5	4.42	0.15	0.2197	0.0075	0.01141	0.00021	0.1125	73.1	1.4	Core	
26B	77.9	2.2	5.31	0.16	1.131	0.021	0.02153	0.00053	0.16059	137.3	3.3	Rim	
27A	72.9	2.6	4.15	0.14	0.947	0.014	0.01875	0.00043	0.019239	119.7	2.7	Core	X
27B	68.2	2.8	4.42	0.18	1.061	0.02	0.01983	0.00055	0.26803	126.6	3.5	Core	X
27C	251	10	5.37	0.16	0.3702	0.0062	0.01453	0.00024	0.23511	93	1.5	Core	X

[1] Grain is numbered, points within grains are lettered.

[2] $^{207}Pb/^{235}U$ vs. $^{206}Pb/^{238}U$

[3] Grain is fish-shaped and indicates a top-to-the-southwest sense of shear

Table 8.8: U-Pb titanite data from the Stone Corral ridge shear zone sample H3. The table also includes the locations of analyzed points (i.e., core or rim of grain) and denotes which grains have been deformed into fish that indicate a top-to-the-southwest sense of shear.

[1]Grain	~U (ppm)	+2σ	~Pb (ppm)	+2σ	$^{207}Pb/^{235}U$	+2σ	$^{206}Pb/^{238}U$	+2σ	[2]Error Correlation	$^{206}Pb/^{238}U$ Age	+2σ	Core/ Rim	[3]s.b
1A	96.2	5.1	6.12	0.24	1.03	0.053	0.02015	0.00075	0.51077	128.6	4.7	Core	
1B	187.9	6.2	6.25	0.22	0.564	0.02	0.0153	0.0004	0.44363	97.9	2.5	Core	
1C	28.2	1.8	4.41	0.18	2.383	0.087	0.0356	0.0016	0.66263	225.3	9.7	Core	
1D	95.7	3.7	5.31	0.14	0.895	0.018	0.01971	0.00047	0.47651	125.8	2.9	Rim	
2A	59.9	1.7	5.07	0.16	1.352	0.023	0.02391	0.00058	0.07573	152.3	3.6	Rim	
2B	55.5	2.5	4.87	0.16	1.477	0.038	0.02538	0.00067	0.64364	161.6	4.2	Core	
3B	302	18	4.83	0.12	0.326	0.012	0.01256	0.00026	0.56264	80.4	1.7	Core	
3C	117.1	4.9	5.17	0.15	0.826	0.026	0.01836	0.0008	0.60822	117.3	5.1	Rim	
3D	42.7	0.99	4.61	0.11	1.718	0.038	0.02806	0.0007	0.43586	178.4	4.4	Rim	
3E	429	20	7.4	0.21	0.2872	0.0073	0.01384	0.00025	0.60674	88.6	1.6	Core	
3F	355	21	7.95	0.39	0.347	0.01	0.01454	0.00027	0.47894	93	1.7	Core	
3G	248	17	6.45	0.21	0.466	0.022	0.01528	0.00043	0.61575	97.7	2.7	Core	
4A	467	22	9.91	0.25	0.346	0.013	0.01419	0.0003	0.48779	90.8	1.9	Core	
4B	66.1	4	6.23	0.21	1.583	0.046	0.0263	0.00066	0.63056	167.3	4.2	Rim	
4C	144.7	9.8	6.99	0.31	0.827	0.026	0.01895	0.00047	0.66603	121.5	3.1	Core	
5A	54.9	1.3	6.33	0.21	1.891	0.034	0.02896	0.00062	0.51775	184	3.9	Core	
5B	49.9	1.1	7.31	0.2	2.436	0.084	0.0345	0.001	0.59403	218.7	6.5	Core	
5C	85.2	2.7	9.58	0.52	1.856	0.075	0.0277	0.0012	0.055957	175.8	7.6	Rim	
5D	251.6	8.1	8.8	0.48	0.548	0.027	0.01333	0.0007	0.2313	85.4	4.4	Rim	
5E	382	12	10.75	0.7	0.488	0.023	0.01204	0.00048	0.4891	77.2	3.1	Rim	
5F	639	81	13.19	0.64	0.456	0.067	0.01357	0.00068	0.85079	86.9	4.3	Rim	
6A	99.3	2.8	4.75	0.14	0.759	0.029	0.0204	0.00075	0.37573	130.1	4.8	Core	
6B	53.5	2.3	4.52	0.15	1.436	0.025	0.02512	0.00058	0.35264	159.9	3.7	Core	
6C	42	1.6	4.97	0.17	1.907	0.031	0.02971	0.00075	0.23544	188.7	4.7	Core	
7A	48.9	1.8	4.66	0.18	1.549	0.029	0.02621	0.00058	0.45311	166.7	3.6	Core	
8a	117.7	3.8	6	0.21	0.83	0.014	0.01867	0.00038	0.33769	119.3	2.4	Core	
8b	72.6	2.2	5.3	0.17	1.215	0.026	0.02261	0.00066	0.093428	144.1	4.2	Core	
9A	206.9	6	5.2	0.16	0.472	0.011	0.01619	0.00026	0.33406	103.5	1.6	Core	
10A	144	5.3	4.94	0.13	0.611	0.012	0.01681	0.00033	0.50324	107.5	2.1	Core	
10B	89.1	6.2	5.19	0.16	1.017	0.048	0.02062	0.00051	0.62071	131.5	3.2	Core	
10C	61	2.1	5.12	0.16	1.414	0.045	0.02291	0.00099	0.59986	146	6.2	Rim	
11A	114.9	5.7	5.63	0.18	0.778	0.022	0.01855	0.00044	0.66137	118.5	2.8	Core	
11B	81.4	2.3	6.86	0.5	1.363	0.052	0.02264	0.00078	0.46804	144.3	4.9	Core	
12A	49.1	2.9	5.47	0.14	1.833	0.071	0.02915	0.00088	0.74479	185.2	5.5	Rim	X
12B	66.3	5	4.22	0.16	1.08	0.051	0.0225	0.0012	0.66442	143.3	7.3	Rim	X
12C	22.56	0.96	3.99	0.17	2.803	0.051	0.0402	0.001	0.35773	254.3	6.4	Core	X
12D	31.4	1.3	3.54	0.16	1.857	0.039	0.0294	0.00071	0.29078	186.7	4.4	Core	X
12E	34.3	1.8	4.71	0.19	2.226	0.075	0.0322	0.0015	0.42133	204	9.1	Core	X
12F	31.46	0.79	4.04	0.14	2.079	0.034	0.03039	0.00068	0.17646	193	4.2	Core	X
12G	30.2	1.4	5.4	0.28	2.854	0.066	0.0384	0.0012	0.55804	243	7.2	Core	X
12H	35.56	0.46	4.63	0.14	2.172	0.05	0.0307	0.0012	0.46704	195.1	7.4	Rim	X
12I	22.39	0.54	3.881	0.095	2.82	0.062	0.0396	0.0011	0.3701	250.1	6.7	Rim	X
13A	203.7	4	5.54	0.24	0.494	0.017	0.01316	0.00047	0.19688	84.3	3	Rim	X
13B	37.58	0.78	5.09	0.21	2.06	0.11	0.0307	0.0015	0.55068	195	9.5	Rim	X
13C	150	13	5.78	0.46	0.683	0.069	0.0158	0.0012	0.48107	100.9	7.7	Rim	X
13D	42.7	2	4.53	0.3	1.578	0.046	0.0261	0.0012	0.066367	165.8	7.5	Rim	X
13E	157.7	3.4	6.04	0.2	0.661	0.015	0.01751	0.00033	0.24273	111.9	2.1	Core	X
13F	211.2	3.5	5.8	0.13	0.472	0.011	0.01555	0.0003	0.32887	99.5	1.9	Core	X
13G	103.2	5.4	6.85	0.17	1.159	0.038	0.0216	0.00062	0.73482	137.7	3.9	Core	X
14A	47	1.2	8.03	0.3	2.78	0.081	0.0387	0.0013	0.76267	244.7	7.8	Rim	X
14B	596	16	7.94	0.39	0.249	0.01	0.01343	0.00051	0.59377	86	3.3	Core	X
14C	292.4	5.6	8.23	0.27	0.4886	0.0089	0.01656	0.00023	0.47493	105.8	1.4	Core	X
14D	161.7	5.3	7.95	0.37	0.833	0.019	0.01973	0.00038	0.46982	125.9	2.4	Core	X
14E	158.8	4.7	7.79	0.22	0.828	0.031	0.01815	0.00026	0.13276	115.9	1.7	Core	X
14F	74.35	0.8	11.35	0.19	2.509	0.046	0.03354	0.00059	0.6566	212.7	3.7	Core	X
14G	62.6	2.7	6.2	0.23	1.624	0.041	0.02505	0.00064	0.36247	159.5	4	Core	X
14H	747	11	8.26	0.34	0.2201	0.008	0.01049	0.00019	0.098386	67.3	1.2	Rim	X
14I	491	17	6.95	0.42	0.2667	0.0092	0.01032	0.00022	0.44569	66.2	1.4	Rim	X
15A	505	23	4.44	0.11	0.207	0.0042	0.01266	0.0002	0.68875	81.1	1.3	Core	
15B	69.7	1.7	4.05	0.14	1.007	0.019	0.02209	0.00054	0.093651	140.9	3.4	Core	

[1] Grain is numbered, points within grains are lettered.
[2] $^{206}Pb/^{238}U$ vs. $^{207}Pb/^{235}U$
[3] s.b. = grain is within a shear band that crosscuts the foliation

Table 8.9: U-Pb titanite data from the Stone Corral ridge shear zone sample SCM-19. The table also includes the locations of analyzed points (i.e., core or rim of grain) and denotes which grains were located within shear bands that crosscut the foliation.

Grain	~U (ppm)	+2σ	$^{207}Pb/^{235}U$	+2σ	$^{206}Pb/^{238}U$	+2σ	*Error Correlation	$^{206}Pb/^{238}U$ Age	+2σ
1	221	18	0.0734	0.0023	0.01077	0.00019	0.39932	69.1	1.2
2	670	140	0.071	0.0029	0.01107	0.00023	0.016316	70.9	1.4
3	570.8	6.6	0.0737	0.0015	0.01126	0.00019	0.42455	72.2	1.2
4	125.4	8.8	0.0719	0.0021	0.0113	0.00019	0.20498	72.5	1.2
5	85.7	5.4	0.0781	0.0055	0.01139	0.00021	0.10748	73	1.4
6	43.7	5.8	0.08	0.014	0.01144	0.00038	0.0016712	73.3	2.4
7	70	11	0.07	0.006	0.01171	0.00041	0.19255	75	2.6
8	498	88	0.0769	0.0021	0.0117	0.00019	0.12489	75	1.2
9	24.6	2.6	0.0764	0.0096	0.01173	0.00054	0.033718	75.1	3.4
10	40.7	2.3	0.082	0.01	0.01173	0.00042	0.11047	75.1	2.7
11	99.2	1.3	0.0762	0.0041	0.01182	0.00021	0.11986	75.7	1.4
12	1635	52	0.07711	0.00087	0.01186	0.00013	0.24117	75.98	0.82
13	850	26	0.0756	0.0013	0.01186	0.00021	0.43058	76	1.3
14	398	20	0.0785	0.0017	0.01202	0.00024	0.36456	77	1.5
15	30.4	3	0.089	0.015	0.01207	0.00064	0.13964	77.3	4.1
16	577	22	0.0807	0.0011	0.01207	0.00011	0.24768	77.34	0.72
17	664	62	0.0813	0.0016	0.01212	0.00014	0.44589	77.63	0.88
18	162	13	0.0786	0.0096	0.0122	0.0008	0.65305	78.1	5.1
19	267	40	0.0852	0.0027	0.01247	0.0002	0.19224	79.9	1.3
20	222	81	0.0812	0.0029	0.01251	0.00023	0.25993	80.1	1.5
21	87.8	8.2	0.0924	0.0059	0.01516	0.00064	0.437	97	4.1
22	470	28	2.12	0.18	0.153	0.011	0.99448	918	64
23	626	40	2.589	0.084	0.1857	0.0055	0.99296	1097	30
24	179	12	3.456	0.074	0.2418	0.0044	0.86571	1396	23

$*^{206}Pb/^{238}U$ vs. $^{207}Pb/^{235}U$

Table 8.10: U-Pb zircon data from the Brown's Canyon granite sample AZSC-6.

Country Rock Samples		Whole Sample	Rims	Cores	Shear bands	Foliation
Sample HQ-D	Age (Ma)	71.0 ± 2.1	71.6 ± 3.9	71.0 ± 2.3	70.5 ± 32	71.5 ± 3.1
	MSWD	4.1	2.3	4.5	4.6	3.6
	No. of grains analyzed	20	5	19	14	6
	No. of points analyzed	40	5	35	25	15
Sample SCM-6	Age (Ma)	72.0 ± 1.7	66.7 ± 6.2	72.4 ± 1.9	67.5 ± 8.0	72.4 ± 2.8
	MSWD	10	7.1	9.9	2.2	16
	No. of grains analyzed	12	4	12	2	10
	No. of points analyzed	27	7	20	11	16
Sample SCM-48-2	Age (Ma)	75.6 ± 4.0	79 ± 37	72.7 ± 5.4		
	MSWD	7.6	6.5	7.4		
	No. of grains analyzed	6	3	6		
	No. of points analyzed	21	3	18		
Discrete Shear Zone Samples		**Whole Sample**	**Rims**	**Cores**	**Fish Shaped**	**Not Fish Shaped**
Sample H1	Age (Ma)	69.1 ± 2.5	72.1 ± 6	68.2 ± 2.7	68.7 ± 4.8	68.8 ± 3.9
	MSWD	3.1	4	2.7	3.1	4
	No. of grains analyzed	28	17	26	16	12
	No. of points analyzed	62	23	39	38	24
Sample SCM-17	Age (Ma)	67.9 ± 2.4	65.9 ± 6.4	68.9 ± 3.0	67.3 ± 3.1	68.9 ± 4.9
	MSWD	9.7	15	8.6	10.3	9.2
	No. of grains analyzed	15	7	15	9	6
	No. of points analyzed	28	7	21	18	10
Sample SCM-12	Age (Ma)	74.7 ± 2.4	75.0 ± 6.4	74.6 ± 3.0	81.1 ± 4.3	74.6 ± 3.0
	MSWD	17	13	19	3.9	22
	No. of grains analyzed	8	4	8	2	6
	No. of points analyzed	31	5	26	14	17
Sample SCM-51	Age (Ma)	70.7 ± 1.7	72.1 ± 3.1	69.8 ± 2.2		
	MSWD	8.4	8.6	8.3		
	No. of grains analyzed	22	9	15		
	No. of points analyzed	34	10	24		
Stone Corral Mtn. Mylonite		**Whole Sample**	**Rims**	**Cores**	**Fish Shaped**	**Not Fish Shaped**
Sample H3	Age (Ma)	69.4 ± 2.2	65.4 ± 3.1	70.4 ± 2.7	70.0 ± 2.9	68.9 ± 3.2
	MSWD	10.3	6	10.3	7.2	12
	No. of grains analyzed	27	20	26	10	17
	No. of points analyzed	70	29	41	26	44
Stone Corral Mtn. Protomylon.		**Whole Sample**	**Rims**	**Cores**	**Shear bands**	**Foliation**
Sample SCM-19	Age (Ma)	71.6 ± 3.0	53.9 ± 3.7	75.3 ± 2.4	69.2 ± 6.4	72.8 ± 2.9
	MSWD	33	12	16	54	18
	No. of grains analyzed	15	10	15	3	12
	No. of points analyzed	60	21	39	25	35

Table 8.11: Summary of titanite data for all samples. For each sample, the age of the entire sample, the age of the rims of the grains, and the age of the cores of the grains are provided. For the country rock and protomylonite samples, the ages of the grains within crosscutting shear bands and the ages of the remaining grains that lay parallel to the foliation are provided. For the mylonitic samples, the ages of highly deformed fish-shaped grains that indicate a top-to-the-southwest sense of shear and the ages of the remaining grains that are less deformed are provided. The MSWD, number of grains analyzed, and number of points analyzed are also provided for each date.

Sample AZSC-6	**Lower Intercept Age (Ma)**	75.7 ± 1.8
	Upper Intercept Age (Ma)	1672 ± 22
	MSWD	8.8
	No. of grains analyzed	24
	No. of points analyzed	24

Table 8.12: Summary of zircon data for the Brown's Canyon granite sample AZSC-6.

Chapter 9: Synthesis

The many methods used to study the rocks of the Stone Corral study area in the Harquahala Mountains served to answer two important questions related to the origins of the area's shear zones: 1) What are the physiochemical processes responsible for the localization of shear into the discrete zones in the northern part of the study area?, and 2) Did the shear zones form during Miocene metamorphic core complex (MCC) deformation or during an earlier event? A synthesis of all the data is presented in this chapter, and the two major questions of this study are addressed in detail.

9.1 The Structural and Chemical Processes Responsible for Strain Localization

9.1.1 Antecedent Fractures: A Macroscopic Control on the Development of the Discrete Shear Zones

Field and petrographic work provide ample evidence for the localization of shear strain along fractures. The discrete shear zones all share similar orientations, and some of them contain deformed quartz and/or epidote veins that must have precipitated in fractures before undergoing deformation. The shear zones have very sharp boundaries and are very narrow (most with $\leq$5 cm widths), consistent with their localization on fractures (Figures 1.4, 1.5). Several shear zones, when traced laterally along strike, die out into fractures that extend much further along strike until exposure is lost (Figure 2.4). A few shear zones were identified that are defined by about a millimeter of shear along fracture walls, which provides strong evidence for at least some shearing along fractured surfaces, and may represent how shearing appeared in its initial stages. One of the large shear zones in the field area appears to bifurcate into several different zones along its length, resembling a fracture splay (Figure 1.5F).

Fourier Transform Infrared (FTIR) spectroscopy analyses of intragranular quartz reveal that the quartz in the discrete shear zone mylonites contains higher water contents than the quartz in the country rocks, the Stone Corral ridge shear zone mylonites, and the isolated mylonites in the southern part of the study area (see Chapter 6). This result indicates that more water was present during mylonitization of the discrete zones and is consistent with the shear zones having formed on fractures as the fractures would have acted as conduits for the fluid.

The localization of shear strain into discrete zones along brittle precursors, such as fractures or the boundaries of veins or dikes, has been documented in a wide range of settings and conditions, ranging from greenschist to eclogite facies (Segall and Simpson, 1986; Christiansen and Pollard, 1997; Tourigny and Tremblay, 1997; Mancktelow and Pennacchioni, 2005; Pennacchioni and Mancktelow, 2007; Goncalves et al., 2012). The reactivation of fractures as discrete shear zones may, in fact, be a common process during the cooling of granitic intrusions (Pennacchioni, 2005). The fieldwork, petrography, FTIR spectroscopy, and U-Pb titanite geochronolgy data collected from the Stone Corral study area indicate that the discrete shear zones of the Harquahala Mountains provide another example of shear strain localization along antecedent fractures during plutonic cooling.

9.1.2 Formation of the Shear Zones with the Central Veins, Bleached Haloes, and Flanking Paired Shear Zones Morphology

The central vein in the shear zones with bleached haloes and flanking paired shear zones indicates that these discrete zones also must have formed on precursor fractures. However, the bleached haloes and flanking paired shear zones require that different degrees of strain softening occurred from the vein outward. Flanking paired shear zones in Alpine discrete shear zones with this same morphology described by Mancktelow and

Pennacchioni (2005) are interpreted to form from a rheological difference between the bleached haloes and the adjacent rock. In this case, the veins and bleaching occurred first, creating a rheologically strong bleached halo, and then shear zones initiated on the edges of the bleached halo. Conversely, the flanking paired shear zones in this study appear to have formed during fluid infiltration and metamorphism rather than afterwards. The evidence for fluid infiltration and metamorphism synchronous with deformation is provided in the following section, followed by an explanation for how the shear zones developed this unique morphology during the fluid-rich metamorphism.

9.1.2.1 Fluid infiltration and metamorphism synchronous with deformation

The FTIR spectroscopy analyses of intragranular quartz from the discrete shear zones with the central epidote vein, bleached halo, and flanking paired shear zones morphology indicate that higher water contents are present in these shear zones than in the discrete shear zones without this morphology, as well as country rock, Stone Corral ridge shear zone mylonites, and the isolated mylonites in the southern part of the study area. This result suggests that more water was present in these zones during deformation, which likely contributed to the development of the unique morphology (see Section 6.3.2). Although the epidote veins must have precipitated from a fluid before they could be deformed, the presence of optically continuous fibers that connect separate parts of the vein grains implies that the veins were still growing as they were being pulled apart, and that fluid infiltration and vein deformation were therefore synchronous (Figure 3.11B). The dramatic increase in the amount of opaque minerals, epidote, and locally titanite and garnet in the bleached haloes near the epidote veins provides evidence that these minerals are metamorphic and formed during fluid infiltration (Figure 3.12). The higher abundance of biotite and garnet in the more sheared portions of the rocks than in the

country rocks also suggests a metamorphic origin for these minerals that is related to the development of the shear zones.

One of the main causes of the bleached appearance of the haloes is the extensive replacement of feldspar by oligoclase, both in a symplectic form (i.e., myrmekite) and a non-symplectic form. In the incipient shear zone sample, HQ-C, several examples of deflected myrmekite are preserved, in which comma shaped myrmekitic lobes are deflected in the same sense of shear as the C'-type shear bands that crosscut and reorient the country rock foliation (Figure 3.19). This microstructure is indicative of myrmekite growth (and therefore of fluid filtration and metamorphism) during deformation (Simpson, 1985; Simpson and Wintsch, 1989).

The extensive presence of myrmekite in the bleached haloes and flanking paired shear zones is also evidence for fluid infiltration during deformation. Myrmekite that forms before the onset of deformation does not tend to be preserved during deformation because the plagioclase lobes and the delicate quartz vermicular intergrowths recrystallize so readily (Vernon, 1991). In the discrete shear zones with this unique morphology, however, small myrmekitic intergrowths are preserved in porphyroclasts within the highly strained flanking paired shear zones. The size of the myrmekite lobes and the quartz vermicules within the lobes decreases from the bleached halo outwards into the paired shear zones, and therefore appears to be dependent on the degree of strain experienced by the grains, providing further evidence for its synkinematic origin. The myrmekite and non-symplectic oligoclase have also undergone extensive dynamic recrystallization, the degree of which also increases with increasing strain away from the vein, which further demonstrates that the replacement reactions must have been synchronous with mylonitization (Tsurumi et al., 2003).

Another important feature of the shear zones is that the transition from the bleached haloes to the flanking paired shear zones is typically gradual and irregular. Although this transition can appear sharp in some of the discrete zones, particularly when viewed in the field (Figure 1.5C, D), the boundary more commonly is gradational, which is best visible in cross-sectional views in hand samples (Figure 2.14) and thin sections (Figure 3.14). The shear zones, on the other hand, are planar and not affected by the irregular nature of the bleached halo margins (Figure 2.14B). In the majority of the shear zones, the rock becomes progressively less bleached from the vein outward as a result of progressively more biotite and finer grain sizes. The same myrmekite and non-symplectic oligoclase replacement textures that are largely responsible for the bleached appearance of the haloes are still widespread in the more highly sheared areas. The difference in color between the bleached rock and the sheared rock, therefore, seems not to be a function of the amount of replacement of the feldspars by oligoclase and myrmekite, but rather is a function of the biotite content and the overall grain size.

Fluid infiltration must have continued through the waning stages of deformation in some of the shear zones. Numerous samples contain thick layers of quartz in the bleached haloes and the flanking paired shear zones that have undergone only a small amount of deformation. In the shear zones, the feldspar grains surrounding these quartz layers are often highly recrystallized and are deformed into σ-type mantled porphyroclasts. The quartz, however, shows only undulose extinction and minor high temperature grain boundary migration (GBM) recrystallization on its grain boundaries. This difference suggests that these quartz layers were veins that were precipitated late during the deformation after the bulk of the shearing had ceased. Additionally, a few of the epidote veins in the bleached haloes crosscut the foliation and are undeformed or little

deformed (Figure 3.10), which suggests they precipitated near the end of deformation or after the cessation of deformation in the bleached haloes.

The field and microstructural evidence indicate that fluid flow must have been a continuous process. Fluids infiltrated fractures in the granite, precipitated veins, and altered the surrounding rock replacing existing feldspar with oligoclase and myrmekite, and forming new metamorphic minerals. Fluids continued infiltrating during deformation of the veins, bleached haloes, and flanking paired shear zones, and then precipitated more veins after the majority of the deformation had ceased.

9.1.2.2 Reactivation of parallel fractures

If the flanking paired shear zones did not localize on rheological boundaries between a rigid bleached zone and country rock, then a different physical or chemical process must have controlled their location near the edges of the bleached haloes. As previously stated, the main differences between the bleached haloes and the paired shear zones are the greater amount of biotite and the smaller sizes of the grains in the shear zones. Importantly, the paired shear zone rocks also have more biotite than the country rocks (Tables 3.1, 3.2), which indicates that some of the biotite in the shear zones must have nucleated or grown during metamorphism rather than simply having formed from the recrystallization of pre-existing grains.

The replacement of potassium feldspar grains by myrmekite and non-symplectic oligoclase would have resulted in the release of potassium from the feldspar grains (see section 5.3.4). Some of this potassium was utilized in the crystallization of biotite grains within the non-symplectic oligoclase replacement patches (Figure 3.15A-C), but many of the replaced feldspar grains are not associated with any biotite, and the bleached halo does not contain any other potassium-bearing minerals. This lack of potassium-bearing

minerals in the bleached halo suggests that much of the potassium that was released during the replacement reactions must have been released into solution and diffused or migrated away from the bleached haloes. Once the fluid became sufficiently saturated with potassium and other ions, a potassium-rich phase, such as biotite, would have formed. Although the biotite-rich shear zones may reflect a diffusion front which resulted in growth of a weaker phase, the planar nature of the shear zones adjacent to irregular, gradational bleached zones (Figure 2.14) suggest that the flanking paired shear zones formed along parallel antecedent fractures in the same way as the other discrete shear zones (i.e., those not associated with veins and bleaching). These fractures would have had greater porosity than the fractures filled with rheologically strong epidote veins, and therefore would have allowed for continued substantial fluid migration. Thus although the presence of biotite, resulting from reactions within the bleached haloes, allowed more intense shearing, the presence of adjacent fractures was needed for the discrete shear zones to form.

Several field observations support this hypothesis. The discrete shear zones (including those not associated with veins and bleaching) are nearly all found in multiple closely spaced sets, typically of three or more shear zones per set. Some of the shear zones within a set are roughly equally spaced, whereas others are not. Similarly, some of the bleached haloes around central epidote veins are symmetric (Figure 1.5C, D) and others are not (Figures 1.5H, 2.10C). For example, the shear zone pictured in Figure 1.5H is characterized by a central epidote vein with an extremely asymmetric bleached halo. The halo is considerably better developed above the epidote vein than below it. The shear zone that flanks the halo above the vein has reoriented the country rock foliation into parallelism. Conversely, no well-developed shear zone is present below the epidote vein, and the country rock foliation can be followed upwards into the weakly bleached

halo until it is crosscut by the epidote vein. The more weakly bleached halo below the vein and the absence of a flanking shear zone could be attributed to the distribution of the antecedent fractures. In this case, only two initial closely spaced fractures may have been present, the fracture in which the vein precipitated and the fracture that was reactivated by the shear zone above the vein. The halo above the epidote vein may be better developed because the two closely spaced fractures would have allowed for more fluid-rock interaction to occur between them than outside of them.

The fractures that were occupied by the rheologically strong epidote veins were less capable of accommodating the same amount of deformation as the fractures without epidote veins. This difference is best seen by thin section observations of sample HAR-16. The central vein in this sample is composed mainly of epidote in some parts and mainly of quartz in other parts (Figure 2.14C). In the thin section of the epidote-rich part of the vein, the epidote grains display brittle deformation as some grains are fractured and pulled apart (Figure 3.13A, B). The small amount of vein quartz in this part of the vein is present in pods that are surrounded by epidote vein grains (Figure 3.13A, B). The quartz is very coarse-grained and only minimally deformed. The feldspars in the surrounding bleached halo have undergone different degrees of dynamic recrystallization, but are not sheared (Figure 3.15A, C). Conversely, in the thin section of the quartz-rich part of the vein, which was cut from the same hand sample (Figure 2.14C), both the vein and the surrounding rock are much more deformed (Figures 3.11C, 3.13C, D). The quartz grains are smaller, are very elongate, and are oblique to mica seams that define a foliation, which results in an S-C fabric (Figure 3.13C). Some of the epidote grains form fish that indicate a top-to-the-southwest sense of shear, and the feldspar porphryoclasts in the surrounding bleached halo are much more deformed. Some of the mantled porphyroclasts form minor σ-type shapes that also indicate a top-to-the-southwest sense

of shear. These microstructures provide good evidence that the fracture could not accommodate shearing where it was occupied by an epidote-rich vein, and the surrounding bleached halo was protected from more extensive deformation.

A small number of the flanking paired shear zones also appear bleached (e.g., Figure 2.14A). These zones likely began as fractures that were infiltrated by fluid that caused bleaching, but because no epidote veins were precipitated to strengthen the bleached rock, these zones were able to accommodate deformation and underwent similar magnitudes of shearing as the biotite-rich flanking shear zones. The higher modal percentage of quartz in these shear zones may mean a quartz vein precipitated in the fracture that was not preserved after ultramylonitization. The presence of pronounced bleaching in some flanking shear zones indicates that the bleached rock was not rheologically stronger. Therefore the reactivation of adjacent fractures as discrete shear zones provides a more viable explanation for shear zone formation than does the activation of a boundary between relatively rheologically strong and rheologically weak rocks.

9.1.3 Strain Softening Mechanisms: Microscopic Controls on the Development of the Discrete Shear Zones

In a seminal paper, White et al. (1980) summarized a number of strain softening processes that may operate in ductile shear zones. Many of these processes appear to have been active during the deformation of the discrete shear zones in the Stone Corral study area, specifically the processes of chemical softening (in this case, hydrolytic weakening), reaction softening, geometric softening (i.e., grain rotation and lattice reorientation for easy slip), continual recrystallization, and pore fluid effects. The importance of fluid infiltration during the deformation and the metamorphism of the shear zones cannot be overstated as it was likely responsible for both the instigation and

the maintenance of the strain softening mechanisms. The strain softening mechanisms operated in both the discrete shear zones that were not affected by bleaching and veins and in the paired shear zones that flank the edges of the bleached haloes. The flanking paired shear zones seem to have been affected by the processes to a greater degree, likely because more fluid was available during deformation.

The infiltration of fluid during deformation would have instigated a number of strain softening effects. The introduction of water into the quartz crystal lattice would have resulted in chemical softening through hydrolytic weakening. The weakening of quartz would also have aided geometric softening by facilitating lattice reorientation and the development of a strong crystallographic preferred orientation (CPO). The fluids would have activated reaction softening by catalyzing metamorphic reactions that produce hydrous phases, particularly biotite which is rheologically weak, and would also allow for the formation of myrmekite and non-symplectic oligoclase. Because myrmekite recrystallizes readily (and the non-symplectic oligoclase also appears to recrystallize readily), the feldspar would have underwent continual recrystallization. Pore fluid effects would have played a major role in the initiation of the shear zones. The porosity provided by the antecedent fractures was a prerequisite for significant fluid infiltration. The production of metamorphic myrmekite and oligoclase would have resulted in volume decreases that may have created transient pore space that would provide more permeability for fluid flow and the transfer of ions in solution (Simpson and Wintsch, 1989; Wintsch and Yi., 2002; Menegon et al., 2006).

Ample evidence for these strain softening processes is apparent in the data collected during this study. The FTIR spectroscopy results show greater intragranular water contents in quartz of the discrete shear zones than the country rocks, suggesting hydrolytic weakening played an important role during deformation (Tables 6.1-6.3).

Strong quartz CPOs are evident in thin section and in the electron backscatter diffraction (EBSD) results (Figures 3.17A, 4.3), which indicate lattice reorientation did occur, and the biotite content in the discrete shear zones is systematically higher than in the country rock samples (Tables 3.1, 3.2).

Experimental work indicates that when a weak phase, such as biotite, becomes through-going in a deforming rock, the result will be the localization of strain along the weak layers (Holyoke and Tullis, 2006a, 2006b). Because the deformation of the Stone Corral rocks occurred at amphibolite-facies conditions, the alignment and connection of the biotite grains in the samples was likely caused by crystallization or recrystallization of the grains with their (001) planes subparallel to the foliation, rather than by mechanical rotation of the grains (Simpson, 1985). The resulting interconnected strands and through-going bands of biotite with (001) planes aligned would likely enable biotite grains to deform by dislocation creep (Wintsch and Yi, 2002). These grains would deform more readily than the other phases in the rock and would therefore concentrate shear. The easier deformation of biotite may result in the widespread creation of microextensional sites along the shear bands which would provide pore space for more fluid to infiltrate (Wintsch and Yi, 2002). Additionally, bonding between biotite (001) faces and neighboring grains is weak compared to other grain boundaries, and fluid is expected to move across the bands more freely (Vernon et al., 1983). The higher degree of bulging (BLG) recrystallization or neocrystallization of feldspar adjacent to biotite bands in many of the discrete shear zone samples may be evidence of increased fluid flow along the bands (Figure 3.18)

Continued fluid infiltration along biotite shear bands would promote additional myrmekite and oligoclase replacement of the adjacent feldspar, which would result in a volume decrease, allowing for further fluid infiltration and replacement (Simpson and

Wintsch, 1989; Wintsch and Yi., 2002; Menegon et al., 2006). These replacement reactions would also result in the further release of potassium that could be used for further biotite nucleation or growth. Quartz undergoing dislocation creep would also likely incorporate more fluid into its structure resulting in more hydrolytic weakening and further concentrating shear. The increased shear along the weaker layers may also result in increased recrystallization of myrmekite and oligoclase replacement textures, which would result in significant grain size reduction of the feldspars and would provide new strain-free grains that could further accommodate deformation (White et al., 1980). The cyclic nature of these processes is clear, and similar feedback loops have been proposed in myrmekite-rich mylonites in other settings (Tsurumi et al, 2003; Menegon et al. 2006).

The lack of extensive biotite in a minority of the paired shear zone samples indicates that other processes besides biotite alignment and interconnectedness were more significant for initiating and maintaining shear in these samples (Figure 2.14A). These samples tend to have more quartz than the other samples. The quartz is extensively recrystallized and displays a very strong CPO. In these areas, quartz and recrystallized myrmekite and oligoclase were likely the weakest layers that were most responsible for concentrating shear.

The incipient shear zone sample, HQ-C, provides a unique opportunity to examine the initial stages of strain softening in the shear zones with the central vein, bleached halo, and flanking paired shear zones morphology where fluid flow was more pronounced than in the shear zones without this morphology. In this sample, the flanking paired shear zones are not mylonitized but are instead characterized by biotite-rich C'-type shear bands that crosscut and reorient the country rock foliation (Figure 3.18). C'-type shear bands are generally understood to form during the late stages of mylonitization after a strong foliation has been developed, possibly because a second suite of folia is

needed to enable further strain accommodation (see Vernon, 2004 and Passchier and Trouw, 2005 for reviews). C'-type shear bands may also form as a means of abolishing an older fabric to manufacture a newer, softer fabric in a rock (White et al., 1980; Gapais and White, 1982).

In the incipient shear zone sample, HQ-C, the C'-type shear bands progressively increase in abundance from the vein outwards and the spacing between the bands becomes progressively smaller. Near the central vein where the bands are fewer in number and farther apart, the bands crosscut the country rock foliation (Figure 3.18A). Farther away from the vein where the bands are abundant and close together, the bands reorient the country rock foliation into parallelism (Figures 3.17C, 3.18B). The degree of recrystallization of the quartz and feldspar grains between the bands is greater where the bands are closer together (Figure 3.18B). In the most strained part of this sample, the biotite-rich C'-type shear bands are abundant and the intermediary quartz and feldspar grains have undergone near complete recrystallization (Figure 3.18C, D). The result is a new fabric in which the foliation is parallel to the biotite bands. This fabric is nearly indistinguishable from the ultramylonitic fabric that is present in many of the flanking paired shear zones from the well-developed shear zone samples (compare Figures 3.18D and 3.14E, F). The shear bands in the incipient shear zone sample, therefore, may provide an example of the development of C'-type shear bands as a precursor to the formation of a new mylonitic fabric at relatively high metamorphic temperatures.

9.2 Stone Corral Mylonites: Late Cretaceous or Miocene?

The geochronology and petrography provide ample evidence that the majority of the shear zones in the Stone Corral study area formed during a Late Cretaceous event, rather than during Miocene metamorphic core complex exhumation as previously

interpreted. Only the scattered, isolated shear zones on the crest of Stone Corral ridge and possibly the mylonitic veneers on fractured surfaces in the northern part of the study area appear to be related to core complex exhumation. This conclusion is based on U-Pb, petrographic, and EBSD data that indicate the majority of the shear zones yield Late Cretaceous syn-mylonitic titanite ages, formed at amphibolite-facies conditions, and exhibit a top-to-the-southwest sense of shear. In contrast, metamorphic core complex shear zones in the region yield Miocene ages on the basis of $^{40}Ar/^{39}Ar$ thermochronology, formed at greenschist-facies conditions, and exhibit a top-to-the-northeast sense of shear.

The results of this study show that the rocks of the Stone Corral study area are the product of a more complex history than previously understood, and record at least three different episodes of deformation. These episodes resulted in the development of the Late Cretaceous amphibolite facies gneissic metagranite, the Late Cretaceous amphibolite facies mylonitic shear zones, and finally, the rare, scattered Miocene greenschist facies mylonitic shear zones.

9.2.1 Ages of Deformation

9.2.1.1 Late Cretaceous deformation

The U-Pb data for titanite in the country rocks and shear zone mylonites in the northern part of the study area all yielded Late Cretaceous ages of ~68-75 Ma, and are interpreted as dating the deformation of the country rock, the deformation of the discrete shear zones in the northern part of the study area, and at least some of the deformation of the Stone Corral ridge shear zone (see Section 8.3). The titanite grew during the amphibolite facies metamorphism and deformation as shown by its increase in abundance within the discrete shear zones (as well as in the more deformed country rock), intimate

association with other syn-mylonitic metamorphic minerals, and parallelism to the foliation (see section 8.3.2).

These ages and the high temperature microstructures of these samples (see section 9.2.2) are consistent with the $^{40}Ar/^{39}Ar$ thermochronologic work of Richard (1988) and Richard et al. (1990). $^{40}Ar/^{39}Ar$ age dating was conducted on samples from the Brown's Canyon granite (or inclusions of older rock within it), which borders and/or hosts the mylonitic shear zones of this study. The results of the $^{40}Ar/^{39}Ar$ age dating study indicate that the rocks cooled through the hornblende closure temperature at ~63-70 Ma. As the $^{40}Ar/^{39}Ar$ closure temperature for hornblende is ~480-550 °C (Harrison, 1981; McDougall and Harrison, 1999), the ages show that rocks in the Stone Corral study area were last subjected to amphibolite facies temperatures during the Late Cretaceous (Richard, 1988; Richard et al., 1990).

$^{40}Ar/^{39}Ar$ age dating was also performed on muscovite and biotite in the Brown's Canyon granite west of the study area, and the results show that the rocks cooled through the muscovite closure temperature at ~30 Ma and the biotite closure temperature at ~20 Ma (Richard, 1988; Richard et al., 1990; Richard et al., 1998). The $^{40}Ar/^{39}Ar$ closure temperature for muscovite is ~350-400 °C (McDougall and Harrison, 1999; Harrison et al., 2009) and the closure temperature for biotite is ~300-350 °C (McDougall and Harrison, 1999). The relatively young muscovite age of ~30 Ma was obtained from a disturbed spectrum that was interpreted to have been the product of either Early Tertiary cooling proceeded by an early Miocene thermal perturbation that resulted in argon loss, or the product of slow cooling of the pluton (Richard et al., 1990; Richard et al., 1998). $^{40}Ar/^{39}Ar$ dating of muscovite in pegmatites that are associated with the Brown's Canyon granite but are located further west in the range yielded an age of ~51 Ma (Richard, 1988), although these pegmatites are structurally higher than the rocks of the study area.

This muscovite and biotite data indicate that during the commencement of MCC unroofing at ~21 Ma, the muscovite $^{40}Ar/^{39}Ar$ system was closed, whereas the biotite $^{40}Ar/^{39}Ar$ system remained open. In the Harquahala Mountains, however, some MCC mylonitization has been interpreted to have initiated slightly prior to this time because some mylonites are crosscut by 22.3 Ma dikes, but mylonitization must have also continued beyond the timing of dike emplacement because other dikes have been deformed (Richard, 1988). On the basis of the results of this thesis study, however, the possibility also exists that the mylonites crosscut by the dikes may have formed during the Late Cretaceous. Regardless, the $^{40}Ar/^{39}Ar$ ages indicate that MCC mylonitization initiated at temperatures between 300 °C and 400 °C, temperatures which are lower than indicated by the microstructures and the minerals present in the amphibolite facies mylonites that must have formed at temperatures >500 °C. Thus, this data strongly supports the Late Cretaceous age of deformation that is indicated by the U-Pb titanite dates and does not support a Miocene MCC-type origin for much of the mylonitization in the Stone Corral study area.

9.2.1.2 Miocene deformation

Conversely, the $^{40}Ar/^{39}Ar$ data do support a Miocene MCC-type origin for the greenschist facies mylonites of the isolated shear zones in the southern part of the study area near the crest of Stone Corral ridge (see section 9.2.2.5). Richard et al. (1990) inferred that the top of this mountain was located only 50-100 m below the detachment fault on the basis of a greater degree of chloritic alteration and fracturing. The character and magnitude of this alteration and fracturing is similar to that of rocks in other areas of the Harquahala Mountains that are 50-100 m below the exposed detachment fault. The greenschist facies deformation conditions and the top-to-the-northeast sense of shear

suggested by the microstructures in the mylonites from the isolated shear zones are consistent with an MCC detachment fault related origin.

9.2.2 Petrographic Evidence for Temperatures of Deformation

9.2.2.1 Country rock deformation

The quartz and feldspar in the crudely foliated, gneissic country rocks recrystallized predominantly by GBM and subgrain rotation (SGR), respectively, which is typical of deformation at temperatures >500 °C (Figures 3.1, 3.5, 3.6; Stipp et al., 2002; Tullis, 2002). Myrmekite is extensive in all the country rocks (Figures 3.1A, 3.6A, B), and quartz-epidote symplectites are widespread in the country rocks of the northern part of the study area (Figures 3.2B-D, 3.3A, B). Although myrmekite may form as an igneous exsolution texture, the development of myrmekite during fluid-present deformation at upper greenschist- to amphibolite-facies conditions is well documented (Simpson, 1985; Gapais, 1989; Menegon et al. 2006). Similarly, although epidote-bearing symplectites may form during mineral reactions within a crystallizing melt (Owen, 1991; Zen and Hammarstrom, 1984), the intergrowths are more commonly formed during amphibolite facies metamorphism (Liou et al., 1981; Siddiqui and Ahmed, 2005; Abbot and Draper, 2007; Bisnath et al., 2008) and possibly during upper greenschist facies metamorphism (Chalokwu and Kuehner, 1992). The epidote-bearing symplectites in the Stone Corral area are most certainly of metamorphic origin as magmatic epidote in massive granites has not been documented (Schmidt and Poli, 2004) and experimental results indicate that the stability of magmatic epidote in granite plutons requires very high pressures of $\geq$ 8 kbar (Naney, 1983). These pressures are significantly higher than those experienced by the rocks of the Stone Corral study area. Additionally, the epidote-bearing symplectites of the Stone Corral rocks are closely associated with

other metamorphic minerals, including titanite, apatite, biotite, and opaque minerals (Figure 3.4A). The stability of green (in plane polarized light) amphibole may also suggest that amphibolite-facies conditions prevailed during country rock deformation, although the composition of the amphibole is unknown.

9.2.2.2 Discrete shear zones and the Stone Corral ridge shear zone

The mylonites in the discrete shear zones in the northern part of the study area, the mylonites in the larger Stone Corral ridge shear zone in the central part of the study area, and the protomylonite collected from the northern boundary of the Stone Corral ridge shear zone all crosscut and reorient the country rock foliation. This deformation, therefore, must be younger than the country rock deformation. However, the mylonites and protomylonite of these shear zones appear to have formed under similar conditions as the country rock deformation because they also exhibit extensive GBM recrystallization in quartz and SGR recrystallization in feldspar (Figures 3.7, 3.8, 3.13, 3.22, 3.23). The stability of green (in plane polarized light) amphibole (Figure 3.8C), the extensive presence of deformation-induced myrmekite (Figures 3.7A, 3.14, 3.15C, D, 3.19, 3.22B), and the growth of quartz-epidote symplectites (Figure 3.3C-F) provide mineralogical evidence that amphibolite-facies conditions persisted through mylonitization.

The discrete shear zone mylonites share the same metamorphic assemblage as the country rocks, including epidote, titanite, biotite, opaque minerals, apatite, and garnet (Figure 3.4). The epidote and titanite display different habits than the epidote and titanite in the country rock. Much of the grains are fish-like or sigmoidal in character, exhibit a top-to-the-southwest sense of shear, and are significantly finer grained (Figures 3.9; 8.7C-F). Metamorphic garnet is present in many of the discrete zones with the central epidote vein, bleached halo, and flanking paired shear zones morphology. This garnet is

significantly smaller than much of the garnet in the country rocks, lacks the pink tint visible in plane-polarized light of some of the country rock garnet, and is sometimes intimately associated with metamorphic titanite (as inclusions or interlocking grains; Figure 3.4C, D), epidote (with adjacent faces touching; Figure 3.4D, E), or recrystallized biotite (Figure 3.4F). The greater abundance of the garnet in the discrete shear zones implies that it is associated with the metamorphism that caused the bleaching in the haloes and the biotite growth in the flanking paired shear zones. The growth of both garnet and biotite during metamorphism also implies that amphibolite-facies conditions prevailed (e.g., Mancktelow and Pennacchioni, 2005).

Although the mylonites in the northern part of the Stone Corral ridge shear zone share the same abundant metamorphic minerals as the discrete shear zone mylonites and the northern country rock, the mylonites in the central and southern part of the Stone Corral ridge shear zone contain only a very minor amount of these minerals, which may indicate they underwent less fluid infiltration during deformation. Similarly, the country rocks in the southern part of the study area (i.e., south of the Stone Corral ridge shear zone) also contain only trace amounts of these minerals and likely experienced less fluid flow. The southern country rocks and the mylonites in the southern and central part of the Stone Corral ridge shear zone also are less strained than their northern counterparts. The lower degree of strain may have made fluid infiltration more difficult.

9.2.2.3 Cooling during Late Cretaceous deformation

The mylonitic samples from the central and southern part (i.e., structurally higher part) of the Stone Corral ridge shear zone also display GBM recrystallization of quartz and SGR recrystallization of feldspar as is seen in the samples from the northern part (i.e., the structurally lower part). However, these samples also display a greater degree of

SGR recrystallization of quartz and BLG recrystallization of feldspar than do the samples from the northern part, and therefore, may have been deformed at slightly lower temperature conditions. This difference may suggest uplift or cooling during mylonitization. Alternatively, the samples may be showing a small degree of overprint by lower temperature Miocene deformation (see section 9.2.3).

Some of the discrete shear zone samples in the northern part of the study area show some evidence of cooling during deformation from even higher temperatures. In some samples, a small number of quartz grains within the quartz layers are very large (~1 mm) and display rectangular shapes. A few of the feldspar porphyroclasts are extremely elongate, which suggests they underwent lattice reorientation (Figure 3.17D). These features are characteristic of higher temperatures of deformation, such as those active during middle to upper amphibolite-facies conditions, rather than the lower to middle amphibolite-facies conditions that otherwise seem to have prevailed during deformation. These features may record deformation that initiated at higher temperatures and continued during relatively rapid uplift and cooling of the pluton. $^{40}Ar/^{39}Ar$ thermochronology of rocks collected from a traverse across the Harquahala Mountains indicates that a significant period of cooling and uplift did occur throughout the range at the end of the Late Cretaceous (Richard, 1988). This period of cooling and uplift was not restricted to the Harquahala Mountains, but appears to have occurred regionally throughout southeastern California and west-central Arizona as is suggested by extensive thermochronology studies and the identification of widespread sedimentary unconformities throughout the region (Davis et al., 1982; Howard et al, 1982; John, 1982; Reynolds et al., 1986; Anderson, 1988; Foster et al., 1988; Hoisch et al., 1988).

9.2.2.4 Late Cretaceous mylonitization outside of the study area

Although the Late Cretaceous shear zones in the Stone Corral study area are focused around the northern boundary of the Stone Corral pluton, Late Cretaceous mylonites were also found ~5 km northwest of the study area during reconnaissance fieldwork. A thin section from a mylonite in this area looks nearly identical to the amphibolite facies shear zone rocks of the Stone Corral study area. The sample displays GBM recrystallization in quartz, SGR recrystallization in feldspar, and contains the same characteristic metamorphic mineral assemblage, including abundant titanite fish that indicate a top-to-the-southwest sense of shear. This minor reconnaissance work implies that other mylonites in the MCC that have been interpreted as forming during Miocene MCC exhumation may in fact have formed during the Late Cretaceous as well.

9.2.2.5 Isolated shear zones on the crest of Stone Corral ridge

In stark contrast to the country rock deformation and to the mylonitic deformation in the discrete shear zones and the Stone Corral ridge shear zone, the mylonites in the isolated shear zones near the crest of Stone Corral ridge have microstructures that suggest lower deformation temperatures typical of greenschist-facies conditions. The feldspars in these samples are much less recrystallized than in the amphibolite facies samples, and the dominant feldspar recrystallization mechanism was BLG recrystallization. Quartz is highly strained and highly recrystallized by SGR recrystallization (Figure 3.24). Myrmekite is uncommon in these samples. Where myrmekite is present, it is found protected inside large feldspar porphyroclasts rather than present on the rims, which suggests it may be preserved from an older event. These samples also lack the metamorphic mineral assemblages of titanite, epidote, biotite, apatite, and garnet.

9.2.3 Kinematics

Field, petrographic, and EBSD analysis observations indicate that the three different deformation episodes occurred under different kinematic regimes. The gneissic deformation of the country rocks was likely associated with a minor degree of top-to-the-northeast shear as suggested by the top-to-the-northeast rotation of the EBSD pole figures for the country rock samples (Figure 4.3) and by the presence of quartz grains in thin section that are subtly inclined in a top-to-the-northeast direction in some of the quartz layers. Late Cretaceous top-to-the-northeast deformation has also been recognized in the gneissic and migmatitic country rock exposed in the nearby Mesquite Mountains, AZ, a mountain range that was likely incised from a MCC footwall into the hanging wall of the Whipple detachment system (Figure 1.1; Knapp, 1989).

The timing of the discrete top-to-the-northeast brittle and ductile shear bands that crosscut the country rock foliation is more difficult to decipher (Figure 3.2). The ductile shear bands contain the same metamorphic minerals as the country rock, but whether these minerals formed before or during shear band development is unclear. The titanite grains in the shear bands yield the same U-Pb age as the grains that parallel the country rock foliation; however, the titanite could have simply rotated into parallelism with the bands during a later deformation and not been reset. If the shear bands are Late Cretaceous, they may represent antithetic fractures to the top-to-the-southwest mylonites.

The discrete shear zones of the northern part of the study area were unquestionably deformed in a top-to-the-southwest direction on the basis of clear field, petrographic, and EBSD analysis evidence (Figures 2.12, 3.7, 3.8, 3.9, 3.13C, D, 3.17-3.19, 4.3, 8.7D-F). Similar evidence shows many of the mylonites in the Stone Corral ridge shear zone were also deformed in a top-to-the-southwest direction (Figure 4.4). However, the sense of shear in some of the other mylonites from this major shear zone is

ambiguous, and the a-axis EBSD pole figure for sample B-3, collected from the middle of the shear zone, suggests a top-to-the-northeast sense of shear (Figure 4.4). In thin section, both top-to-the-northeast and top-to-the-southwest shear sense indicators are present in this sample (Figure 3.21B). The c-axis pole figure for this sample is defined by basal <a>, rhomb <a>, and prism <a> slip, which suggests lower mylonitization temperature conditions than are suggested by the thin section (Figures 3.22B, 4.4). The prevalence of GBM recrystallization in quartz and SGR recrystallization in feldspar in the thin section implies deformation temperatures ≥500 °C (Stipp et al., 2002; Tullis, 2002). This c-axis pole figure for B-3 is also at odds with the pole figure for the other Stone Corral ridge shear zone sample, H3, which is dominated by prism <a> slip, also indicative of deformation temperatures ≥500 °C (Figure 4.4; Stipp et al., 2002).

In the thin section of sample B-3, the abundant muscovite grains are aligned parallel to the foliation and are also subtly folded or bended parallel to the foliation, indicating a later deformation of an earlier formed foliation (Figure 3.21). This petrographic evidence, coupled with the c-axis pole figure which suggests a greater amount of basal <a> slip than the pole figure for the other sample, may imply that a younger, lower temperature deformation overprinted an older, higher temperature mylonitization event. The abundant large, aligned mica grains in the sample may have caused it to be weaker than the other mylonites of the Stone Corral ridge shear zone, and therefore made it better able to accommodate strain during a younger period of deformation (such as MCC unroofing). The top-to-the-northeast sense of shear suggested by the EBSD <a> axis pole figure, therefore, may not be a record of the shear sense of the oldest episode of Stone Corral ridge shear zone deformation. However, the protomylonite sample (SCM-19), which was collected from the northern boundary of the Stone Corral ridge shear zone, also displays a clear top-to-the-northeast sense of shear,

and therefore the possibility exists that the sense of shear within the Stone Corral ridge shear zone was not consistent either across its width or throughout the duration of the Late Cretaceous mylonitization episode. Conversely, the shear zone may have accommodated predominantly coaxial strain as suggested by the <a> axis pole figures (Figure 4.4), or may be the result of heterogeneous flow in the shear zone, or caused by the effect of heterogeneous rheologies within the shear zone.

The greenschist facies mylonitization event evident in the isolated shear zones near the crest of Stone Corral ridge occurred under a top-to-the-northeast kinematic regime as is shown by the shear sense indicators in thin section (Figures 3.24A, 4.5) and by the EBSD pole figure for sample B-9 (Figure 4.4). This sense of shear is consistent with that of the MCC mylonites in the other metamorphic core complex ranges of the lower Colorado River extensional corridor.

9.3 Structural and Tectonic Setting of the Late Cretaceous Shear Zones

The rocks that compose the northeastern Harquahala Mountains were rotated during MCC unroofing, which means that the present orientations of the shear zones that yielded Late Cretaceous ages (i.e., the discrete shear zones and the Stone Corral ridge shear zone) are different than they would have been during their formation. However, the degree of rotation that occurred during MCC unroofing can be estimated. A suite of mafic dikes was intruded into extension fractures in the northeastern and central Harquahala Mountains during the early phases of detachment faulting (Richard et al., 1990), and if the assumption is made that the dikes intruded subvertically, then the Late Cretaceous shear zone orientation data can be rotated about the axis that would bring the dikes into a vertical orientation. This rotation would provide an estimate of the orientation of the Late Cretaceous shear zones before Miocene MCC exhumation. If the

shear zones did not undergo significant rotation between Late Cretaceous and Miocene time, then this estimate may approximate the original orientation of the shear zones during their formation.

Richard et al. (1990) collected 157 measurements of the orientations of the Miocene dikes, and calculated a principle eigenvector of distribution for poles to the dikes of 24°, 218°. These data suggest the dikes have been rotated ~24° about an azimuth of 308°. The foliation and lineation data for the discrete shear zones and for the Stone Corral ridge shear zone, which are plotted in Figure 2.11A and C, respectively, were rotated about this axis using the program Stereonet 7 (Allmendinger et al., 2012). The rotation results in southeast dips for both the discrete shear zones and the Stone Corral ridge shear zone (Figure 9.1A, C). The data for the discrete shear zone foliations provide an average shear zone dip of 35°, but the individual measurements vary widely (Figure 9.1A). Conversely, the data for the Stone Corral ridge shear zone foliations provide a much shallower average shear zone dip of ~15°, but the individual measurements also show some spread (Figure 9.1C).

The lineations measured on the shear zone foliations trend subparallel to the strikes of the shear zone foliations for both the discrete shear zones and the Stone Corral ridge shear zone (Figure 9.1B, D), suggesting the shear zones accommodated movement primarily along strike. The discrete shear zones may have also accommodated a minor amount of normal slip as the mean strike of the shear zone foliations (242°) varies from the mean lineation on the foliations by ~15°. The shear sense indicators in the rocks still indicate a top-to-the-southwest sense of shear after the rotation. However, if the shear zones were rotated during the uplift and cooling of the Late Cretaceous pluton after mylonitization ceased and prior to metamorphic core complex exhumation, this restoration would not provide the original orientations of the shear zones.

The results of the restoration are, however, consistent with the orientation of other Late Cretaceous deformation in the region. A Late Cretaceous gently dipping to subhorizontal shear zone has also been recognized in the Chemehuevi Mountains MCC, California, and some evidence suggests that this shear zone extends into the Sacramento Mountains MCC and Whipple Mountains MCC as well (John and Mukasa, 1990). The timing of mylonitization in this shear zone has been loosely constrained between ~68-75 Ma based on U-Pb zircon age dating of mylonitized and undeformed plutonic bodies within the Late Cretaceous Chemehuevi Mountains plutonic suite. Mylonitization occurred within the time interval of plutonic emplacement in the Chemehuevi Mountains, and this also seems to be the case in the Harquahala Mountains. Zircon crystallization ages of the granitic intrusions in the northeastern Harquahala Mountains provide ages that range from ~65 Ma to ~77 Ma (Isachsen et al., 1999; Prior, unpublished data; this study), and the U-Pb analyses of synmylonitic titanite in this study yielded ages of ~68-71 Ma, meaning mylonitization of some of the older bodies occurred before plutonic intrusion of younger bodies in the northeastern part of the range had ceased.

Other Late Cretaceous shear zones have been recognized in the Harcuvar Mountains MCC, which also was affected by extensive Late Cretaceous plutonism (Wong et al., 2013), and in the adjacent Little Buckskin Mountains MCC (Figure 1.1; Singleton, 2011). Late Cretaceous or early Tertiary shear zones are present in the Santa Catalina MCC as well, and these were also active around the same time as plutonic activity in the range (Bykerk-Kauffman, 1990). The widespread occurrence of Late Cretaceous mylonitization implies the shearing may have recorded a regional deformation event closely related in space and time to plutonic activity. The reactivation of these regionally extensive Late Cretaceous shear zones for MCC exhumation may be a widespread phenomenon. Interestingly, the Harquahala Mountains MCC is the only

known location where Late Cretaceous mylonitization occurred primarily with a top-to-the-southwest, rather than a top-to-the-northeast or top-to-the-east, sense of motion.

Whether the Late Cretaceous deformation is an expression of contractional or extensional processes remains elusive (John and Mukasa, 1990; Bykerk-Kauffman, 1990), but synconvergent extensional deformation during this time period has been recognized throughout the region, typically in the form of normal shear zones (Hodges and Walker, 1992, and references therein; Boettcher and Mosher, 1998; Wells and Hoisch, 2008). A number of different basic tectonic models have been proposed to explain how the middle crust may have accommodated synconvergent extension during Late Cretaceous time. Many of the models involve regional subhorizontal or shallowly dipping shear zones. The models include: 1) Gravitationally-driven extension of overthickened crust (Wells and Hoisch, 2008); 2) Flat-slab subduction, which may have resulted in significant traction between the Farallon plate and the lower crust, leading to substantial shearing in the lower and middle crust (Richard, 1988); 3) A midcrustal extensional allochthon (i.e., a block of crust, up to 20 km thick, detached from the upper and lower crust) may have been extruded westward (Hodges and Walker, 1992); and 4) Channel flow of rocks in the middle crust from the Sevier orogenic hinterland may have occurred eastward into the Colorado Plateau (McQuarrie and Chase, 2000). The study of the Late Cretaceous deformation exposed in the MCC footwalls, including in the Harquahala Mountains, still requires much more work, and therefore the viability of these tectonic models cannot yet be meaningfully critiqued in this region

9.4 CONCLUSIONS

Several important basic conclusions may be derived from the data analyses and interpretations presented in this study. These conclusions are a summary of the original contributions of this thesis.

1. *The discrete shear zones reactivated antecedent fractures.* Flanking paired shear zones near the edges of bleached haloes also formed from the reactivation of precursor fractures.
2. *The discrete shear zones were infiltrated with fluid during deformation that locally caused veins and bleaching.* The fluid was igneous or metamorphic in origin and may have been sourced from nearby crystallizing plutons or from magmatism or prograde metamorphism at depth. Hydrolytic weakening of quartz was a significant strain softening mechanism that aided in shear zone localization. The degree of fluid-rock interaction in the shear zones may have been an important variable in morphology development. The shear zones characterized by central epidote veins, bleached haloes, and flanking paired shear zones may have developed due to a higher degree of fluid-rock interaction.
3. *The development of the flanking paired shear zones near bleached haloes was greatly aided by fluid enhanced reaction softening mechanisms.* The oligoclase and myrmekite replacement of potassium feldspar resulted in the release of potassium that was subsequently utilized in biotite growth in the flanking paired shear zones. The abundant metamorphic biotite in the flanking paired shear zones deformed readily and concentrated deformation. Myrmekite and oligoclase replacement products recrystallized readily, resulting in significant grain size reduction. These

processes also operated to a lesser degree in the discrete shear zones not affected by the central vein, bleached halo, and flanking paired shear zones morphology.

4. *Many of the mylonites in the Harquahala MCC are of Late Cretaceous age, not of Miocene age as previously interpreted*. The discrete shear zones in the northern part of the study area and the Stone Corral ridge shear zone formed around ~68-71 Ma during cooling of the Late Cretaceous (~75.5 Ma) Brown's Canyon granite.

5. *Late Cretaceous shear zones look very similar to Miocene shear zones in the field*. The shear zones share similar foliation orientations and stretching lineation orientations. They can be distinguished in thin section based on mineralogy and microstructures. The Late Cretaceous mylonites contain abundant myrmekite, and many contain metamorphic epidote, titanite, garnet, biotite, and apatite. These shear zones formed at amphibolite-facies conditions and display top-to-the-southwest or ambiguous senses of shear, whereas the Miocene shear zones formed at greenschist-facies conditions and show a top-to-the northeast sense of shear.

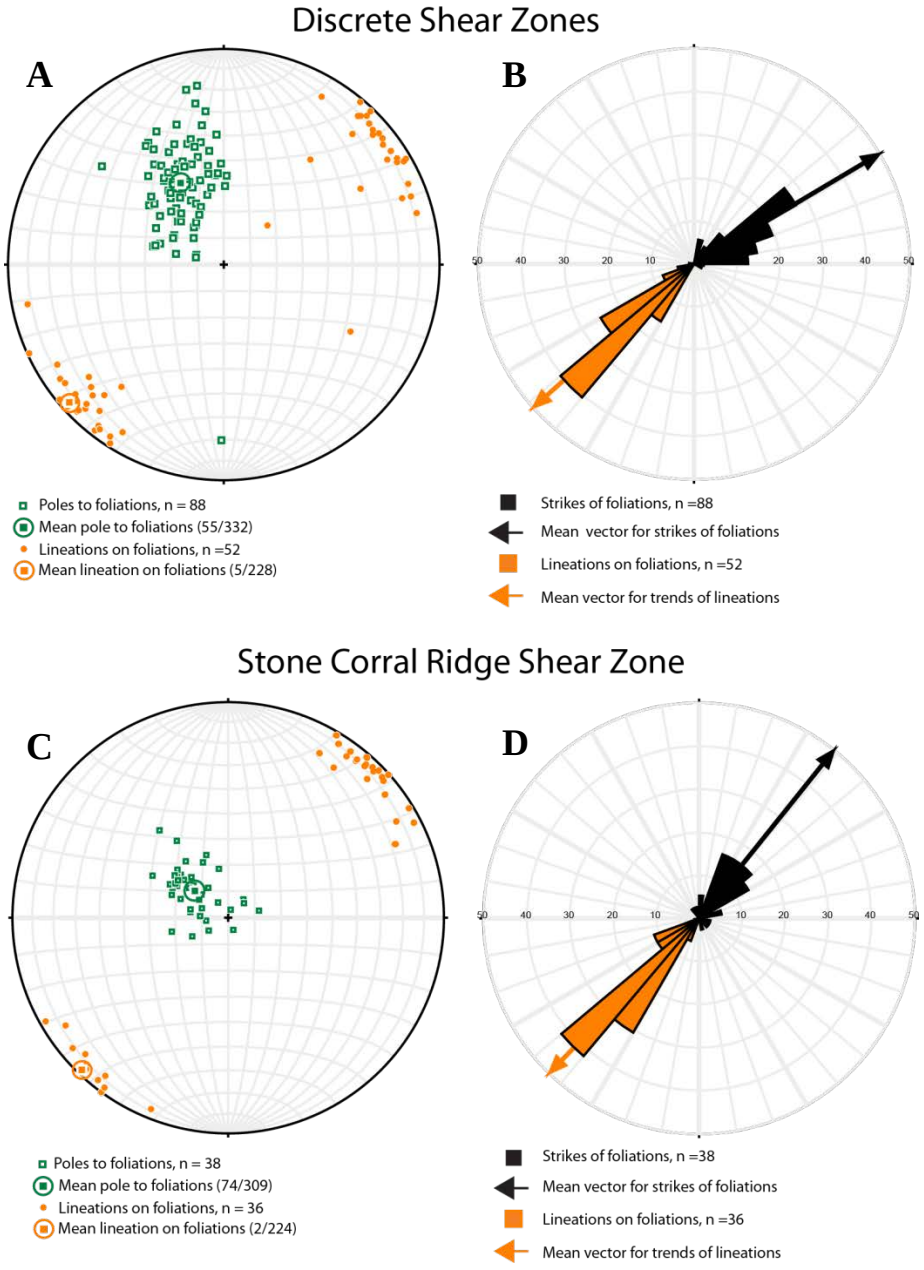

Figure 9.1: Stereograms and rose diagrams of Late Cretaceous structural features in mylonitized rocks after restoration to their positions before MCC exhumation. The structural data displayed in Figure 2.11A, C were rotated 24° about a horizontal axis with an azimuth of 308°. A, C) Stereograms show the shear zones are gently southeast dipping and lineations are gently northeast and southwest plunging. B, D) Rose diagrams show that lineation trends are subparallel to foliation strikes. Equal area, lower hemisphere projections.

Appendix A: FTIR Peaks

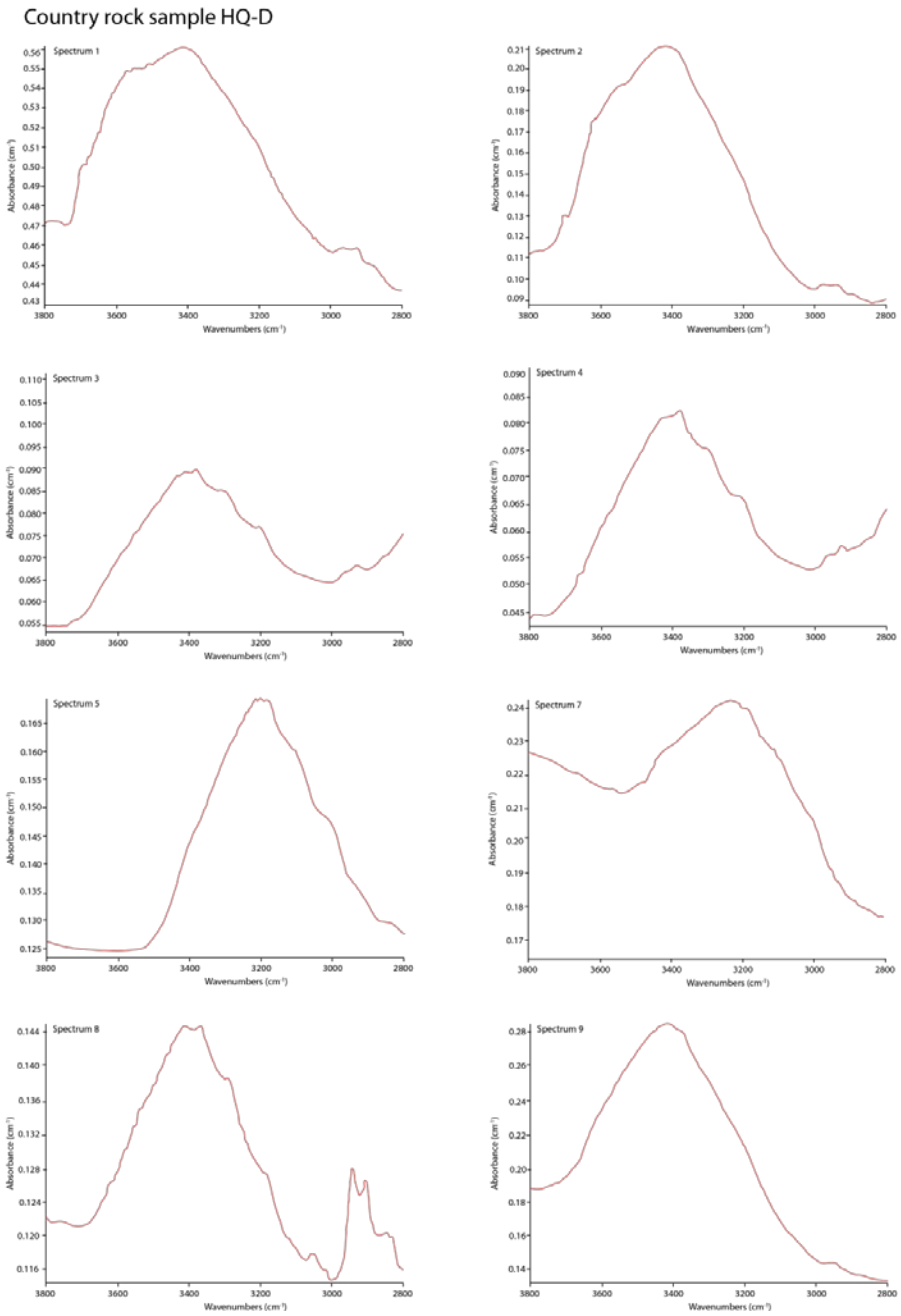

Figure A.1: FTIR point spectra collected from the interiors of individual quartz grains in the country rock sample, HQ-D. Absorbances have not been normalized for sample point thicknesses. The spectrum for Point 6 is missing (continued on next page).

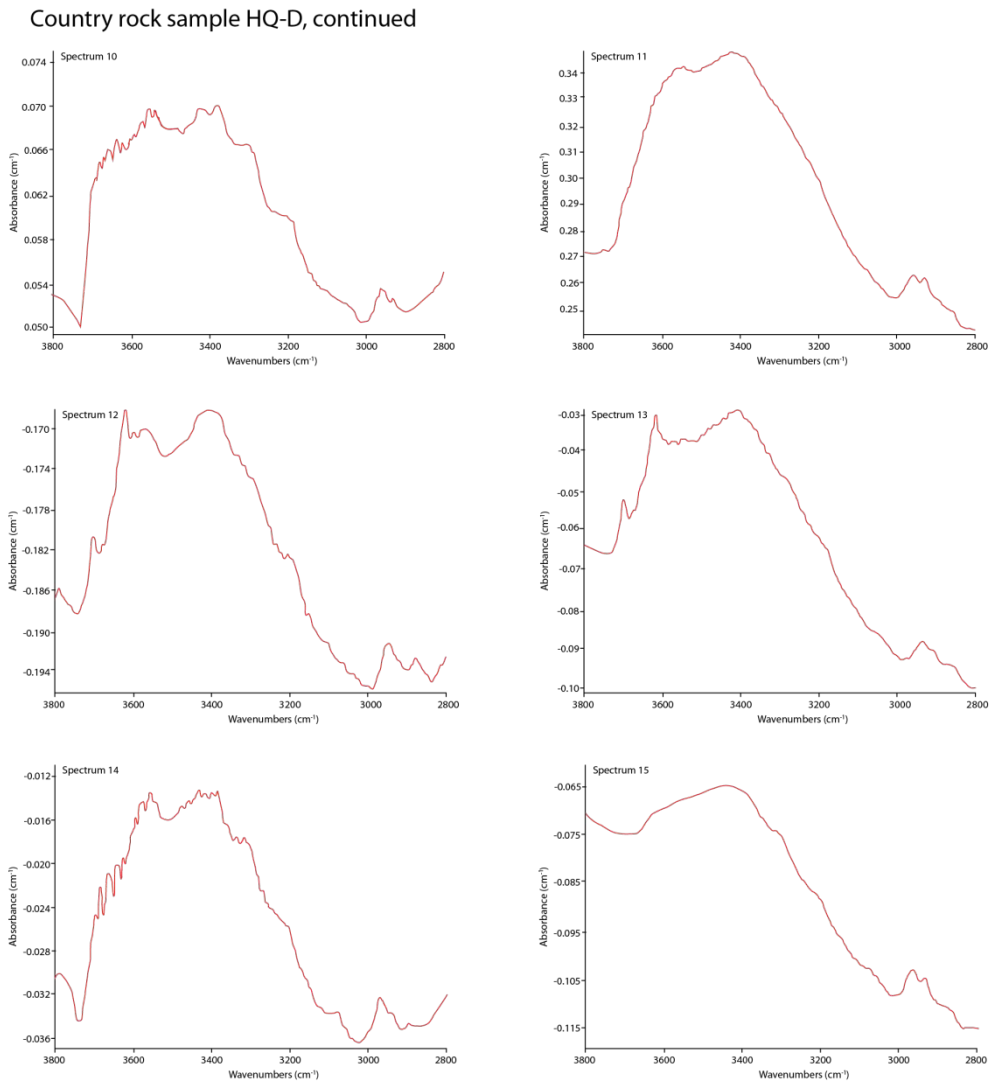

Figure A.1: (continued from previous page).

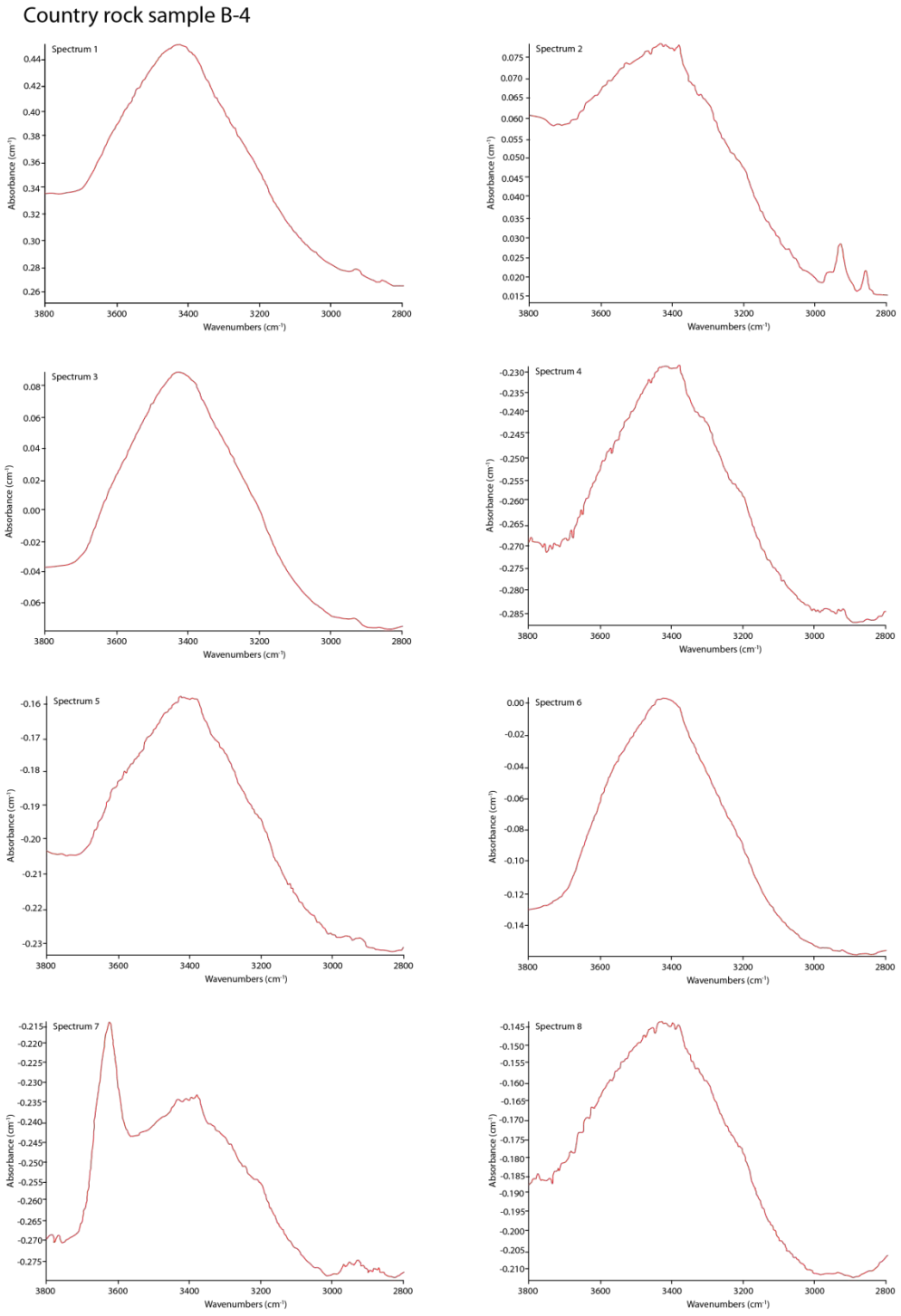

Figure A.2: FTIR point spectra collected from the interiors of individual quartz grains in the country rock sample, B-4. Absorbances have not been normalized for sample point thicknesses (continued on next page).

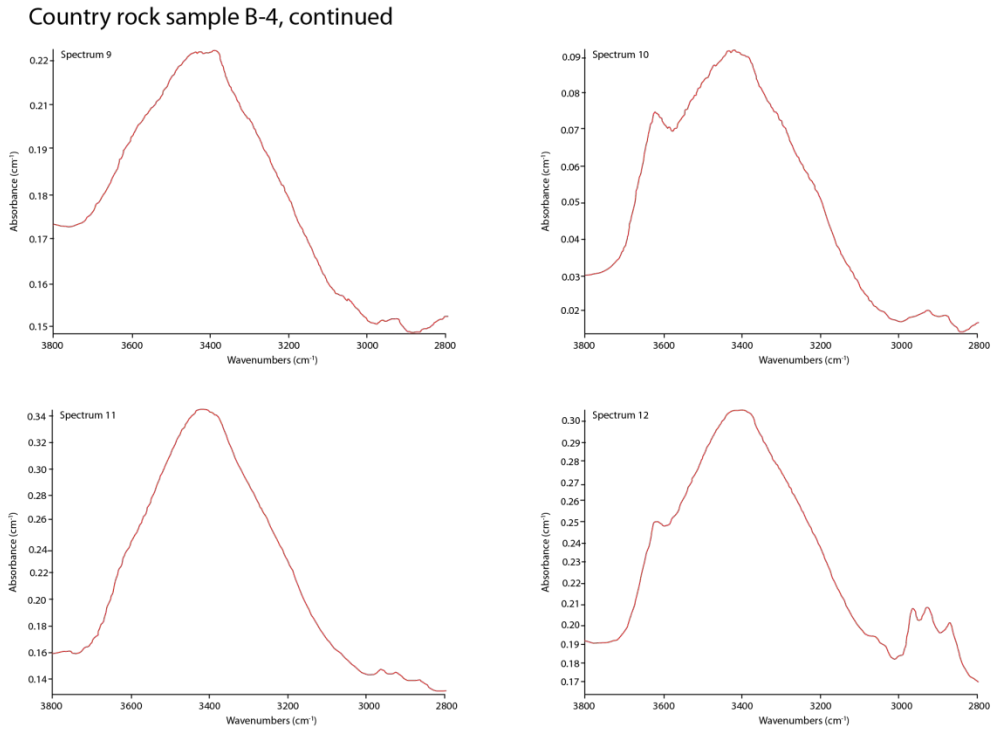

Figure A.2: (continued from previous page).

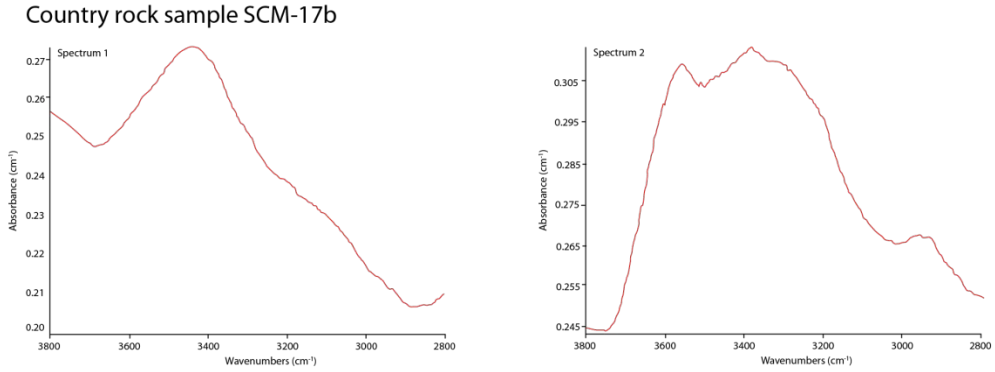

Figure A.3: FTIR point spectra collected from the interiors of individual quartz grains in the country rock sample, SCM-17b. Absorbances have not been normalized for sample point thicknesses (continued on next page).

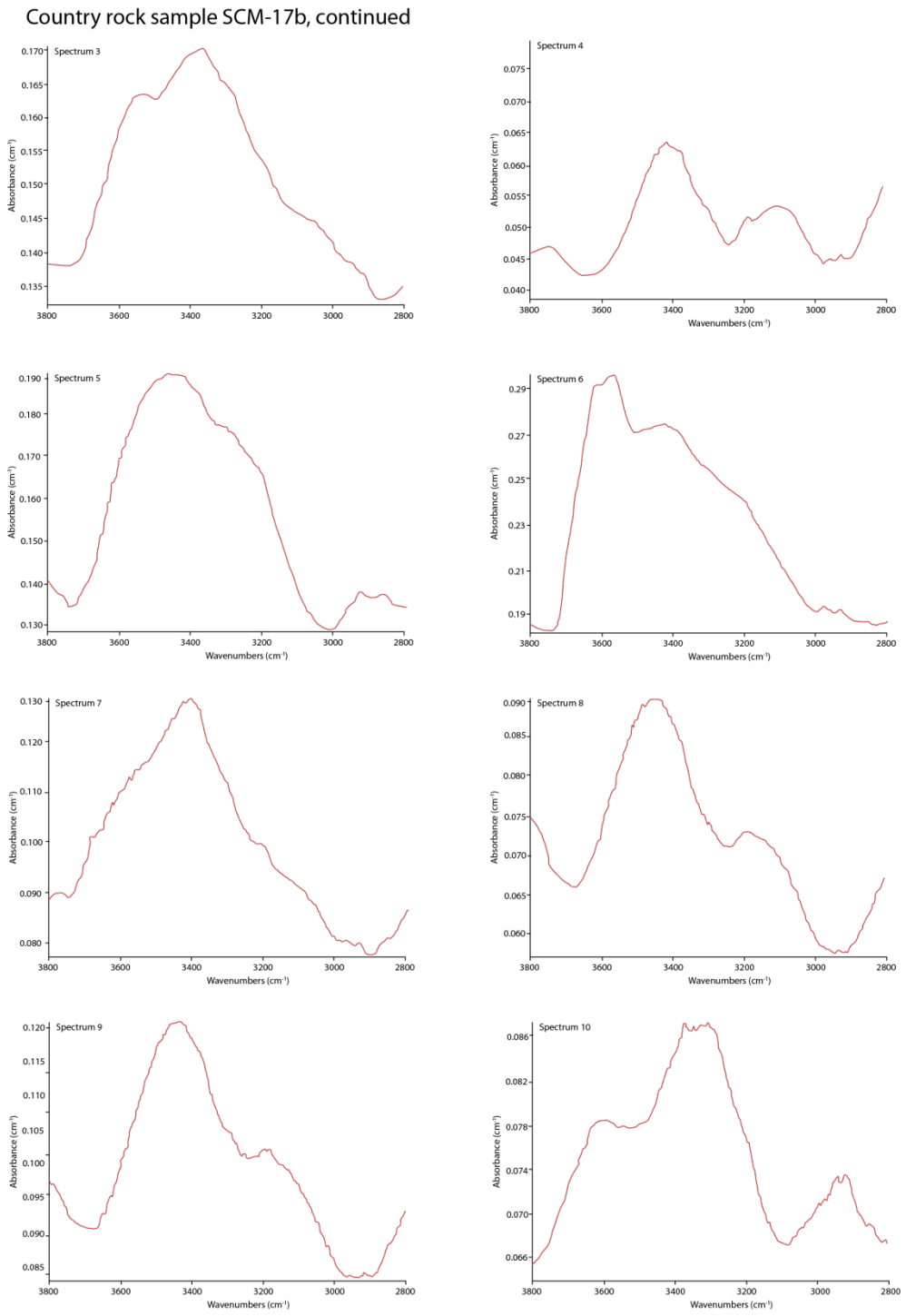

Figure A.3: (continued from previous page).

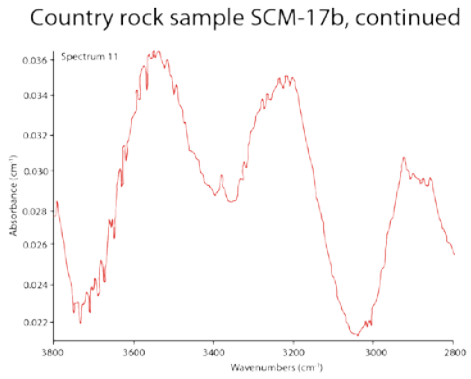

Figure A.3: (continued from previous page).

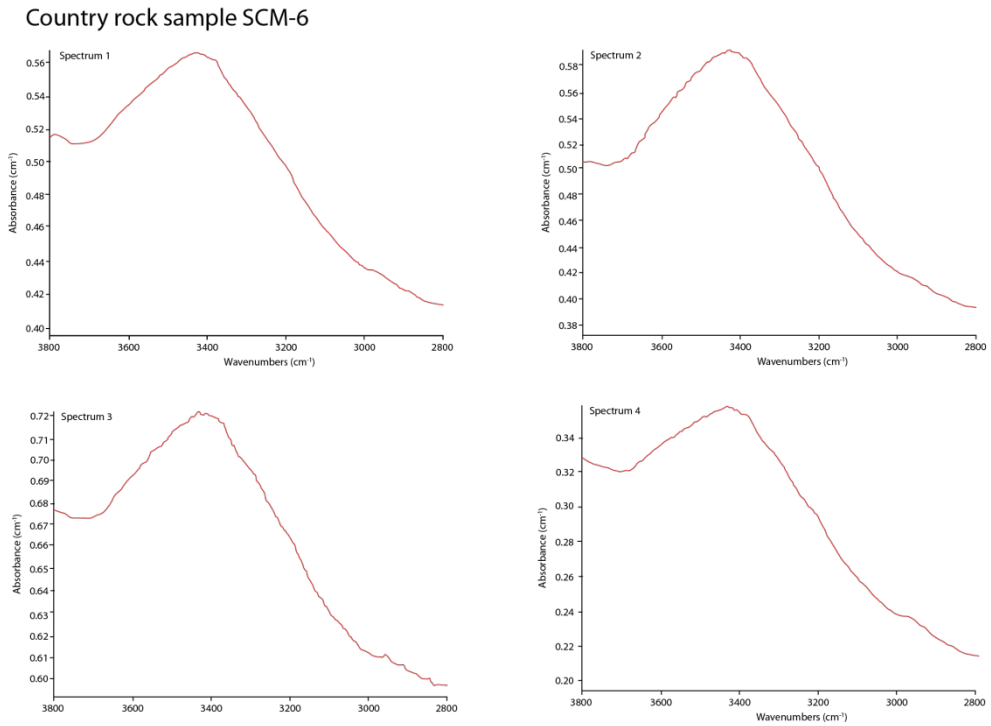

Figure A.4: FTIR point spectra collected from the interiors of individual quartz grains in the country rock sample, SCM-6. Absorbances have not been normalized for sample point thicknesses (continued on next page).

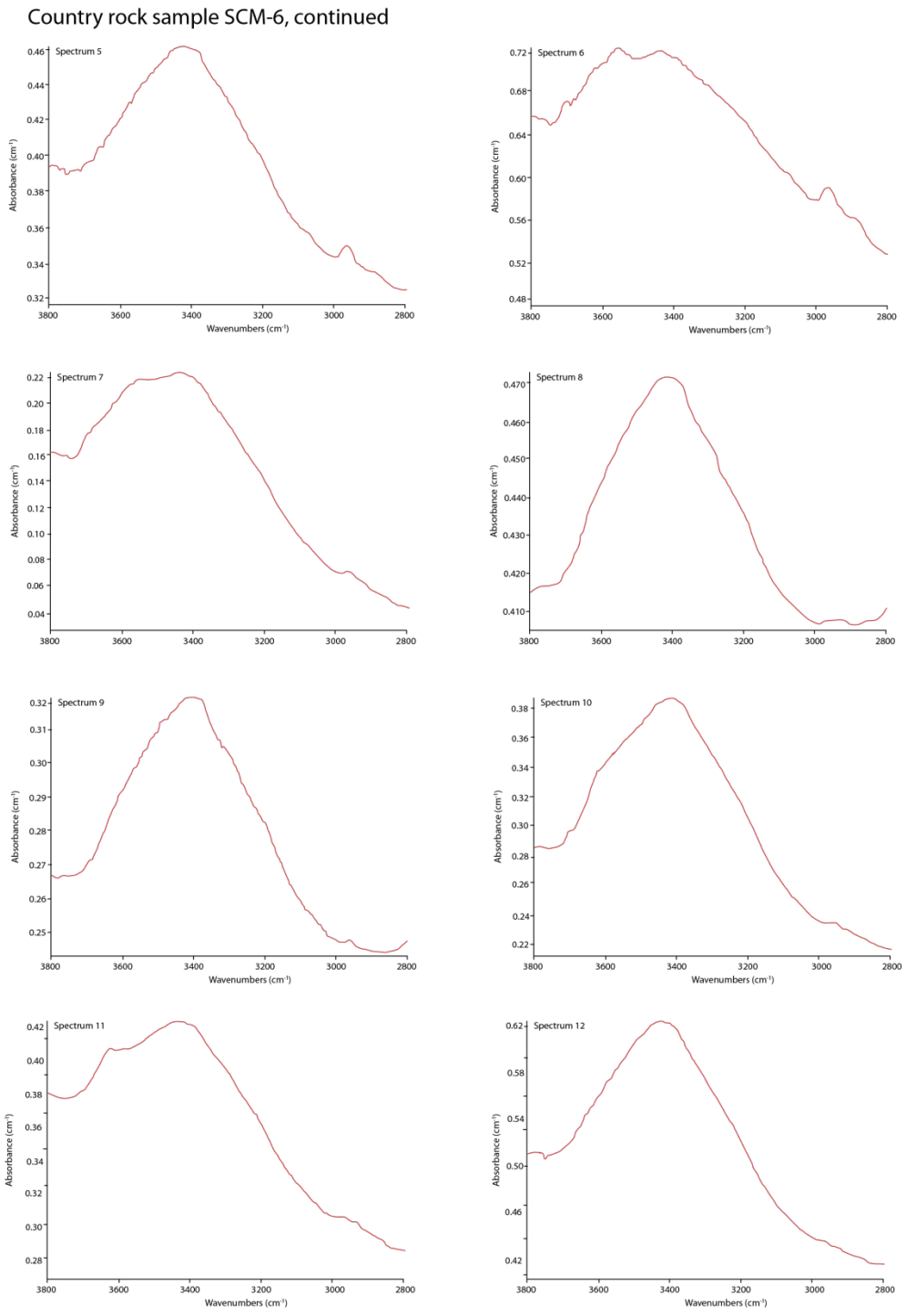

Figure A.4: (continued from previous page).

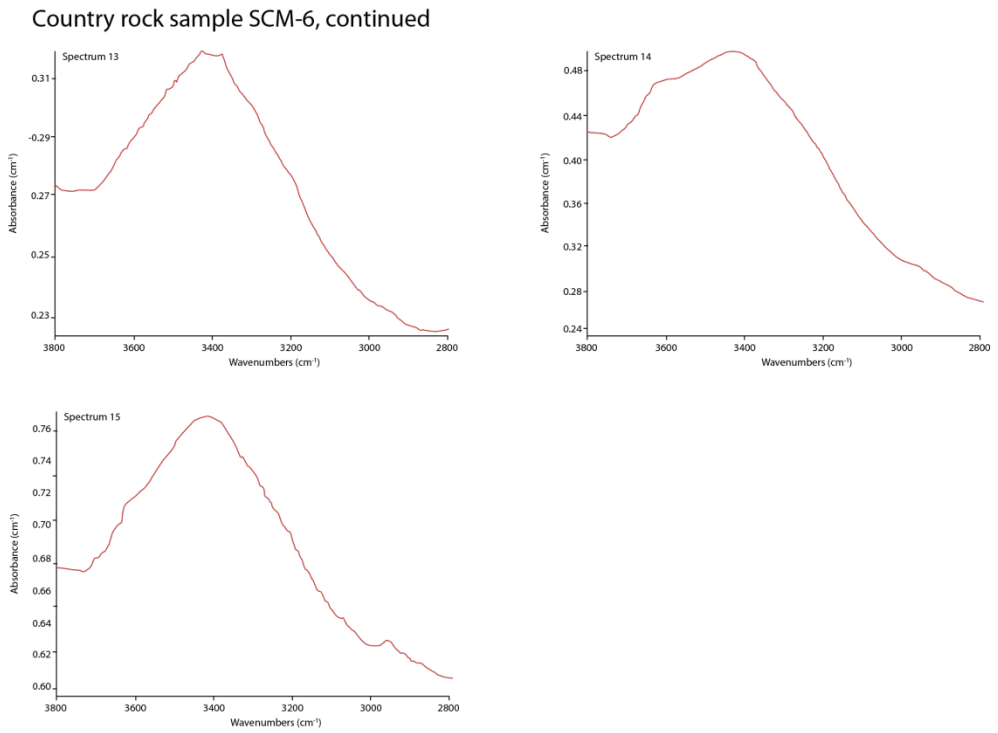

Figure A.4: (continued from previous page).

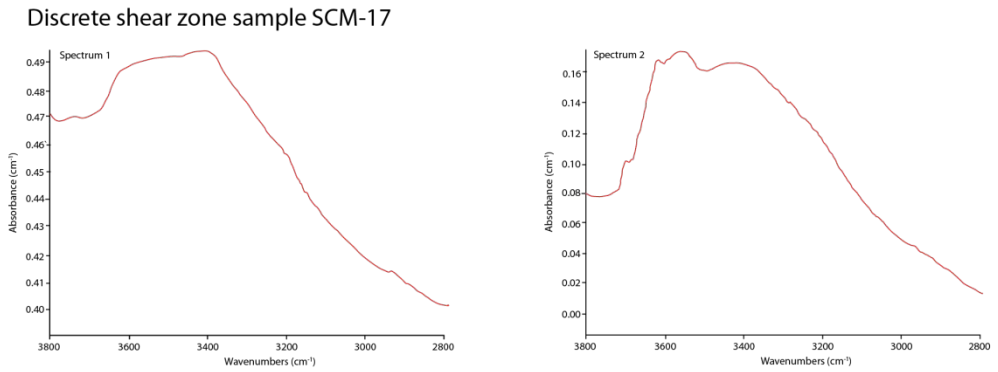

Figure A.5: FTIR point spectra collected from the interiors of individual quartz grains in the discrete shear zone mylonite sample, SCM-17. Absorbances have not been normalized for sample point thicknesses (continued on next page).

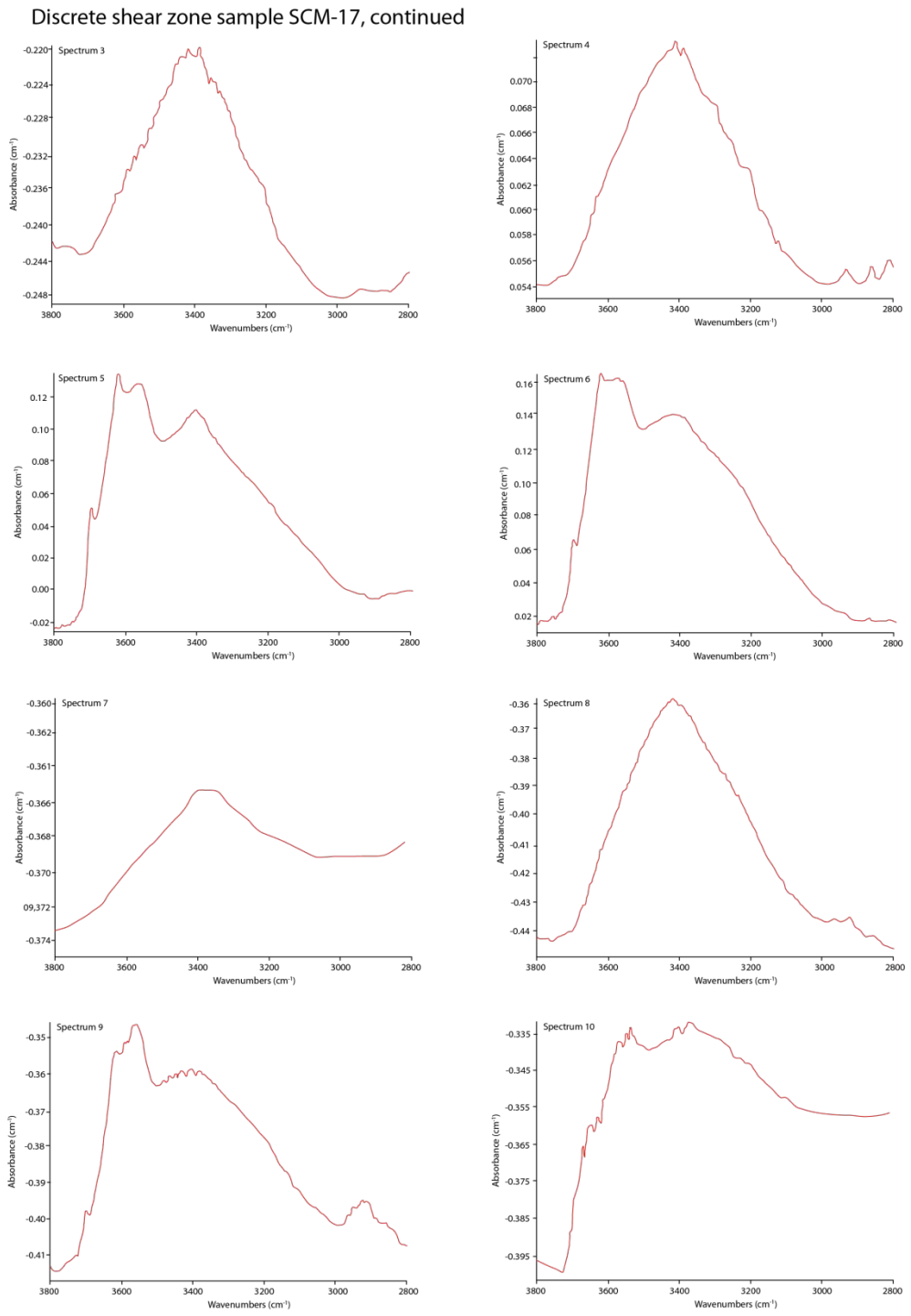

Figure A.5: (continued from previous page).

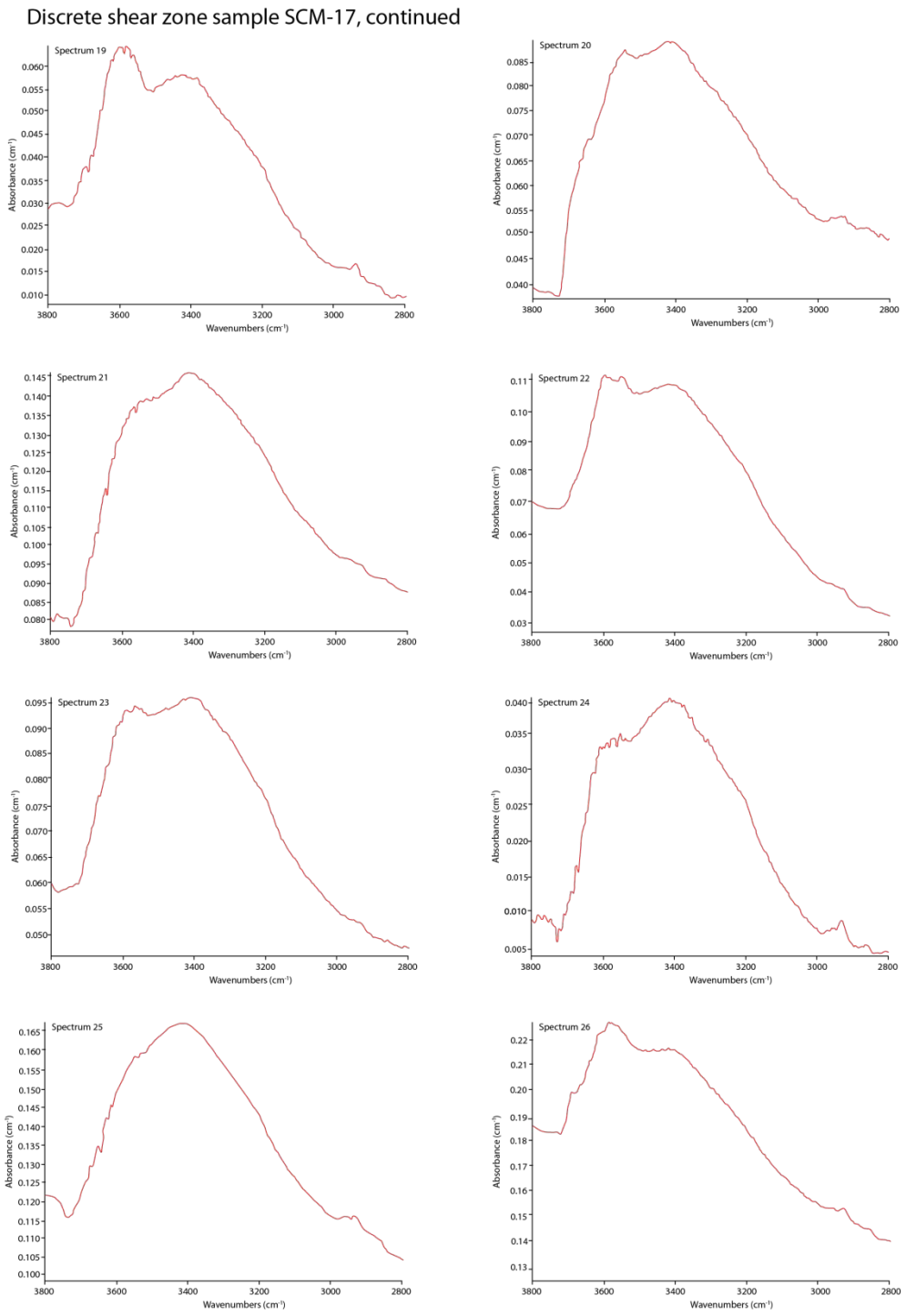

Figure A.5: (continued from previous page).

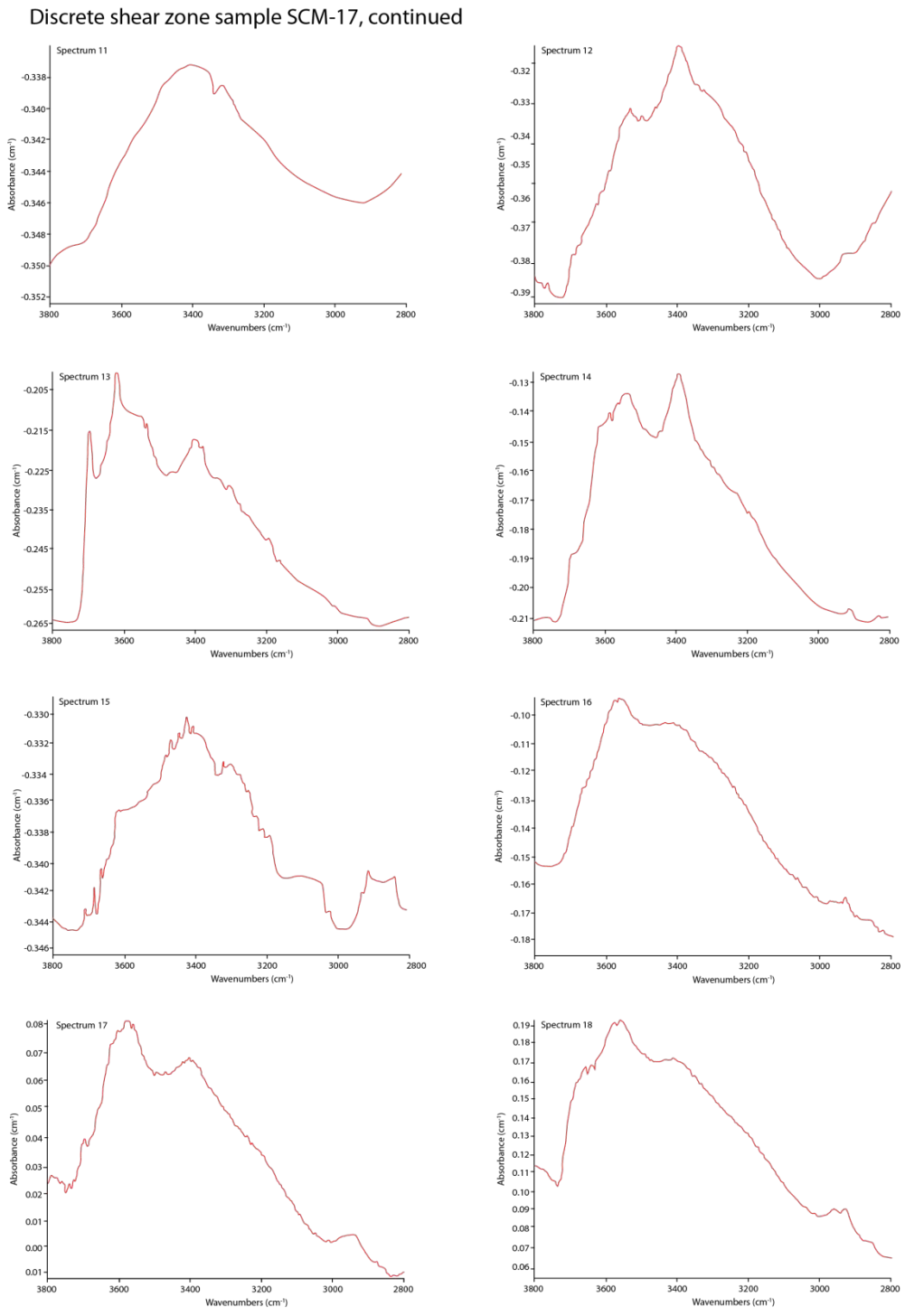

Figure A.5: (continued from previous page).

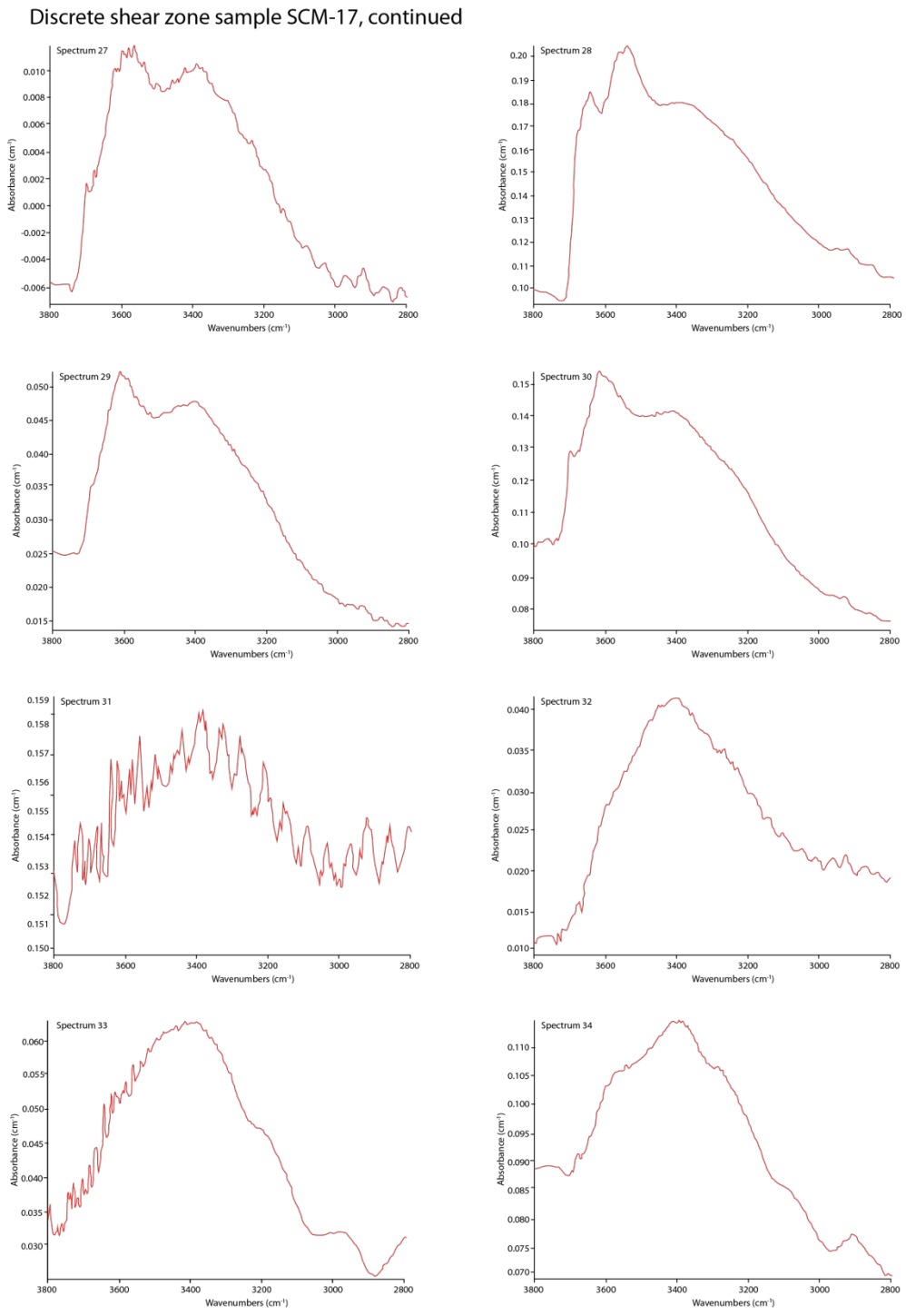

Figure A.5: (continued from previous page).

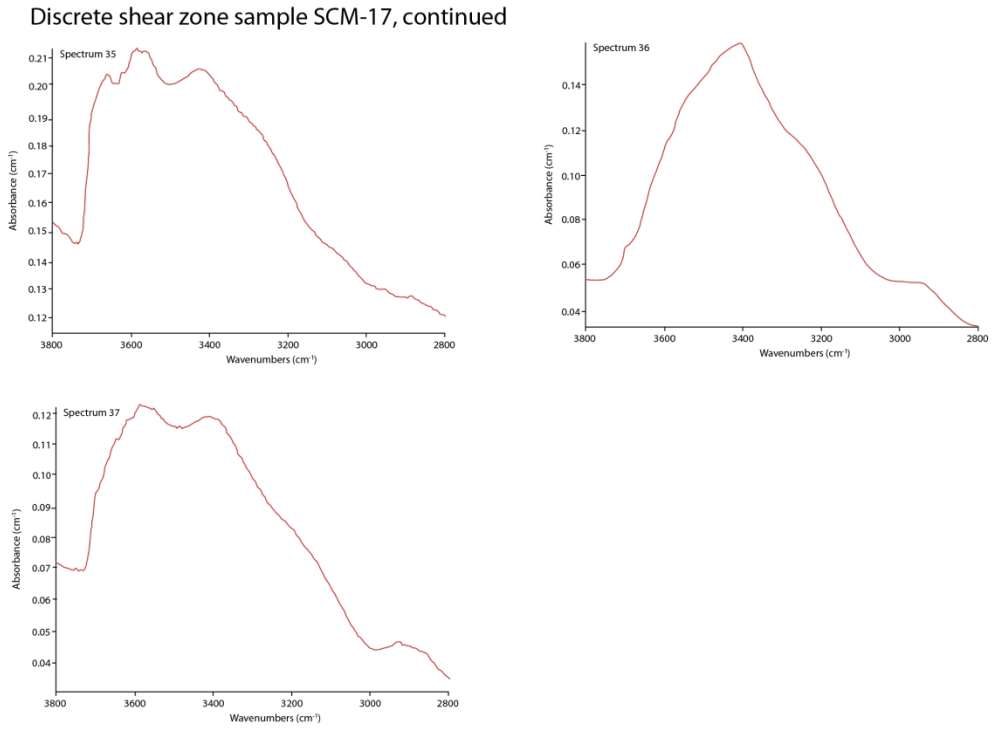

Figure A.5: (continued from previous page).

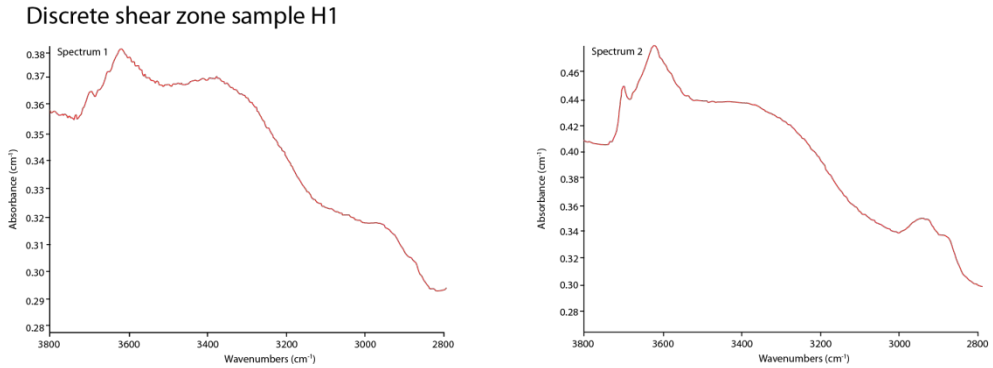

Figure A.6: FTIR point spectra collected from the interiors of individual quartz grains in the discrete shear zone mylonite sample, H1. Absorbances have not been normalized for sample point thicknesses (continued on next page).

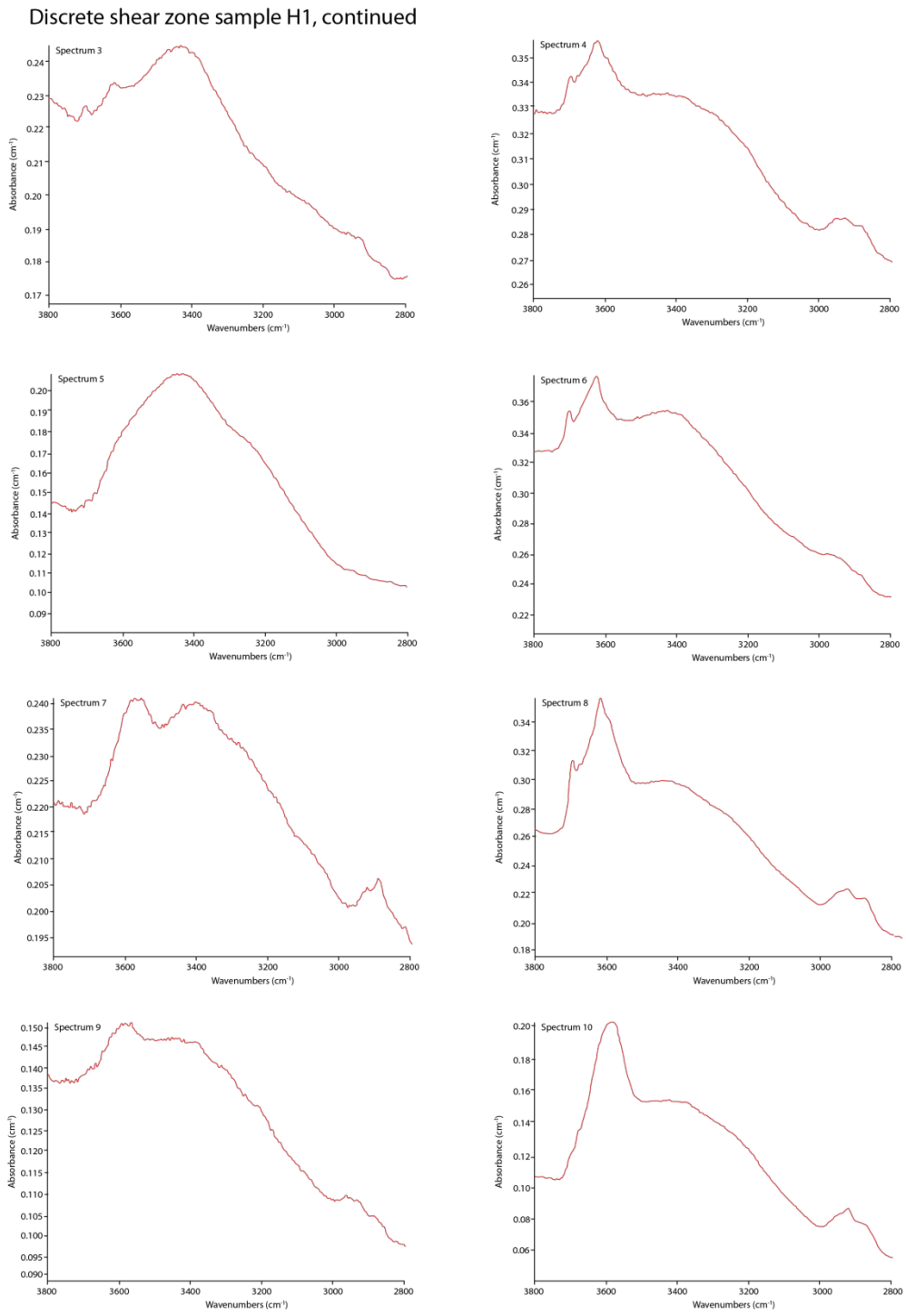

Figure A.6: (continued from previous page).

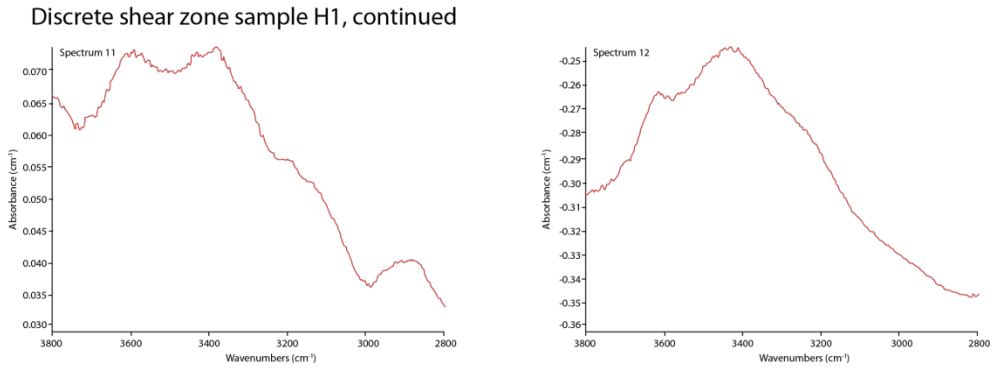

Figure A.6: (continued from previous page).

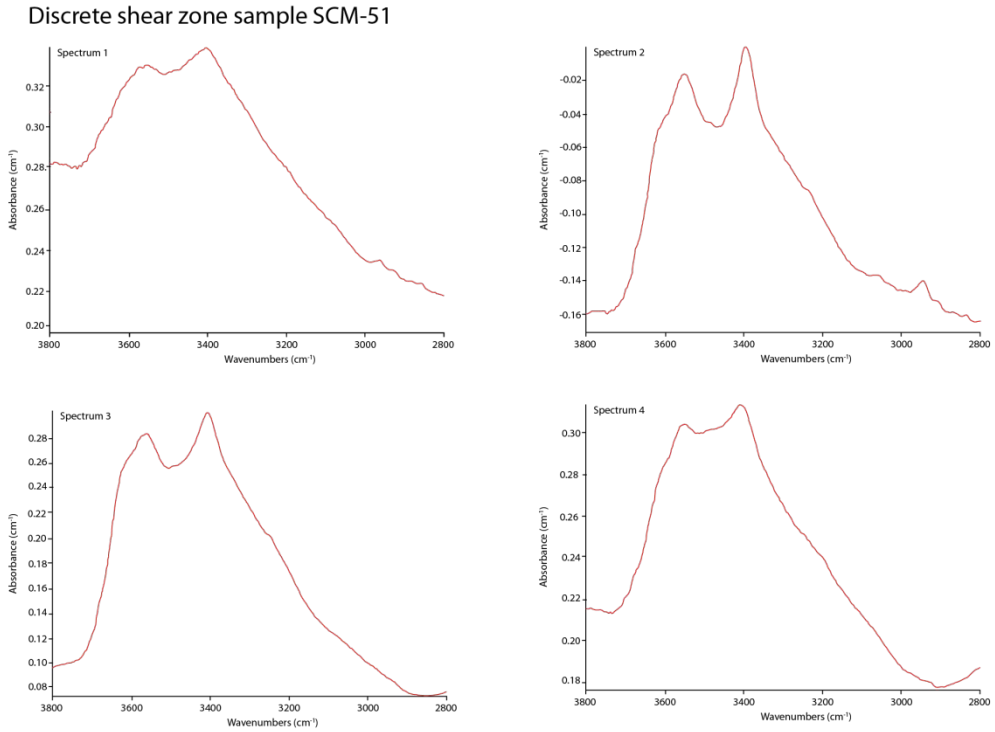

Figure A.7: FTIR point spectra collected from the interiors of individual quartz grains in the discrete shear zone mylonite sample, SCM-51. Absorbances have not been normalized for sample point thicknesses (continued on next page).

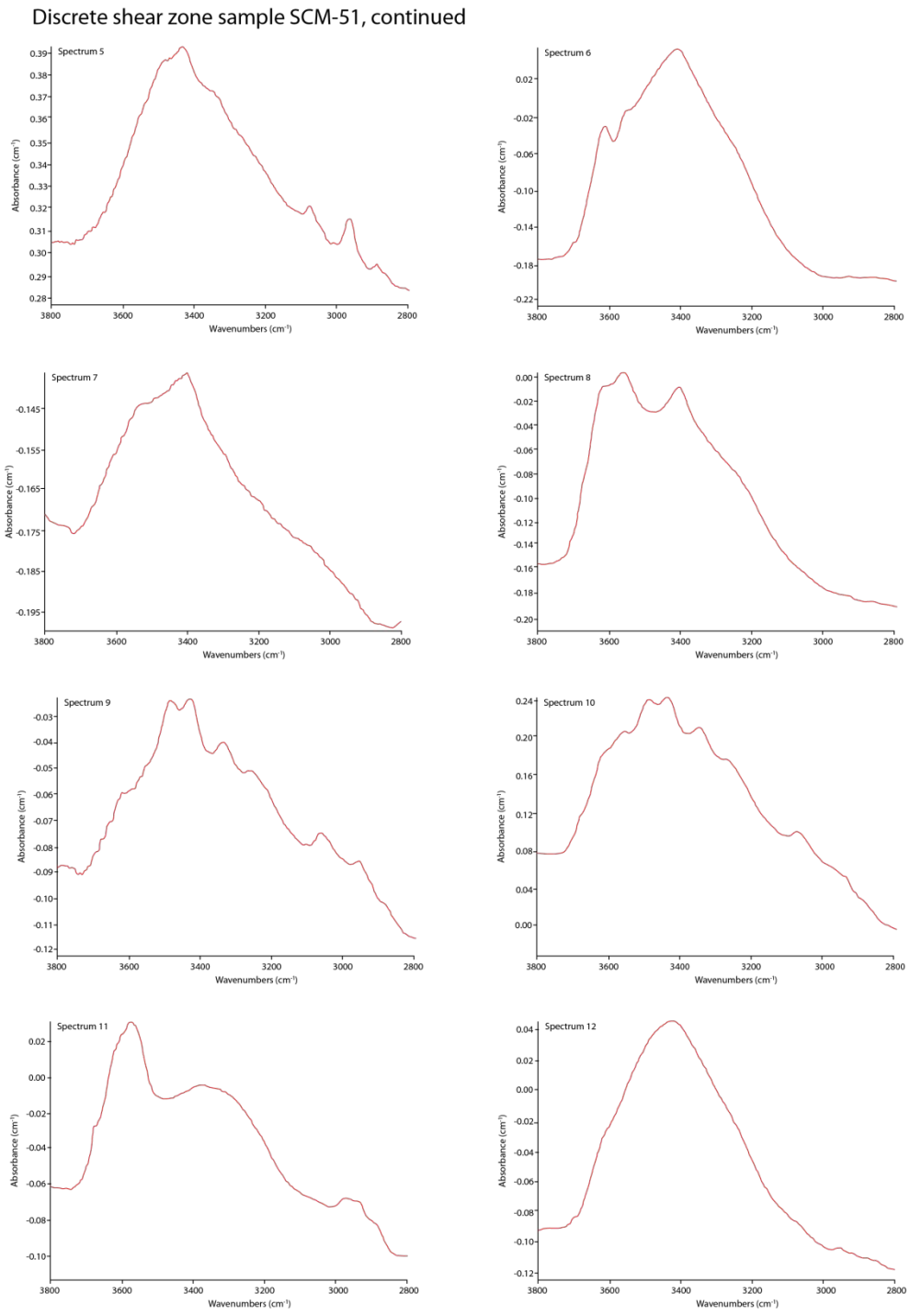

Figure A.7: (continued from previous page).

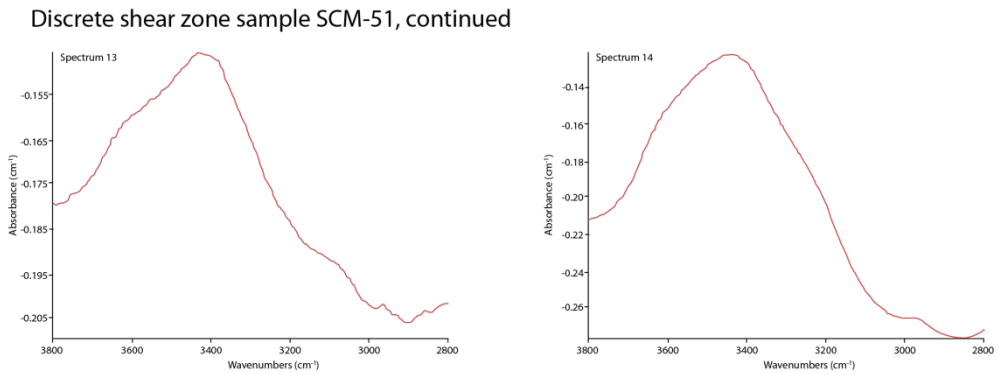

Figure A.7: (continued from previous page).

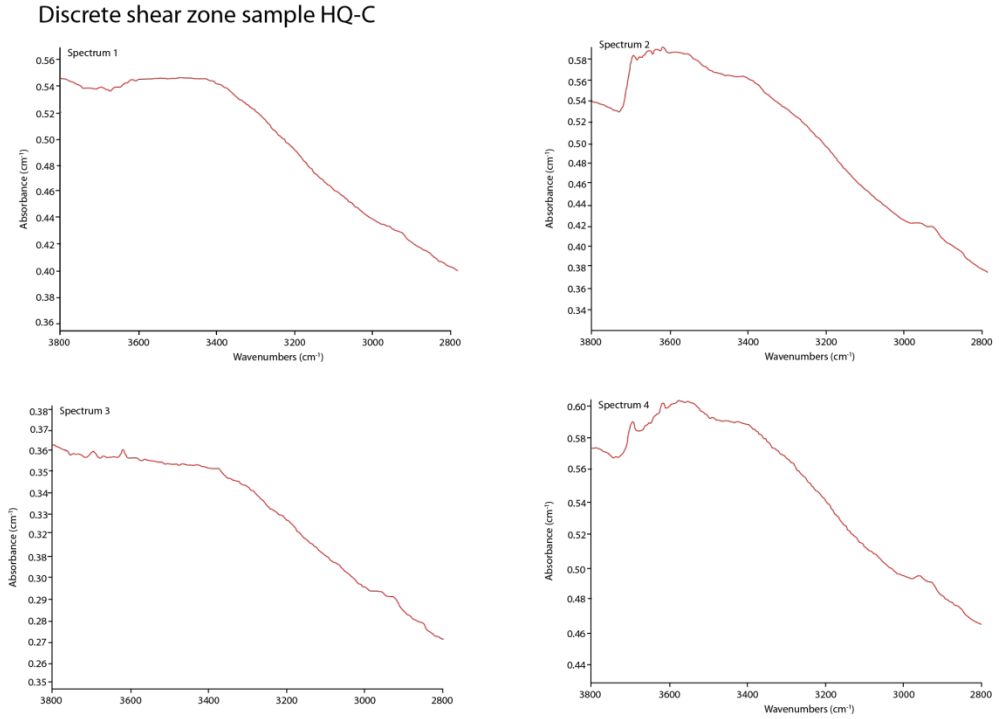

Figure A.8: FTIR point spectra collected from the interiors of individual quartz grains in the discrete shear zone mylonite sample, HQ-C. Absorbances have not been normalized for sample point thicknesses. The spectrum for Point 16 is missing (continued on next page).

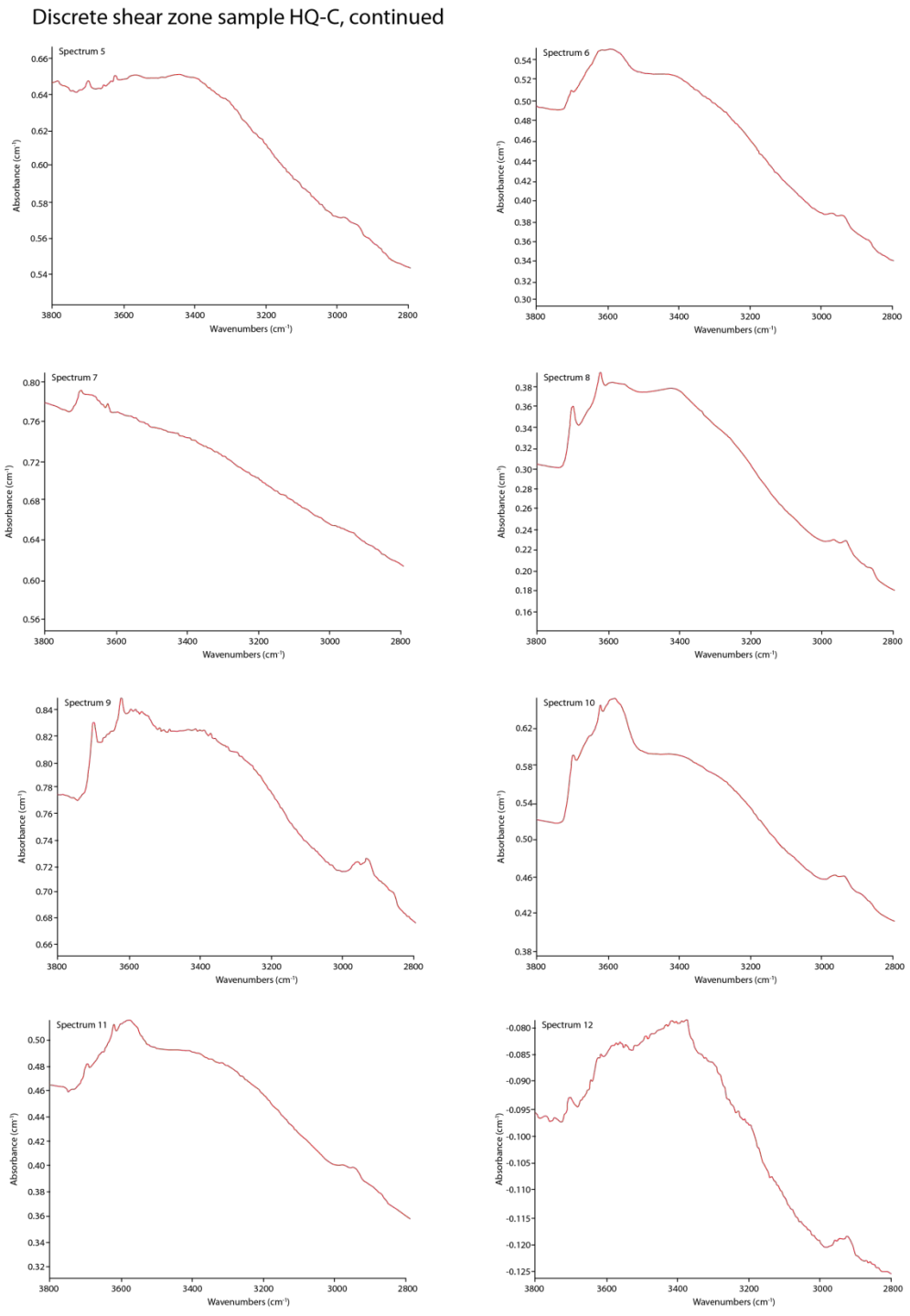

Figure A.8: (continued from previous page).

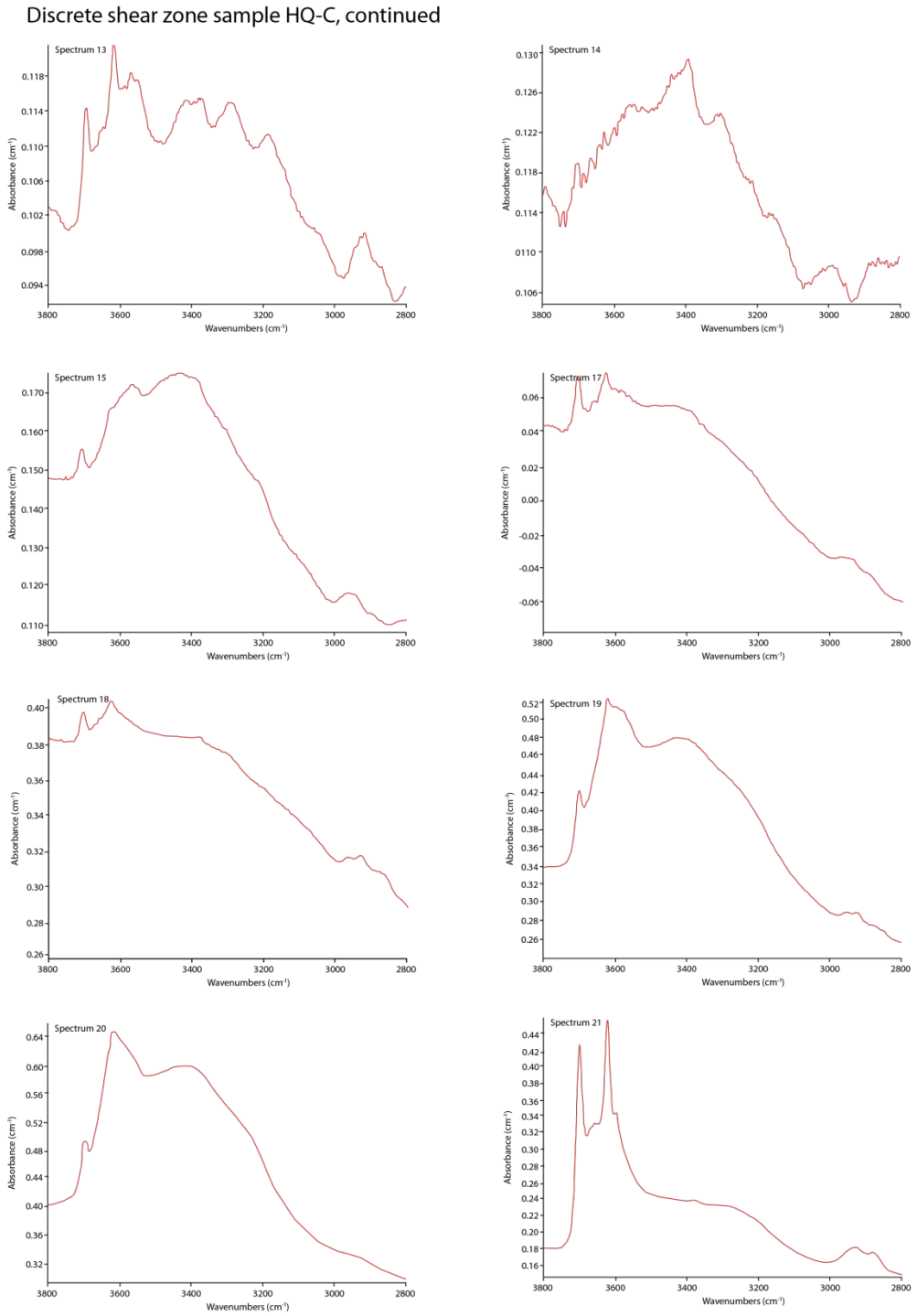

Figure A.8: (continued from previous page).

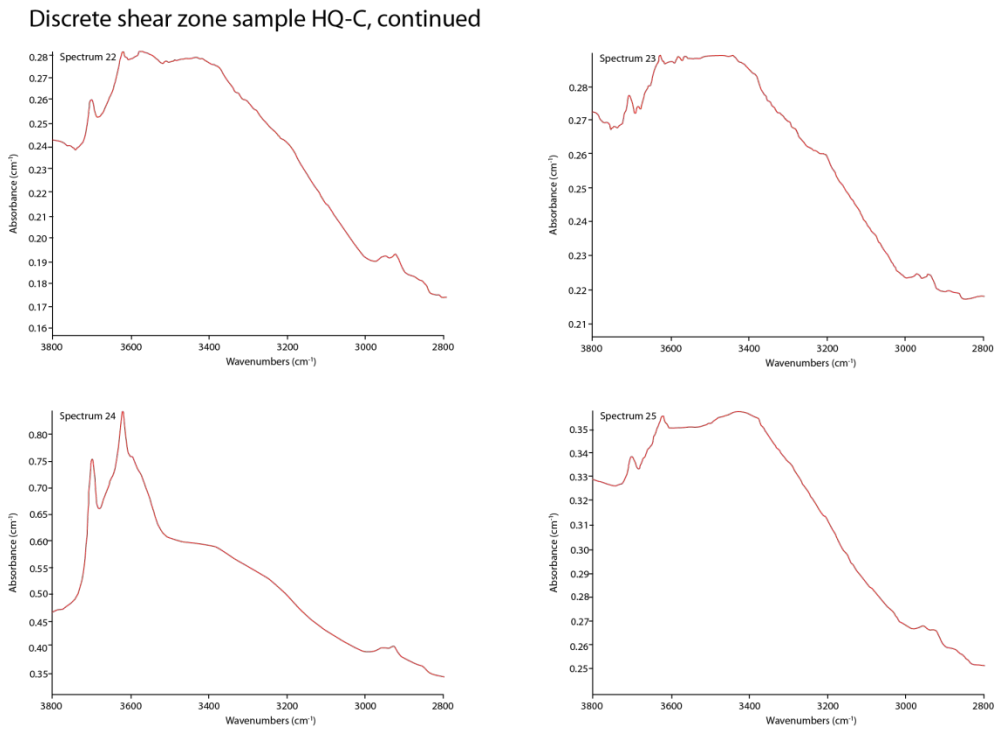

Figure A.8: (continued from previous page).

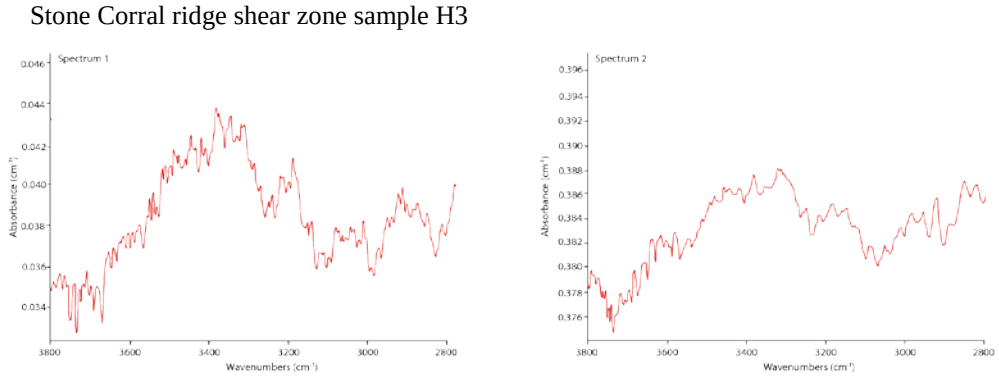

Figure A.9: FTIR point spectra collected from the interiors of individual quartz grains in the Stone Corral ridge shear zone sample, H3. Absorbances have not been normalized for sample point thicknesses (continued on next page).

Stone Corral ridge shear zone sample H3, continued

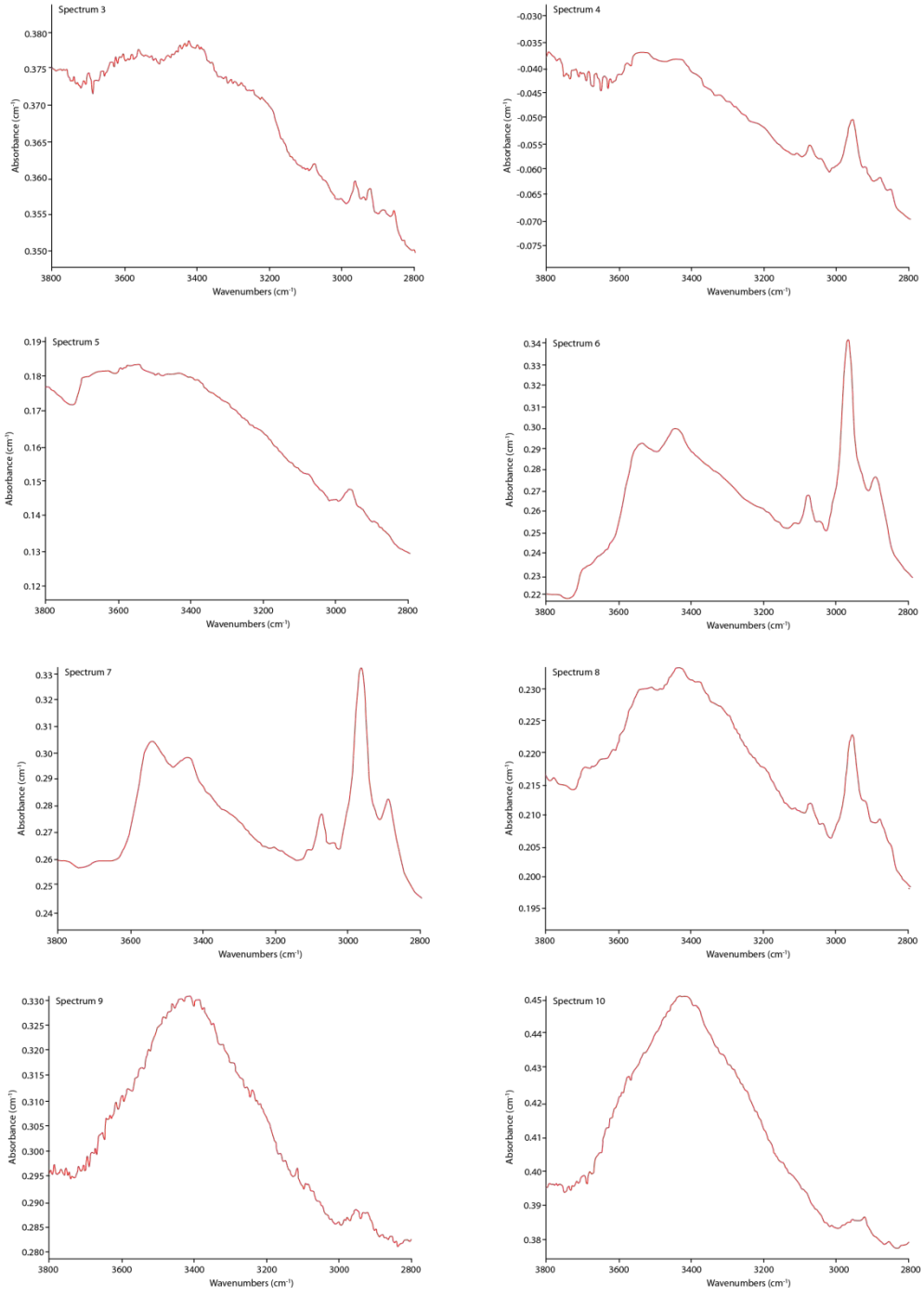

Figure A.9: (continued from previous page).

Stone Corral ridge shear zone sample H3, continued

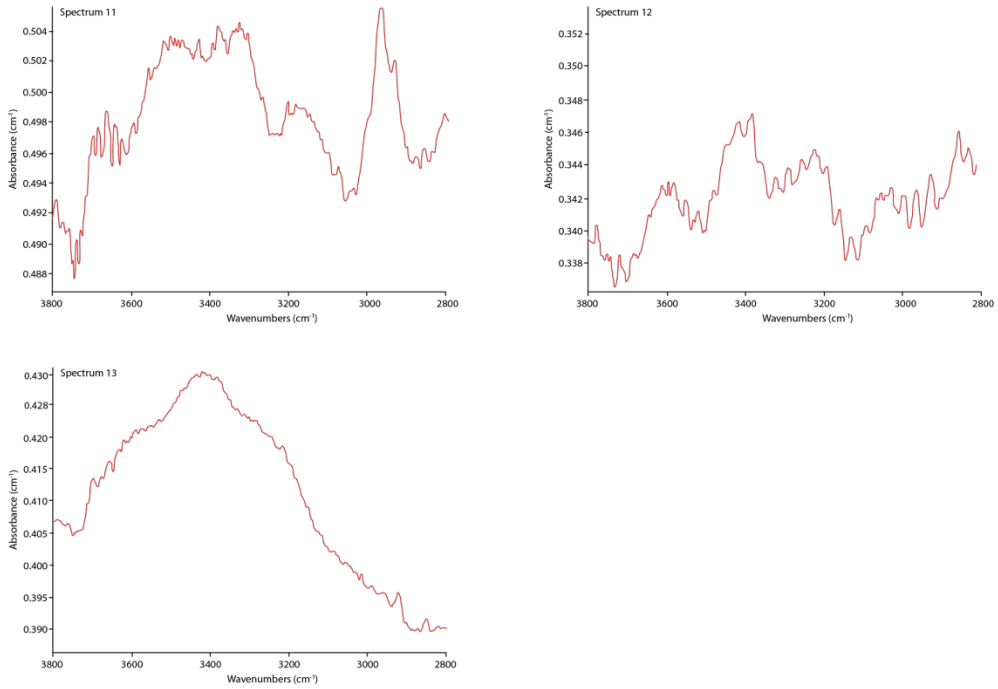

Figure A.9: (continued from previous page).

Stone Corral ridge shear zone sample B-3

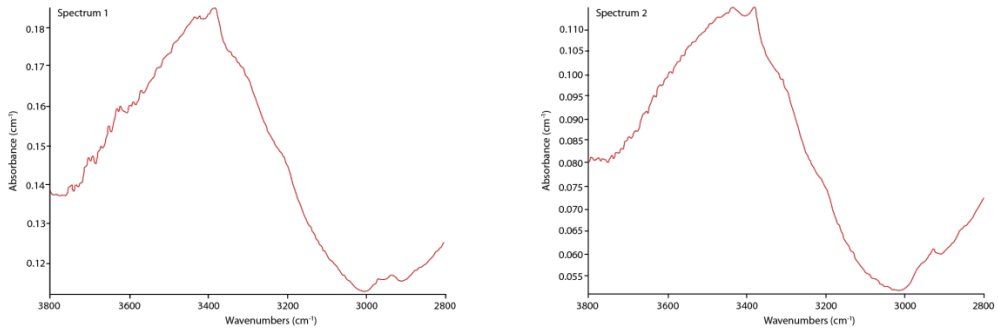

Figure A.10: FTIR point spectra collected from the interiors of individual quartz grains in the Stone Corral ridge shear zone sample, B-3. Absorbances have not been normalized for sample point thicknesses (continued on next page).

Stone Corral ridge shear zone sample B-3, continued

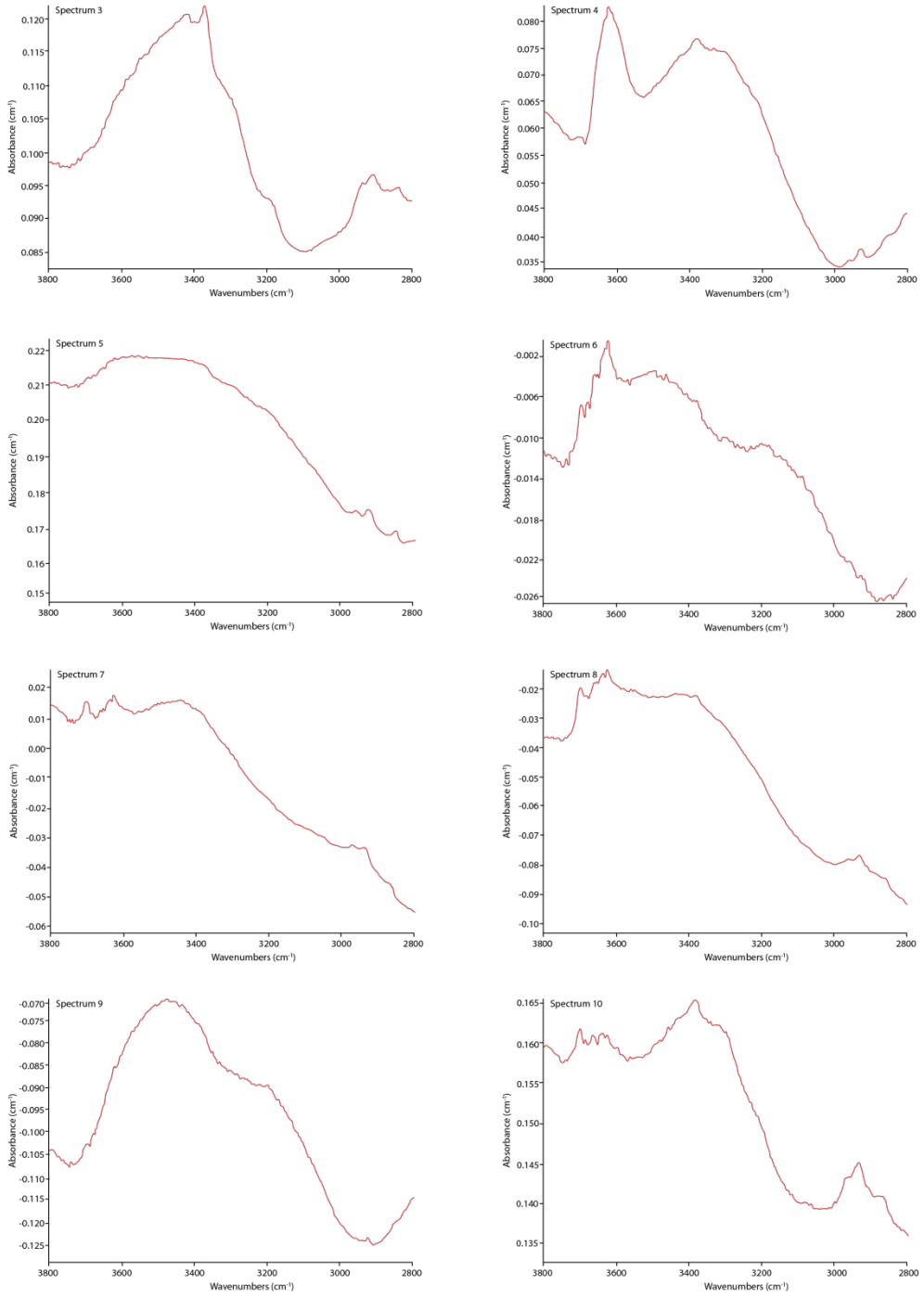

Figure A.10: (continued from previous page).

Stone Corral ridge shear zone sample B-3, continued

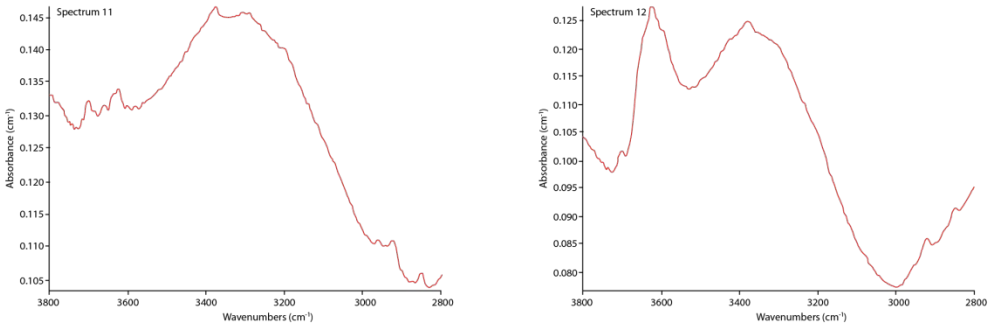

Figure A.10: (continued from previous page).

Isolated shear zone sample B-5

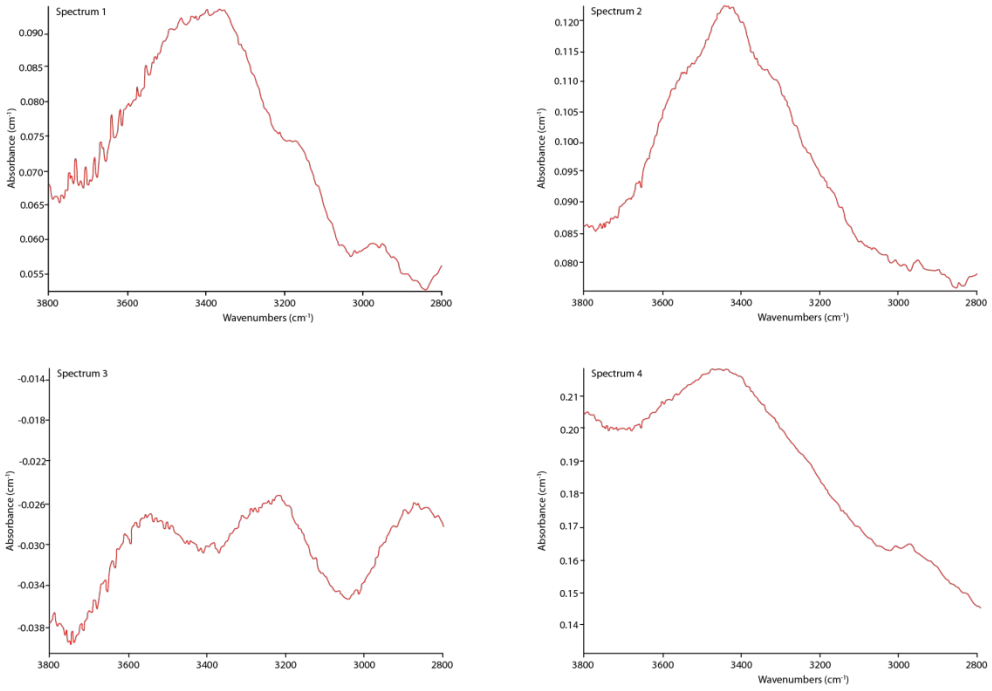

Figure A.11: FTIR point spectra collected from the interiors of individual quartz grains in the isolated shear zone sample, B-5. Absorbances have not been normalized for sample point thicknesses (continued on next page).

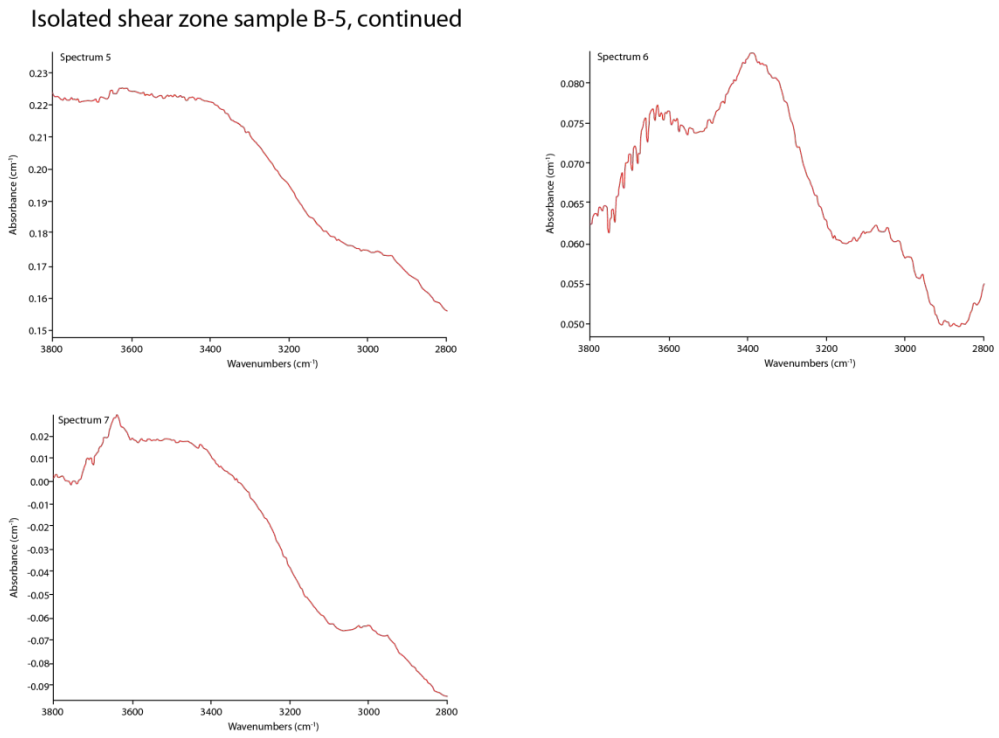

Figure A.11: (continued from previous page).

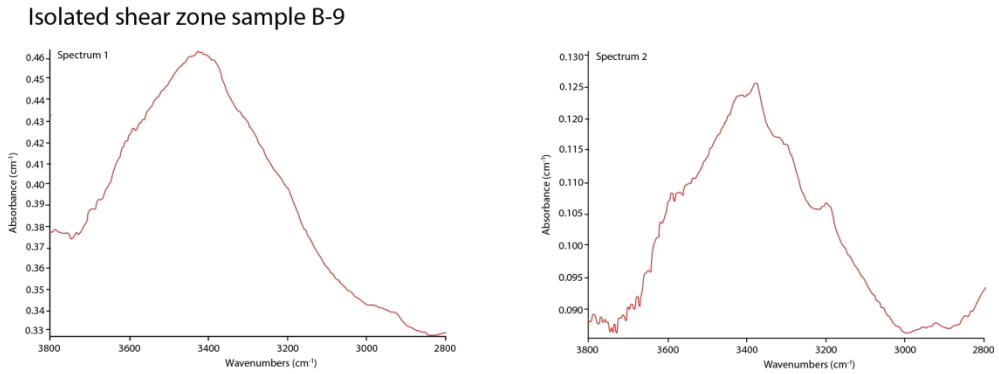

Figure A.12: FTIR point spectra collected from the interiors of individual quartz grains in the isolated shear zone sample, B-9. Absorbances have not been normalized for sample point thicknesses (continued on next page).

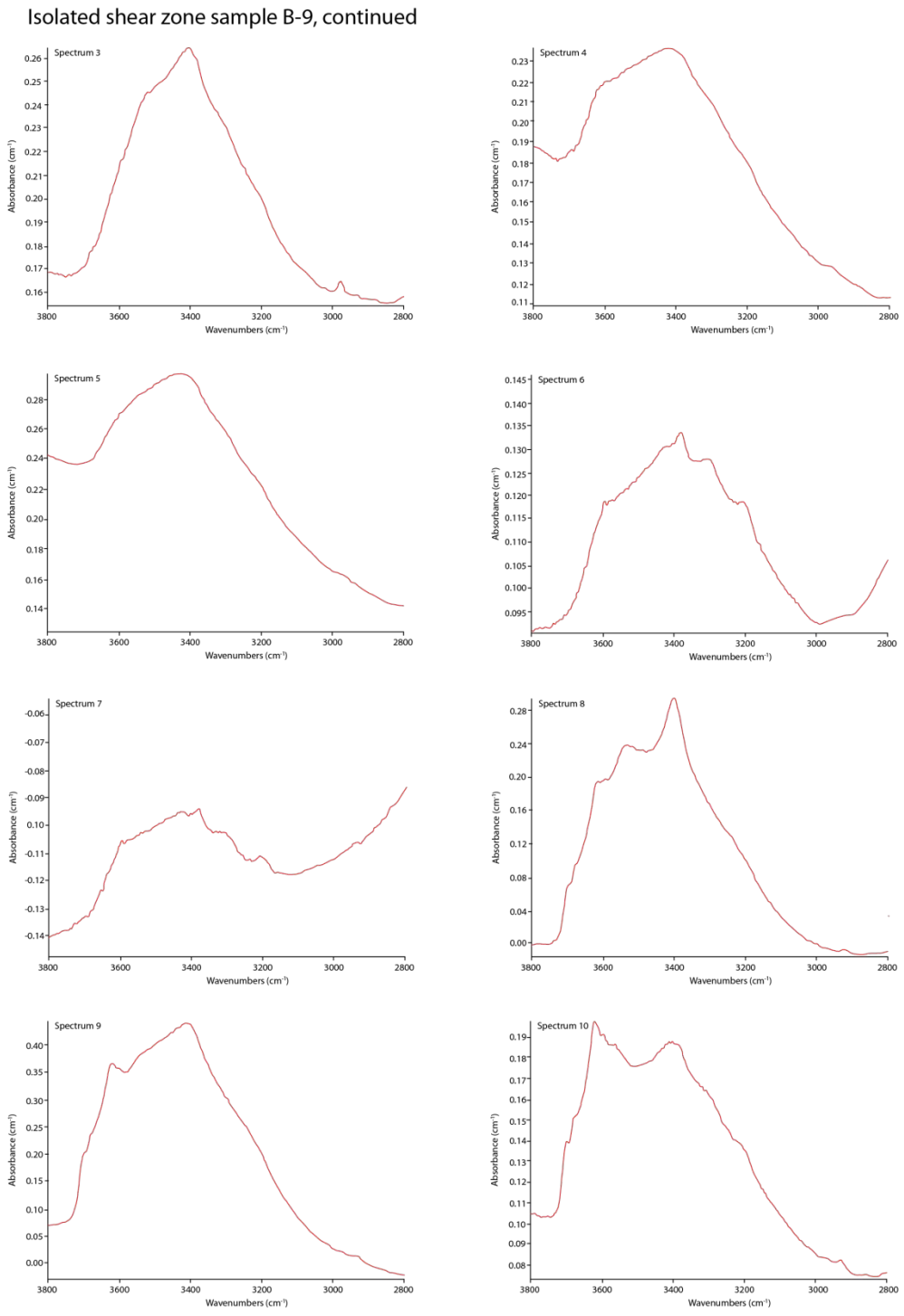

Figure A.12: (continued from previous page).

Isolated shear zone sample B-9, continued

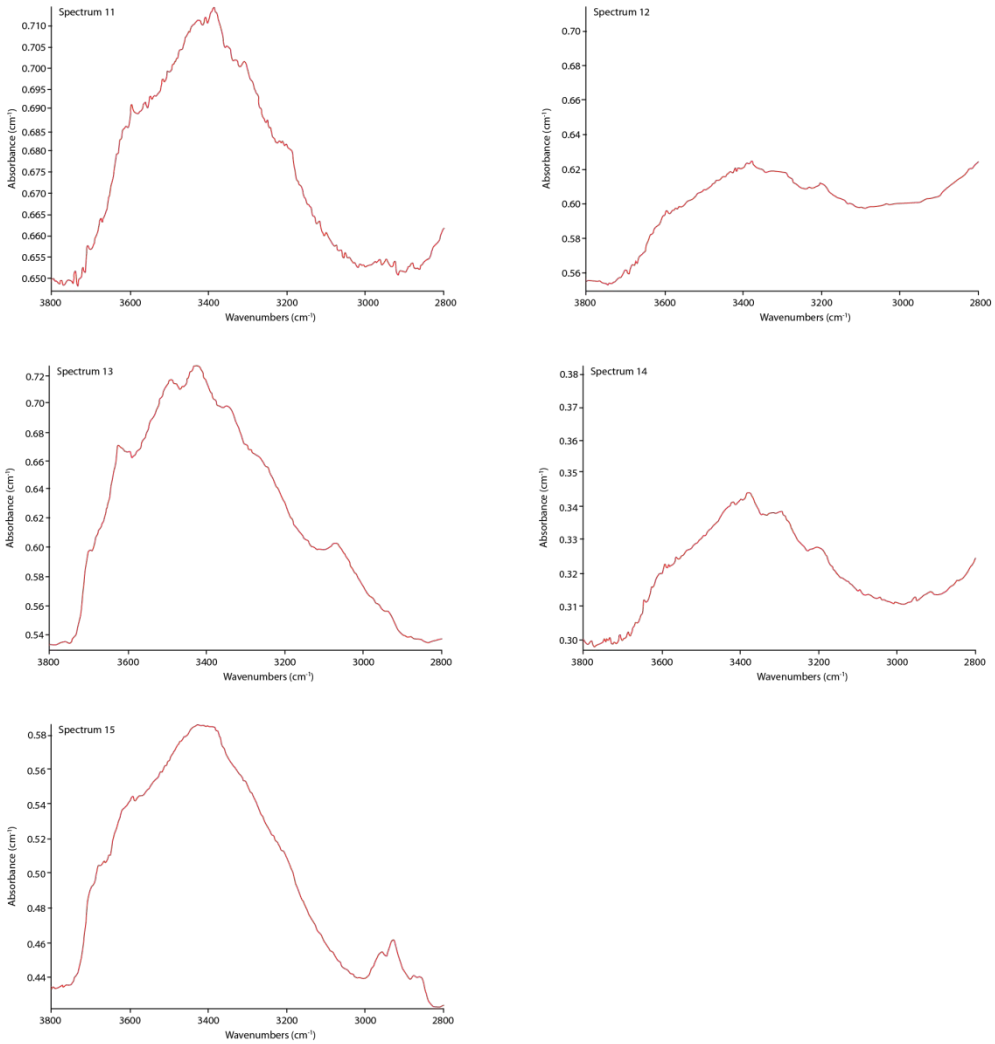

Figure A.12: (continued from previous page).

Appendix B: Oxygen Stable Isotope Geothermometry

Quartz-feldspar geothermometry was performed on two samples from discrete shear zones that exhibited bleaching (samples SCM-51 and HQ-B), and quartz-epidote geothermometry was also performed on sample SCM-51, in an effort to obtain an estimate of the temperature of discrete shear zone mylonitization.

B.1 METHODS

The methods used for stable isotope analysis are described in detail in Chapter 7 (see also Table B.1 for a data summary). Quartz-feldspar geothermometry was performed using the data from two of the discrete shear zone samples that displayed bleaching (HQ-B and SCM-51), and quartz-epidote geothermometry was performed using the data from the sample with the central epidote vein (SCM-51). The calibrations of Chiba et al. (1989) and Matthews (1994) were used, and calculations followed the form: $1000 \ln \alpha = A \times 10^6 T^{-2}$, where $1000 \ln \alpha$ (mineral 1, mineral 2) $\approx \Delta^{18}O_{\text{min 1 – min 2}} \approx \delta^{18}O_{\text{mineral 1}} - \delta^{18}O_{\text{mineral 2}}$, and where A is the fractionation coefficient. The fractionation coefficient is dependent on the composition of the feldspar for the quartz-feldspar geothermometer (see Chacko et al., 2001 for a review), and on the composition of the epidote for the quartz-epidote geothermometer (Matthews, 1994). For the quartz-feldspar geothermometer, the coefficient for quartz-albite and quartz-potassium feldspar is 0.94 whereas the coefficient for quartz-anorthite is 1.99. For compositions intermediate to the albite and anorthite end members, the fractionation coefficient is determined by the formula $A_{\text{quartz-plagioclase}} = A_{\text{quartz-albite}} + 1.05X_{An}$, where X_{An} is the anorthite component of the plagioclase (Matthews, 1994). For the quartz-epidote geothermometer, the fractionation coefficient for quartz-zoisite is 2.00. For epidote with a pistacite

component, the coefficient is determined by the formula $A_{quartz\text{-}epidote} = A_{quartz\text{-}zoisite} + 0.75X_{ps}$, where X_{ps} is the mole fraction of pistacite (Matthews, 1994).

The anorthite and pistacite contents were estimated from the semi-quantitative EDS data collected from feldspar and epidote, respectively, in sample SCM-51 (see Chapter 5). Because both potassium and plagioclase feldspar were included in the feldspar separates that were analyzed for oxygen isotope compositions, the quartz-feldspar geothermometry was performed using anorthite contents between 0% (for potassium feldspar) and 20% (for the plagioclase feldspar). The quartz epidote-geothermometry was performed using pistacite contents of 18-26%. These contents were calculated with the assumption that all of the iron in the epidote that was analyzed by EDS is Fe^{3+}, which is a reasonable assumption since Fe^{2+} tends to be extremely low in most epidote minerals (Franz and Liebscher, 2004).

B.2 RESULTS

The quartz-feldspar geothermometer, which was used on samples from two shear zones affected by bleaching, yielded temperatures of ~400-475 °C for sample HQ-B (without vein) and ~400-465 °C for sample SCM-51 (with vein; Table B.1). The quartz-epidote geothermometer yielded a temperature of ~440-450 °C for sample SCM-51 (with vein), which is within the range of the quartz-feldspar temperature estimates. These temperatures are typical of greenschist-facies conditions.

B.3 DISCUSSION

At high temperatures (>600 °C), the oxygen diffusion coefficients of quartz and feldspar are within an order of magnitude of each other, whereas at lower temperatures, the diffusion coefficients deviate, and the oxygen in quartz diffuses at a much slower rate than in feldspar (Giletti and Yund, 1984). This difference in exchange rate causes a

difference in the oxygen isotopic closure temperatures of the two minerals. The exact closure temperatures for the minerals will differ for different rocks in different settings, and will depend on a number of factors, including cooling rates, grain sizes, the presence of fluids, deformation and recrystallization experiences, water fugacity, and mineral modes (Valley, 2001). In general, a slower cooling rate, smaller grain size, deformation, and recrystallization all tend to result in lower closure temperatures.

Many different factors determine the oxygen isotope values of minerals, and make the correlation of oxygen isotope fractionation temperatures to deformation events challenging. Three main conditions must be met for deformation temperatures to be recorded in the isotope fractionation record of mineral pairs (O'Hara et al., 1997): 1) the deformation temperature must not be higher than the closure temperature of the system (otherwise exchange will occur until the rocks cool below the closure temperature); 2) the deformation must result in isotopic re-equilibration; and 3) the system cannot experience further isotopic disruption after deformation has ceased.

Determining if the first condition above has been met is difficult. The mechanical and chemical processes that operate during mylonitization, such as fracturing, recrystallization, and neocrystallization, tend to result in smaller grain sizes of both quartz and feldspar. As grain size gets smaller, the closure temperatures for the minerals will lower (Dodson, 1973). If the deformation occurs at a temperature above the closure temperatures of the minerals in the rock, then the temperature of the mylonitic system will be the temperature at which the second to last mineral to close is reached (O'Hara et al., 1997). If the rock is mica-rich, then the feldspar and mica would continue to exchange after quartz had closed. Exchange would stop only after either mica or feldspar closed, whichever occurred first. If, on the other hand, the granite is mica-poor and feldspar- and quartz-rich, then the feldspar could only undergo limited exchange with the

mica and the quartz-feldspar thermometer would produce the closure temperature of the quartz.

O'Hara et al. (1997) calculated closure temperatures for feldspar, mica, and quartz with grain sizes on the scale of tens of microns to thousands of microns using Dodson's (1973) closure temperature model. The finest grained feldspars (30 μm radii) closed at ~145 °C, and the coarsest grained feldspars (5000 μm radii) closed at ~330 °C. The micas (50-100 μm radii) closed at ~220-260 °C. Fine grained quartz (15 μm radii) closed at ~360 °C, whereas coarser grained quartz (500 μm radii) closed at ~470 °C. In the Harquahala study area, both the quartz and the feldspar grains in the bleached portion of the discrete shear zone sample SCM-51 are similar in size to the coarser grains in the O'Hara et al. (1997) study and therefore should have similar closure temperatures.

The quartz and feldspar grains picked from sample SCM-51 for isotope analysis were picked from the mica-poor bleached zone, so the temperature calculated (400-465 °C) may well be the closure temperature of quartz in the sample. If deformation occurred at a temperature above the quartz closure temperature, as suggested by the mineralogy and microstructures (see Chapter 3), then it would not be the temperature preserved in the mineral pair isotope values. If the deformation occurred at a temperature similar to or below the quartz closure temperature, then the calculated temperature would give the temperature of deformation.

The other sample analyzed from a discrete shear zone that was also affected by bleaching (HQ-B) provided a similar temperature (400-475 °C) as sample SCM-51. However, this sample was comprised of a significant amount of biotite, so it is unusual the system did not record a lower temperature because the feldspar and biotite should have continued to exchange. Some of the biotite was coarser grained than that analyzed by O'Hara et al. (1997), which would result in a higher closure temperature, but perhaps

a better explanation is that the sample was not at isotopic equilibrium. Isotopic homogenization of a system is only achieved if extensive neocrystallization or recrystallization occurs during deformation to produce strain-free grains. In the analyzed portions of samples SCM-51 and HQ-B, many of the feldspar grains are fractured and display undulatory extinction, and many are only partially replaced by myrmekite and non-symplectic oligoclase. Many of the quartz grains also display undulatory extinction and some grains exhibit evidence for lattice reorientation as they appear to have been deformed into elongate ribbon grains. Some grains also exhibit minor subgrain development, but not extensive SGR recrystallization. These features indicate the quartz is strained, and although some recovery has occurred, it is not extensive. Both quartz and feldspar grains in the samples, therefore, are likely not isotopically homogeneous and therefore should not be expected to produce reliable geothermometry results.

The third condition that the isotopic system is not disrupted again after the cessation of deformation appears to be met. If the Harquahala Mountain shear zones are related to MCC deformation, they have not undergone further deformation. If they are Late Cretaceous in age, then they would have been subsequently uplifted and exposed during Miocene MCC unroofing. However, evidence of further deformation that would have affected the isotopic compositions is lacking.

In summary, the temperatures calculated by the oxygen isotope geothermometers would only represent the deformation temperature of the mylonites if the deformation occurred near or below the closure temperature for quartz, and if the system was isotopically re-equilibrated during deformation, both of which appear unlikely for these rocks. Alternatively, the temperatures may represent the closure temperature for quartz, in which case the temperatures may be viewed as a minimum estimate of a deformation temperature (O'Hara et al., 1997). The three temperatures provided by the isotope

thermometers for the study area samples are strikingly consistent, which may indicate they are meaningful, but the strained condition of the minerals suggests the system may not have re-equilibrated. Regardless, the temperatures yielded by the geothermometers are not the peak temperatures for deformation.

Sample	Quartz $\delta^{18}O$ (‰)	Feldspar $\delta^{18}O$ (‰)	Epidote $\delta^{18}O$ (‰)	$\Delta_{Qtz-Fsp}$ (‰)	$\Delta_{Qtz-Epid}$ (‰)	Geothermometry			
						Qtz-$Epid_{1a}$ (°C)	Qtz-$Epid_{2e}$ (°C)	Qtz-An_0 (°C)	Qtz-An_{20} (°C)
H2	9.40±0.05‰	7.83±0.05	-	1.57	-	-	-	-	-
SCV-6	9.10±0.06‰	6.48±0.25	2.57±0.06	2.62	6.53	-	-	325	396
B-4	9.20±0.05‰	7.63±0.05	-	1.57	-	-	-	-	-
H1	8.51±0.05‰	8.15±0.05	-	0.36	-	-	-	-	-
SCV-51	9.03±0.06‰	6.52±0.25	4.83±0.06	2.11	4.2	440	450	395	465
HQ-B	9.48±0.06‰	7.43±0.25	-	2.05	-	-	-	-	-
B-3	9.68±0.05‰	8.13±0.05	-	1.55	-	-	-	-	-
B-9	9.35±0.05‰	8.00±0.05	-	1.35	-	-	-	-	-

Table B.1: Summary table of oxygen isotope data and geothermometry results. Quartz-feldspar geothermometry was performed using anorthite contents of 0% and 20%. Quartz-epidote geothermometry was performed using pistacite contents of 18% and 26%.

References

Abbott, R., and Draper, G., 2007, Petrogenesis of UHP eclogite from the Cuaba Gneiss, Rio San Juan Complex, Dominican Republic: International Geology Review, v. 49, p. 1069-1093.

Allmendinger, R., Cardozo, N. and Fisher, D., 2012, Structural geology algorithms: Vectors and tensors: Cambridge University Press, Cambridge, 301 p.

Anderson, J., 1988, Core complexes of the Mojave-Sonoran desert: Conditions of plutonism, mylonitization, and decompression, in: Ernst, W. (Ed.), Metamorphism and Crustal Evolution of the Western United States: Prentice-Hall, Englewood Cliffs, p. 503-525.

Anderson, J., Barth, A., and Young, E., 1988, Mid-crustal Cretaceous roots of Cordilleran metamorphic core complexes: Geology, v. 16, p. 366-369.

Asmerom, Y., Damon, P., Shafiqullah, M., Dickinson, W., and Zartman, R., 1991, Resetting of Rb-Sr ages of volcanic rocks by low-grade burial metamorphism: Chemical Geology, v. 87, p. 167-173.

Barth, N., Hacker, B., Seward, G., Walsh, E., Young, D., and Johnston, S., 2010, Strain within the ultrahigh-pressure Western Gneiss region of Norway recorded by quartz CPOs, in: Law, R., Butler, R., Holdsworth, R., Krabbendam, M. and Strachan, R. (Eds.), Continental Tectonics and Mountain Building: The Legacy of Peach and Horne: Geological Society, London, Special Publications, v. 335, p. 663-685.

Bisnath, A., McCourt, S., Frimmel, H., and Buthelezi, S., 2008, The metamorphic evolution of mafic rocks in the Tugela Terrane, Natal Belt, South Africa: South African Journal of Geology, v. 111, p. 369-386.

Boettcher, S., and Mosher, S., 1998, Mid- to Late Cretaceous ductile deformation and thermal evolution of the crust in the northern Dome Rock Mountains, Arizona: Journal of Structural Geology, v. 20, p. 745-764.

Bouchez, J., 1977, Plastic deformation of quartzites at low temperature in an area of natural strain gradient: Tectonophysics, v. 39, p. 25-50.

Bunge, H., 1982, Texture analysis in materials science: Mathematical models, Butterworths, London, 593 p.

Bykerk-Kauffman, A., 1990, Structural evolution of the northern Santa Catalina Mountains, Arizona: A glimpse of the pre-extension history of the Catalina complex [Ph.D. dissertation]: Tucson, University of Arizona, 195 p.

Chacko, T., Cole, D., and Horita, J., 2001, Equilibrium oxygen, hydrogen, and carbon isotope fractionation factors applicable to geologic systems, in: Valley, J., and Cole, D. (Eds.), Stable Isotope Geochemistry: Reviews in Mineralogy and Geochemistry, Mineralogical Society of America, v. 43, p. 1-81.

Chalokwu, C., and Kuehner, S., 1992, Mineral chemistry and thermobarometry of a southern Appalachian amphibolite with epidote + quartz symplectite: American Mineralogist, v. 77 p. 617-630.

Chiba, H., Chacko, T., Clayton, R., and Goldsmith, J., 1989, Oxygen isotope fractionations involving diopside, forsterite, magnetite, and calcite: Application to geothermometry: Geochimica et Cosmochimica Acta, v. 53, p. 2985-2995.

Christiansen, P., and Pollard, D., 1997, Nucleation, growth, and structural development of mylonitic shear zones in granitic rock: Journal of Structural Geology, v. 19, p. 1159-1172.

Clark, C., Schmidt Mumm, A., and Faure, K., 2005, Timing and nature of fluid flow and alteration during Mesoproterozoic shear zone formation, Olary Domain, South Australia: Journal of Metamorphic Geology, v. 23, p. 147-164.

Corfu, F., and Muir, T., 1989, The Hemlo-Heron Bay greenstone belt and Hemlo Au-Mo deposit, Superior Province, Ontario, Canada 2. Timing of metamorphism, alteration and Au mineralization from titanite, rutile, and monazite U-Pb geochronology: Chemical Geology (Isotope Geoscience Section), v. 79, p. 201-223.

Corfu, F., and Stone, D., 1998, The significance of titanite and apatite U-Pb ages: Constraints for the post-magmatic thermal-hydrothermal evolution of a batholithic complex, Berens River area, northwestern Superior Province, Cananda: Geochimica et Cosmochimica Acta, v. 62, p. 2979-2995.

Crowley, J., and Giletti, B., 1983, Patterns of oxygen isotope depletion, multiple hydrothermal circulation systems, and the cooling history of the Stony Mountain intrusive complex, Colorado: Earth and Planetary Science Letters, v. 64, p. 231-243.

Davis, G., Anderson, J., Martin, D., Krummenacher, Frost, E., and Armstrong, R., 1982, Geologic and geochronologic relationships in the lower plate of the Whipple detachment fault, Whipple Mountains, southeastern California: A progress report, in: Frost, E., and Martin, D. (Eds.), Mesozoic-Cenozoic Tectonic Evolution of the Colorado River Region, California, Arizona, and Nevada: Cordilleran Publishers, San Diego, p. 409-432.

Dodson, M., 1973, Closure temperature in cooling geochronological and petrological systems: Contributions to Mineralogy and Petrology, v. 40, p. 259-274.

Ferreira, V., Valley, J., Sial, A., Spicuzza, M., 2003, Oxygen isotope compositions and magmatic epidote from two contrasting metaluminous granitoids, NE Brazil: Contributions to Mineralogy and Petrology, v. 145, p. 205-216.

Fitz Gerald, J., and Stünitz, H., 1993, Deformation of granitoids at low metamorphic grade I: Reactions and grain size reduction: Tectonophysics, v. 221, p. 269-297.

Foster, D., Harrison, T., Miller, C., and Howard, K., 1988, Mesozoic and Cenozoic thermal history of the eastern Mojave Desert, California: Insights from 40Ar/39Ar geochronology: Geological Society of America Abstracts with Programs, v. 20, p. A-17.

Foster, D., Harrison, T., Miller, C., and Howard, K., 1990, The 40Ar/39Ar thermochronology of the Eastern Mojave Desert, California, and adjacent western Arizona with implications for the evolution of metamorphic core complexes: Journal of Geophysical Research, v. 95, p. 20,005-20,024.

Franz, G., and Liebscher, A., 2004, Physical and chemical properties of the epidote minerals: An introduction, in: Liebscher, A., and Franz, G. (Eds.), Epidotes: Reviews in Mineralogy and Geochemistry, Mineralogical Society of America, v. 56, p. 1-81.

Fricke, H., Wickham, S., and O'Neil, J., 1992, Oxygen and hydrogen isotope evidence for meteoric water infiltration during mylonitization and uplift in the Ruby Mountains-East Humboldt Range core complex, Nevada: Contributions to Mineralogy and Petrology, v. 111, p. 203-221.

Frost, B., Chamberlain, K., and Schumacher, J., 2000, Sphene (titanite): phase relations and role as a geochronometer: Chemical Geology, v. 172, p. 131-148.

Gao, X., Zheng, Y., Chen, Y., and Guo, J., 2012, Geochemical and U-Pb age constraints on the occurrence of polygenetic titanites in UHP metagranite in the Dabie orogen: Lithos, v. 136-139, p. 93-108.

Gapais, D., 1989, Shear structures within deformed granites: Mechanical and thermal indicators: Geology, v. 17, p. 1144-1147.

Gapais, D., and White, S., 1982, Ductile shear bands in a naturally deformed quartzite: Textures and Microstructures, v. 5, p. 1-17.

Gillespie, P., Johnston, J., Loriga, M., McCaffrey, K., Walsh, J., and Watterson, J., 1999, Influence of layering on vein systematics in line samples, in: MacCaffrey, K., Lonergan, L., and Wilkinson, J. (Eds.), Fractures, Fluid Flow and Mineralization: Geological Society, London, Special Publications, v. 155, p. 35-56.

Giletti, B., 1986, Diffusion effects on oxygen isotope temperatures of slowly cooled igneous and metamorphic rocks: Earth and Planetary Science Letters, v. 77, p. 218-228.

Giletti, B., and Yund, R., 1984, Oxygen diffusion in quartz: Journal of Geophysical Research, v. 89, p. 4039-4046.

Gleason, G., and DeSisto, S., 2008, A natural example of crystal-plastic deformation enhancing the incorporation of water into quartz: Tectonophysics, v. 446, p. 16-30.

Goncalves, P., Oliot, E., Marquer, D., and Connolly, J., 2012, Role of chemical processes on shear zone formation: an example from the Grimsel metagranodiorite (Aar massif, Central Alps): Journal of Metamorphic Geology, v. 30, p. 703-722.

Gregory, R., and Criss, R., 1986, Isotopic exchange in open and closed systems, in: Valley, J., Taylor, H., and O'Neil, J. (Eds.), Stable Isotopes in High Temperature Geological Processes: Reviews in Mineralogy, Mineralogical Society of America, v. 16, p. 91-127.

Gregory, R., Criss, R., and Taylor, H., 1989, Oxygen isotope exchange kinetics of mineral pairs in closed and open systems: Applications to problems of hydrothermal alteration of igneous rocks and Precambrian iron formations: Chemical Geology, v. 75, p. 1-42.

Griggs, D., and Blacic, J., 1965, Quartz: Anomalous weakness of synthetic crystals: Science, v. 147, p. 292-295.

Hardy, J., 1984, The structural geology, tectonics, and metamorphic geology of the Arrastre Gulch window, south-central Harquahala Mountains, Maricopa County, Arizona [M.S. thesis]: Flagstaff, Northern Arizona University, 99 p.

Harris, C., Faure, K., Diamond, R., and Scheepers, R., 1997, Oxygen and hydrogen isotope geochemistry of S- and I-type granitoids: the Cape Granite suite, South Africa: Chemical Geology, v. 143, p. 95-114.

Harrison, T., 1981, Diffusions of $^{40}Ar/^{39}Ar$ in hornblende: Contributions to Mineralogy and Petrology, v. 78, p. 324-331.

Harrison, T., Celerier, J., Aikman, A., Hermann, J., Heizler, M., 2009, Diffusion of 40Ar in muscovite: Geochimica et Cosmochimica Acta, v. 73, p. 1039–1051.

Hodges, K., and Walker, J., 1992, Extension in the Cretaceous Sevier orogeny, North American Cordillera: Geological Society of America Bulletin, v. 104, p. 560-569.

Hoisch, T., Miller, C., Heizler, M., Harrison, T., and Stoddard, E., 1988, Late Cretaceous regional metamorphism in southeastern California, in: Ernst, W. (Ed.), Metamorphism and Crustal Evolution of the Western United States: Prentice-Hall, Englewood Cliffs, p. 538-571.

Holyoke, C., and Tullis, J., 2006a, Formation and maintenance of shear zones: Geology, v. 34, p. 105-108.

Holyoke, C., and Tullis, J., 2006b, Mechanisms of weak phase interconnection and the effects of phase strength contrast on fabric development: Journal of Structural Geology, v. 28, p. 621-640.

Hooker, J., Laubach, S., Gomez, L., Marrett, R., Eichhubl, P., Diaz-Tushman, K., and Pinzon, E., 2011, Fracture size, frequency, and strain in the Cambrian Eriboll Formation sandstones, NW Scotland: Scottish Journal of Geology, v. 47, p. 45-56.

Howard, K., Stone, P., Pernokas, M. and Marvin, R., 1982, Geologic and geochronologic reconnaissance of the Turtle Mountains area, California: West border of the Whipple detachment terrane, in: Frost, E., and Martin, D. (Eds.), Mesozoic-Cenozoic Tectonic Evolution of the Colorado River Region, California, Arizona, and Nevada: Cordilleran Publishers, San Diego, p. 341-354.

Isachsen, C., Gehrels, G., Riggs, N., Spencer, J., Ferguson, C., Skotnicki, S., and Richard, S., 1999, U-Pb geochronologic data from zircons from eleven granitic rocks in central and western Arizona: Arizona Geological Survey Open-File Report 99-5, 27 p.

John, B., 1982, Geologic framework of the Chemehuevi Mountains, southeastern California, in: Frost, E., and Martin, D. (Eds.), Mesozoic-Cenozoic Tectonic Evolution of the Colorado River Region, California, Arizona, and Nevada: Cordilleran Publishers, San Diego, p. 317-325.

John, B., and Mukasa, S., 1990, Footwall rocks to the Mid-Tertiary Chemehuevi detachment fault: A window into the middle crust in the Southern Cordillera: Journal of Geophysical Research, v. 95, p. 463-485.

Kats, A., 1962, Hydrogen in alpha quartz: Philips Research Report, v. 17, p. 133-279.

Keane, S., and Morrison, J., 1997, Distinguishing magmatic from subsolidus epidote: laser probe oxygen isotope compositions: Contributions to Mineralogy and Petrology, v. 126, p. 265-274.

Kerrich, R., 1988, Detachment zones of Cordilleran metamorphic core complexes: thermal, fluid, and metasomatic regimes: Geologische Rundschau, v. 77, p. 157-182.

Kerrich, R., and Rehrig, W., 1987, Fluid motion associated with Tertiary mylonitization and detachment faulting: 18O/16O evidence from the Picacho metamorphic core complex, Arizona: Geology, v. 15, p. 58-62.

Kerrich, R., Rehrig, W., and Willmore, L., 1984, Deformation and hydrothermal regimes in the Picacho metamorphic core complex detachment—Arizona: Oxygen isotope evidence: EOS Transactions, American Geophysical Union, v. 65, p. 1124.

Knapp, J., 1989, Structural development, thermal evolution, and tectonic significance of a Cordilleran basement thrust terrane, Maria Fold and Thrust Belt, West-central Arizona [Ph.D. dissertation]: Cambridge, Massachusetts Institute of Technology, 262 p.

Kronenberg, A., 1994, Hydrogen speciation and chemical weakening of quartz, in: Heany, P., Prewitt, C., and Gibbs, G. (Eds.), Silica: Physical Behavior, Geochemistry, and Materials Applications: Reviews in Mineralogy, Mineralogical Society of America, v. 29, p. 123-176.

Kronenberg, A., and Wolf, G., 1990, Fourier transform infrared spectroscopy determinations of intragranular water content in quartz-bearing rocks: implications for hydrolytic weakening in the laboratory and within the earth: Tectonophysics, v. 172, p. 255-271.

Kronenberg, A., Segall, P., and Wolf, G., 1990, Hydrolytic weakening and penetrative deformation within a natural shear zone, in: Duba, A., Durham, W., Handin, J., and Wang, H. (Eds.), The Brittle-Ductile Transition in Rocks: The Heard Volume: American Geophysical Union Monograph, v. 56, p. 21-36.

Kruger, J., Faulds, E., and Reynolds, S., 2006, Seismic reflection crustal structure and 3-D geometry of Cordilleran metamorphic core complexes in West-Central Arizona: EOS Transactions, American Geophysical Union, v. 87 (52), Abstract S43A-1368.

Kuiper, N., 1960, Tests concerning random points on a circle: Proceedings of the Koninklijke Nederlandse Akademie van Wetenschappen, v. 63, p. 38-47.

Liou, J., Ernst, W., and Moore, D., 1981, Geology and petrology of some polymetamorphosed amphibolites and associated rocks in Northeastern Taiwan: Geological Society of America Bulletin: v. 92, p. 609-748.

Lister, G., and Dornsiepen, U., 1982, Fabric transitions in the Saxony granulite terrain: Journal of Structural Geology, v. 4, p. 81-92.

Lister, G., and Williams, P., 1979, Fabric development in shear zones: theoretical controls and observed phenomena: Journal of Structural Geology, v. 1, p. 283-297.

Livaccari, R., and Geissman, J., 2001, Large-magnitude extension along metamorphic core complexes of western Arizona and southeastern California: Evaluation with paleomagnetism: Tectonics, v. 20, p. 625-648.

Mainprice, D., 2005, PFch5 [Computer software], ftp://www.gm.univmontp2.

fr/mainprice//CareWare_Unicef_Programs/

Mancktelow, N., 2009, Fracture and flow in natural rock deformation: Trabajos de Geología, v. 29, p. 29-35.

Mancktelow, N., and Pennacchioni, G., 2005, The control of precursor brittle fracture and fluid-rock interaction on the development of single and paired ductile shear zones: Journal of Structural Geology, v. 27, p. 645-661.

Matthews, A., 1994: Oxygen isotope geothermometers for metamorphic rocks: Journal of Metamorphic Geology, v. 12, p. 211-219.

McDougall, I., and Harrison, T., 1999, Geochronology and Thermochronology by the 40Ar/39Ar Method, 2nd ed., Oxford University Press, New York, 288 p.

McQuarrie, N., and Chase, C., 2000, Raising the Colorado Plateau: Geology, v. 28, p. 91-94.

Menegon, L., Pennacchioni, G., and Stünitz, 2006, Nucleation and growth of myrmekite during ductile shear deformation in metagranites: Journal of Metamorphic Geology, v. 24, p. 553-568.

Morrison, J., 1994, Meteoric water-rock interaction in the lower plate of the Whipple Mountain metamorphic core complex, California: Journal of Metamorphic Geology, v. 12, p. 827-840.

Morrison, J., 2004, Stable and radiogenic isotope systematics in epidote group minerals, in: Liebscher, A., and Franz, G. (Eds.), Epidotes: Reviews in Mineralogy and Geochemistry, Mineralogical Society of America, v. 56, p. 607-628.

Muto, J., Nagahama, H., and Hashimoto, T., 2005, Water distribution in dynamically recrystallized quartz grains: cathodoluminescence and micro-infrared spectroscopic mapping, in: Bruhn, D., and Burlini, L. (Eds.), High-Strain Zones: Structure and Physical Properties: Geological Society, London, Special Publications, v. 245, p. 397-407.

Nakashima, S., Matayoshi, H., Yuko, T., Michibayashi, K., Masuda, T., Kuroki, N., Yamagishi, H., Ito, Y., and Nakamura, A., 1995, Infrared microspectroscopy analysis of water distribution in deformed and metamorphosed rocks: Tectonophysics, v. 245, p. 263-276.

Naney, M., 1983, Phase equilibria of rock-forming ferromagnesian silicates in granitic systems: American Journal of Science, v. 283, p. 993-1033.

Niimi, N., Aikawa, N., and Shinoda, K., 1999, The infrared absorption band 3596 cm-1 of the recrystallized quartz from Mt. Takamiyama, southwest Japan: Mineralogical Magazine, v. 63, p. 693-701.

O'Hara, K., Sharp, Z., Moecher, D., and Jenkin, G., 1997, The effect of deformation on oxygen isotope exchange in quartz and feldspar and the significance of isotopic temperatures in mylonites: The Journal of Geology, v. 105, p. 193-204.

Okudaira, T., Takeshita, T., Hara, I., and Ando, J., 1995, A new estimate of the conditions for transition from basal <a> to prism [c] slip in naturally deformed quartz: Tectonophysics, v. 250, p. 31-46.

Owen, J., 1991, Significance of epidote in orbicular diorite from the Grenville Front zone, eastern Labrador: Mineralogical Magazine, v. 55, p. 173-181.

Passchier, C., and Trouw, R., 2005, Microtectonics: Springer, Berlin Heidelberg, 366 p.

Paterson, M., 1989, The interaction of water with quartz and its influence in dislocation flow – an overview, in: Karato, S., and Toriumi, M. (Eds.), Rheology of Solids and of the Earth: Oxford University Press, Oxford, p. 107-142.

Pennacchioni, G., 2005, Control of the geometry of precursor brittle structures on the type of ductile shear zone in the Adamello tonalites, Southern Alps (Italy): Journal of Structural Geology, v. 27, p. 627-644.

Pennacchioni, G., and Mancktelow, N., 2007, Nucleation and initial growth of a shear zone network within compositionally and structurally heterogeneous granitoids under amphibolite facies conditions: Journal of Structural Geology, v. 29, p. 1757-1780.

Pidgeon, R., Bosch, D., and Bruguier, O., 1996, Inherited zircon and titanite U-Pb systems in Archaean syenite from southwestern Australia: implications for U-Pb stability of titanite: Earth and Planetary Science Letters, v. 141, p. 187-198.

Post, A., and Tullis, J., 1998, The rate of water penetration in experimentally deformed quartzite: implications for hydrolytic weakening: Tectonophysics, v. 295, p. 117-137.

Prior, M., and Stockli, D., 2013, Late extension inception and rapid fault-slip at the southern edge of the lower Colorado River extensional corridor: Harquahala Mountains core complex, west-central Arizona: Geological Society of America Abstracts with Programs, v. 45, p. 609.

Resor, P., Chamberlain, K., Frost, C., Snoke, A., and Frost, B., 1996, Direct dating of deformation: U-Pb age of syndeformational sphene growth in the Proterozoic Laramie Peak shear zone: Geology, v. 24, p. 623-636.

Reynolds, S., and Lister, G., 1987, Structural aspects of fluid-rock interactions in detachment zones: Geology, v. 15, p. 362-366.

Reynolds, S., and Spencer, J., 1985, Evidence for large-scale transport on the Bullard detachment fault, west-central Arizona: Geology, v. 13, p. 353-356.

Reynolds, S., Okaya, D., Kruger, J., Faulds, J., Potochnik, A., 1994, Three-dimensional geometry of detachment faults and metamorphic core complexes from industry seismic reflection profiles, western and central Arizona: Geological Society of America Abstracts with Programs, v. 26, p. A-250.

Reynolds, S., Richard, S., Haxel, G., Tosdal, R., and Laubach, S., 1988, Geologic setting of Mesozoic and Cenozoic metamorphism in Arizona, in: Ernst, W. (Ed.), Metamorphism and Crustal Evolution of the Western United States: Prentice-Hall, Englewood Cliffs, p. 466-501.

Reynolds, S., Spencer, J., Richard, S., and Laubach, S., 1986, Mesozoic structures in west-central Arizona, in Beatty, B. and Wilkinson, P. (Eds.), Frontiers in Geology and Ore Deposits of Arizona and the Southwest, Arizona Geological Society Digest, v. 16, p. 35-51.

Richard, S., 1988, Bedrock Geology of the Harquahala Mountains, West-Central Arizona: Mesozoic shear zones, cooling, and Tertiary unroofing [Ph.D. dissertation]: Santa Barbara, University of California, 277 p.

Richard, S., Fryxell, J., and Sutter, J., 1990, Tertiary Structure and Thermal History of the Harquahala and Buckskin Mountains, West Central Arizona: Journal of Geophysical Research, v. 95, p. 19973-19987.

Richard, S., McWilliams, M., and Gans, P., 1998, 40Ar/39Ar dates from the Harquahala and Little Harquahala Mountains, west-central Arizona. Part I: Arizona Geological Survey Open File Report, OFR-98-25, 25 p.

Schmid, S., and Casey, M., 1986, Complete fabric analysis of some commonly observed quartz c-axis patterns, in: Hobbs, B., and Heard, C. (Eds.), Mineral and rock deformation: Laboratory studies: The Paterson volume, American Geophysical Union Monograph, v. 36, p. 246-461.

Schmidt, M., and Poli, S., 2004, Magmatic epidote, in: Liebscher, A., and Franz, G. (Eds.), Epidotes: Reviews in Mineralogy and Geochemistry, Mineralogical Society of America, v. 56, p. 1-81.

Scott, D., and St-Onge, M., 1995, Constraints on Pb closure temperature in titanite based on rocks from the Ungava orogen, Canada: Implications for U-Pb geochronology and P-T-t path determinations: Geology, v. 23, p. 1123-1126.

Segall, P., and Simpson, C., 1986, Nucleation of ductile shear zones on dilatant fractures: Geology, v. 14, p. 56-59.

Siddiqui, M., and Ahmed, Z., 2005, Mineralogy of the Swat kaolin deposits: The Arabian Journal for Science and Engineering, v. 30, p. 195-218.

Simpson, C. 1985, Deformation of granitic rocks across the brittle-ductile transition: Journal of Structural geology, v. 7, p. 503-511.

Simpson, C., and Wintsch, R., 1989, Evidence for deformation-induced K-feldspar replacement by myrmekite: Journal of Metamorphic Geology, v. 7, p. 261-275.

Singleton, J., 2011, Kinematic and geometric evolution of the Buckskin-Rawhide metamorphic core complex, west-central Arizona [Ph.D. dissertation]: Austin, University of Texas, 235 p.

Singleton, J., and Mosher, S., 2012, Mylonitization in the lower plate of the Buckskin-Rawhide detachment fault, west-central Arizona: Implications for the geometric evolution of metamorphic core complexes: Journal of Structural Geology, v. 39, p. 180-198.

Smith, B., and Reynolds, S., 1985, Oxygen and hydrogen isotope study of mylonitization and detachment faulting, South Mountains, central Arizona: EOS Transactions, American Geophysical Union, v. 66, p. 1138.

Smith, B., Reynolds, S., Day, H., and Bodnar, R., 1991, Deep-seated fluid involvement in ductile-brittle deformation and mineralization, South Mountain metamorphic core complex, Arizona: Geological Society of America Bulletin, v. 103, p. 559-569.

Spencer, J., and Reynolds, S., 1989, Tertiary structure, stratigraphy, and tectonics of the Buckskin Mountains, in: Spencer, J., and Reynolds, S. (Eds.), Geology and mineral resources of the Buckskin and Rawhide Mountains, west-central Arizona: Arizona Geological Survey Bulletin 198, p. 103-167.

Spencer, J., and Reynolds, S., 1990, Relationship between Mesozoic and Cenozoic tectonic features in West Central Arizona and adjacent Southeastern California: Journal of Geophysical Research, v. 95, p. 539-555.

Spencer, J., and Reynolds, S., 1991, Tectonics of mid-Tertiary extension along a transect through west central Arizona: Tectonics, v. 10, p. 1204-1221.

Spencer, K., Hacker, B., Kylander-Clark, A., Andersen, T., Cottle, J., Stearns, M., Poletti, J., and Seward, G., 2013, Campaign-style titanite U-Pb dating by laser-ablation ICP: Implications for crustal flow, phase transformations and titanite closure: Chemical Geology, v. 341, p. 84-101.

Stipp, M., Stünitz, H., Heilbronner, R., Schmid, S., 2002, The eastern Tonale fault zone: a ‘natural laboratory’ for crystal plastic deformation of quartz over a temperature range from 250 to 700 °C: Journal of Structural Geology, v. 24, p. 1861-1884.

Stüwe, K., 1998, Tectonic constraints on the timing relationships of metamorphism, fluid production and gold-bearing quartz vein emplacement: Ore Geology Reviews, v. 13, p. 219-228.

Taylor, H., 1968, The oxygen isotope geochemistry of igneous rocks: Contributions to Mineralogy and Petrology, v. 19, p. 1-71.

Taylor, H., 1973, O18/O16 evidence for meteoric-hydrothermal alteration and ore deposition in the Tonopah, Comstock Lode, and Goldfield Mining Districts, Nevada: Economic Geology, v. 68, p.747-764.

Taylor, H., and Sheppard, S., 1986, Igneous rocks: I. Processes of isotopic fractionation and isotope systematics, in: Valley, J., Taylor, H., and O’Neil, J. (Eds.), Stable Isotopes in High Temperature Geological Processes: Reviews in Mineralogy, Mineralogical Society of America, v. 16, p. 227-271.

Taylor, H., 1990, Oxygen and hydrogen isotope constraints on the deep circulation of surface waters into zones of hydrothermal metamorphism and melting, in: The Role of Fluids in Crustal Processes: National Academy Press, Washington, DC, p. 72-95.

Tourigny, G., and Tremblay, A., 1997, Origin and incremental evolution of brittle/ductile shear zones in granitic rocks: natural examples from the southern Abitibi Belt, Canada: Journal of Structural Geology, v. 19, p. 15-21.

Toy, V., Prior, D., and Norris, R., 2008, Quartz fabrics in the Alpine Fault mylonites: Influence of preexisting preferred orientations on fabric development during progressive uplift: Journal of Structural Geology, v. 30, p. 602-621.

Tsurumi, J., Hosonuma, H., and Kanagawa, K., 2003, Strain localization due to a positive feedback of deformation and myrmekite-forming reaction in granite and aplite mylonites along the Hatagawa Shear Zone of NE Japan: Journal of Structural Geology, v. 25, p. 557-574.

Tullis, J., 2002, Deformation of granitic rocks: Experimental studies and natural examples, in: Karato, S., and Wenk, H. (Eds.), Plastic Deformation of Minerals and Rocks: Reviews in Mineralogy and Geochemistry, Mineralogical Society of America, v. 51, p. 51-95.

Valley, J., 2001, Stable isotope thermometry at high temperatures, in: Valley, J., and Cole, D. (Eds.), Stable Isotope Geochemistry: Reviews in Mineralogy and Geochemistry, Mineralogical Society of America, v. 43, p. 365-413.

Vernon, R., 1991, Questions about myrmekite in deformed rocks: Journal of Structural Geology, v. 13, p. 979-985.

Vernon, R., 2004, A Practical Guide to Rock Microstructures: Cambridge University Press, Cambridge, 606 p.

Vernon, R., Williams, V., and D'Arcy, W., 1983, Grain-size reduction and foliation development in a deformed granitoid batholith: Tectonophysics, v. 92, p. 123-145.

Verts, L., Chamberlain, K., and Frost, C., 1996, U-Pb sphene dating of metamorphism: the importance of sphene growth in the contact aureole of the Red Mountain pluton, Laramie Mountains, Wyoming: Contributions to Mineralogy and Petrology, v. 125, p. 186-199.

Vollmer, F., 1990, An application of eigenvalue methods to structural domain analysis: Geological Society of America Bulletin, v. 102, p. 786-791.

Wells, M., and Hoisch, T., 2008, The role of mantle delamination in widespread Late Cretaceous extension and magmatism in the Cordilleran orogeny, western United States: Geological Society of America Bulletin, v. 120, p. 515-530.

White, S., Burrows, S., Carreras, J., Shaw, N., and Humphreys, F., 1980, On mylonites in ductile shear zones: Journal of Structural Geology, v. 2, p. 175-187.

Wickham, S., and Taylor, H., 1990, Hydrothermal systems associated with regional metamorphism and crustal anatexis: Examples from the Pyrenees, France, in: The Role of Fluids in Crustal Processes: National Academy Press, Washington, D.C., p. 96-112.

Wintsch, R., and Yi, K., 2002, Dissolution and replacement creep: a significant deformation mechanism in mid-crustal rocks: Journal of Structural Geology, v. 24, p. 1179-1193.

Wong, M., Singleton, J., Baughman, J., and Bunting, K., 2013, Evidence for Miocene reactivation of a Late Cretaceous to Early Tertiary shear zone in the Harcuvar and Buckskin-Rawhide metamorphic core complexes, Arizona: Geological Society of America Abstracts with Programs, v. 45, p. 523.

Žák, K., Pudilová, M., and Breiter, K., 2005, Oxygen isotope study of the highly fractionated Podlesí granite system, Krušné hory Mts., Czech Republic: Bulletin of Geosciences, v. 80, p. 139-143.

Zen, E., and Hammarstrom, J., 1984, Magmatic epidote and its petrologic significance: Geology, v. 12, p. 515-518.